THERMAL DECOMPOSITION OF BARIUM TITANYL OXALATE MIXTURES AND THE APPLICATIONS OF THE NANOPRODUCTS

Thesis submitted to
the University of Calicut in partial fulfillment of
the requirements for the award of the degree of

DOCTOR OF PHILOSOPHY IN CHEMISTRY

SINDHU N. V.

DEPARTMENT OF CHEMISTRY
UNIVERSITY OF CALICUT
KERALA- 673 635
SEPTEMBER-2018

CERTIFICATE

This is to certify that the dissertation, entitled **"Thermal decomposition of barium titanyl oxalate mixtures and the applications of the nanoproducts"**, submitted to the University of Calicut, in partial fulfillment of the requirements for the award of the **Degree of Doctor of Philosophy in Chemistry** is a bonafide record of research work done by **Ms. SINDHU N. V.** during the period **2012-2018** in the Department of Chemistry at University of Calicut, under my supervision and guidance and the thesis has not formed the basis for the award of any Degree / Diploma / Associateship / Fellowship or other similar title to any candidate of any University.

University of Calicut
24.09. 2018

Dr. K. Muraleedharan
Professor
Department of Chemistry
University of Calicut

CERTIFICATE

This is to certify that the dissertation, entitled **"Thermal decomposition of barium titanyl oxalate mixtures and the applications of the nanoproducts"**, submitted to the University of Calicut, in partial fulfillment of the requirements for the award of the **Degree of Doctor of Philosophy in Chemistry** is a bonafide record of research work done by **Ms. SINDHU N. V.** during the period **2012-2018** in the Department of Chemistry at University of Calicut, under my supervision and guidance and the thesis has not formed the basis for the award of any Degree / Diploma / Associateship / Fellowship or other similar title to any candidate of any University. I also hereby certify that the corrections/suggestions from the adjudicators have been incorporated in the revised thesis. Content of the CD submitted and the hardcopy of the thesis is one and the same.

University of Calicut
24.09. 2018

Dr. K. Muraleedharan
Professor
Department of Chemistry
University of Calicut

DECLARATION

I, **Sindhu N. V.**, hereby declare that the thesis, entitled **"Thermal decomposition of barium titanyl oxalate mixtures and the applications of the nanoproducts"**, submitted to the University of Calicut, is a bona fide record of research work done by me during the period **2012-2018** under the supervision and guidance of **Dr. K. Muraleedharan**, Professor, Department of Chemistry, University of Calicut and the same has not formed the basis for the award of any Degree / Diploma / Associateship / Fellowship or other similar title to any candidate of any University**.**

University of Calicut, **Sindhu N. V.**
24. 09. 2018

AKNOWLEDGEMENTS

First of all, I would like to express my sincere and hearty gratitude to Dr. K. Muraleedharan, Professor, Department of Chemistry, University of Calicut, for his timely guidance, encouragement, motivation and support from the introductory to the concluding level, which enabled me to accomplish my research.

I would like to thank Dr. P. Raveendran, Head of the Department of Chemistry, University of Calicut, and Dr. V. M. Abdul Mujeeb, former Head of the Department of Chemistry, University of Calicut for providing me with adequate facilities in this regard.

I would like to make a special reference to my teacher Dr. M. P. Kannan, retired Professor, Former Head of the Department of Chemistry, University of Calicut, for his support and inspiration. I thank Dr. P. P. Pradyumnan, Associate Professor, Department of Physics, University of Calicut, for carrying out the XRD analysis and also to Central Sophisticated Instrumentation Facility (CSIF), University of Calicut and Sophisticated Test and Instrumentation Centre (STIC), CUSAT for carrying out the FE-SEM, SEM and TEM analysis which facilitated in completing my research work in time. I also thank Dr. P. R. Manish Kumar, Professor & Ms. Ahlam Abdul Aziz, Department of Biotechnology, University of Calicut for helping me in conducting the antibacterial studies.

I wish to express my warm and sincere thanks to Dr. K. G. Krishnamohan, Assistant Professor, Marbaselios College of Engineering and Technology, Nalanchira, Trivandrum to introduce me into the world of VASP in computational chemistry. I acknowledge Dr.

Raghu Chathanathodi, Associate Professor, Computational materials sciences, NIT Calicut since he clarified many introductory doubts in the area, VASP. I also thank Dr. A Sujith, Department of Chemistry, NIT Calicut, and Mr. V. Omprakash, Publication officer, University of Calicut for their timely help. I would also like to mention the names of Dr. K. Sarada, Assistant Professor, Govt. College Chittur, Palakkad, and Jayan Manual, Research Scholar NIT Calicut, for helping me a lot during the research period.

It is my ardent wish to acknowledge the enthusiastic support and valuable inputs offered to me by my group members Nusrath K., Vijisha K. Rajan, Shameera Ahammad T. K., Sabira K., Sivanad C. K., Elsy shareena and other lab mates especially Jyothi P. R., Jaseela P. K. for giving their valuable suggestions and support. I also extend my sincere thanks to all other faculty members and non teaching staff of the Department of Chemistry, University of Calicut, for their help, cooperation and support.

Words cannot express how grateful I am to my father: Mr. N. Vasu (retired teacher), mother: Mrs. M. K. Omana and my sisters; and they have always supported my dreams and aspirations. I also thank my husband Mr. P. Balamuralikrishna, for his spontaneous support and encouragement that lead me ahead.

Above all; my heartful gratitude is to the Almighty to be the light on my way, in pursuit of knowledge.

Sindhu N. V.

CONTENTS

CHAPTER 1

INTRODUCTION

1.1 General introduction

Why "*nano*"? In the quest for this, a substantial research attention has been focused over the past few years on the development of '*nanomaterials*'. It is part of the new materials invented. '*New materials*' refers to all those novel materials capable of bringing about revolutions the current material world and can provide new colours to material chemistry. They are with specific features and are considered as the backbone of modern devices. The discovery and design of 'new *materials*'; *i.e*., new alloys, composite materials, optical fibers, polymers and plastics, nano materials, biomaterials, newer semiconducting materials, ceramic materials, dielectric materials, smart materials *etc*. are utilized for technological development [1]. Many scientists and researchers still focus on these materials which form the most challenging area of scientific and technologic research because of their fabulous potentials associated with them [2]. These new materials often possess unique electric, magnetic, optical, catalytic, sensing, super conducting and plasmonic properties that provide for biomedical purposes also [3-5].

Recently, a synthesis on '*nanomaterials*' has become a focal area in materials research, due to their many superior properties than the bulk properties: mechanical strength, thermal stability, photo catalytic activity, electrical conductivity, magnetic properties and optical properties [6]. These properties of '*nanomaterials*' can be different at the nano scale for the reasons: '*nanomaterials*' have a relatively larger surface properties when compared to the same mass of material produced in a larger form. Nanoparticles can make materials

chemically more reactive and affect their strength, and also quantum effects can begin to dominate the behavior of matter at the '*nanometer length scale*' and exploitation of novel properties (physical, chemical, biological) at that length scale. These particles have special physical and chemical properties as compared to their bulk materials due to their large reactive and surface area. They are broadly used in many fields such as chemistry, electronics, photochemisty, and in biomedicine [7-8].

Nanoparticles are promising multifunctional molecules; and are used for wide range of imaging and therapeutic functions [9-10]. Nanoparticles deal with a wide area including electronics, medicine, food industry, environmental, cosmetics applications, *etc.* [11]. Generally, a physical approach is required to modify or to pick up the pharmacodynamics and pharmacokinetic property of drugs. Scattering of preformed polymerization of monomers and ionic gelation or coacervation of hydrophilic polymer, polymers are a variety of techniques used for synthesis of nanoparticles [12-13]. Nanoparticle plays a vital role in opportunities and possibilities for the growth of sensing tools. In last decade, sensing of selective biomolecules using functionalized gold nanoparticles has become a major research power. Gold nano particles based on biosensors are likely to alter the very basics of sensing and detecting biomolecules [14]. Nanoparticles are used for different purposes, from medical treatment, used in a mixture of branches of industry fabrication such as oxide fuel batteries for energy storage and solar, large range materials on a daily basis life such as cosmetics and textiles [15]. Large surfaces of nanoparticles

are capable to join, absorb, transmit further compounds for example drugs, proteins, *etc*. They might be chemically more reactive because of their surface, compared to their well analogues [16-18].

Thermal decomposition of alkaline earth metal titanyl oxalate yields–titanate nanoparticles. Hence metal titanyl oxalates act as precursors for the synthesis of titanate nanoparticles. Further, these titanates have industrial uses and many analytical applications. The new developments in modern industries have generated an increasing need for new types of materials. In this respect, the application of mixed metal oxides as catalytic, photo catalytic, photoelectric, and dielectric materials has shown tremendous promise [19-22]. Metal oxides exhibit very diverse properties, including optical, electrical, magnetic, *etc*. They have high hardness, high chemical resistance, and high thermal stability. These oxides have been widely used as ceramics, electronics, catalysts, and coatings. It has found numerous applications because of its use as an optical material, thermal and electrical insulator, and material with high hardness and chemical stability.

Ferroelectric and dielectric oxides of perovskite structure ($MTiO_3$) are widely used in electronics. The perovskite lead zirconate titanate ($PbZr_{1-x}Ti_xO_3$) is a ferroelectric and piezoelectric material. $SrTiO_3$ is used for high Curie temperature superconducting films. Highly porous oxide materials like silica [23] and titania [24, 25] synthesized by sol gel process have also received much attention recently because of their application in low-loss dielectrics, catalysis, filtering and photonics. High surface areas of the porous materials

yield good agents for catalysis. These materials have very low density and can be used for low-loss electronic devices due to a very low dielectric constant. Semiconducting oxides have band gaps in the UV light spectrum. Titanium oxide (TiO_2) is one of the most promising wide-band-gap (respectively 3.2 and 3.0 eV for anatase and rutile phase) materials which has been used as a pigment because of its refractive index, absence of absorption of visible light, stability, and nontoxicity [26]. Titania did not find applications for structural ceramics due to its poor fracture toughness. However, it is widely used as the catalyst support for different oxides such as molybdena, tungsta, and vanadia [27]. This catalyst has been used for selective oxidation of hydrocarbons, decomposition of isopropanol, ammoxidation of aromatic hydrocarbons, and reduction of nitric acid [27, 28]. UV light illumination of the TiO_2 surfaces using light with higher energy than the TiO_2 band gap (shorter than 410 nm for rutile phase and 385 nm for anatase phase) causes the photoexitation of electrons from the valence band (O^{2-} 2p-orbitals) to the unoccupied conduction band (Ti^{4+} 3d-orbitals) [26]. Light irradiation causes a production of the highly active holes and increases the photocatalytic and photooxidative activity of titanium oxide. Some mixed-metal oxides ($BaCeO^{3-}$, $BaPb_{1-x}Bi_xO^{3-}$, $CaTiO_3$) can conduct ions and transport oxygen due to oxide ion mobility [29]. They conduct electrons and oxide ions and supply oxygen from the oxide to surface which allows for oxidizing different hydrocarbons [30, 31].

Currently, researchers in the area of chemistry, physics, biochemistry, and engineering explore a new class of nanosized

catalysts for applications in various fields [32]. These nanocatalysts have many applications in our daily life which are more useful for human beings. Salini *et al*., discussed the various application of nano sized catalyst in water purification; fuel cell; energy storage; in composite solid rocket propellants; bio diesel production; in medicine, in dye; application of carbon nano tubes in biological fields, *etc*. [33]. Gobara *et al*., prepared alumina- supported metal nano catalyst *via* the microwave method and it could be applied in different petrochemical processes [34].

A growing knowledge in nanocrystals research allows the production of different materials on the nanometer scale, a better understanding of their properties, and control of their synthesis. The novel and unique properties of nanomaterials are a result of the finite-size effect when the electronic bands are converted into molecular orbital with the decrease in particle sizes. In nanoparticles, a high number of particle atoms are located on the surface of the grains or interface boundaries, and hence the physical and chemical properties of nanomaterials are different from the isolated atoms or bulk materials. One of the specific properties of nanomaterials is the surface-to-volume ratio. This size dependent effect includes a high percentage of surface atoms. The high distribution of electrons confines the quantized energy levels. This quantum confinement is used in semiconductors and optoelectronics. A high percentage of surface atoms lead to an increase in surface activity. In addition, the highly exposed surface stimulates the chemical reactions and promotes the catalysis.

Recently, an increasing number of studies have been focused on the exploitation of nanoparticles especially barium titanate nano particles (BTNPs) in the biomedical field, owing to the high biocompatibility of BTNPs and their peculiar non-linear optical properties that have encouraged their use as nanocarriers for drug delivery and as label-free imaging probes [35]. The exploration of BTNP potential in biomedical/therapeutic applications, such as cancer therapy through hyperthermia, and drug/gene delivery, has recently started in nanomedicine, based on the encouraging results observed in the biocompatibility assessments [36]. In another study, Städler *et al.* [37] investigated cellular responses to five non-linear active nanomaterials, including BTNPs, in order to discover the best candidate for biomedical imaging.

There are many methods which can be employed for the preparation of BTNPs such as so-gel [38], combustion [39], crystal growth [40], thermal decomposition [41] and different chemical route [42]. Among these, thermal decomposition using oxalate precursor has been widely used due to its simplicity and the precise stoichiometry of the produced BT phase. Barium titanyl oxalate is the best precursor for the preparation of BTNPs *via* thermal decomposition. Thermal decomposition studies on oxalates seem pertinent because they have industrial uses, many analytical applications and because in many ways their thermal stability and decomposition serve as examples for the decompositions of many other oxysalts. A review on the thermal decomposition of some solid oxalates has been given by Harris and colleagues [43]. The aware of kinetic parameters, the reaction rate and

activation energy of the thermal decomposition reaction is used to determine the reaction mechanisms in solid-state phases. When changes in the mechanisms are observed, this can lead to a unique characteristic and hence a better knowledge of the materials. Besides this, there are also more practical reasons to know the reaction rates and their temperature dependence. Using an appropriate approximation method, the thermo-analytical experiments can be applied for the tuning of industrial thermal processes. The outputs of the kinetic study of thermo-analytical reactions in the solid state can also be applied to problems such as useful lifetime of certain components, oxidative and thermal stability and quality control.

1.2 Review of literature

The thermal decomposition of a large number of bivalent metal titanyl oxalates has been studied [44]. At higher temperatures, these compounds yield the corresponding metal titanates, the compounds of technical interest because they have industrial uses, many analytical applications. The kinetics and mechanisms of thermal decomposition of solids have been reviewed by L'vov [45].

Muraleedharan *et al*. [46] investigated the kinetic studies on the thermal decomposition of potassium titanium oxalate, $K_2TiO(C_2O_4)_2 2H_2O$ by using thermogravimetry (TG), differential thermal analysis (DTA) and the kinetic parameters were estimated using isoconversional methods [47]. Potassium titanium oxalate has many chemical and pharmaceutical applications. Prajic *et al.* used potassium titanyl oxalate as analytical reagents for micro quantitative

determination of quercetin in pharmaceutical formation [48]. Kuntic *et al.* determined the quercetin in pharmaceutical formations *via* its reaction with potassium titanyl oxalate, and also determined the stability constant of that particular complex [49]. Broadbent *et al.* [50] reported thermal decomposition of potassium titanyl oxalate, potassium aluminium oxalate and the related oxalates using thermogravimetry and differential thermal analysis under non-isothermal conditions in air, nitrogen and carbon dioxide atmospheres, well explained the dehydration of the potassium titanyl oxalate starts at 343 K and proceeds in several stages until completion at 473 K. The anhydrous oxalate is not stable although only 1 % mass loss is observed between 473 and 548 K, but the decomposition is rapid above 548 K. The titanate formed as the final product is the result of the initial decomposition of the anhydrous complex at 1373 K.

Sharma *et al.* [51] described the preparation, characterization and thermal investigation of zinc and cadmium titanyl oxalates. The TG and DTG curves of the thermal decomposition of zinc and cadmium titanyl oxalate hydrate proceed through three major steps, *viz*. dehydration followed by the decomposition of the oxalate to the carbonate and finally the decomposition of the carbonate to the respective metal titanate. Gopalakrishna Murthy *et al.* [52] prepared lead titanyl oxalate tetrahydrate and the thermal decomposition was investigated by employing thermoanalytical and evolved gas analysis techniques. The decomposition in air or oxygen proceed through three main steps; dehydration, decomposition of the oxalate to carbonate and decomposition of the carbonate to lead metatitanate as the final

product.

Thomas *et al.* [53] reported the studies on the thermal decomposition of calcium copper titanyl oxalate and in a similar way for alkaline earth metal titanyl oxalates by Murthy *et al.* [54]. In this case, the decomposition product, calcium copper titanate, a well known electroceramic is associated with giant dielectric constants which have increasing demand in electronic devices owing to the miniaturization [54]. Galwey *et al.* identified and discussed studies on the thermal decomposition of silver oxalate [55]. Kinetic studies on the thermal decomposition of cobalt oxalate, and manganese (II) oxalate dihydrate and manganese (II) oxalate trihydrate using TG, DTA and X-ray diffraction techniques were reported [55]. Padmanabhan *et al.* have reported the thermal decomposition of some metal oxalates [56]. Dollimore and Nicholson reported the variations in the surface areas of the solid products which occur when heavy metal oxalates are heated at various temperatures [57].

Balyaev *et al.* [58] reported the preparation and thermal decomposition of cobalt titanyl oxalate, a molecular precursor for $CoTiO_3$ obtained when $CoCl_2.H_2O$ was reacted with potassium titanyl oxalate solution, crystallization of $CoTiO_3$ occurres at temperatures as low as 923 K. Dhage *et al.* [59] carried out a detailed work on the preparation of $PbTiO_3$ using potassium titanyl oxalate and pointed out that the anionic species $TiO(C_2O_4)_2^{2-}$, obtained by dissolving potassium titanyl oxalate in water, is stable over a narrow range of pH and is destabilized by the addition of $PbCl_2$ solution to produce the mixed metal oxalates, PbC_2O_4 and $TiO(C_2O_4)$. Brown *et al.* reported the TG analysis of

several metal oxalates in various atmospheres [60]. Dollimore reviewed the thermal decomposition and stability of many metal oxalates and explained their characteristic features [61]. In non-isothermal analysis, the temperature at which decomposition takes place depends on the heating rate. It is observed that the thermal decomposition of oxalates is associated with a considerable induction period especially at lower temperatures [62].

The importance for the preparation of pure and fine-grained stoichiometric metatitanates of bivalent metals which leads to the development of chemical kinetic and thermodynamic methods in research fields [63]. These metatitanates can be prepared by the thermal decomposition of the corresponding metal titanyl oxalates. They are mainly prepared by the chemical reaction between suitable reagents; chemically prepared materials have better sinter ability than those prepared by other ceramic methods. Chemical reactivity, particle size and sinter ability of the metatitanates are influenced by the calcination temperature of the metal titany1 oxalates. This has necessitated the investigation of the decomposition characteristics of titanyl oxalates [64].

The alkaline earth metal titanyl oxalates can be prepared by simple precipitation technique and various kinds of mesoporous metal oxides with good crystallinity can be prepared by thermal decomposition method. Using thermal decomposition method, particle size and shape can be effectively controlled. It can produce highly homogeneous and crystalline nano particles. It requires shorter preparation time and fewer impurities in the final product.

1.2.1 Thermal decomposition of alkaline earth metal titanyl oxalates

The research, technological and industrial importance of alkaline-earth metal titanyl oxalate has given fast movement to the development of chemical methods for preparing them as high-purity materials. Thermal decomposition of alkaline earth metal titanyl oxalates gives metal titanates. Since metal titanates have interesting electrical properties that are strongly influenced by the temperature of calcinations, a systematic kinetic study has been made on the thermal decomposition reaction of metal titanyl oxalate leading to the formation of titanates. The requirement for pure, fine-grained metatitanates of bivalent alkaline earth metals, led to the development of chemicaI methods for their preparation. Ultrafine and stoichiometric metatitanates can be prepared by the thermal decomposition of the corresponding titanyl oxalates.

Strizhakov *et al.* have reported the thermal decomposition of the titanyl oxalates of alkaline earth metals and lead [65]. GalIagher *et al.* have investigated the mode of decomposition of barium and the thermal decomposition of some substituted barium titanyl oxalates and its effect on the semiconducting properties of the doped materials [66]. Chemically prepared materials have better sinterability than those prepared by ceramic methods. Chemical reactivity, particle size and sinterability are influenced by the calcination temperature of the precursors, *viz*., the corresponding titany1 oxalates. This has necessitated the investigation of the decomposition characteristics of titanyl oxalates. The decomposition is a multistep kinetic mechanism,

and it can be summarized as: (i) dehydration, (ii) decomposition of the anhydrous oxalates to the carbonate (iii) the carbonate decomposition with formation of the metal titanates [67].

1.2.1.1 Thermal decomposition of beryllium titanyl oxalate

Sharma *et al.* prepared beryllium titanyl oxalate tetrahydrate [68] and the thermal behavior under non-isothermal conditions was investigated by thermogravimetric and differential scanning calorimetric techniques. The decomposition is a multi step reaction, including dehydration of the hydrate, decomposition of the oxalate to carbonate and decomposition of the carbonate to oxide.

$$BeTiO(C_2O_4)_2.4H_2O \xrightarrow{613-753K} BeTiO(C_2O_4)_2 + 4H_2O$$

$$2BeTiO(C_2O_4)_2 \xrightarrow{753-813K} Be_2Ti_2O_5CO_3 + 4CO + 3CO_2$$

$$Be_2Ti_2O_5CO_3 \xrightarrow{813-913K} 2BeTiO_3 + CO_2$$

1.2.1.2 Thermal decomposition of magnesium titanyl oxalate

Gopalakrishna Murthy *et al.* also studied the thermal decomposition of magnesium titanyl oxalates in flowing oxygen, nitrogen, carbon dioxide and vacuum using thermo analytical techniques like DTA and TGA. The thermal decomposition of magnesium titanyl oxalate heptahydrate, consists of four steps; dehydration, two steps of oxalate decomposition to give a carbonate, and decomposition of the carbonate to yield $MgTiO_3$ which has the ilmenite structure [69]. In the temperature range 293-533 K, the

dehydration takes place in three steps with the elimination of 2, 3 and 2 water molecules per mole, respectively. The first stage of oxalate decomposition occurs in the range 523-653 K, isothermal heating of magnesium titanyl oxalate at 573 K for 48 h produces the intermediate $Mg_2Ti_2O_4(C_2O_4)CO_3$. The second stage of oxalate decomposition occurs in the range of 653-793 K, in this endothermic reaction, carbon monoxide and carbon dioxide is evolved in equal proportions. Isothermal heating of magnesium titanyl oxalates at 673 K produces the intermediate $Mg_2Ti_2O_5CO_3$ which decomposes between 793 and 973 K giving crystalline $MgTiO_3$ of ilmenite structure with a = 5.03 and c = 13.44 A^0, compared to the reported values of 5.95 and 13.90 A^0 for 'a' and 'c' respectively [70]. The following step is proposed for the decomposition of magnesium titanyl oxalates in air:

$$MgTiO(C_2O_4)_2.7H_2O \xrightarrow{293–533K} MgTiO(C_2O_4)_2 + 7H_2O$$
$$2MgTiO(C_2O_4)_2 \xrightarrow{533–653K} Mg_2Ti_2O_4(C_2O_4)CO_3 + 3CO + 2CO_2$$
$$Mg_2Ti_2O_4(C_2O_4)CO_3 \xrightarrow{653–793K} Mg_2Ti_2O_5CO_3 + CO + CO_2$$
$$Mg_2Ti_2O_5CO_3 \xrightarrow{793–973K} 2MgTiO_3 + CO_2$$

Miao *et al.* [71] synthesized nano-crystalline magnesium titanate materials at low temperatures by the sol–gel method, using butyl titante and magnesium nitrate as precursors. Thermal decomposition behavior of the gel was analyzed by thermogravimetry-differential thermal analysis. Crystallinity of $MgTiO_3$ powders was examined by transmission electron microscopy. The surface morphology was observed by scanning electron microscopy. The average grain size of $MgTiO_3$ crystals was between 10 and 30 nm at

873 K and $MgTi_2O_5$ disappeares completely at 973 K. Yanovskaya *et al.* [72] also prepared sintered $MgTiO_3$ using alkoxy derived powders. The precursor powders prepared from $Mg(OBu)_2Ti(OBu)$ in butanol under reflux. The sintered $MgTiO_3$ particles were obtained at the temperature range 1413-1493 K.

1.2.1.3 Thermal decomposition of calcium titanyl oxalates

Gopalakrishna Murthy *et al.* studied the thermal decomposition of cacium titanyl oxalate hexahydrate using TG, DTA in different atmospheres. The decompositions proceed through three major steps: dehydration, decomposition of the oxalate to a carbonate and the decomposition of the carbonate to yield $CaTiO_3$. In the initial stage, cacium titanyl oxalate hexahydrate dehydrates into the tetrahydrate and then to anhydrous oxalate. The carbonate $Ca_2Ti_2O_4(CO_3)_2$ decomposes in the temperature range of 723-873 K to give $Ca_2Ti_2O_5CO_3$ and carbon dioxide. The final crystalline residue $CaTiO_3$ is formed by the release of CO_2 from the intermediate $Ca_2Ti_2O_5CO_3$, in the temperature range of 813- 933 K [73].

$$CaTiO\left(C_2O_4\right)_2.6H_2O \xrightarrow{293-403K} CaTiO\left(C_2O_4\right)_2.4H_2O + 2H_2O$$

$$CaTiO\left(C_2O_4\right)_2.4H_2O \xrightarrow{403-523K} CaTiO\left(C_2O_4\right)_2 + 4H_2O$$

$$2CaTiO\left(C_2O_4\right)_2 \xrightarrow{523-723K} Ca_2Ti_2O_4\left(CO_3\right)_2 + 4CO + 2CO_2$$

$$Ca_2Ti_2O_4\left(CO_3\right)_2 \xrightarrow{723-813K} Ca_2Ti_2O_5CO_3 + CO_2$$

$$Ca_2Ti_2O_5CO_3 \xrightarrow{813-933K} 2CaTiO_3 + CO_2$$

Mallik *et al.* [74] prepared nano calcium titanate powders from the equimolar solution of calcium oxide, ethanol and Titanium (IV) isopropoxide. The phase analysis and morphology of powder particles were studied by XRD which confirms the presence of phase pure crystalline $CaTiO_3$ nanoparticles with stoichiometric ratio can be prepared through sol-gel process after drying at 373 K for 24 h, while TEM analysis confirms about 13 nm sizes of $CaTiO_3$ particles and some agglomerated particle of 20-30 nm. Gralic *et al.* [75] evaluated the quantity of the formation of calcium titanate with perovskite structure from alternative sources of titanium [76]; the precursors were sintered at high temperatures in the range 1273-1673 K.

1.2.1.4 Thermal decomposition of strontium titanyl oxalates

Thermal decomposition of strontium titanyl oxalate tetrahydrate was studied by employing TG, DTA in flowing oxygen, nitrogen, vacuum, cabon dioxide gas and chemical analysis. Thermal decomposition of anhydrous metal titanyl oxalate proceeds through multi step complex reactions to form titanates [77]. The three major steps: dehydration, decomposition of the oxalate to a carbonate and the decomposition of the carbonate to yield the final product, metal titantes. GalIagher *et al.* have investigated the mode of decomposition of strontium titanyl oxalates [78]. It was prepared by the method of Clabaugh *et al.* [79) by substituting strontium chloride for barium chloride. The yield of STO was only around 50 %, owing to the solubility of STO in acid medium.

Sairam Patra *et al.* [80] studied the thermal decomposition of anhydrous strontium titanyl oxalate, and found that the thermal decomposition proceeded through a series of complex reactions to form strontium metatitanate at high temperatures. Among them the decomposition of oxalate is the first major thermal event. A kinetic study of oxalate decomposition in the temperature range 553–593 K has been carried out by the authors under cooled gas pressure, in vacuum. The results has been fitted to the *Zhuravlev equation* for almost the entire α-range (0.05–0.92) indicating the occurrence of a diffusion-controlled, three-dimensional rate process. The activation energy has been calculated to be 164±10 kJ/mol. Results from elemental analysis, TGA, IR and SEM studies of undecomposed and partially decomposed samples have been used to supplement kinetic observations in formulating the mechanism for oxalate decomposition.

$$SrTiO\left(C_2O_4\right)_2.4H_2O \xrightarrow{293-523K} SrTiO\left(C_2O_4\right)_2 + 4H_2O$$

$$2SrTiO\ \left(C_2O_4\right)_2 \xrightarrow{523-703K} Sr_2Ti_2O_{4+x}\left(CO_3\right)_{2-x}\left(CO_2\right)_x + 4CO + 2CO_2$$

$$Sr_2Ti_2O_{4+x}\left(CO_3\right)_{2-x}\left(CO_2\right)_x \xrightarrow{703-843K} Sr_2Ti_2O_5CO_3 + \left(CO_2\right)$$

$$Sr_2Ti_2O_5CO_3 \xrightarrow{843-1003K} 2SrTiO_3 + CO_2$$

Fan *et al.* [81] prepared strontium titanate using strontium titanyl oxalate as precursor; it is synthesized from chlorides of Sr and Ti and oxalic acid. Thermal decomposition of STO was studied by means of TG and DTG and compared to X-ray diffraction

measurements. Highly crystalline strontium titanate can be obtained by heating the STO precursor in air at 1173 K. Roy *et al.* [82] prepared $SrTiO_3$ powder from Sr-oxalate and TiO_2 precursors, instead of using titanyl oxalate. The crystallization and formation were investigated by thermal analysis using TGA and DTA which reveals that upon heating; it dehydrates in two stages (due to the presence of two different types of Sr-oxalate hydrates) during the temperature range 1073-1173 K. The nanosized (90 nm in size) $SrTiO_3$ crystallites are produced at 1373 K, due to the lower calcination temperature [83]. Rout *et al.* [84] prepared $SrTiO_3$ and Ni doped $SrTiO_3$ by solid state reaction route, and studied the electrical properties of these samples using impedance spectroscopy and mentions the important applications. Lee *et al.* [85] used a simple chemical route and synthesized highly sinterable $SrTiO_3$ as a porous powder with a particle size of 300 nm and recognized the phase transition at 1573 K.

1.2.1.5 Thermal decomposition of barium titanyl oxalate

Solid state reactions are carried out to obtain more important solid and to gain understanding of the factors influencing these reactions [86-93]. The process of forming titanates in crystalline mixtures has become very important in the ceramic industry and other technologies. Many reports are available for the preparation of barium titanyl oxalate [94-98]. Yen *et al*. [99] reported that a high purity barium titanate could be prepared by precipitating barium titanyl oxalate and subsequently converting to barium titanate by calcinations. Balek *et al.* [100] also reported the optimum conditions for the formation of BTO in detail and the formation of $BaTiO_3$ by thermal

decomposition of BTO and the kinetic parameters are investigated by thermal analysis (TG-DTA) and EGA.

Ragulya *et al*. synthesised and dicussed the sintering of nanocrystalline barium titanate powder under nonisothermal conditions and also the control of dispersity of barium titanate during its synthesis from barium titanyl oxalate [101]. Fang *et al.* repored the thermal analysis of precursors of barium titanate prepared by co-precipitation method and discussed the factors affecting the preparation of barium titanyl oxalate tetrahydrate [102]. Amala sekar *et al.* [103] synthesised the fine-particle of titanates by the pyrolysis of oxalate precursors and repored the morphology of these titanates.

The decomposition kinetics of barium titanyl oxalate tetrahydrate has been extensively studied by many researchers [104-106]. Otta *et al*. studied the kinetics and mechanism of the thermal decomposition of barium titanyl oxalate [107]. Gallagher and Thomson [108] suggested that the first stage in the thermal decomposition is the loss of four moles of water in the temperature range 293-523 K. After the loss of water of crystallization, oxygen is adsorbed to form active $BaCO_3$ and TiO_2 which reacts to form $BaTiO_3$ in the temperature range 773-973 K and CO_2 is released.

The thermal behavior of $BaTiO_3$ prepared in the temperature range 873-1173 K was studied by Swillam and Gadalla [109]. They have shown that when lower temperature was used for the calcination of $BaTiO_3$, samples with extremely fine pores are formed, whereas higher temperature agglomerates to shrink to form too much smaller

particles, eliminating these pores. The formation of barium titanate by the thermal decomposition of barium titanyl oxalate was shown to proceed in several steps; the role of H_2O and CO_2 removal in barium titanyl oxalate and the effect of doping and the mixing conditions of reactant molecules on reactivity in this system was described [110].

Dutta *et al.* [111] studied the formation of barium titanate from barium titanyl oxalate precursor by thermal decomposition method and also the molecular structure of the mixed oxalate determined by Raman spectroscopy consist of a Ti_4O_4 ring which contains a titanyl (Ti=O) unit. The mixed oxalate was heated from room temperature to 1073 K, and the structural changes that occurred were followed by Raman spectroscopy at ambient temperature. When temperature increases, the bidentate oxalate ligand changes to a bridged oxalate, followed by decomposition to ligated carbonate and then to ionic carbonate. All traces of the ligand disappear beyond 1073 K. The intermediate that exists in the temperature range 523-873 K is a Ba-Ti amorphous complex and $BaTiO_3$ forms above 973 K.

Gopalakrishna Murthy *et al.* [112], have investigated the thermal decomposition of barium titanyl oxalate by employing gas and chemical analysis techniques. The decomposition is not affected much by surrounding gaseous atmosphere and it proceeds in five steps. Step one, which is dehydration of the tetrahydrate, is followed by a low temperature decomposition of the oxalate groups. In the temperature range of 453-523 K, carbon monoxide is evolved with the formation of a transient intermediate substance containing both carbonate and oxalate groups. The oxalate groups are completely destroyed in the

temperature range 523-723 K, resulting in the formation of a carbonate which retains free CO_2 in the matrix. The trapped CO_2 is released in the temperature range 723-873 K. The final decomposition of carbonate takes place in the temperature range 873-1023 K and yields barium titanate. Thermal decomposition reaction of barium titanyl oxalate can be brought through the following schemes:

$$BaTiO(C_2O_4)_2.4H_2O \xrightarrow{393-453K} BaTiO(C_2O_4)_2 + 4H_2O$$

$$BaTiO(C_2O_4)_2 \xrightarrow{453-523K} Ba_2Ti_2O_2(C_2O_4)_3CO_3 + CO$$

$$Ba_2Ti_2O_2(C_2O_4)_3.CO_3 \xrightarrow{523-723K} Ba_2Ti_2O_5CO_3(CO_2) + 2CO_2 + 3CO$$

$$Ba_2Ti_2O_5CO_3(CO_2) \xrightarrow{723-873K} Ba_2Ti_2O_5CO_3 + CO_2$$

$$Ba_2Ti_2O_5CO_3 \xrightarrow{873-1023K} 2BaTiO_3 + CO_2$$

Barium titanate formation from BTO comes through the evolution of H_2O, CO and CO_2. Initial low temperature reaction is known as the dehydration (<500 K) and low temperature decomposition occurs >500 K forming the carbonate intermediate. Succeeding steps involves the decomposition of carbonate intermediate with the evolution of CO and CO_2. Barium titanate, the "*first ferroelectric ceramic*", is a good candidate for various applications in electronic industry as a capacitor material due to its super conductivity, excellent dielectric, ferroelectric and piezoelectric properties, catalytic properties, *etc*. Many of these properties strongly depend on material defects like vacancies, dislocations, stacking faults, subgrain boundaries, *etc*. These defects affect local oxygen bonding which can be achieved by doping and mechanical mixing. The thermal

decomposition of mixed metal titanyl oxalates yield mixed metal oxide nano particles that have wide range of applications in electronics and opto-electronic field.

1.2.2 Thermal decomposition of mixed metal titanyl oxalates

Thermal decomposition of mixed metal titanyl oxalates is one of the important methods of preparation of pure or mixed metal titanates having multi functional properties. The thermodynamic and kinetic aspects of solid state decomposition reactions can be complex and multistep reactions and posses a large number of parameters to investigate. The calculated thermodynamic kinetic parameters indicate the multi-step nature of the process and the decomposition stage is a high energy pathway and reveals a very hard mechanism [113]. Celis *et al*. [114] have reported in detail the kinetic analysis of the thermal decomposition of calcium and strontium oxalates and the mixtures of both. Thermal decomposition of titanyl oxalate, barium oxalate and a mixture of these two have been carried out, using various thermo analytical methods, to verify the scheme of thermal decomposition of barium titanyl oxalate proposed [115]. Muraleedharan *et al.* [113] investigated the kinetics of the thermal decomposition of potassium doped barium titanyl oxalate by using differential scanning calorimetry (DSC) and kinetic deconvolution procedure was utilized to perform the overall kinetics of formation of pure and doped $BaTiO_3$.

Thermal decomposition of mixed Ce and Gd oxalates and the thermal properties of mixed Ce and Gd oxides were studied by Ubaldini *et al.* [116] and concluded that, the mechanisms of

decomposition of Ce and Gd oxalate are different, and mixed oxalates $(Ce_{1-x}Gd_x)_2(C_2O_4)_3.nH_2O$ behave in an intermediate way. The dehydration stages are more similar to those of Gd oxalate, as not all of the water molecules are equivalent as in the case of cerium oxalate. The decomposition leads to $(Ce_{1-x}Gd_x)\ O_{2-\ x/2}$ (x is close to 0 or 1) two solid solutions exist, for the central composition; the presence of a biphasic region cannot be excluded.

Deb *et al*. [117] has investigated on solid-state pyrolytic decomposition of barium trihemiaquatris (oxalato) lanthanate (III) decahydrate using TG–DTA in air and DSC in nitrogen. Deb also synthesized mixed metal oxalate precursors, calcium (II) bis (oxalato) cobaltate (II) hydrate, strontium (II) bis (oxalato) cobaltate (II) pentahydrate and barium (II) bis (oxalato) cobaltate (II) octahydrate for determining their thermal stability [118]. Hwu *et al*. [119], examined whether barium titanyl oxalate tetrahydrate $[BaTiO(C_2O_4)_2.4H_2O]$, known as the precursor of $BaTiO_3$, can be prepared by homogeneous precipitation. The morphology and particle size of $BaTiO(C_2O_4)_2.\ 4H_2O$ was controlled by reaction temperature, pH and solvent ratio and further $BaTiO_3$ was obtained by the calcination of barium titanyl oxalate tetrahydrate above 873 K or hydrothermally in a basic solution at 473 K. This highly pure $BaTiO_3$ was used in a polymer-ceramic composite for embedded capacitor application.

Khollam *et al.* [120] prepared barium–strontium titanyl oxalate (BSTO): $Ba_{1-x}Sr_xTiO(C_2O_4)_2.4H_2O$ (x = 0.25) by a simple one-step cation-exchange reaction between the stoichiometric solutions of ammonium titanyl oxalate (ATO), barium hydroxide and strontium

nitrate at room temperature. The pyrolysis of BSTO at 1003 K/4 h in air produces barium–strontium titanate ($Ba_{1-x}Sr_xTiO_3$; BST) powders. The characterization of BSTO and BST powders by various physico-chemical techniques: micro and chemical analysis, DTA, TG, XRD, FTIR, X-ray fluorescence (XRF) and SEM reveals that the powders formed are cubic, highly pure, stoichiometric and sub-micron in size with nearly uniform size and shape distribution. The ceramic compacts obtained by sintering the BST pellets at 1573 K/4 h shows comparable dielectric properties [121].

The quantitative precipitation of barium–strontium titanyl oxalate: ($Ba_{0.6}Sr_{0.4}TiO\ (C_2O_4)_2.4H_2O$) precursor powders prepared by Li *et al.* [122] through oxalate co-precipitation method. The decomposition of BSTO at 1073K/4h produces the barium–strontium titanate (BST) ($Ba_{0.6}Sr_{0.4}TiO_3$) powders. Two kinds of dispersants namely ammonium salt of poly mathacrylic acid (PMAA-NH_4) and polyethylene glycol were added respectively during the co-precipitation procedure. The powders were characterized by XRD, SEM, *etc*. Experimental results show that the addition of the dispersants reduces the yield of BST powders. The BSTO and BST powders obtained by above mentioned technique without dispersants were homogeneous with quasi-orbicular morphology. The particles grew into spindle shape with the effect of polyethylene glycol. The barium–strontium titanyl oxalate ($Ba_{0.6}Sr_{0.4}TiO(C_2O_4)_2.4H_2O$) precursor powders was also prepared by the modified oxalate co-preparation method [123], which was based on the cation-exchange reaction between the stoichiometric solutions of oxalotitanic acid

($H_2TiO(C_2O_4)_2$), barium and strontium nitrate solution containing stoichiometric quantities of Ba and Sr ions. The pyrolysis of BSTO at 1073 K/4 h in air produces the homogeneous cauliflower-like barium–strontium titanate ($Ba_{0.6}$ $Sr_{0.4}$ TiO_3) powders [124].

1.2.3 Applications of mixed metal oxides

Doping or mechanical mixing of barium titanyl oxalate with other elements (K, P, La and Sm) enhances the oxygen ion conductivity and the mechanical properties. The mixed metal oxides have wide range of applications in optics, electronics, catalysis, *etc*. The properties and applications [125] of perovskite phase mixed-metal oxides, $MTiO_3$, $(Ba,Sr)TiO_3$, $Pb(Sr,Ti)O_3$, $K((Ta,Nb)O_3$, $Pb(Mg_{1/3}$ $Nb_{2/3})O_3$, *etc*., are based on their intrinsic dielectric, ferroelectric, piezoelectric, and pyroelectric properties of relevance in corresponding electronics applications such as electromechanical devices, transducers, capacitors, actuators, high-k dielectrics, dynamic random access memory, field effect transistors, and logic circuitry [126-127]. Another area attracting a good deal of interest has been the use of ferroelectric mixed-metal oxide thin films as nonvolatile computer memories. The use of ferroelectric materials as electro-optic switching devices for optical computers is an important application currently under investigation [125]. These mixed-metal oxides, which are capable of high oxygen transport fluxes at elevated temperatures (T >873 K). $SrCeO_3$ and $SrTiO_3$ have been successfully used for oxygen transport. The stability and high oxygen flux potential at high temperatures of these materials have provided for their consideration in a number of high-temperature membrane reactor applications,

including in oxidation reactions [128-129]. Perovskite type oxides with typically very high melting points also exhibit a number of interesting chemical properties including heterogeneous catalytic activity and they are often utilized for CO oxidation, oxidation of hydrocarbons and chlorinated volatile organic compounds, partial oxidation of methane to synthesis gas, N_2O decomposition, NO_x reduction, hydrogenation reactions of alkenes, SO_2 reduction, as well as in various types of electro and photocatalytic reactions [130-131].

Mixed alkaline earth metal titanates, a perovskite ferroelectric material, finds extensive application in electronic industry as a capacitor material. Because of the considerable variation in its structural and physical properties this material has great interest both in ceramic and in single crystal forms. Due to their high dielectric constant, large polarization and high breakdown voltage, ferroelectric materials have a wide range of applications such as in high density dynamic random access memories, non-volatile ferroelectric random access memory and infra red detectors and also in several high frequency devices such as filters, resonators, oscillators, frequency multipliers and tunable microwave devices, various microwave communication and optoelectronic devices. [132]. Perovskite-based (ABO_3) structures are of significant interest in the field of photocatalysis and photovoltaics [133]. The development and utilization of solar energy in environmental remediation and water splitting is being intensively studied worldwide. Perovskite materials can be used as photocatalysts for water splitting reaction for hydrogen production and photo-degradation of organic dyes in wastewater as

well as for photoanodes in dye-sensitized solar cells and light absorbers in perovskite-based solar cells for electricity generation [134]. Xee *et al.* reviewed to provide a current summary of recent progress in perovskite materials for use in important areas and to provide some useful guidelines for future development in these hot research areas [135].

The metal titanates such as $SrTiO_3$ /$BaTiO_3$ have shown excellent photocatalytic activity is of particular interest in the production of hydrogen from water using solar energy because of their structural simplicity and flexibility [136]. Shi *et al.* reported a general review of perovskite photocatalysts active under UV and visible light [137]. Further, conversion of CO_2 to hydrocarbons (fuels) is also of significant interest, as it is a solution to reduce CO_2 emissions across the globe [138]. Apart from the clean energy generation, photocatalysis has several promising applications in the environmental field. Some of the applications include degradation of volatile organic compounds for water treatment [139], germicide and antimicrobial action [140], de-coloration of industrial dyes [141], nitrogen fixation in agriculture [142], and removal of the air pollutants NO_x/SO_x [143].

The compounds such as $CaCu_3Ti_4O_{12}$, Ba_2EuBiO_6, Ba_2SmBiO_6, and Ba_2CeBiO_6 showes high photocatalytic activity [144] and also the compounds, Ba_2CoWO_6, Ba_2NiWO_6, Sr_2CoWO_6 and Sr_2NiWO_6 are stable perovskites compounds for O_2 evolution using sacrificial agents [145]. W doping in Sr_2FeNbO_6 has also been studied and demonstrated enhancement to hydrogen evolution under visible radiation [146]. Oxynitride compounds such as $CaNbO_2N$, $SrNbO_2N$,

$BaNbO_2N$, and $LaNbON_2$ belong to the perovskite type crystal structures [147], photocatalytic hydrogen evolution has been reported under visible light from methanol solution. Compounds such as $CaTaO_2N$ and $BaTaO_2N$ were loaded with Pt co-catalyst and coupled with Pt/WO_3 used for water splitting [148]. Solid solution of $BaTaO_2N$ and $BaZrO_3$ was formulated for hydrogen and oxygen evolution, and it showes improved performance compared with the individual photocatalysts under visible light [149].

Sarkas *et al.* [150] shared the preliminary evidence for catalytic activity by unsupported mixed metal oxide nanocrystlline materials. The results of this study show that a nanophase form of Li-MgO has begun to exhibit catalytic activity by 573 K which is at least 200 degrees below the temperature at which conventional Li-MgO catalysts exhibit comparable activity. Furthermore, at higher temperatures, the same nanophase composition shows enhanced activities and somewhat improved hydrocarbon selectivities over conventional Li-MgO catalysts**.** The rational design and efficient synthesis of nanostructured mixed metal oxides with controlled shapes, sizes, compositions and morphology, improves the performance of electrochemical energy conversion and storage devices along with their applications as electrode materials for lithium-ion batteries and electrochemical capacitors, and function as efficient electrocatalysts for the oxygen reduction reaction in metal–air batteries and fuel cells [151-152].

Gawande *et al.* studied the role of mixed metal oxides in catalysis science and explained its versatile applications in organic

synthesis such as reduction, oxidation, multicomponent, Mannich alkylation, condensation, deprotection, cycloaddition, hydroxylation, dehydration, dehydrogenation, trans-esterification reactions involving biomimetic oxygen-evolving catalysts and other important C–C bond forming reactions on the surface of mixed metal oxides under a variety of reaction conditions [153]. They were also be used for selective reduction of C=O in α, β-unsaturated carbonyls through catalytic hydrogen transfer reaction [154], study of chemical structures and performance of perovskite oxides [155], epoxidation on MoO_3/TiO_2 oxide [156] and study of the effect of phosphate ions on the textural and catalytic activity of titania–silica mixed oxide [157]. The recent applications of mixed metal oxides are in important organic reactions, industrial applications, and green chemistry and are also used as essential components in most refining and petrochemical processes [158].

Mixed metal oxides have been widely used for various applications such as pigments in coatings. Mixed metal oxide pigments help to achieve an opaque coating by pigment mixing to achieve the desired color [159]. Strontium titanate of perovskite structure is a highly efficient and promising anticorrosion pigment. Kantorová *et al.* [160] synthesized strontium titanate and are used to prepare solvent type epoxy-ester resin based coatings with varying pigment volume concentration (15-20 vol. %) of the strontium titanate pigment which exhibit high anticorrosive efficiencies. The physical-mechanical properties of the paints with the $SrTiO_3$ content have more advantages than in pigmentation with other compounds. It has been reported that

$CaTiO_3$ pigment of perovskite structure has also shows high anticorrosion efficiency [159]. The anticorrosion properties of the paint that contains mixed metal oxides-based pigments, TiO_2.ZnO, $SrTiO_3$, Zn_2TiO_4, $MgTiO_3$, $CaTiO_3$, TiO_2.ZnO.MgO, and TiO_2.ZnO.SrO were synthesized as potential anticorrosion pigments and shows high physical-mechanical properties [161].

Kulkarni *et al*. [162] investigated the structural and dielectric properties on BST-BZT composites. Barium StrontiumTitanate system is well known ferroelectric materials for a variety of applications in the tunable microwave devices, high permittivity capacitors, pyroelectric sensors and piezoelectric transducers, *etc*. Piagai *et al*. prepared magnesium-calcium titanate ($Mg_{0.95}Ca_{0.05}TiO_3$) powders and was used as microwave dielectric ceramics by alkoxide precursor method. Its thermal decomposition behavior has been investigated using thermal analysis, XRD, FT-IR, and SEM [163].

Arunachalam *et al*. synthesized manganese-doped barium titanate, which exhibit high electrical resistivity and high dielectric constant with an increasing insensitivity to temperature and therefore suitable as dielectric for multilayer capacitors with base metal electrodes [164]. Lin *et al*. studied the magnetic behavior in Fe doped $BaTiO_3$ and $Ba(Ti_{0.3}Fe_{0.7})O_3$ a multifunctional ceramic material was prepared and the effect of annealing atmosphere on magnetism has been investigated [165]. Takin *et al*. [166] explored the applications of barium titanate core–gold shell nanoparticles for hyperthermia treatment against cancer cells and proposed that these nanoshells have suitable cytocompatibility at concentrations up to 50 ηg/L.

Azim Araghi *et al*. synthesized barium strontium titanate ($Ba_{0:6}Sr_{0:4}TiO_3$) nanocrystalline powder by a modified sol-gel process [167]. Enhessari *et al*. [168] prepared nanostructured barium strontium titanate by improved methods; barium strontium titanate ($Ba_{1-x}Sr_xTiO_3$, BST) ferroelectric materials have attracted considerable attentions due to their chemical stability, high permittivity, high tunability and low dielectric losses [169]. The physicochemical properties of these nanomaterials are highly sensitive to their size, shape, and composition [170].

Dong *et al.* [171] investigated barium strontium titanate (BST) solid solutions with high dielectric susceptibility under the DC electric field due to their potential applications in tunable microwave devices, such as phase shifters, resonators, capacitors and phased array antennas [172-173]. And also in a variety of electronic applications in multi-layer and voltage-tunable capacitors, dynamic random access memories, tunable filters, oscillators, uncooled infrared sensors, *etc*., due to the moderate dielectric constant, good dielectric temperature stability, nonlinear variation of dielectric constant with the electric field, ferroelectricity, pyroelectricity and high tunability of tunable materials required for these applications [174]. Zhang *et al*. [175] studied sintering temperature effects on the energy-storage properties in barium strontium titanate glass–ceramics by polarization hysteresis measurements, found that with increase in sintering temperature, the crystallinity degree of primary ferroelectric phase increases.

Elmer N. Bunting [176] studied the properties of calcium-barium titanate dielectrics, which was valuable for the production of

capacitors for use at temperatures above 1773 K. Singh *et al.* discussed the structural and electrical properties of barium calcium titanate (BCT) thin films prepared by sol-gel method. The dielectric measurements of thin films shows that dielectric constant decreases with the substitution Ca and also the ferroelectric character of BCT thin films which decreases with increase in the concentration of Ca content on barium titanate [177]. Kuper *et al*. [178] discussed the photorefractive properties of ferroelectric barium-calcium titanate crystals such as high Bragg selectivities, large two-beam coupling efficiencies, reversibility and large refractive index changes even for low power illumination with fascinating applications like volume holographic memories or self-pumped phase conjugators. Kotlyarchuk *et al*. [179-180] synthesized calcium doped nanocrystalline barium titanate powder by oxalate route. Varatharajan *et al*. [181] studied the ferroelectric properties of barium calcium titanate single crystals, and proved that dielectric constants decreases with increase in the concentration of Ca due to the doping of non-ferroelectric calcium titanate in ferroelectric barium titanate [182].

George *et al*. [183] discussed the preparation and properties of barium-magnesium titanate dielectrics and found that the addition of magnesium to barium titanate resulted in high electrical losses, so these materials are used for electrical communications and instrumentation. Lee *et al*. [184] studied the microwave dielectric properties of magnesium calcium titanate thin films prepared by the metal organic solution deposition technique (MOSD). Samyuktha *et al*. [185] synthesized $Mg_{(1-x)}Ca_xTiO_3$ by conventional solid state diffusion

method, the calcium doped magnesium titanate ceramic materials of different compositions shows that the dielectric constant and dielectric loss increases with temperature and decreases with frequency and enhances the dielectric constant. The dielectric loss was constant at high frequency, so these materials can be used for high frequency devices. $Mg_{(1-x)}Ca_xTiO_3$(x=0.1, 0.3 & 0.5) ceramic materials are suitable for microwave device applications [186].

Dong *et al.* [187] synthesized compositionally inhomogeneous barium strontium calcium titanate ceramics with weak dielectric temperature sensitivity and retain high tunability by phase-mixed method. Addition of Ca decreases the dielectric constant from ~2800 to ~1500 and enhances the dielectric temperature stability and also the tunability. The temperature-dependent dielectric constants of BSCT ceramics also depend on the method of addition of Ca; BSCT ceramics are potential materials for tunable microwave applications. Gomma *et al.* [188] reported that the electrical and mechanical properties of alkali $BaTiO_3$ alumino–borosilicate glass ceramics contain Sr or Mg and its micro hardness depends on SrO/BaO or MgO/Al_2O_3. The measurement of mechanical properties, hardness and elastic modulus of sintered $BaTiO_3$ ceramic shows the grain size dependence of densification, and found that the micro hardness increases with decrease in grain size [189].

1.2.3.1 Applications of Alkaline earth metal titanates $MTiO_3$

Alkaline earth metal titanates $MTiO_3$ (M = Ba, Sr, Ca, Mg) have become very important which are widely employed in the

ceramic and electronic industries [190]. These electroceramic substances have numerous applications due to their specific structures and physical properties, such as interconnect, packaging and substrates materials for microelectronics or as individual circuit components, particularly as capacitors or sensors [191–192]. Perovskites with general formula, ABX_3 due to their excellent electric and magnetic properties are extensively used for electronic devices and gas sensors [193].

$BaTiO_3$ have been extensively applied in various fields such as multilayer ceramic capacitors (MLCCs), integral capacitors in printed circuit boards (PCB), dynamic random access memories (DRAM), resistors with positive temperature coefficient of electrical resistivity (PTCR), temperature-humidity-gas sensors, electrooptic devices, piezoelectric transducers, actuators, and thermistors [194]. Xue *et al*. [195] reported a room temperature synthesis of Ba/Ti oxides mixtures, by milling under nitrogen which contains several technologically important electronic materials and electro-optic components [196]. Ferroelectric properties and a high dielectric constant make $BaTiO_3$ useful in an array of applications such as gate dielectrics, waveguide modulators, IR detectors, and holographic memory [197]. Recently, an increasing number of studies have been focused on the exploitation of BTNPs in the biomedical field, owing to their high biocompatibility and peculiar non-linear optical properties that have encouraged their use as nanocarriers for drug delivery and as label-free imaging probes [198]. The exploration of BTNP potential in biomedical/therapeutic applications, such as cancer therapy through hyperthermia, and

drug/gene delivery, has recently started in nanomedicine, based on the encouraging results observed in the biocompatibility assessments [199]. Hsieh *et al.* [200] investigated the bioconjugation of barium titanate nano-crystals with immunoglobulin G antibody for second harmonic radiation imaging probes.

$SrTiO_3$ a highly technologically important perovskite electro-ceramic material, is widely used in PTC resistors, capacitors and sensors, *etc*. [201]. Poth *et al.* [202] have devised a combustion-synthesis of $SrTiO_3$, the important applications are its use as grain-boundary barrier layer capacitor (GBBLC) materials [203], as thin film in dynamic random access memories (DRAM's) [165], as substrate for the hetero-epitaxial growth of high *Tc*-superconductors [204], as oxygen gas sensor [205], as varistor [206] and as material in low-voltage electron-excitation display [207].

$CaTiO_3$ is a material of perovskite structure with considerable interest in geology, metallurgy and ceramics [208]. $CaTiO_3$ shows distinct structural, electrical and optical properties and, therefore, is of great scientific and technological interest. This material can act as a noble candidate for next generation communication devices [209], and is a key component of *synroc* (a type of synthetic rock used to store nuclear waste) [210-211]. Calcium titanate has high dielectric constant, low dielectric loss and large temperature coefficient of resonant frequency, making it a promising component in the production of communication equipment operating at microwave frequencies (ultra high frequency (UHF) and super high frequency (SHF)), which in turn are used in microwave dielectric applications as resonators and filters

and finds applications in manufacture of ceramic capacitors, PTC thermal resisters, microwave antennas, filler and stainless steel electrode [212-214]. Also, it is a material that can be employed as a thermally sensitive resistor element due to its negative temperature coefficient, and for the immobilization of highly radioactive products [215], and is a refractory material with high resistance to caustic corrosion [216].

Calcium titanate containing mold compositions and methods for casting titanium and titanium aluminide alloys are also find extensive application in solar cell manufacture and holds big promise in the world markets [217]. Recently, visible photoluminescence properties at room temperature in disordered structurally perovskite calcium titanates and highly emissive red-emitting phosphors have been reported [218–223]. Currently, nanosized calcium titanate is used for biomedical applications [224]. In this regard, calcium titanate nanoparticles were reported as good substrate for apatite growth *in vitro* with the potential to enhance osseointegration and osteoconductivity [225-226]. The beneficial effect of addition of $CaTiO_3$ to HA encourages the development of electrically active biomaterial for bone replacement [227-228].

$MgTiO_3$ is a well-known microwave low loss dielectric ceramic material [229] with wide applications such as multilayer capacitors [230], band-pass filters [231-232], antennas for communication [233], direct broadcasting satellite and global positioning system operating at microwave frequencies [234-235]. In addition, $MgTiO_3$ could also be used for optical communication in

planar light-wave circuits (PLC) as a buffer layer for sapphire and $LiNbO_3$ [236]. Dharmaraj *et al*. [237] pointed out that, $MgTiO_3$ exists most frequently in nature as the mineral geikielite with the ilmenite structure, is an oxide ceramic material possessing a relatively low dielectric constant that varies only slightly with temperature and frequency [238]. Magnesium titanate has many useful applications such as in dew sensors, resonators, cellular telephones, radar, pigments and in the electrical and electronic industries as a dielectric material for manufacturing on chip capacitors, high frequency capacitors and temperature compensating capacitors [239]. Generally, the choice of the synthetic procedure has a direct influence on the formation and the properties of $MgTiO_3$. The nanostructured $MgTiO_3$ materials exhibit particular catalytic properties [240–241] due to the extremely low crystallite sizes and morphology.

Potential growth of the $BaTiO_3$ nano particle is due to the unique physical and chemical properties, they possessed wide variety of applications in material science including catalysis, electronics, sensors, *etc*. The emergence of these nano particles became great importance to nanomedicines and the researchers to think about the unknown biological effects underlying the nanoparticles.

1.2.4 Computational Approach

Computational material science, which describe quantum mechanical computational calculations used to study the different properties of solids within the density functional theory (DFT). Density functional theory is a powerful tool for predicting material properties of matter such as structure, optics, color, electric and magnetic, vibrational properties, *etc*., using theoretical methods. Kotochigova *et al*. used DFT to compute the ground state energies of every atom in the periodic table to six significant figures [242]. In the DFT approach, the most successful method for studying the electronic structure of atoms, the molecules and solids was formulated by Hohenberg and Kohn [243] in such a way that knowing the average density of electrons at all point in space is enough to uniquely determine the total energy, and therefore all of the other properties of the system. DFT is used to solve the many-body Schrodinger equation numerically, and allows the derivation of properties like ferroelectric polarization, structure, magnetic properties, *etc*., on length scales that can be difficult to achieve experimentally.

Recent studies have shown that interfaces between different nanostructure metal oxides can show new electronic and magnetic properties. These nanostructures and interface engineering has many potential applications and is a large area of research [244]. Quantum mechanical computational calculations were performed to study the ground state electronic structure of barium titanate within the density functional theory [245]. The static and dynamic properties of $BaTiO_3$ characterized by theoretical calculations especially structure, equation

of state, phase stability, and phase transformations was studied in Generalized Gradient Approximation using Density Functional Theory. The structure and equation of state of stable phase of $BaTiO_3$ were investigated and computed results were compared with the available experimental data and theoretical calculations. Vienna Ab-initio Simulation Package (VASP), commercial software, was used for DFT calculations to solve the quantum mechanical problem of materials. The program and the techniques have been used successfully for a large number of different systems (liquid and amorphous semiconductors, liquid samples and transition metals, metallic and semiconducting surfaces, phonons in simple metals, transition metals, and semiconductors) and turned out to be very reliable, uses pseudo potential method with a plane wave basis set which can modeling the systems with maximum number of atoms in the range of 100-200 [246]. VASP has also been used for the calculations of electronic structure of states (EOS), and structural optimization [247].

Jiang *et al.* [248] presented the different ferroelectric behaviors of $MTiO_3$ on the basis of theoretical and experimental techniques. Meyer *et al.* [249] have performed plane-wave calculations within DFT using ultrasoft pseudopotentials for surfaces of the cubic perovskite $MTiO_3$ compounds. Feng *et al.* have performed the first principle calculations to study the ground state electronic properties of barium titanate within the density functional theory. The band structure, total density of states (TDOS) and partial density of states (PDOS) have been conducted to investigate the electronic

configuration of this prototype ferroelectric perovskits compound [250].

Schimka *et al*. have reported the lattice constants and cohensive energies of alkali and alkaline earth metals, introduction to density functional theory and its implementation within the plane-wave VASP code [251]. Theoretical analysis of the properties of crystal structure and bonding in relation to thermal decomposition process in chosen anhydrous metal oxalates are discussed [252]. The experimental and theoretical studies of doped metal titanates, their structure, electrical properties and chemical stability are well explained by Koleżyński *et al*. [253] and reported the theoretical analysis of the electronic and crystal structural properties and bonding in relation to thermal decomposition process in anhydrous calcium oxalate. The proposed theoretical approach can be considered as hopeful and consistent tool for theoretical analysis, allowing explanation and prediction of the properties of the structure and bonding and can explain the most probable way of thermal decomposition process to take place in such structures [254].

1.3 Aim and scope of the work

The present investigation aims at the synthesis and characterization of binary titanyl oxalate mixtures of potassium and barium and the study of their multi stage thermal decomposition behavior by different techniques of thermal analysis, the knowledge of which helps in the modification of the properties of the decomposition products by suitably altering the properties of the oxalate precursor.

The effect of doping on multistage decomposition kinetics, the overall reaction kinetics parameters calculated *via* kinetic deconvolution analysis of the non isothermal data using different kinetic model functions for solid state decomposition reactions. So far, nobody appears to have reported on the multi stage thermal behavior of barium titanyl oxalate and their mixed oxalates by applying kinetic deconvolution principle. The study also intends to carry out some application studies of the as prepared mixed metal oxides. Theoretical studies was performed by density functional theory and VASP to identify the convergence of lattice parameter, *k*-point grid, and plane wave energy cut off for $BaTiO_3$ and K doped $BaTiO_3$. The plane wave basis sets with proper exchange correlation functional GGA+LDA method is accurate to predict the electronic structures and found that the observations are in good agreement with the experimental results.

1.4 References

1. Yoshida M, Lahann J. Smart nanomaterials. ACS Nano. 2008;2: 1101–07.

2. Gao J, Xu B. Applications of nanomaterials inside cells. Nano Today. 2009;4:37–51.

3. Zunger A, Wagner S, Petroff PM. Metal-oxide and sulfide nanocrystals and nanostructures. J. Electronc. Mater. 1993;22:03-04.

4. Kobayashi Y, Tanase T, Tabata T, Miwa T, Konno M. Fabrication and dielectric propreties of the $BaTiO_3$-polymer nano-composite thin films. J. Eur. Ceram. Soc. 2008;28:117-22.

5. Genchi G G, Ciofani G. Bioapplications of boron nitride nanotubes. J. Nanomed. UK. 2015;10:3315–19.

6. Seifert A, Sagalowicz L , Muralt P, Setter N. Combustion synthesis of nanostructured barium titanate. J. Mater. Res. 1999;14:2012-22

7. Hao R, Xing R, Xu Z, Hou Y, Gao S, Sun S. Synthesis, functionalization, and biomedical applications of multifunctional magnetic nanoparticles. J. Adv. Mater. 2010;6:2729–42.

8. Abhilash M. Potential applications of nanoparticles. Int J. Pharm. Bio. Sci. 2010;1:1-12.

9. Kim D, Jon S. Gold nanoparticles in image-guided cancer therapy. J Inorg. Chim. Acta. 2012;393:154-64.

10. Zhao J, Wallace M, Melancon M P. Cancer theranostics with gold nanoshells. J. Nanomed. UK. 2014;9:2041–57.

11. Mendoza KC, McLane VD, Kim S, Griffin JD. Invitro application of gold nanoprobes in live neurons for phenotypical classification, connectivity assessment, and electrophysiological recording. J. Brain Res. 2010;1325:19-27.

12. Aarti PN, Mukesh PR, Silpa PC, Nanoparticles – An overview. Int. J. Res. Dev. Pharm. L. Sci. 2014;3:1121-27.

13. Doane TL, Burda C. The unique role of nanoparticles in nanomedicine: imaging, drug delivery and therapy. J. Chem. Soc. Rev. 2012;41:2885–911.

14. Yong KT, Ouyang Q, Zeng S. Review on functionalized gold nanoparticles for biosensing applications. Plasmonics. 2011;6:491–506.

15. Dubchak S, Ogar A ,Mietelski JW, Turnau K. Influence of silver and tianium nanoparticles on arbuscular mycorhiza colonization and acumulation of radiocaesium in Helianthus anus. Span. J. Agric. Res. 2010;8:103-08.

16. Borm PJ, Kreyling W. Toxicological hazards of inhaled nanoparticles potential implications for drug delivery. J. Nanosci. Nanotech. 2004;46:1-11.

17. Rawat M. Singh D, Saraf S. Nanocarriers: Promising vehicle for bioactive drugs. J. Biol. Pharm. Bull. 2006;29:1790- 98.

18. Xie J, Lee S, Chen X. Nanoparticle-based theranostic agents. J. Adv. Drug Deliv. Rev. 2010;62:1064–79.

19. Parker J. Nanoscale materials in chemistry. Wiley Interscience, New York. 2001:279-85.

20. Kato H, Kudo A. Visible-light-response and photocatalytic activities of TiO_2 and $SriO_3$ photocatalysts Co doped with antimony and chromium. J. Phys. Chem. B. 2002;106:5029-34.

21. Kutty TRN, Avudaithai M. Photocatalysis on fine powders of perovskite oxides. J. Catal. Rev. Sci. Eng. 1992;34:373-89.

22. Kesselman JM, Kumar A, Lewis NS. Photocatalytic purification and treatment of water and air. Elsevier, Amsterdam, New York. 1993; 19-37.

23. Velev OD, Jede TA, Lobo RF, Lenhoff AM. Porous silica *via* colloidal crystallization. Nature. 1997;389:447-48.

24. Winjnhoven JEGJ, Vos WL. Preparation of photonic crystals made of air spheres in titania. Science.1998;281:802-04.

25. Holland BT, Blanford CF, Stein A. Synthesis of macroporous minerals with highly ordered three-dimensional arrays of spheroidal voids. Science.1998;281:538-40.

26. Schneider M, Baiker A. Titania-based aerogels. Catal. Today.1997; 335:39-365.

27. Bond GC, Fischer SF. Mesoporous SBA-15: Introduction and Literature survey. J. Appl. Catal. 1991;71:1-31.

28. Knözinger H, Taglauer E. Preparation of solid catalysts. Wiley-VCH 1993.

29. Fu Q, Cui Z, Xuea Y. Size dependence of the thermal decomposition kinetics of nano- CaC_2O_4□: A theoretical and experimental study. Eur. Phys. J. Plus. 2015;130:1-14.

30. Voorhoeve RJH, Remeika JP, Freeland PE, Matthias BT. Nanosized alkaline earth metal titanates. Science. 1972;277:353-54.

31. Zhang HM, Shimizu Y, Teraoka Y, Miura N, Yamazoe N. Oxygen sorption and catalytic properties of lanthanum strontium cobalt iron oxide perovskite type oxides. J. Catal. 1990;121:432-32.

32. Zunger A, Wagner S, Petroff PM. New materials and structures for photovoltaics. J. Electron. Mater. 1993;22:3-16.

33. Chaturvedi S, Dave PN. Applications of nano-catalyst in new era. J. Saudi Chem. Soc. 2012;16:307–25.

34. Gobara HM. Various characteristics of Ni and Pt-Al_2O_3 nanocatalysts prepared by microwave method to be applied in some petrochemical processes. Egypt. J. Pet. 2014;23:105–18.

35. Hao R, Xing R, Xu Z, Hou Y, Gao S, Sun S. Synthesis, functionalization, and biomedical applications of multifunctional magnetic nanoparticles. J. Adv. Mater. 2010;6:2729–42.

36. Xie J, Lee S, Chen X. Nanoparticle-based theranostic agents. J. Adv. Drug Deliv. Rev. 2010;62:1064–79

37. Städler D. Harmonic nanocrystals for biolabeling: a survey of optical properties and biocompatibility. ACS Nano. 2012;6:2542–49.

38. Battisha IK, AbouHamad AB, Mahani RM. Structure and dielectric studies of nano-composite Fe_2O_3: $BaTiO_3$ prepared by sol-gel method. J. Phys. B. 2009;404:2274-79.

39. Zhong Z, Gallagher PK. Combustion synthesis and characterization of $BaTiO_3$. J. Mater. Res. 1995;10:942-52.

40. Saldan JM, Mullierb B, Schneidera GA. Preparation of $BaTiO_3$ single crystals using the modified SiO_2-exaggerated grain growth method. J. Eur. Ceram. Soc. 2002;22:681-88.

41. Lu SW, Lee BI, Wang ZL, Samuels WD. Hydrothermal synthesis and structural characterization of $BaTiO_3$ nanocrystals. J. Cryst. Growth. 2000;219:269-76.

42. Zeng M. Surface reaction characteristics at low temperature synthesis $BaTiO_3$ particles by barium hydroxide aqueous solution and titanium tetraisopropoxide. J. Appl. Surf. Sci. 2011;257:6636-43.

43. Krishnamurty KV, Harris GM. The chemistry of the metal oxalato complexes. J. Chem. Rev. 1961;61:213-41.

44. Reddy VB, Goel SP, Mehrotra PN. Investigations on formation of zinc titanates *via* thermal decomposition of zinc titanyl oxalate hydrate. J. Mater. Chem. Phys. 1984;10:365-73.

45. L'vov BV. The physical approach to the interpretation of the kinetics and mechanisms of thermal decomposition of solids: the state of the art. Thermochim. Acta. 2001;373:97-124.

46. Muraleedharan K, Labeeb P. Kinetics of the thermal dehydration of potassium titanium oxalate, $K_2TiO\ (C_2O_4)_2\ 2H_2O$. J. Therm. Anal. Calorim. 2012; 109:89–96.

47. Muraleedharan K, Viswalekshmi CH, Sarada K. Synthesis, characterization and thermal dehydration and degradation kinetics of chitosan Schiff bases of o-, m- and p- nitrobenzaldehyde. J. Polym. Bull. 2017;74:39-54

48. Pejic N, Kuntic V, Malesev D. Potassium titanyloxalate as analytical reagents for micro-quantitative determination of quercetin. Pharmazie. 2001;56:216-17.

49. Kuntic V, Pejic N, Misic S, Vukojevic V, Vujic Z, Malesev D. Determination of quercetin in pharmaceutical formations via its reaction with potassium titanyloxalate. Determination of the stability constants of the quercetin titanyloxalato complex. J. Serb. Chem. Soc. 2005;70:753-53.

50. Broadbent D, Dollimore D, Dollimore J. Thermogravimetry and differential thermal analysis studies on potassium titanyl oxalate and potassium aluminium oxalate and related oxalates. J. Analyst. 1969; 94:543-53.

51. Sharma AK, Kumar S, Kaushik NK. Thermal studies on zinc and cadmium titanyl oxalates. Thermochim. Acta. 1981;49:385-90

52. Gopalakrishna Murthy HS, Subba Rao M, Narayanan Kutty TR. Thermal decomposition of titanyl oxalates-III, Lead titanyl oxalate. J. Inorg. Nucl. Chem. 1976; 38:417-19.

53. Thomas P, Dwarkanath K, Varama KBR, Kutty TRN. Nanoparticles of the giant dielectric material, $CaCu_3Ti_4O_{12}$ from a precursor route. J. Phys. Chem. Solids. 2008;69:2594-604.

54. Gopalakrishna Murthy HS, Subba Rao M, Narayanan Kutty TR. Thermal decomposition of a mixture of barium and titanyl oxalates. J. Ind. Insti. Sci. 1978;60.

55. Galwey AK, Brown ME. An appreciation of the chemical approach of V. V. Boldyrev to the study of the decomposition of solids. J. Therm. Anal. Calorim. 2007;90:9-22.

56. Padmanabhan VM, Saraiya SC, Sundaram AK. Thermal decomposition of some oxalates. J. Inorg. Nucl. Chem. 1960;12:356-59.

57. Dollimore D, Nicholson D. The thermal decomposition of oxalates. Part I. The variation of surface area with the temperature of treatment in air. J. Chem. Soc. 1962;96:606-11.

58. Carter C, Norton M. Ceramic Materials: Science and Engineering, Springer, New York, 2007.

59. Dhage SR, Khollam YB, Potdar HS, Deshpande SB, Sarwade BD. Chemical co-precipitation of mixed (Pb+Ti) oxalates precursor for the synthesis of $PbTiO_3$ powders. J. Mater. Lett. 2002;56:564-70.

60. Brown ME, Dollimore D, Galwey AK. Reactions in the solid state. Elsevier: Amsterdam, the Netherlands. 1980.

61. Gadalla AMM. Kinetics of the decomposition of hydrated oxalates of calcium and magnesium in air. Thermochim. Acta. 1984;74:255-72.

62. Krishnan K, Ninan KN, Madhusudanan PM. A comprehensive study of the influence of sample mass on the kinetic parameters in isothermal dehydration reactions. Thermochim. Acta. 1985;90:229-50.

63. SharmaYK, Kharkwal M, Uma S, Nagarajan R. Synthesis and characterization of titanates of the formula $MTiO_3$ (M = Mn, Fe, Co, Ni and Cd) by co-precipitation of mixed metal oxalates. Polyhedron. 2009;28:579–85.

64. Strizhkov BV, Lapitskil AV, Vlasov LG. Physico-chemical studies of decomposition of double salts of barium titanyl oxalate. Zh. Priklad. Khim. 1960;33:2009-14.

65. Kuwabara M. Lead titanate ceramics with positive temperature coefficients of resistivity. J. Am. Ceram. Soc. 1990;73:1438-39.

66. Gallagher PK, Frank Schrey, DiMarcello FV. Preparation of semiconducting titanates by chemical methods. J. Am. Ceram. Soc. 1963;46:359-65.

67. Moon J, Li T, Randall CA, Adair JH. Low temperature synthesis of lead titanate by a hydrothermal method. J. Mater Res. 1997;12:189-97.

68. Sharma AK, Kumar S, Kaushik NK. Thermal studies on beryllium titanyl/zirconyl oxalates. J. Anal. Appl. Pyrol. 1981;3:271-79.

69. Gopalakrishna Murthy HS, Subba Rao M, Narayanan Kutty TR. Thermal decomposition of titanyl oxalates-v. Magnetium titanyl oxalate. J. Inorg. Nucl. Chem. 1976;38:596-97.

70. Swanson HE, Gilfrich N T, Ugrinic GM. Standard X-ray Diffraction Powder Patterns. Natl. Bur. Stand. Circ. 1955;539:36-57.

71. Miao YM, Zhang QL, Yang H. Low-temperature synthesis of nano-crystalline magnesium titanate materials by the sol-gel method. J. Mater. Sci. Eng. B. 2006;128:103–06.

72. Yanovskaya MI, Kotova NM, Golubko NV, Turova NY. Reactions of magnesium and titanium alkoxides. Preparation and characterization of alkoxy-derived magnesium titanate powders and ceremics. J. sol-gel sci. Technol. 1998;11:23-29.

73. Gopalakrishna Murthy HS, Subba Rao M, Narayanan Kutty TR. Thermal decomposition of titanyl oxalates IV. Strontium and calcium titanyl oxalates. Thermochim. Acta. 1975;13:183-91.

74. Mallik PK. Characterisation of sol-gel synthesis of phase pure $CaTiO_3$ nano powders after drying. 2015 IOP Conf. Ser.: Mater. Sci. Eng. 75 012005

75. Pfaff G. Synthesis of calcium titanate powders by the sol-gel process. J. Chem. Mater. 1994;6:58-62.

76. Mi G, Murakami Y, Shindo D, Saito F. Microstructural investigation of $CaTiO_3$ formed mechanochemically by grinding of a CaO-TiO_2 mixture. Powder Technol. 1999;104:75-78.

77. Zaware SK, Jadhav SS. Kinetics and mechanism of thermal decomposition of binary mixture of barium oxalate and ferrous oxalate in the (1:1) mole ratio. J. Chem. & Cheml. Sci. 2013;3:13-30.

78. Gallagher PK, Thomson J. Thermal analysis of some barium and strontium titanyl oxalates. J. Am. Ceram. Soc. 1965;48:644–47.

79. Clabaugh WS, Swiggard EM, Gilchrist R. Preparation of barium titanyl oxalate tetrahydrate for conversion to barium titanate of high purity. J. Res. Natl. Bur. Std. 1956;56:289-91.

80. Sairam Patra B, Otta S, Bhattamisra SD. A kinetic and mechanistic study of thermal decomposition of strontium titanyl oxalate. Thermochim. Acta. 2006;441:84–88.

81. Fan W, Niinisto L. Preparation of strontium titanate using strontium titanyl oxalate as precursor. J. Mater. Res. Bull. 1994;29:451-58.

82. Bera J, Sarkar D. Formation of $BaTiO_3$ from barium oxalate and TiO_2. J. Electroceram. 2003;11:131-37.

83. Gallagher PK. Thermal decomposition of barium and strontium trisoxalatoferrates(III). Inorg. Chem. 1965;4:965-70.

84. Rout SK, Panigrahi S, Bera J. Study on electrical properties of Ni doped $SrTiO_3$ ceramics using impedance spectroscopy. J. Bull. Mater. Sci. 2005;28:275-79.

85. Lee BW, Auh K. Effect of grain size and mechanical processing on the dielectric properties of $BaTiO_3$. J. Mater. Res. 1995;10:1418-23.

86. Muraleedharan K, Mallikassery JJ, Sarada K, Kannan MP. Isothermal decomposition of $K_2C_2O_4$. J. Therm. Anal. Calorim. 2014;116:1055–60.

87. Vyazovkin S, Wight CA. Isothermal and non-isothermal kinetics of thermally stimulated reactions of solids. Int. Rev. Phys. Chem. 1998;17:407–33.

88. S□esták, S□atava J, Wendlandt V. The study of heterogeneous processes by thermal analysis. Thermochim. Acta.1973;7:333−56.

89. Boldyrev VV. Thermal decomposition of silver oxalate. Thermochim. Acta. 2002;388:63–90.

90. Brown ME, Dollimore D, Galwey AK. Reactions in the solid state. Elsevier: Amsterdam. The Netherlands, 1980.

91. Sestak J. Thermophysical properties of solids: Their measurements and theoretical thermal analysis. Elsevier: Amsterdam. The Netherlands. 1984.

92. Galwey AK. Structure and order in thermal dehydrations of crystalline solids. Thermochim. Acta. 2000;355:181−238.

93. Koga N, Tanaka H. A physico-geometric approach to the kinetics of solid-state reactions as exemplified by the thermal dehydration and decomposition of inorganic solids. Thermochim. Acta. 2002; 388:41−61.

94. Limin G, Hiroyuki A, Norio T. Synthesis of mesoporous metal oxide by the thermal decomposition of oxalate precursor. Langmuir. 2013; 29:4404–12.

95. Kudaka K, Ilzumi K, Sasaki K. Preparation of stoichiometric barium titanyl oxalate tetrahydrate. J. Am. Ceram. Soc. Bull. 1982;61:1236-36.

96. Fang TT, Lin HB, Hwang JB. Thermal analysis of precursors of barium titanate prepared by co-precipitation. J. Am. Ceram. Soc. 1990;73:3363–67.

97. Yamamura H, Watanabe A, Shirasaki S, Moriyoshi Y, Tanada M. Preparation of barium titanate by oxalate method in ethanol solution. Ceram. Int. 1985;11:17–22.

98. John MJ, Muraleedharan K, Kannan MP, Ganga DT. Effect of semiconducting metal oxide additives on the kinetics of thermal decomposition of sodium oxalate under isothermal conditions. Thermochim. Acta. 2012;534:71-76

99. Yen FS, Chang CT, Chang YH. Characterization of BTO tetrahydrate. J. Am. Ceram. Soc. 1990;73:3422-27.

100. Balek V, Kaisersberger E. Preparation of $BaTiO_3$ by thermal decomposition of BTO simultaneously investigated by emanation thermal analysis, TG-DTA and EGA. Thermochim. Acta. 1985;85:207–10.

101. Ragulya AV, Vasylkiv OO, Skorokhod VV. Synthesis and sintering of nanocrystalline barium titanate powder under nonisothermal conditions. I. Control of dispersity of barium titanate during its synthesis from barium titanyl oxalate. Powder Metall. Met. Ceram. 1997;36:170–75.

102. Fang TT, Lin HB. Factors affecting the preparation of barium titanyl oxalate tetrahydrate. J. Am. Ceram. Soc. 1989;72:1899–906.

103. Amala sekar M, Dhanaraj G, Bhat HL, Patil KC. Synthesis of fine-particle titanates by the pyrolysis of oxalate precursors. J. Mater. Sci. 1992;3:237–39.

104. Kiss K, Magder J, Vukasovigh MS, Lockhart RJ. Ferroelectrics of ultrafine particles size:1.synthesis of titanate powders of ultrafine particle size. J. Am. Ceram. Soc. 1966;49:291-95.

105. Saburi O. Semiconducting bodies in the family of barium titanates. J. Am. Ceram. Soc. 1961;44:54–63.

106. Tsay JD, Fang TT. Effects of temperature and atmosphere on the formation mechanism of barium titanate using the citrate process. J. Am. Ceram. Soc. 1996;79:1693-96.

107. Otta S, Bhattamisra SD. Kinetics and mechanism of the thermal decomposition of barium titanyl oxalate. J. Therm. Anal. 1994;41:419–33.

108. Gallagher PK, Frank Schrey. Thermal decomposition of some substituted barium titanyl oxalates and its effect on the semiconducting properties of the doped materials. J. Am. Ceram. Soc.1963;46:567-73.

109. Swilam MN, Gadalla AM. Decomposition of barium titanyl oxalate and assement of barium titanate produced at various temperatures. Trans. J. Brit. Ceram. Soc. 1975;74:159-63.

110. Fu Q, Cui Z, Xuea Y. Size dependence of the thermal decomposition kinetics of nano-CaC_2O_4□: A theoretical and experimental study. Eur. Phys. J. Plus. 2015;130:1-14.

111. Dutta PK, Gallagher PK, Twu J. Raman spectroscopic study of the formation of barium titanate from an oxalate precursor. J. Chem. Mater. 1993;5:1739–43.

112. Gopalakrishna Murthy HS, Rao MS, Kutty TRN. Thermal decomposition of titanyl oxalates--1. Barium titanyl oxalate. J. Inorg. Nucl. Chem. 1975;37:891–98.

113. Sindhu NV, Muraleedharan K. Kinetic modelling of formation of K^{+} doped $BaTiO_3$ bones from barium titanyl oxalate *via* multi stage thermal decomposition. J. Mater. Res. Bull. 2017;94:231–40.

114. Celis K, Driessche IV, Mouton R, Vanhoyland G, Hoste S. Kinetics of consecutive reactions in the solid state: Thermal decomposition of oxalates. J. Meas. Sci. Rev. 2001;1:77-98.

115. Gopalakrishna Murthy HS, Subba rao M, Narayanan kutty TR. Thermal decomposition of titanyl oxalates. II. Kinetics of decomposition of barium titanyl oxalate. J. Inorg. Nucl. Chem. 1975;37:1875-78.

116. Ubaldini A, Artini C, Costa GA, Carnasciali MM, Masini R. Thermal decomposition of mixed Ce and Gd oxalates and thermal properties of mixed Ce and Gd oxides. J. Therm. Anal. Calorim. 2006;84:207–11.

117. Nidhuban D. An investigation on solid-state pyrolytic decomposition of barium trihemiaquatris(oxalato)lanthanate(III)decahydrate using TG–DTA in air and DSC in nitrogen. J. Therm. Anal. Calorim. 2013; 112:1415-21.

118. Nidhuban Deb. An investigation on the solid state pyrolytic decomposition of bimetallic oxalate precursors of Ca, Sr and Ba with cobalt: A mechanistic approach. J. Anal. Appl. Pyrol. 2007;80:389–99.

119. Hwu JM, Yu WH, Yang WC, Chen YW, Chou YY. Characterization of dielectric barium titanate powders prepared by homogeneous precipitation chemical reaction for embedded capacitor applications. J. Mater. Res. Bull. 2005;40:1662–79.

120. Khollam YB, Deshpande SB, Potdar HS, Bhoraskar S V. Simple oxalate precursor route for the preparation of barium-strontium titanate□: $Ba_{1-x}Sr_xTiO_3$ powders. J. Mater. Charact. 2005;54:63–74.

121. Bethe K, Welz F. Preparation and properties of (Ba, Sr) TiO_3 single crystal. J. Mater. Res. Bull. 1971; 6:209-17.

122. Li M, Xu M. Effect of dispersant on preparation of barium-strontium titanate powders through oxalate co-precipitation method. J. Mater. Res. Bull. 2009;44:937–42.

123. Roeder RK, Slamovich EB. Stoichiometry control and phase selection in hydrothermally derived $Ba_xSr_{1-x}TiO_3$ powders. J. Am. Ceram. Soc. 1999;82:1665-75.

124. Li M, Xu M. Oxalate co-precipitation method. J Alloy. Compd. 2009;474:311–15.

125. Auciello O, Scott JF, Ramesh R. The Physics of Ferroelectric Memories. J. Phys. Today 1998;51:22-27.

126. Schrott AG, Misewich JA, Nagarajan V, Ramesh R. Ferroelectric field effect transistor with a $SrRu_xTi_{1-x}O_3$ channel. J. Appl. Phys. Lett. 2003;82:4770-72.

127. Tao S, Irvine JTS. A redox-stable efficient anode for solid-oxide fuel cells. J. Nat. Mater. 2003;2:320-23.

128. Chung SY, Kim ID, Kang SJL. Strong nonlinear current-voltage behaviour in perovskite derivative calcium copper titanate. J. Nat. Mater. 2004;3:774-78.

129. Perez-Ramirez J, Vigeland B. Perovskite membranes in ammonia oxidation: Towards process intensification in nitric acid manufacture. Angew. Chem. Int. Ed. 2005;44:1112-15.

130. Kiennemann A, Petit C, Roger AC, Pitchon V. Perovskites: a versatile material in heterogeneous catalysis. Curr. Topics in Catal. 2002;3:147-160.

131. Lombardo EA, Ulla. MA. Perovskite oxides in catalysis: past, present and future. J. Res. Chem. Intermed. 1998;24:581-92.

132. Scott JF. Applications of modern ferroelectrics. Science. 2007; 315:954−59.

133. Wang W, Shao Z. Research progress of perovskite materials in photocatalysis and photovoltaics related energy conversion and environmental treatment. J. Chem. Soc. Rev. 2012;42:1-38.

134. Zhang WF, Tang J, Ye J. Photoluminescence and photocatalytic properties of $SrSnO_3$ perovskite. J. Chem. Phys. Lett. 2006;418:174–78.

135. Zee JH, Nersisyan HH, Lee HH, Won CW. Structure, surface morphology and optical properties of $BaTiO_3$ powders prepared by wet chemical method. J. Mater. Sci. 2004;39:1397-99.

136. Cook TR, Dogutan DK, Reece SY, Surendranath Y, Teets TS, Nocera DG. Solar energy supply and storage for the legacy and nonlegacy worlds. J. Chem. Rev. 2010;110:6474–502.

137. Shi J, Guo L. ABO_3-based photocatalysts for water splitting. Prog. Nat. Sci. Mat. Int. 2012;22:592–615.

138. Izumi Y. Recent advances in the photocatalytic conversion of carbon dioxide to fuels with water and/or hydrogen using solar energy and beyond. J. Coord. Chem. Rev. 2013;257:171–86.

139. Tan YN, Wong CL, Mohamed AR. An overview on the photocatalytic activity of nano-doped TiO_2 in the degradation of organic pollutants. ISRN Mat. Sci. 2011;18:450-57.

140. Dalrymple OK, Stefanakos E, Trotz MA, Goswami DY. A review of the mechanisms and modeling of photocatalytic disinfection. J. Appl. Catal. B. 2010;98:27–38.

141. Ahmed S, Rasul MG, Martens W, Brown R, Hashib MA. Advances in heterogeneous photocatalytic degradation of phenols and dyes in waste water: A Review. Water Air Soil Pollut. 2011;215:3–29.

142. Bickley RI, Vishwanathan V. Photocatalytically induced fixation of molecular nitrogen by near UV radiation. Nature. 1979;280:306–08.

143. Wang H, Wu Z, Zhao W, Guan B. Photocatalytic oxidation of nitrogen oxides using TiO_2 loading on woven glass fabric. Chemosphere. 2007;66:185–90.

144. Hatakeyama T, Takeda S, Ishikawa F, Ohmura A, Nakayama A, YamadaY, Matsushita A, Yea J. Photocatalytic activities of Ba_2RBiO_6 (R = La, Ce, Nd, Sm, Eu, Gd, Dy) under visible light irradiation. J. Ceram. Soc. Jpn. 2010;118: 91–95.

145. Iwakura H, Einaga H, Teraoka Y. Photocatalytic properties of ordered double perovskite oxides. J. Novel Carbon Resour. Sci. 2011;3:1–5.

146. Borse PH, Lim KT, Yoon JH, Bae JS, Ha MG, Chung EH, Jeong ED, Kim HG. Investigation of the physico-chemical properties of $Sr_2FeNb_{1-x}W_xO_6$ ($0.0 \leq x \leq 0.1$) for visible-light photocatalytic water-splitting applications. J. Korean Phys. Soc. 2014;64:295–300.

147. Siritanaratkul B, Maeda K, Hisatomi T, Domen K. Synthesis and photocatalytic activity of perovskite niobium oxynitrides with wide visible-light absorption bands. J. Chem. Sus. Chem. 2011;4:74–78.

148. Higashi M, Abe R, Takata T, Domen K. Photocatalytic overall water splitting under visible light using $ATaO_2N$ (A = Ca, Sr, Ba) and WO_3 in a IO_3^-/I^- shuttle redox mediated system. J. Chem. Mater. 2009;21:1543–49.

149. Maeda K, Domen K. Preparation of $BaZrO_3$–$BaTaO_2N$ solid solutions and the photocatalytic activities for water reduction and oxidation under visible light. J. Catal. 2014;310:67–74.

150. Sarkas HW, Arnold ST, Hendricks JH, Kidder LH, Jones CA, Bowen KH. An investigation of catalytic activity in mixed metal oxide nanophase materials. Z. Phys. D. 1993;26:46-50.

151. Yuan C, Wu HB, Xie Y, Wen Xiong. Mixed transition metal oxides: design, synthesis, and energy-related applications. Angew. Chem. Int. Ed. 2014;53:1488-504.

152. Guo BY, Hu J, Wan L. Nanostructured materials for electrochemical energy conversion and storage devices. J. Adv. Mater. 2008;20:2878–87.

153. Gawande MB, Pandey RK, Jayaram RV. Role of mixed metal oxides in catalysis science-versatile applications in organic synthesis. J. Catal. Sci. Technol. 2012;2:1113–25.

154. Sonavane SU, Jayaram RV. Selective reduction of C=O in α,β-unsaturated carbonyls through catalytic hydrogen transfer reaction over mixed metal oxides. J. Synlett. 2004;1:146-48.

155. Pena MA, Fierro JL. Chemical structures and performance of perovskite oxides. J. Chem. Rev. 2001;101:1981-2017.

156. Kanai H, Ikeda Y, Imamura S. Epoxidation of allyl acetate with tert-butyl hydroperoxide catalyzed by MoO_3/TiO_2. Appl. Catal. A 2003;247:185-91; (b) Samantaray SK, Parida K. Effect of phosphate ion on the textural and catalytic activity of titania–silica mixed oxide. J. Appl. Catal. A. 2001; 220:9-20.

157. Jackson SD, Hargreaves JSJ. Metal Oxide Catalysis, Wiley-VCH, 2008, ISBN-10: 3527318151; (b) Cui H, Zayat M, Levy D. Sol-gel synthesis of nanoscaled spinels using propylene oxide as a gelation agent. J. Sol-Gel Sci. Technol. 2005;35:175-81.

158. Védrine JC, Fechete I. Heterogeneous partial oxidation catalysis on metal oxides. CR Chim. 2016;19:1203–25.

159. Fouad OA, Hassan AM, El-Wahab HA, Eldin AM, Naser ARM, Wahba OAG. Synthesis, characterization and application of some nanosized mixed metal oxides as high heat resistant pigments: Ca_2CuO_3, $Ca_3Co_2O_6$, and $NiSb_2O_6$. J. Alloys. Compd. 2012;537:165–70.

160. García A, Galindo R, Gargori C, Cerro S, Llusar M, Monrós G. Ceramic pigments based on chromium doped alkaline earth titanates. Ceram. Int. 2013;39:4125-32.

161. Kantorová M, Veselý D. Mixed metal oxides with the structure of perovskite for anticorrosion organic coatings. 10th International conference on solid state chemistry. Pardubice, Czech Republic. Physics Procedia. 2013;44:213-23.

162. Kulkarni SB, Veer SS, Salunkhe DJ, Kokare SR, Joshi PB. Structural and dielectric investigations on BST-BZT composites. J. Mat. Sci. Res. Ind. 2008;5:183-86.

163. Piagai I, Kim J, Park Y, Kim. Preparation of magnesium-calcium titanate powders by alkoxide precursor method. J. Am. Ceram. Soc. 1998;64:1361–64.

164. Arunachalam LM, Chakravorty D, Subbarao EC. Synthesis and properties of manganese-doped barium titanate. J. Bull. Mater. Sci. 1987;9:159-68.

165. Lin, Jiang D, Ma X, Shi W. Effect of annealing atmosphere on magnetism for Fe-doped $BaTiO_3$ ceramic. Physica. B. Condens. Matter. 2008;403:2525–29.

166. Takin EF,Ciofani G, Puleo GL, de Vito G, Filippesch C, Mazzolai B, Piazza V, Mattoli V. Barium titanate core-gold shell nanoparticles for hyperthermia treatments. Int. J. Nanomed. 2013;8:2319–31.

167. Azim araghi ME. Synthesis and characterization of nanocrystalline barium strontium titanate powder by a modified sol-gel processing. J. Mater. Sci. 2016;34:63–68.

168. Enhessari M, Parviz A, Ozaee K, Habibi AH. Synthesis and characterization of barium strontium titanate (BST) micro/nanostructures prepared by improved methods. J. Nano Dim. 2011;2:85–103.

169. Xiao W, Gang X, Zhaohui R, Yonggang W, GeS, Gaorong H. Composition and shape control of single-crystalline $Ba_{1-x}Sr_xTiO_3$ (x = 0–1) nanocrystals via a solvothermal route. J. Cryst. Growth. 2008; 310:4132-37.

170. Ezhilvalavan S, Tseng TY. Progress in the developments of $(Ba,Sr)TiO_3$ (BST) thin films for Gigabit era DRAMs. J. Mater. Chem. Phys. 2000;65:227-48.

171. Mohammadi MR, Fray DJ. Sol-gel derived nanocrystalline and mesoporous barium strontium titanate prepared at room temperature. Particuology. 2011;9:235–42.

172. Tagantsev AK, Sherman VO, Astafiev KF, Venkatesh J, Setter N. Ferroelectric materials for microwave tunable applications. J. Electroceram. 2003;11:5-66.

173. Sengupta LC, Sengupta S. Breakthrough advances in low loss, tunable dielectric materials. J. Mater. Res. Innov. 1999;2:278-82.

174. Wodecka-Dus B, Lisinska-Czekaj A, Orkisz T, Adamczyk M, Osinska K, Kozielski L. The sol-gel synthesis of barium strontium titanate ceramics. J. Mater. Sci. Poland. 2007;25:791-09.

175. Huang JJ, Zhang Y, Ma T, Li HT, Zhang LW. Correlation between dielectric breakdown strength and interface polarization in barium strontium titanate glass ceramics. J. Appl. Phys. Lett. 2010;96: 42902.

176. Bunting EN, Shelton GR, Creamer AS. Properties of calcium-barium titanate dielectrics. Nat. Bur. Stand. 1949;43:237–44.

177. Singh B, Kumar S, Arya GS, Negi NS. Room temperature structural and electrical properties of barium calcium titanate (BCT) thin films. 2015. AIP Conf. Proc. 1661,060005. doi.org/10.1063/1.4915375

178. Kuper C, Buse K, Van SU, Ferroelectrics electrooptic and photorefractive properties of ferroelectric barium-calcium titanate crystals. J. Ferroelectrics.1998;208:213–23.

179. Kotlyarchuk A, Klymenko V, Dubovitskaya N, Lobunets T, Shatskikh S, Ragulya A. Doped barium titanate at intermediate stages of synthesis of BTO. Proceedings of the international conference nanomaterials: applications and properties. 2012;1:3.

180. Tuna O, Selament Y, Aygun G, Ozyuzer L. High quality ITO thin films grown by dc and RF sputtering without oxygen. J. Phys. D: Appl. Phys. 2010;43:55402-07.

181. Varatharajan R, Samanta SB, Jayavel R, Subramanian C, Narlikar A V, Ramasamy P. Ferroelectric characterization studies on barium calcium titanate single crystals. J. Mater. Charact. 2000;45:89–93.

182. Verbitskaya TN, Svetlova LN, Sokolova LS, Laverko EN, Raevskaya EB. Influence of added calcium titanate on the structure and properties of ferroelectric solid solutions based on $BaTiO_3$. Sov. Phys. Crystallogr. 1988;33:609-10.

183. Shelton GR, Creamer AS, Bunting EN. Properties of barium-magnesium titanate dielectrics II. Preparation of specimens and methods. Nat. Bur. Stand.1948;41:17–26.

184. Lee BD, Lee HR, Yoon HK, Cho YS. Microwave dielectric properties of magnesium calcium titanate thin films. J. Ceram. Int. 2005;31:143–46.

185. Samyuktha VS, Subbarao T, Suvarna RP, Kumar AG, Pradesh A, Krishnadevaraya S. Synthesis, characterization, dielectric and thermoelectric properties of calcium doped magnesium titanate. J. Ovonic. Res. 2017;13:33–43.

186. Samyuktha VS, Kumar AGS, Rao TS, Suvarna RP. Synthesis, structural and dielectric properties of magnesium calcium. Mater. Today Proc. [Internet]. Elsevier Ltd. 2016;3:1768–71.

187. Dong H, Jin D, Xie C, Cheng J, Chen J, Chen J. Dielectric properties of barium strontium calcium titanate ceramics with compositional inhomogeneity. Conf. 2014. DOI:10.1109/ICEPT.2014.6918719

188. Gomaa MM, Abo-Mosallam HA, Darwish H. Electrical and mechanical properties of alkali barium titanium alumino borosilicate glass-ceramics containing strontium or magnesium. J. Mater. Sci: Mater. El. 2009;20:507–16.

189. Haung Q, Gao L, Sun J. Effect of adding carbon nanotubes on microstructure, phase transformation, and mechanical property of $BaTiO_3$ ceramics. J. Am. Ceram. Soc. 2005;88:3515–18.

190. Phule PP, Risbud SH. Low-temperature synthesis and processing of electronic materials in the $BaO\text{-}TiO_2$ system. J. Mater. Sci. 1990; 25:1169-83.

191. Cross LE. Ferroelectric materials for electromechanical transducer applications. J. Mater. Chem. Phys. 1996;43:108–15.

192. Kelly G, Alderman J, Lyden C, Barrett J. Micro system packaging: Lessons from conventional low cost IC packaging. J. Micromech. Microeng. 1997;7:99–103.

193. Moulson AJ, Herbert JM. Electroceramics: Materials, properties, applications. 2nd Ed. Wiley, New York. 2003.

194. Huang C, Chen K, Chiu P, Sze P, Wang Y. The Novel formation of barium titanate nanodendrites. J. Nanomater. 2014;2014:1-7

195. Xue J, Wang J, Wan D. Mechanochemical synthesis of nanosized lead titanate powders from mixed oxides. J. Am. Ceram. Soc. 1998;39:364-69.

196. Moura F, Simoes AZ, Stojanovie BD, Zaghete MA, Longo E, Varela JA. Dielectric and ferroelectric characteristics of barium zirconate titanate ceramic prepared from mixed oxide method. J. Alloys. Comp. 2008;462:129–34.

197. Smith MB, Page K, Siegrist T, Redmond PL, Walter EC, Seshadri R, Brus LE, Steigerwald ML, Barbara S. Crystal structure and the paraelectric-to-ferroelectric phase transition of nanoscale $BaTiO_3$. J. Am. Chem. Soc. 2008;130:6955–63.

198. Graziana G, Istituto G, Marino A, Italiano I, Mattoli V, Italiano I, Politecnico GC, Barium titanate nanoparticles□: Promising multitasking vectors in nanomedicine. J. Nanotechnol. 2016;27:232001.

199. Ciofani G, Danti S, Alessandro D, Moscato S, Petrini M , Menciassi A , Barium titanate nanoparticles: highly cytocompatible dispersions in glycol-chitosan and doxorubicin complexes for cancer therapy. Nanoscale Res. Lett. 2010;5:1093–101.

200. Hsieh CL, Grange R, Pu Y, Psaltis D. Bioconjugation of barium titanate nano-crystals with immunoglobulin G antibody for second harmonic radiation imaging probes. J. Biomater. 2010;31:2272-07.

201. Wang XH, Chen RZ, Gui ZL, Li LT. The Grain size effect on dielectric properties of $BaTiO_3$ based ceramics. J. Mater. Sci. Eng. 2003;99:199–202.

202. Poth J, Haberkorn R, Beck HP. Combustion synthesis of $SrTiO_3$. Part I. Synthesis and properties of the ignition products. J. Europ. Ceram. Soc. 2000;20:715-23.

203. Fujimoto M, Kingery WD. Microstructures of $SrTiO_3$ internal boundary layer capacitors during and after processing and resultant electrical properties. J. Am. Ceram. Soc. 1985;68:169-173.

204. Burn I, Smyth DM. Energy storage in ceramic dielectrics. J. Mater. Sci. 1972;7:339–43.

205. Gerblinger J, Lampe U, Meixner H, Perczel IV, Giber J. Cross-sensitivity of various doped strontium titanate films to CO, CO_2, H_2, H_2O and CH_4. Sens. Actuators. B. 1994;19:529-34.

206. Richerson DW. A review of: Modern ceramic engineering, Marcel Dekker, New York, 1992.

207. Sadovska G, Wolf G. Enthalpy of dissolution and thermal dehydration of calcium oxalate hydrates. J. Therm. Anal. Calorim. 2015;119:2063-68.

208. Ganesh R, Goo E. Dielectric and ordering behavior in $Pb_xCa_{1-x}TiO_3$. J. Am. Ceram. Soc. 1997;80:653-62.

209. Hao J, Si W, Xi XX, Guo R, Bhalla AS, Cross LE. Dielectric properties of pulsed-laser-deposited calcium titanate thin films. J. Appl. Phys. Lett. 2000;76:3100

210. Lutze W, Ewing RC. Eds. Radioactive waste forms for the future. Amsterdam: Elsevier. 1988:233–334.

211. Muthuraman M, Patil KC, Senbagaraman S. Sintering, microstructural and dilatometric studies of combustion synthesized synroc phases. J. Mater. Res. Bull. 1996;31:1375–81.

212. Lencka MM, Riman RE. Thermodynamics of the hydrothermal synthesis of calcium titanate with reference to other alkaline-earth titanates. J. Chem. Mater.1995;7:18-25.

213. Cavalcante LS, Marques VS, Sczancoski JC. Synthesis, structural refinement and optical behavior of $CaTiO_3$ powders: A comparative study of processing in different furnaces. Chem. Eng. J. 2008;143: 299–307.

214. Cavalcante LS, Simões AZ, Santos LPS. Dielectric properties of Ca $(Zr_{0.05}Ti_{0.95})O_3$ thin films prepared by chemical solution deposition. J. Solid State Chem. 2006;179:3739–43.

215. Feteira A. Negative temperature coefficient resistance (NTCR) ceramic thermistors: an industrial perspective. J. Am. Ceram. Soc. 2009;92:967– 83.

216. Mi G, Murakami Y, Shindo D, Saito F. Microstructural investigation of $CaTiO_3$ formed mechanochemically by grinding of a $CaO\text{-}TiO_2$ mixture. Powder Technol. 1999;104:75–78.

217. Sibum H, Günther V, Roidl O, Habashi F, Wolf HU. Titanium, titanium alloys, and titanium compounds in Ullmann's encyclopedia of industrial chemistry 2005, Wiley-VCH, Weinheim.

218. Marques VS, Cavalcante LS, Sczancoski JC. Synthesis of $(Ca,Nd)TiO_3$ powders by complex polymerization, Rietveld refinement and optical properties. Spectrochim. Acta A. 2009;74: 1050–59.

219. de Lazaro S, Milanez J, de Figueiredo AT. Relation between photoluminescence emission and local order–disorder in the $CaTiO_3$ lattice modifier. J. Appl. Phys. Lett. 2007;90:111904.

220. Pan Y, Su Q, Xu H. Synthesis and red luminescence of Pr^{3+}-doped $CaTiO_3$ nanophosphor from polymer precursor. J. Solid State Chem. 2003;174:69–73.

221. Haranath D, Khan AF, Chander H. Bright red luminescence and energy transfer of Pr^{3+} doped $(Ca,Zn)TiO_3$ phosphor for long decay applications. J. Phys. D: Appl. Phys. 2006;39:4956-60.

222. Zhang X, Zhang J, Nie Z. Enhanced red phosphorescence in nanosized $CaTiO_3:Pr^{3+}$phosphors. J. Appl. Phys. Lett. 2007; 90:151911.

223. Okamoto S, Kobayashi H, Yamamoto H. Enhancement of characteristic red emission from $SrTiO_3$: Pr^{3+} by Al addition. J. Appl. Phys. 1999;86:5594.

224. Ali R, Yashima M. Space group and crystal structure of the perovskite $CaTiO_3$ from 296 to 1720 K. J. Solid State Chem. 2005; 178:2867-72.

225. Thomas W, Ergun J, Doremus C, Lanford HR, William A. Characterisation of sol-gel synthesis of phase pure $CaTiO_3$ nano powders after drying. J. Biomed. Mater. Res. Part. A. 2003;67:975.

226. Dubey AK, Tripathi G, Basu B. Characterisation of sol-gel synthesis of phase pure $CaTiO_3$ nano powders after drying. J. Biomed. Mater. Res. Part. B: Appl. Biomed. 2010;95:320-28

227. Fukada E, Yasuda I. On the piezoelectric effect of bone J. Phys. Soc. Jap.1957;12:1158-62.

228. Dubey AK, Mallik PK, Kundu S, Basu B. Dielectric and electrical conductivity properties of multi-stage spark plasma sintered HA–$CaTiO_3$ composites and comparison with conventionally sintered materials. J. Eur. Ceram. Soc. 2013;33:3445-53.

229. Wakino K. Recent development of dielectric resonator materials and filters in Japan. Ferroelectrics. 1989;91:69-86.

230. Bernard J, Houivet D. $MgTiO_3$ for Cu base metal multilayer ceramic capacitors. J. Eur. Ceram. Soc. 2004;4:1877-81.

231. Huang CL, Chen YB. Structure and electrical characteristics of RF magnetron sputtered $MgTiO_3$. J. Surf. Coat. Technol. 2006; 200:3319–25.

232. Miao YM, Zhang QL, Yang H. Low-temperature synthesis of nano-crystalline magnesium titanate materials by the sol-gel method. J. Mater. Sci. Eng. B. 2006;128:103–06.

233. Cho WW, Kakimoto K, Ohsato H, Mater. Microwave dielectric properties and low-temperature sintering of $MgTiO_3$-$SrTiO_3$ ceramics with B_2O_3 or CuO. Sci. Eng. B. 2005;121:48-53.

234. Surendran KP, Wu AY, Vilarinho PM, Ferreira VM. Sol-gel synthesis of low-loss $MgTiO_3$ thin films by a non-methoxyethanol route. J. Chem. Mater. 2008;20:4260–67.

235. Stubicar N, Tonejc A, Stubicar M. Microstructural evolution of some $MgO–TiO_2$ and $MgO–Al_2O_3$ powder mixtures during high-energy ball milling and post-annealing studied by X-ray diffraction. J. Alloys Compd. 2004;370:296–301.

236. Choi YH, Lee J. $MgTiO_3$ thin films prepared by metal organic solution deposition and their properties. Thin Solid Films. 2001; 385:43-47.

237. Reynard B, Guyot F. High-temperature properties of geikielite ($MgTiO_3$-ilmenite) from high-temperature high-pressure raman spectroscopy-some implications for $MgSiO_3$-ilmenite. J. Phys. Chem. Mineral. 1994;21:441-50.

238. Tang B, Zhang S, Zhou X, Deng C, Yu S. Preparation of pure $MgTiO_3$ powders and the effect of the $ZnNb_2O_6$-dope onto the property of $MgTiO_3$-based ceramics. J. Alloys Compd. 2010; 492:461–65.

239. Abothu IR, Prasada Rao AV, Komarneni S. Nanocomposite and monophasic synthesis routes to magnesium titanate. J. Mater. Lett. 1999;38:186-89.

240. Lopez T, Ventura JH, Aguilar DH, Quintana P. Thermal phase stability and catalytic properties of. nanostructured TiO_2-MgO sol-gel mixed oxides. J. Nanosci. Nanotechnol. 2008;8:6608-17.

241. Parthasarathy G. Electrical resistivity of nano-crystalline and natural $MgTiO_3$−geikielite at high-pressures up to 8 GPa. J. Mater. Lett. 2007;61:4329-31.

242. Kotochigova S, Levine ZH, Shirley EL, Stiles MD, Clark CW. Local-density-functional calculations of the energy of atoms. J. Phys. Rev. A 1997;55:191-99.

243. Hohenberg P, Kohn W. Inhomogeneous electron gas. Phys. Rev. B. 1964;136:864-71.

244. Uludogan M, Agın TC. First principles approach to $BaTiO_3$. Turk. J. 2006;30:277-285.

245. Kumar L, Monkhorst HJ, Harris FE. Electronic-structure studies of solids. III. Hartree-Fock band functions and energies for cubic lithium crystals. J. Phys. Rev. B. 1974;9:4084-89.

246. Kresse G, Hafner J. Ab initio molecular dynamics for open-shell transition metals. J. Phys. Rev. B. 1993;48:13115-18.

247. Kresse G. Furthmuller J. Efficient iterative schemes for ab initio total energy calculations using plane-wave basis set. J. Phys. Rev. B. 1996;54:11169-86.

248. Chen ZX, Chen Y, Jiang YS. Comparative Study of ABO_3 Perovskite Compounds. 1. $ATiO_3$. (A = Ca, Sr, Ba, and Pb) Perovskites. J. Phys. Chem. B. 2002;106:9986-92.

249. Meyer B, Padilla J, Vanderbilt D. Theory of $PbTiO_3$, $BaTiO_3$, and $SrTiO_3$ surfaces. Faraday Discuss. 1999;114:395-405.

250. Feng HJ, Liu FM. Electronic structure of barium titanate: an abinitio DFT study. Dept. Physics, School of Sciences, Beijing University of Aeronautics &Astronautics, Beijing 100083.

251. Schimka L. Lattice constants and cohesive energies of alkali, alkaline-earth, and transition metals. J. Phys. Rev. B. 2013; 214102:1–8.

252. Kolezyn´ski A, Małecki A. Theoretical analysis of electronic structure and structural properties of anhydrous calcium oxalate. J. Therm. Anal. Calorim. 2009;99:947–55.

253. Drozdz E, Kolezynski A. The structure, electrical properties and chemical stability of Nb- doped $SrTiO_3$ experimental and theoretical studies, RSC Adv. 2017;7:288898-908.

254. Kolezynski A, Małecki A. Theoretical approach to thermal decomposition process of chosen anhydrous oxalates. J. Therm. Anal. Calorim. 2009;97:77–83.

CHAPTER 2

THERMAL DEHYDRATION KINETIC STUDIES OF BARIUM TITANYL OXALATE TETRAHYDRATE

2.1 Introduction

Thermal decomposition of alkaline earth metal titanyl oxalates is an important field of material chemistry [1-6]. Thermal decomposition of alkaline earth metal titanyl oxalate yield–titanate nanoparticles. Hence metal titanyl oxalates act as precursors for the synthesis of titanate nanoparticles. Further, these titanates have industrial uses and many analytical applications. The new developments in modern industries have generated an increasing need for new types of nano materials [7]. High purity metal titanyl oxalates can be made by precipitation techniques, in which the metal ions are simultaneously precipitated in the probable stochiometric proportions and provide the possibility of controlling the physical and chemical properties of the final products. Most of the single phase solid solution precipitates assure homogeneity. Though there is a chance of segregation during precipitation, the degree of mixing is far superior to that obtained with conventional mixing techniques [8].

The preparation of barium titanyl oxalate has been done by many authors [9-11]. Clabaugh *et al*., [9] reported that high purity barium titanate could be prepard by precipitating barium titanyl oxalate and subsequently converting to barium titanate by calcinations. Kudaka *et al*. [10] also reported the optimum conditions for the formation of BTO in detail. Yamamura *et al*. [11] employed a revised Clabaugh method to prepare BTO, in which the ethanol solution of the oxalic acid was added to the mixed starting solution of $Ba(NO)_3$ and $TiO(NO_3)_2$. The dehydration and decomposition kinetics of solid state substances has been extensively studied by many researchers [12-16]. Gallagher *et al.*

[14] studied the thermal dehydration of barium titanate hydrate. Four moles of water are lost in the temperature range 293 – 523 K upon heating. After the loss of water of crystallization, oxygen is adsorbed to form active $BaCO_3$ and TiO_2 which react to form $BaTiO_3$ in the temperature range 773 – 973 K and CO_2 is released.

Dehydration rate and activation energy are important kinetic parameters to determine the reaction mechanism in solid phase. The use of thermo-analytical data to evaluate the kinetic parameters of solid state reactions has been investigated by many workers [17-21]. Successful and deliberate attempts to evaluate kinetic and thermodynamic parameters were made by Kotru *et al.* [22] and Schaube *et al.* [23]. Kinetic parameters can be calculated from the kinetic data by applying integral and differential equations [24-25], which are proposed by different workers on the basis of different assumptions to the kinetics of the reaction and the Arrhenius law.

In the present investigation the kinetic parameters of the thermal dehydration of incorporated water molecule from barium titanyl oxalate tetrahydrate (BTO) was studied at four different heating rates under linear non-isothermal conditions. The reaction kinetics was performed on the results obtained from DSC; the curves obtained were analyzed using different isoconversional model free equations *viz* Bosewell, Tang, Starink$^{1.95}$and Starink$^{1.92}$. These methods have been used to elucidate the thermal stability, the nature and extent of the dehydration of barium titanyl oxalate tetrahydrate in nitrogen atmosphere. The values of kinetic parameters calculated for the samples by these methods were used to identify the dependence of the

E_a on the extent of conversion and the most probable *Sestak-Berggren (m, n)* empirical kinetic model. The prepared sample was identified and characterized by means of FT-IR, XRD, SEM and TEM.

2.1.1 Kinetic analysis

Model-free methods are the most consistent methods for calculating the activation energy of thermally activated reactions [26-35]. The benefit of analyzing kinetic data using model-free methods is that they do not assume any model or mechanism to calculate E_a, even at different ranges of temperatures. The main assumption of these methods is that the reaction mechanism does not change with reaction conversion (α), temperature and heating rate. Isoconversional methods are model-free methods that evaluate kinetic parameter E_a at progressive conversion values, α. The isoconversional methods describe the kinetics of the process by using multiple single step kinetic equations, each of which is associated with a certain extent of conversion and allows a complex and multi stage processes to be detected *via* a variation of E_a with α. Conversely, independence of E_a on α is a sign of a single-step process. The isoconversional methods allow the effective activation energy of a process to be definitely estimated as a function of the extent of conversion [36, 37]. The method can be effectively applied to the overall as well as species-specific rate data. The analysis of the resulting dependence provides important clues about changes in reaction mechanism [38, 39].

Model fitting methods are also used during thermal analysis kinetics in which TG and DSC experimentation determine mass or heat

change as a function of temperature or time. In model fitting method, it fits different reaction models *f(α)* or *g(α)* into various general kinetic equation and the values of the activation energy and pre-exponential factors are calculated by regression analysis.

2.1.2 Isoconversional Methods

The kinetic analysis of solid state decomposition is described by two functions, one of the reaction temperature and another of the extent of conversions *i.e*., *k(T)* and *f(α)* respectively. The mathematical equations used to model kinetic reactions generally take the form of

$$\frac{d\alpha}{dt} = k(T) f(\alpha) \tag{2.1}$$

Where *t* is the time and *T* the temperature and α is the extent of conversion, which can be determined from DSC as a fractional heat release. In general *k (T)* is described by an Arrhenius equation:

$$k(T) = Ae^{-E_a/RT}$$

The rate of solid state reaction can generally be expressed by:

$$\frac{d\alpha}{dt} = Ae^{(-E_a/RT)} f(\alpha) \tag{2.2}$$

Where *α* is the fraction reacted at time *t*, *f(α)* is the function representing the reaction model as shown on Table (1). Reza *et al*. [40] and Khawan *et al*. [41] used different kinetic model functions for treating the conversions (*α*) *versus* time for solid state reactions. *A* is

the pre-exponential factor of the Arrhenius equation, R is the gas constant, T is the absolute temperature, and E_a is the activation energy of the reaction.

Equation (1.1) can be put in the integral form as follows:

$$\int_0^{\alpha} \frac{d\alpha}{f(\alpha)} = A\int_0^{T} \exp(\frac{-E_a}{RT})dt$$

$$g(\alpha) = \int_0^{\alpha} \frac{d\alpha}{f(\alpha)}$$

$$g(\alpha) = A\int_0^{T} \exp(\frac{-E_a}{RT})dt$$

The different expressions for $g(\alpha)$ are given in Table 2.1.

In non-isothermal reaction kinetics, which proceeds upon heating the reactants at a constant heating rate β, where:

$$\beta = \frac{dT}{dt}$$

Then equation (2.1) can be written as

$$\frac{\beta d\alpha}{dT} = k(T)f(\alpha) \tag{2.3}$$

From the data of α and T obtained upon heating the reactants at different heating rates, values of dα/dT could be calculated at a constant temperature. Then plotting the values of βdα/dT *versus* $f(\alpha)$ according to equation (2.3) for different reaction models (from Table

2.1), straight lines will be obtained for the model equation $f(\alpha)$, which describes the reaction kinetics [42].

Then for the determination of the activation energy, equation (2.3)

$$g(\alpha) = \frac{A}{\beta}\int_0^T \exp(\frac{-E_a}{RT})dT$$

can be solved by introducing the function:

$$P(x) = \frac{e^{-x}}{x^2}$$

Using Doyle approximation [43]:

$$P(x) = -5.331 - 1.052x$$

Coats and Redfern [44], derived the following equation:

$$\ln\left[g(\alpha) \Big/ T^2 \right] = \ln\left[\frac{AE_a}{R\beta} \right] - \frac{E_a}{RT} \qquad (2.4)$$

The predetermined *f(α)* which describes the reaction according to equation (2.3) corresponds to a *g(α)* equation from Table 2.1. Then using this *g(α)* in equation (2.4), Arrhenius plot could be obtained by plotting ln $g(\alpha)/T^2$ *versus* $1/T$, and the activation energy E_a could be calculated.

Table 2.1 Different kinetic model functions for solid state reactions.

Model (Symbol)	***f(α)***	***g(α)***
Nucleation models		
Power low (P2)	$(2\alpha)^{1/2}$	$(\alpha)^{1/2}$
Power low (P3)	$(3\alpha)^{2/3}$	$(\alpha)^{1/3}$
Power low (P4)	$(4\alpha)^{3/4}$	$(\alpha)^{3/4}$
Avarami-Erofeyev (A2)	$2(1-\alpha)[-\ln(1-\alpha)]^{1/2}$	$[-\ln(1-\alpha)]^{1/2}$
Avarami-Erofeyev (A3)	$3(1-\alpha)[-\ln(1-\alpha)]^{2/3}$	$[-\ln(1-\alpha)]^{1/3}$
Avarami-Erofeyev (A4)	$4(1-\alpha)[-\ln(1-\alpha)]^{3/4}$	$[-\ln(1-\alpha)]^{1/4}$
Prout-Tompkins (B1)	$\alpha(1-\alpha)$	$\ln(\alpha/1-\alpha)]+c^{b}$
Geometrical contraction models		
Contracting area (R2)	$2(1-\alpha)^{1/2}$	$[1-(1-\alpha)^{1/2}]$
Contracting volume (R3)	$3(1-\alpha)^{2/3}$	$[1-(1-\alpha)^{1/3}]$
Diffusion models		
1-D Diffusion (D1)	$1/(2\alpha)$	$(\alpha)^{2}$
2-D Diffusion (D2)	$[-\ln(1-\alpha)]^{-1}$	$[(1-\alpha)\ln(1-\alpha)]+\alpha$
3-D Diffusion-Jander (D3)	$[3(1-\alpha)^{2/3}]/[2(1-(1-\alpha)^{1/3})]$	$[1-(1-\alpha)^{1/3}]^{2}$
Ginstling-Brounshtein (D4)	$3/[2((1-\alpha)^{-1/3}-1)]$	$1-(2\alpha/3)-(1-\alpha)^{2/3}]$
Reaction-order models		
Zero-order (F0/R1)	1	α
First-order (F1)	$(1-\alpha)$	$-\ln(1-\alpha)$
Second-order (F2)	$(1-\alpha)^{2}$	$(1-\alpha)^{-1}-1$
Third-order (F3)	$(1-\alpha)^{3}$	$0.5(1-\alpha)^{-2}-1$
Empirical models		
Systak-Berggren[SB(m,n)]	$\alpha^{m}(1-\alpha)^{n}$	$\alpha^{m}(1-\alpha)^{n}[m/\alpha-n/1-\alpha]$
Johnson-Mehl-Avrami [JMA(m)]	$m(1-\alpha)[-\ln(1-\alpha)]^{1-1/m}$	$-\ln(1-\alpha)^{1/m}$

2.1.3 Calculation of activation energy by isoconversional methods

2.1.3.1 Bosewell method

The Bosewell method [45] is a conventional integral isoconversional method which enables the calculation of activation energy of a solid state decomposition process without the knowledge of the reaction order.

Bosewell equation:

$$\ln\frac{\beta}{T}=\ln\frac{AR}{E_a g(\alpha)}-\frac{E_a}{RT} \tag{2.5}$$

Where, α corresponds to the degree of conversion. The values of slope obtained from the linear least-squares plots of $\ln\frac{\beta}{T}$ *versus 1/T* enables the calculation of E_a.

2.1.3.2 Tang Method

The Tang method [46] allows the activation energy to be determined by plotting ln ($\beta/T^{1.894661}$) *versus 1/T* over a wide range of conversions. The equation is:

$$\ln\left(\frac{\beta}{T^{1.894661}}\right)=\left[\ln\frac{AE_a}{g(\alpha)R}+3.63504095-1.894661\ln E_a\right]-1.00145033\left(\frac{E_a}{RT}\right) \tag{2.6}$$

2.1.3.3 Starink$^{1.95}$ method

The Starink method is based on the Starink approximation [47]:

$$\ln\frac{\beta}{T^{1.95}}=\ln\left[\frac{A}{g(\alpha)}\left(\frac{E_a}{R}\right)^{-0.95}\right]-0.235-\frac{E_a}{RT} \tag{2.7}$$

Linear least squares plot of $\ln\frac{\beta}{T^{1.95}}$ against *1/T* enables the calculation of E_a from the value of slope can be obtained.

2.1.3.4 Starink[1.92] method

$$\ln \frac{\beta}{T^{1.92}} = \ln \left[\frac{A}{g(\alpha)} \left(\frac{E_a}{R} \right)^{-0.92} \right] - 0.312 - 1.0008 \frac{E_a}{RT} \tag{2.8}$$

The values of slope obtained from the linear least-squares plots of $\ln \frac{\beta}{T^{1.92}}$ against *1/T* enables the calculation of E_a.

2.2 Experimental

2.2.1 Materials

AnalaR grade barium nitrate ($Ba(NO_3)_2$) (Merck, India; assay ≥ 99.9 %) and potassium titanyl oxalate ($K_2TiO(C_2O_4)_2$) (BHO Laboratory England; assay ≥ 99.9 %) were used in the present investigation.

Barium titanyl oxalate tetrahydrate (BTO) was synthesized by the precipitation reaction of mixing of aqueous solution of barium nitrate and potassium titanyl oxalate with constant stirring. The white BTO precipitate obtained was filtered, washed with deionised water and dried in an air oven at 323 K for 24 h, powdered in an agate mortar and sieved through the mesh and fixed the particle size in the range 45-53 μm.

2.2.2 Methods

The infra-red (IR) spectrum of the samples in KBr pellet was recorded using a JASCO FT-IR-4100 instrument. The sample was first

compressed with KBr into pellet and analyzed as KBr disc from 400 to 4000 cm^{-1}. The instrument offers high sensitivity, maximum resolution (0.9 cm^{-1}) and high signal to noise ratio (22,000:1).

The X- ray diffraction (XRD) measurements of the samples were performed on a RIGAKU MINI FLEX - 600 X-ray diffraction spectrophotometer using Cu K_α (1.5418 A^0) radiation.

The Scanning Electron Microscope (SEM) analyses of all the samples studied were performed using a Hitachi SU6600 Variable Pressure Field Emission Scanning Electron Microscope (FESEM). The instrument offers a resolution of 1.2 nm/30 kV, 3.0 nm/1 kV and magnification of 500,000 x. For the present investigation, the imaging techniques employed were Secondary electrons (SE), Back scattered electrons (BSE) and Energy dispersive X-ray analysis (EDXA).

The Transmission electron microscopy (TEM) analysis of the particles was achieved by using a JEOL 2100 field emission transmission electron microscope operated at 200 kV with a 0.18 nm resolution. The differential scanning calorimetric (DSC) measurements of the samples were taken on a Mettler ToledoDSC822e. The operational characteristics of the DSC system are as follows: atmosphere: flowing N_2 at a flow rate of 50 mL min^{-1}; sample mass: 5.1 mg; and sample holder: aluminium.

The thermogravimetric (TG) analysis of the samples were made on a T.A. thermal analyzer, model: TGA Q50 V20.2 Build 27 at four different heating rates, *viz*., 2, 5, 7 and 10 K min^{-1}. The operational characteristics of the TG system are; flowing nitrogen atmosphere, at a

flow rate of 20 mL min^{-1}, sample mass: 5.1 mg, sample pan: silica. Duplicate runs were made under similar conditions and found that the data overlap with each other, indicating satisfactory reproducibility.

2.3 Results and Discussion

Fig. 2.1 shows the XRD pattern of the hydrated and dehydrated samples at 2θ values ranging from 10 to 80^0. The crystallite sizes (d) of prepared samples were estimated from the peaks of XRD patterns, using Debye Scherrer's equation, $d = K\lambda / \beta cos\theta$ where, K is the shape coefficient (value between 0.9 and 1.0), λ the wave length (1.5418 A^0), β is the full-width at half-maximum, and θ the diffraction angle shows the structural characteristics of the sample.

Fig. 2.1a shows the XRD pattern of barium titanyl oxalate tetrahydrate at 2θ values at 19.71, 24.16, 31.78, 34.52, 45.11, 56.96 and 69.22^0. The reflections from the sample indicate that BTO show slightly amorphous phase due to the presence of the carbon atoms and the water in the mixture. Fig. 2.1b represents the XRD pattern of the dehydrated sample (510 K) at 2θ values 22.47, 31.78, 39.17 and 45.74, 51.46, 56.52, 66.27, 70.92, 75.37, 79.39^0. After calcinations, at 510 K, the crystalline phase with cubic structure (a = 4.0073 Å) was appeared [48]. From the XRD results, it was clear that the peak intensity and crystalline nature enhances with the calcinations of the sample. The average crystallite size of the hydrated and dehydrated barium titanyl oxalate tetrahydrate was in nanometer range of 15-29.5 nm.

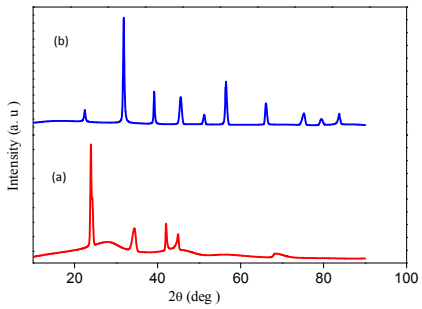

Fig. 2.1 XRD pattern of sample (a), sample calcined at 510 K for 1 h (b).

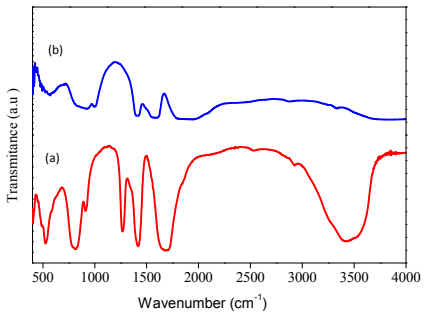

Fig. 2.2 IR spectrum of sample (a), sample calcined at 510 K for 1 h (b)

Fig. 2.2 represents FT-IR spectrum of the hydrated and dehydrated sample. Fig. 2.2a represents FT-IR spectrum of barium titanyl oxalate tetrahydrate. The broad band extending from 2800 to 3600 cm^{-1} can be assigned to the symmetric and asymmetric stretching modes of the water molecules. The strong band appearing in the IR spectrum around 1615 cm^{-1} can be identified as the asymmetric stretching vibrations of CO groups of the $C_2O_4^{2-}$ ions together with the bending mode of water [49]. The IR spectrum of BTO heated to 510 K in vacuum for 1 h presented in Fig. 2.2b. The strong peak around 1316 cm^{-1} can also be assigned to the asymmetric stretching of CO groups.

Fig. 2.3 show the SEM images of the synthesized sample calcined at 450 and 510 K for 1 h, indicating porous microstructure of the sample and the pore size found varying from 1 to 10 µm. Some particles exhibit slightly sharp edges whereas most of the particles have smooth surface and slight depressions presenting different

morphologies, having spherical grain agglomerations with smaller grain size and a porous bone like shape.

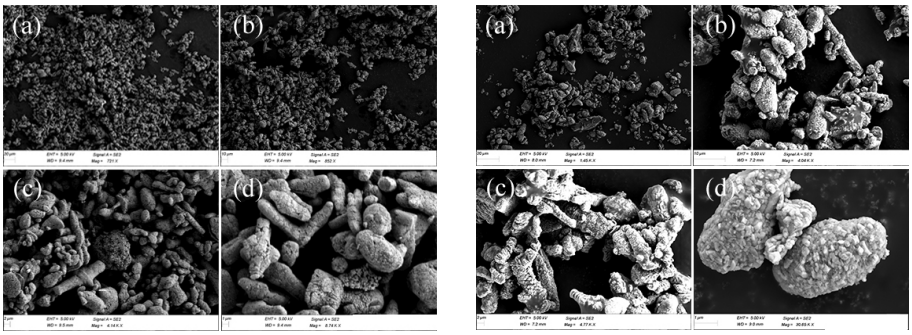

(1) (2)

Fig. 2.3 The SEM images of the sample calcined at 450 (1) and 510 K (2) showing the surface microstructure of the sample at 20 (a), 10 (b), 2 (c) and 1μm (d).

The TEM images also yield the information such as particle size, size distribution and morphology of the sample when it is heated to 510 K for 1 h, (Fig. 2.4). The samples under study exhibits uniform grain size distribution, confirm that the particles were nearly spherical in shape.

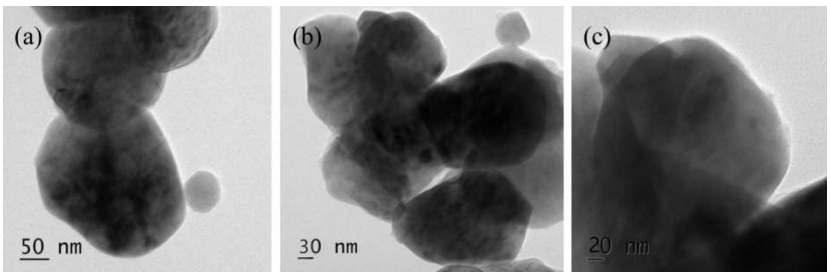

Fig. 2.4 The TEM images of the sample calcined at 510 K for 1 h 50 (a), 30 (b), and 20 nm (c).

Fig. 2.5 shows the TG curves recorded during the decomposition of $BaTiO(C_2O_4)_2.4H_2O$ at different heating rates under nitrogen gas, the results of thermogravimetric analysis of the sample, which confirm the mass change in the various stages on the heating up to 1200 K. TG curve shows five different mass loss stages involving dehydration and decarboxylation. The first major mass loss, of about 16.25 % is within the temperature range from 300 to 463 K, which may be attributed to the dehydration of $BaTiO(C_2O_4)_2.4H_2O$ to $BaTiO(C_2O_4)$. The second mass loss of about 3.45 % appearing in the temperature range 460-530 K, can be attributed to the initial low temperature decomposition of BTO. The third major mass loss of about 20.75 % is set up in the temperature range 530-750 K ascribed to the complete decomposition of the oxalate groups, resulting in the formation of a carbonate with CO_2 and CO.

The fourth stage of mass loss of about 6.42 %, observed at 750-900 K, is due to the evolution of CO_2, the final decomposition of carbonate takes place between 900-1200 K with a mass loss of about 7.4 %, which is due to the formation of $BaTiO_3$. The calculated mass loss of BTO is in good agreement with the theoretical value [50, 51].

The DSC is an effective tool in the investigation of phase transformations and enables very accurate determination of the temperature range and reaction heat in all transformations. It is used for recording the kinetic rate data of the thermal decomposition. The sample of 5.01 mg was weighed in an aluminum pan (6 mm in diameter and 2.5 mm in depth). A reference sample was made under the similar conditions. This method measures the difference in the

amount of heat supplied to the examined sample and reference sample when both are subjected to controlled changes of temperature. The DSC curve of sample was recorded using a DSC instrument in N_2 flowing atmosphere at a rate of 50 mL min^{-1}, samples were subjected to controlled heating in the range 337-510 K at a different heating rates 2, 5, 7, and 10 K min^{-1} (Fig. 2.6).

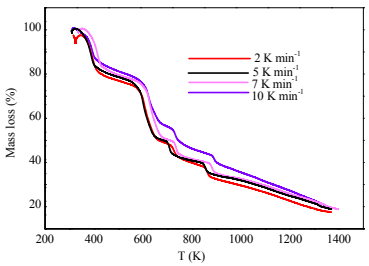

Fig. 2.5 The TG curve for the thermal decomposition of sample at different β

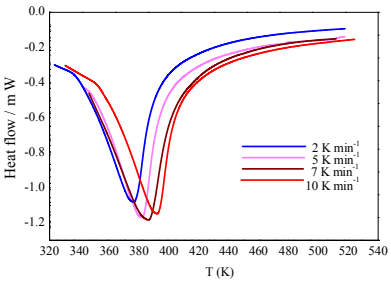

Fig. 2.6 The DSC curves for the thermal of dehydration of sample at different β

The kinetic analysis, using the kinetic data for different β, apparent E_a as a function of the reacted fraction can be determined from isoconversional methods (Table 2.2). All isoconversional methods take their origin in the isoconversional principle that states that the reaction rate at constant extent of conversion is only a function of temperature [52]. The analysis of reaction kinetic parameters was performed on the DSC curves, obtained between 337-510 K using the non-isothermal isoconversional methods are Bosewell, Tang, $Starink^{1.95}$, $Starink^{1.92}$ method. Linear least squares plots of all the samples by the above four isoconversional methods at different

conversions are shown in Fig. 2.7. The slopes of these straight lines have been used to calculate activation energy E_a and their intercepts were used to calculate frequency factor ($log\ A$). The variation of the apparent E_a values as a function of α was almost similar for the above four methods.

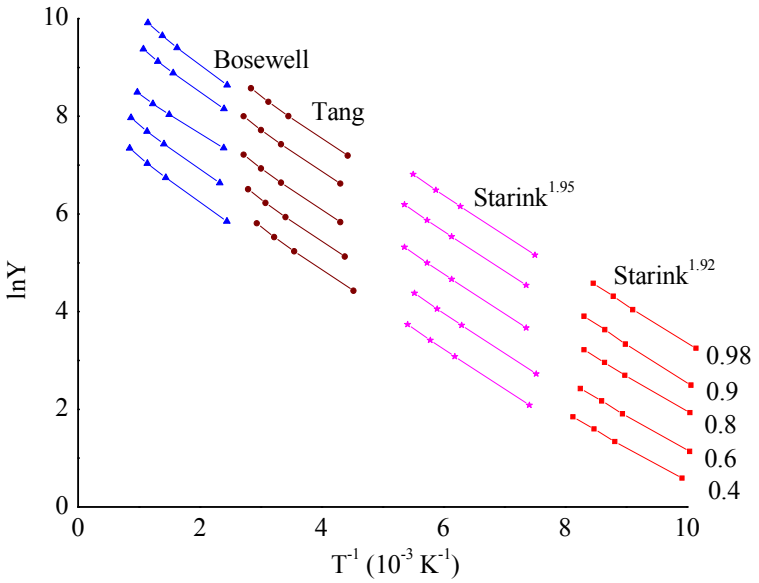

Fig. 2.7 Typical linear least-squares plot for Bosewell, Tang, Starink$^{1.95}$ and Starink$^{1.92}$ method of the sample at different conversion values.

Table 2.2 Values of activation energy (E_a) and correlation coefficient (r) obtained from different integral isoconversional methods for the thermal dehydration of barium titanyl oxalate.

α	Bosewell		Tang		Starink $^{1.95}$		Starink$^{1.92}$	
	E_a / kJ/mol	$-r$	E_a / kJ/mol	$-r$	E_a / kJ/mol	$-r$	E_a / kJ/mol	$-r$
0.05	122.4	0.9980	117.9	0.9971	118.01	0.9986	119.1	0.9999
0.1	159.1	0.9881	156.3	0.9981	112.75	0.9962	157.1	0.9987
0.15	118.4	0.9938	112.8	0.9962	89.57	0.9934	112.7	0.9962
0.2	91.95	0.9958	89.71	0.9934	87.18	0.9833	89.64	0.9833
0.25	77.69	0.9997	72.38	0.9834	80.69	0.9843	76.29	0.9994
0.30	64.95	0.9895	76.96	0.9836	78.08	0.9960	78.51	0.9981
0.35	74.95	0.9986	69.88	0.9972	76.64	0.9902	70.87	0.9998
0.4	72.84	0.9909	66.97	0.9990	72.53	0.9956	68.32	0.9866
0.45	70.31	0.9923	64.21	0.9962	68.21	0.9993	64.72	0.9983
0.5	66.06	0.9929	61.86	0.9744	65.08	0.9961	61.76	0.9997
0.55	62.75	0.9938	56.66	0.9772	60.75	0.9936	59.87	0.9931
0.6	58.93	0.9942	53.39	0.9930	58.02	0.9894	56.64	0.9852
0.65	55.58	0.9962	50.88	0.9938	56.05	0.9947	54.63	0.9894
0.7	54.62	0.9834	48.95	0.9782	54.05	0.9854	53.75	0.9981
0.75	52.46	0.9918	49.26	0.9895	52.04	0.9973	50.71	0.9964
0.8	52.81	0.9841	51.08	0.9914	50.65	0.9857	52.24	0.9824
0.85	54.41	0.9951	54.78	0.9821	50.21	0.9894	55.58	0.9867
0.9	58.21	0.9912	59.88	0.9934	50.79	0.9992	59.02	0.9872
0.95	59.97	0.9836	76.94	0.9852	54.53	0.9883	64.58	0.9934

The dependence of activation energy obtained from DSC data, on conversion for the four isoconversional methods are shown in Fig. 2.8. The activation energy values calculated by using the four methods are compatible with each other and show similar trend. The E_α values obtained for above four methods show decrease with conversion, passes through a minimum at α = 0.8 and then increases with the increase in conversion. The kinetic rate data indicated systematic

shifts to higher temperatures with increasing β, as indicated from the α-T curve (Fig. 2.9) of the dehydration reaction for barium titanyl oxalate. The kinetic methods of Bosewell, Tang, Starink$^{1.95}$ and Starink$^{1.92}$ gives an average value of E_a are 75.18, 73.20, 70.31 and 74.01 kJ/mol ($0.05 \leq \alpha \leq 1$) respectively. In the dehydration step, the value of activation energy obtained from Bosewell is close to that obtained from Tang and Starink$^{1.92}$ method. The values of activation energy calculated using all the methods studied show similar trend. The variation of activation energy during thermal decomposition reflects the changing mechanism during the course of the reaction.

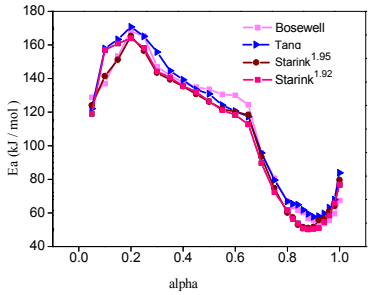

Fig. 2.8 The dependence of activation energy on conversion of BTO for different methods.

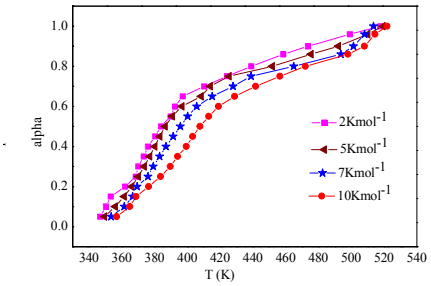

Fig. 2.9 α–T curves for the thermal dehydration of BTO

For the determination of all the kinetic parameters in equation (2.2), *Sestak-Berggren* [53] *SB (m, n)* nuclear kinetic model functions were employed in order to accommodate possible mechanistic feature of the reaction process.

$$f(\alpha) = \alpha^m (1-\alpha)^n \qquad (2.9)$$

Where m and n are characters for the dehydration process, which correspond to empirically obtained kinetic exponents for the reaction steps set to ≈*0-1*. The average calculated kinetic parameters obtained are given in Table 2.3.

Table 2.3 Kinetic parameters used for the thermal dehydration of sample under linear nonisothermal conditions.

Methods	E_a (kJmol^{-1})	A (s^{-1})	*f(α)* *SB (m,n)*
Bosewell	75.18	8.21×10^{14}	m=0.99, n=0.90
Tang	73.20	7.86×10^{14}	m=0.11, n=1.10
Staring [1.95]	70.31	6.82×10^{14}	m=0.30, n=1.12
Staring[1.92]	74.01	7.65×10^{14}	m=0.41, n=0.99

2.4 Conclusion

The dehydration kinetics of BTO under linear non isothermal condition has been studied using DSC. The kinetic parameters and the suitable kinetic model were suggested. The activation energies of the thermal decomposition were calculated using model free equations; Bosewell, Tang, Starink[1.95] and Starink[1.92] and the values were found to be compatible with each other. The activation energy values of the decomposition reactions obtained from Bosewell is close to that obtained from Tang and Starink[1.92] method. The comparison of the results obtained with these procedures; Bosewell, Tang, Starink[1.95] and Starink[1.92]shows that they strongly depend on the choice of model function of the process, by *Sestak-Berggren* (*SB*) method. The results show that the two-parameter *SB (m, n)* is the most suitable for quantitative description of the dehydration process of the sample studied.

2.5 References

1. Gadalla AMM. Kinetics of the decomposition of hydrated oxalates of calcium and magnesium in air. Thermochim. Acta. 1984;74:255-72.

2. Galwey AK, Brown ME. Thermal decomposition of ionic solids. 1st ed. Elsevier: Amsterdam. 1999.

3. Barbara M, Drozdz-ciesla E, Melecki A. Mechanism and kinetics of thermal decomposition of zinc oxalate. Thermochim. Acta. 2004;423:13-28.

4. Unger KK, Kreysa G, Baselt JP. Characterization of Porous Solids I st ed. Amsterdam: Elsevier;2000

5. Cardillo P, Gigante L, Lunghi A, Zanirato P. Revisiting the thermal decomposition of five ortho-substituted phenyl azides by calorimetric technics. J. Therm. Anal. Calorim. 2010;100:191–08.

6. Koga N. Ozawa's kinetic method for analysing thermoanalytical curves. J. Therm. Anal. Calorim. 2013;113:1527–41.

7. Atakol M, Atakol A, Yiğiter AÖ, Svoboda I, Atakol O. Investigation of energetic materials prepared by reactions of diamines with picryl chloride: synthesis, structure and thermal behaviour. J. Therm. Anal. Calorim. 2017;127:1931–40.

8. Hamed MNH, Kamal R. The effect of particle size on the kinetics of thermal decomposition of Co (C_2O_4). $2H_2O$ nanopowders under non-isothermal conditions. J. Therm. Anal. Calorim. 2015;123:675-86

9. Clabaugh WS, Swiggard EM, Gilchrist R. Preparation of barium titanyl oxalate tetrahydrate for conversion to barium titanate of high purity. J. Res. Nat. Bur. Std. 1956;56:289–91

10. Kudaka K, Ilzumi K, Sasaki K. Preparation of stoichiometric barium titanyl oxalate tetrahydrate. J. Amer. Ceram. Soc. Bull. 1982;61:1236-36.

11. Yamamura H, Watanabe A, Shirasaki S, Moriyoshi Y, Tanada

M. Preparation of barium titanate by oxalate method in ethanol solution. Ceram Int. 1985;11:17–22.

12. Sarada K, Muraleedharan K. Effect of addition of silver on the thermal decomposition kinetics of copper oxalate. J. Therm. Anal. Calorim. 2016;123:643-51.

13. Szirtes L, Megyeri J, Kuzmann E. Thermal treatment on tin (II/IV) oxalate, EDTA and sodium inositol-hexaphospate. J. Therm. Anal. Calorim. 2012;110:497-510

14. Gallagher PK, Kurkjian CR. A study of the thermal decomposition of some complex oxalates of iron (III) using the mössbauer effect. Inorg. Chem. 1966;5:214-19.

15. Fang TT, Lin HB. Factors affecting the preparation of barium titanyl oxalate tetrahydrate. J. Amer. Ceram. Soc. 1989;72:1899–906.

16. Muraleedharan K, Viswalekshmi CH, Sarada K. Synthesis, characterization and thermal dehydration and degradation kinetics of chitosan Schiff bases of o-, m- and p-nitrobenzaldehyde. J. Polym. Bull. 2017;74:39-54.

17. Muraleedharan K, Labeeb P. Kinetics of the thermal dehydration of potassium titanium oxalate, $K_2TiO(C_2O_4)_2 2H_2O$. J. Therm. Anal. Calorim. 2012;109:89–96.

18. Gallagher PK, Schrey F. Preparation of semiconducting titanates by chemical methods. J. Amer. Ceram. Soc. 1963;46:567-73.

19. Honcova P, Svoboda R, Pilny P, Sadovska G, Bartak J, Benes L, Hon D. Kinetic study of dehydration of calcium oxalate trihy-drate. J. Therm. Anal. Calorim. 2016;124:151–58.

20. Chambre D, Iditoiu C, Segal E. Non-isothermal dehydration kinetics of acrylic ion exchange resins. J. Therm. Anal. Calorim. 2007;88:673–79.

21. Sadovska G, Wolf G. Enthalpy of dissolution and thermal dehydration of calcium oxalate hydrates. J. Therm. Anal. Calorim. 2015;119:2063–68.

22. Kotru PN, Raina KK, Koul ML. The Kinetics of solid-state decomposition of neodymium tartrate. Indian J. Pure Appl. Phys. 1987;25:220-20.

23. Schaube F, Koch L, Worner A, Steinha HM. A Thermodynamic and kinetic study of the de- and rehydration of $Ca(OH)_2$ at high H_2O partial pressures for thermo-chemical heat storage. Thermochimica. Acta. 2012;538:9–20.

24. Jankovic B, Adnadevic B, Jovanovic J. Isothermal kinetics of dehydration of equilibrium swollen poly (acrylic acid) hydrogel. J. Therm. Anal. Calorim. 2008;92:821–27.

25. Mironov Y, Fedorov V, Drebushchak V. Kinetic and thermodynamic stability of cluster compounds under heating. J. Therm. Anal. Calorim. 2007;88:687–92.

26. Avrami NA, Contineanu I, Popa VT, Contineanu M. Dehydration of irradiated and non-irradiated L-asparagine monohydrate. J. Therm. Anal. Calorim. 2008;94:405–10.

27. Sharma P, Virk HS. Fabrication of nanoparticles of barium carbonate/oxalate using reverse micelle technique. Open Surf. Sci. J. 2009;1:34–39.

28. Dalal PV, Saraf KB, Shimpi NG, Shah NR. Pyro and kinetic studies of barium oxalate crystals grown in agar gel. J. cryst. Process Technol. 2012;2012:156–60.

29. Horowitz HH, Metzger G. New analysis of thermogravimetric traces. Anal. Chem. 1963;35:1464–68.

30. Freeman ES, Carroll B. The Application of thermoanalytical decomposition of calcium oxalate mono hydrate. J. Phys. Chem. 1958;62:394–97.

31. Vyazovkin S. Computational aspects of kinetic analysis, Part C. The ICTAC kinetics project - the light at the end of the tunnel?. Thermochim. Acta. 2000;355:155-63.

32. Vyazovkin S, Sbirrazzuoli N. Isoconversional analysis of the non-isothermal crystallization of a polymer melts. Macromol Rapid Comm. 2002;23:766-70.

33. Vyazovkin S, Sbirrazzuoli N. Estimating the activation energy for non-isothermal crystallization of polymer melts. J. Therm. Anal. Calorim. 2003;72:681-86.

34. Joraid AA, Abu-Sehly AA, El-Oyoun MA, Alamri SN. Non-isothermal crystallization kinetics of amorphous $Te_{51.3}As_{45.7}Cu_3$. Thermochim. Acta. 2008;470:98-104.

35. Starink MJ. The determination of activation energy from linear heating rate experiments: a comparison of the accuracy of isoconversion methods. Thermochim. Acta. 2003;404:163-76.

36. Vyazovkin S, Sbirrazzuoli N. Isoconversional approach to evaluating the hoffman-lauritzen parameters (U^* and Kg) from the overall rates of non-isothermal crystallization. Macromol Rapid Comm. 2004;25:733-38.

37. Khawam A, Flanagan DR. Role of isoconversional methods in varying activation energies of solid-state kinetics: II. Non-isothermal kinetic studies. Thermochim. Acta. 2005;436:101-12.

38. Vyazovkin S. Model-free kinetics, staying free of multiplying entities without necessity. J. Therm. Anal. Calorim. 2006; 83:45-51.

39. Vyazovkin S, Sbirrazzuoli N. Isoconversional kinetic analysis of thermally stimulated processes in polymers. Macromol Rapid Comm. 2006;27:1515-32.

40. Reza EK, Hasan AM, Ali S. Model fitting approach to kinetic analysis of non-isothermal oxidation of molybdenite. Iran. J. Chem. Eng. 2007;26:119-123.

41. Khawan A, Flanagan DR. Basics and applications of solid state kinetics: A pharmaceutical perspective. J. Pharm. Sci. 2006;95:472-98.

42. Osman KI. Synthesis and characterization of $BaTiO_3$ ferroelectric material. Thesis, Cairo University. 2011

43. Doyle C. Estimating isothermal life from thermogravimetric data. J. Appl. Polym. Sci. 1962;6:639-42.

44. Coats AW, Redfern J. Kinetic parameters from thermogravimetric data. Nature. 1964;201:68-69.

45. Bosewell PG. On the calculation of activation energies using a modified Kissinger method. J. Therm. Anal. 1980;18:353–58.

46. Tang W, Liu Y, Zhang H, Wang C. New approximate formula for Arrhenius temperature integral. Thermochim. Acta. 2003;408:39–43.

47. Starink MJ. Activation energy determination for linear heating experiments:deviation due to neglecting the low temperature end of the temperature integral. J. Mater. Sci. 2007;42:483–89.

48. Patterson AL. The Scherrer formula for X-Ray particle size determination. J. Phys Rev. 1939;56:978-82.

49. Rao CNR. Chemical applications of infra red spectroscopy. New York: Academic Press.1963;365-67.

50. Flynn JH, Wall LA. Direct method for the determination of activation energy from thermogravimetric data. J. Polym. Lett. 1966;4:323-28.

51. Ozawa T. A new method of analyzing thermogravimetric data. Bull. Chem. Soc. Jpn. 1965;38:1881-82.

52. Vyazovkin S, Wight CA. Isothermal and non-isothermal kinetics of thermally stimulated reactions of solids. Int. Rev. Phys. Chem. 1998;17:407-33.

53. Sestak J, Berggren G. Study of the kinetics of the mechanism of solid-state reactions at increasing temperatures. Thermochim. Acta. 1971;3:1–12.

CHAPTER 3

THERMODYNAMIC AND KINETIC STUDIES ON THE FORMATION OF BARIUM TITANATE NANO PARTICLES FROM BARIUM TITANYL OXALATE *VIA* MULTI-STAGE THERMAL DECOMPOSITION

3.1 Introduction

The thermal decomposition of barium titanyl oxalates is studied, in view of the application of its decomposition products, barium titanate nanoparticles (BTNPs) on various fields. The BTNPs have been extensively applied in various fields such as multilayer ceramic capacitors (MLCCs), integral capacitors in printed circuit boards (PCB), dynamic random access memories (DRAM), resistors with positive temperature coefficient of resistivity (PTCR), temperature-humidity-gas sensors, electro-optic devices, piezoelectric transducers, actuators, and thermistors [1]. Ferroelectric properties and a high dielectric constant make $BaTiO_3$ useful in an array of applications such as gate dielectrics, waveguide modulators, IR detectors, and holographic memory [2]. Recently, an increasing number of studies have been focused on the exploitation of BTNPs in the biomedical field, owing to the high biocompatibility of BTNPs and their peculiar non-linear optical properties that have encouraged their use as nano carriers for drug delivery and as label-free imaging probes [3]. The exploration of BTNP potential in biomedical/therapeutic applications, such as cancer therapy through hyperthermia, and drug/gene delivery, has recently started in nanomedicine, based on the encouraging results observed in the biocompatibility assessments [4]. In another study, Städler *et al.* [5] investigated cellular responses to five non-linear active nanomaterials with nanoparticles are the best candidate for biomedical imaging and sensing.

Many synthetic methods have been utilized to produce fine $BaTiO_3$ nanoparticles including using a solid-state reaction [6], co-

precipitation (*e.g.,* citrates) [7], oxalates [8]), hydrothermal synthesis [9], a solvo thermal method [10], alkoxide hydrolysis [11], a catecholate process [12], and metal-organic processing [13], low-temperature combustion synthesis [14]. The preparation of BTNPs has been done by many authors [15-28]. Anuradha *et al.* [15] reported the combustion synthesis of cubic nanostructured barium titanate, various samples of $BaTiO_3$were prepared by the solution combustion of three different barium precursors (BaO_2, $Ba(NO_3)_2$and $Ba(CH_3COO)_2$ and fuels such as carbohydrazide, glycine or citric acid in the presence of titanyl nitrate. Zhong and Gallagher also prepared cubic $BaTiO_3$ by igniting the spray-dried mixture of $Ba(NO_3)_2$, $TiO(NO_{32}$ and alanine [16]. Sangjin Lee *et al.* [17] studied the preparation of $BaTiO_3$ nanoparticles by combustion spray pyrolysis, by mixing barium nitrate, $Ba(NO_3)_2$ and titanyl nitrate, $TiO(NO_3)_2$ in distilled water. Shaohua Luo *et al.* [18] studied the nanosized tetragonal barium titanate powders, by the reaction between TiCl, $Ba(NO_3)_2$, citric acid and $NH(NO_4)_3$. Simon-Seveyrat *et al.* [19] reinvestigated the synthesis of $BaTiO_3$ by conventional solid-state reaction and oxalate co precipitation route for piezoelectric applications.

Wang *et al*. [20] used two typical wet-chemistry synthesis methods, in the first method, barium acetate, tetrabutyl titanate, isopropyl alcohol and glacial acetic acid were starting reagents. The average particle size of obtained $BaTiO_3$ nano powder was 50-80 nm. For the second method, the starting reagents were barium stearate, tetrabutyl titanate and stearic acid; the obtained nano-crystallites of $BaTiO_3$ were in the range 25-50 nm. Wada *et al*. [21] reported the

preparation of $BaTiO_3$ nanoparticle of varying size using a hot uniaxial pressing method and Curie point for a grain size of 58 nm.

Boulos *et al*. reported an average particle size 40-70 nm of $BaTiO_3$ powders obtained from TiO_2 at 423 or 523 K [22]. Li *et al.* [23] described the oxalic acid precipitation method which is very similar to the sol-gel acetate method. The particle size prepared by this method was 38.2 nm. Recently, a sol-precipitation process was developed, which is quite similar to the sol-gel method. The advantage of this route is that it requires no further thermal treatment of the product, such as calcinations or annealing to enhance the homogeneity of crystals and crystal growth. Prasadarao *et al*. [24] also investigated on the formation of a stoichiometric co-precipitated precursor for $BaTiO_3$ from potassium titanyl oxalate and barium chloride. A simple and cost-effective method for obtaining BTNPs with tetragonal structure with a particle size in the range and 40–80 nm has been described by Bai *et al.* [25]. They used barium carbonate for the first time as a precursor. Gläsel *et al.* [26], used barium titanium methacrylate as a monomeric metallo-organic precursor of BTNPs, starting from metallic barium, titanium (IV) isopropylate and methacrylic acid in boiling methanol. Solid state polymerization and pyrolysis were allowed to occur simultaneously at temperatures over 473 K. Nucleation and growth of BTNPs was achieved at temperatures between 873 and 1673 K and under inert atmosphere. Depending on temperature and atmosphere, BTNPs could be obtained with size ranging from 10 nm (low T and inert atmosphere) to 1 μm.

In a work from Ashiri *et al.* [27], stoichiometric quantities of barium chloride (in CO_2-free water) and titanium chloride (in ethanol) were mixed, kept at pH = 14 by the addition of sodium hydroxide, and sonicated at 323 K for 45 min in a water bath (53 kHz, 500W), cubic BTNPs with ∼10 nm size and spherical shape were obtained, and no carbonate contaminants were found after synthesis at mild temperature. An emerging method for perovskite nanomaterial synthesis is represented by chemical vapour synthesis (CVS). This method enables the obtainment of highly pure, size-controlled and loosely aggregated nanoparticles in a time-effective and scalable manner. In a work of Mojić-Lanté *et al.* [28], BTNPs were produced for the first time in the literature using laser assisted CVS. The set-up for BTNP synthesis comprised a CO_2 laser flash evaporator, a hot-wall tubular reactor, a thermophoretic particle collector, and a gas supply system. BTNP solid precursors were titanium di (1-propoxide) bis (2,2,6,6,-tetramethyl-3,5-heptanedionate) and barium bis (2,2,6,6,- tetramethyl-3,5-heptanedionate) anhydrous. By varying the reactor length and temperature, partially crystalline, spherical particles with a size of a few nanometers could be achieved.

The decomposition kinetics and the formation of $BaTiO_3$ have been extensively studied by many researchers [29-35]. Otta *et al*. studied the kinetics and mechanism of the thermal decomposition of barium titanyl oxalate [29] and they were suggested that $BaTiO_3$ was formed in the temperature range of 773 – 1073 K. Balek *et al*. [30] were studied the decomposition reactions of barium titanyl oxalate and behavior of the reaction product – $BaTiO_3$ during heating in oxygen,

carbon dioxide, argon, and helium during heating up to 1773 K by thermal analysis, TG, DTA and EGA. Kim *et al*. [31] studied the tetragonality of $BaTiO_3$ derived from barium titanyl oxalate (BTO), various treatments were carried out by considering the thermal decomposition mechanism of BTO in air. The thermal behavior of $BaTiO_3$ prepared at temperatures of 873 – 1173 K was studied by Swillam *et al*. [32]. They have shown that when lower temperatures are used for the calcination of $BaTiO_3$ compacts, samples with extremely fine pores are formed, whereas higher temperatures cause the agglomerates to shrink too much smaller particles, eliminating these pores. Ragulya *et al*. [33] studied the process of synthesis of barium titanate powder from barium titanyl oxalate precursor under nonisothermal conditions and the effect of the heating rate on the specific surface area of the powder and established the advantages of nonisothermal conditions, especially the possibility of flexible control over the barium titanate grain size. Gopalakrishna Murthy *et al*. [34] also investigated the decomposition kinetics of the formation of barium titanate in the temperature range 873-1023 K. Jung *et al*. [35] examined the formation mechanism of $BaTiO_3$ from the thermal decomposition of barium titanyl oxalate.

This work focuses on the kinetic and thermodynamic studies on the formation of barium titanate nanoparticles by means of differential scanning calorimetry (DSC) analysis under non-isothermal heating conditions. The experiments were performed in the temperature range 873 - 1173 K at the heating rates of 5, 7, 10 and 15 K min^{-1} in nitrogen gas atmosphere. Ozawa and Coats Redfern methods were used to

determine the apparent activation energies of the multi step thermal decomposition processes. Kinetic deconvolution analysis was used to perform the overall kinetics of formation of $BaTiO_3$ nanoparticles. In order to predict the physico-geometrical reaction mechanism, empirical kinetic model functions such as phase nucleation and growth-type model, *RO (n)* were employed. The prepared BTNPs were identified and characterized by means of FT-IR, XRD, SEM and TEM.

3.2 Materials and methods

3.2.1 Materials

AnalaR grade barium nitrate ($Ba(NO_3)_2$) (Merck, India; assay ≥ 99.9 %), potassium titanyl oxalate ($K_2TiO(C_2O_4)_2$) (BHO Laboratory England; assay ≥ 99.9 %) were used in the present investigation.

3.2.2 Preparation of $BaTiO_3$ nanoparticles

Barium titanate nanoparticles were prepared *via* chemical precipitation method. Barium titanyl oxalate (BTO) was synthesized by the precipitation reaction of mixing of equi molar aqueous solution of barium nitrate and potassium titanyl oxalate with constant stirring. The white BTO precipitate obtained was filtered, washed with deionised water, and dried in an air oven kept at a constant temperature of 323 K for 24 h. Barium titanate nanoparticles were obtained by the thermal decomposition of BTO in a vacuum oven at 1173 K for 1 h, followed by powdering using an agate mortar. The obtained barium titanate nanoparticles were sieved through the mesh and fixed the particle size in the range 45-53 μm.

3.2.3 Experimental methods

3.2.3.1 FTIR spectral analysis

The infra red (IR) spectrum of the samples in KBr pellet was recorded using a Perkin Elmer Spectrum GXA FTIR spectrometer. The sample was first compressed with KBr into pellet and analyzed as KBr disc from 400 to 4000 cm^{-1}.

3.2.3.2 XRD Analysis

The X-ray diffraction (XRD) measurements of the samples were performed on a RIGAKU MINI FLEX-600 X-ray diffraction spectrophotometer using Cu K_α (1.5418 A^0) radiation.

3.2.3.3 Thermal analysis

The thermo gravimetric (TG) analysis of the samples was made on a T.A. thermal analyzer, model: TGA Q50 v20.2 Build 27 at different heating rates. The operational characteristics of the TG system are as follows: atmosphere: flowing air, at a flow rate of 60 mL min^{-1}; sample mass: 5.6 mg; and sample pan: silica. Duplicate runs were made under similar conditions. The differential scanning calorimetric (DSC) measurements of the samples were taken on a Mettler ToledoDSC822e at different heating rates of 5, 7, 10, 15 K min^{-1} from 973 to 1173 K with sample of mass 5.1 mg. The atmosphere was flowing nitrogen with flow rate of 50 mL min^{-1} and the sample container was made of aluminum. Duplicate runs were always made under similar conditions and found that the data overlap with each other, indicating satisfactory reproducibility.

3.2.3.4 SEM analysis

The Scanning Electron Microscope (SEM) analyses of all the samples studied were performed with SEM-EDS combination using JEOL Model JSM - 6390LV, JEOL Model JED – 2300 used to study specimen topology and morphology.

3.2.3.5 TEM analysis

The Transmission electron microscopy (TEM) analysis of the particles was achieved by using a JEOL 2100 used to study the particle size in nano meter range.

3.3. Results and Discussion

3.3.1 Characterization of sample

3.3.1.1 XRD Analysis

XRD analysis was employed to affirm the composition of as prepared oxide nanoparticles. Fig. 3.1 shows the structural characteristics of barium titanate and their oxide nanoparticles calcined at different temperature obtained from XRD. The prepared sample clearly indicates the presence of crystalline phase indices, the peak positions with 2θ values of 29.4, 36.4, 42.2, 61.3 and 73.4^0 are indexed as (110), (111), (200), (220) and (311) planes, according to the JCPDS file 05-0626. Furthermore, the tetragonal symmetry does not change when the calcinations temperature increases to 1023 K and 1173 K (Fig. 3.1b & c). The relative crystalline sizes are determined from the XRD line broadening using the Scherrer equation: $d = 0.9\lambda/\beta\cos\theta$, where d is the crystallite size, λ is the wavelength used in XRD (1.5418

A^0), θ is the Bragg angle, β is the pure diffraction broadening of a peak at half height, *i.e.*, broadening due to crystallite dimensions. It has been observed that the size of the BTNPs are in the range 22 – 50 nm according to the Scherrer equation [36].

3.3.1.2 FT-IR Analysis

The FTIR spectrum (Fig. 3.2a) at 510 K shows a broad absorption in a wide range from 2400 to 3800 cm^{-1} indicates the presence of H_2O and OH^- in the $BaTiO_3$ nanoparticles. The absorption bands observed near 1600 cm^{-1} are due to CO group, the sharp bands observed near 1400 and 1100 cm^{-1} are due to C-O bonded to Ti ions. The IR spectrum of BTO heated to 1173 K in vacuum for 1 h presented in Fig. 3.2 b shows the absorption band at 800 cm^{-1} is due to metal-oxygen ion stretching vibrations and the band observed near 1200 cm^{-1} is due to metal bonded to Ti ions. The IR bands at 588.5 and 433.5 cm^{-1} are observed corresponding to pure tetragonal phase of perovskite structure [37].

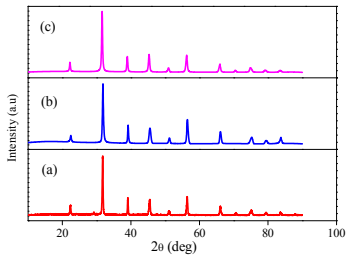

Fig. 3.1 XRD pattern of sample calcined at 973 K (a), 1023 K (b), 1173 K (c) for 1 h

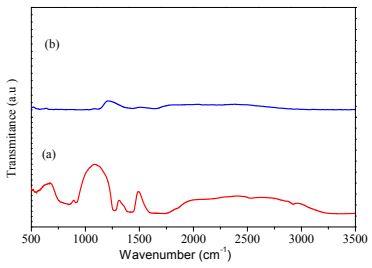

Fig. 3.2 FT-IR spectra of sample calcined at 510 K (a), 1173 K (b) for 1 h

3.3.1.3 DSC-TG Analysis of samples

Differential Scanning Calorimetric (DSC) investigations indicate many endothermic transformations taking place in the prepared sample. The physico-geometrical kinetic behavior and the reaction mechanism under linear non-isothermal condition were illustrated through kinetic analysis. The sample of 5.01 mg was weighed in an aluminium pan (6 mm in diameter and 2.5 mm in depth), a reference sample was made under the similar conditions. This method measures the difference in the amount of heat supplied to the examined sample and reference sample when both are subjected to controlled changes of temperature. The DSC curve of sample was recorded using a DSC instrument in N_2 flowing atmosphere at a rate of 50 mL min^{-1}, in the range 873-1173 K at different heating rates; Fig. 3.3a. Fig. 3.3b shows the result of thermo gravimetric (TG) analysis of the sample, which confirms the mass change in the various stages when the sample heating up to 1173 K. TG curve shows a sequence of five steps corresponding to different mass loss involving dehydration and decarboxylation. The first major mass loss, of about 17.4 % is within the temperature range from room temperature to 469 K, which may be attributed to the dehydration of $BaTiO(C_2O_4)_2.4H_2O$ to $BaTiO(C_2O_4)$. The second stage of mass loss of about 2.09 % appearing in the temperature range 469-529 K, can be attributed to the initial low temperature decomposition of BTO. The third major mass loss of about 17.12 % is found in the temperature range 529-758 K may be attributed to the complete decomposition of the oxalate groups, resulting in the formation of a carbonate with CO_2 and CO as gaseous

products. The fourth stage of mass loss of about 6.23 %, observed in the temperature range 758-873 K, is due to the evolution of entrapped CO_2, the final decomposition of carbonate takes place between 873-1173 K with a mass loss of about 6.9 % , which is due to the formation of $BaTiO_3$ [38]. The α-T curve (Fig. 3.3c) shows the multistep thermal decomposition reaction and the formation of barium titanate nanoparticles, considered to have three steps.

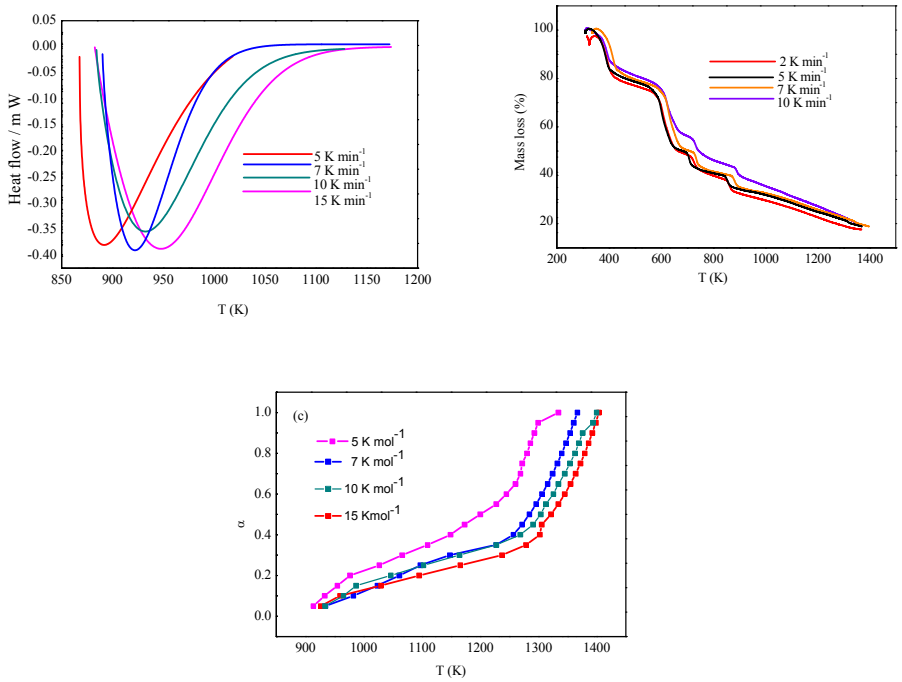

Fig. 3.3 The DSC (a), TG (b) curves for the thermal decomposition of sample and α–T curve (c)

3.3.2. Kinetic Analysis

The DSC curve for the thermal decomposition of BTO recorded under linear non-isothermal conditions at the temperature range

873-1173 K (Fig. 3.3a) was separated into three partially overlapping peaks with satisfactory fit using Fraser-Suzuki function, it is an effective tool in the investigation of phase transformations and enables very accurate determination of the temperature range and reaction heat in all transformations. It is used for recording the kinetic rate data of the thermal decomposition (Fig. 3.4).

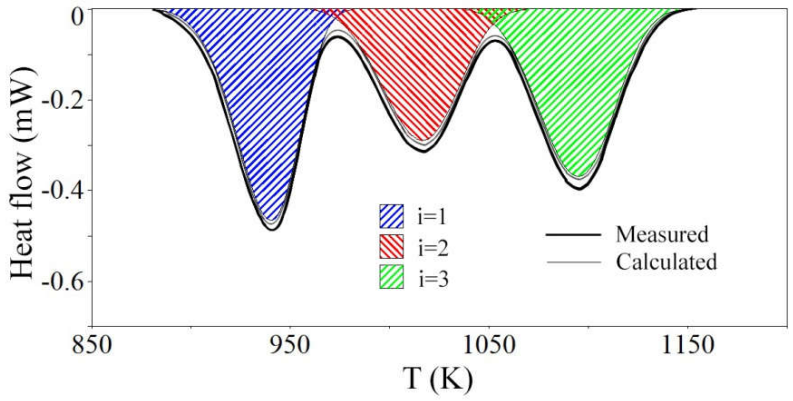

Fig. 3.4 The kinetic rate data at different β derived from the mathematically separated DSC peaks: first (i= 1), second (i= 2) and third peak (i= 3)

To evaluate the overall kinetics of the formation of $BaTiO_3$ nanoparticles by thermal decomposition of BTO, we assumed the following derivative kinetic equation for a single step in a physico geometrical mechanism with constant apparent Arrhenius parameters during the reaction. The deconvoluted DSC curve for the thermal decomposition of the sample at different β were subjected to the formal kinetic analysis by using the fundamental kinetic equation: [39]

$$\frac{d\alpha}{dt} = Ae^{(-E_a/RT)} f(\alpha) \tag{3.1}$$

where t is the time, T the temperature, R the ideal gas constant, A the apparent Arrhenius pre‐ exponential factor, E_a the apparent activation energy, and $f(\alpha)$ the apparent kinetic model function used to describe the physico-geometrical reaction mechanism as a function of the fractional reaction, α. Using the kinetic data for different β, apparent E_a as a function of the reacted fraction can be determined from the Ozawa [40] and the Coats & Redfern methods [41].

3.3.2.1 Calculation of activation energy by integrated isoconversional methods

3.3.2.1.1 The Ozawa Method

The Ozawa method has been widely used for kinetic data analysis [42]. This integral method compared heating rates with temperatures under the same conversion rates. The kinetic parameters of decomposition process were evaluated by using Ozawa equation.

$$Log\,\beta = Log\left(\frac{AE_a}{R}\right) - 2.315 - 0.4567\left(\frac{E_a}{RT}\right) - Log(\alpha) \tag{3.2}$$

Where β is the heating rate (K min^{-1}), A is the pre-exponential factor (s^{-1}), R is the gas constant (8.314 J $mol^{-1}K^{-1}$), E_a is the energy of activation, and α is the fraction of decomposition.

By plotting graphs between log β *versus* $1/T$ a straight line at different conversion rates as shown in Fig. 3.3, the activation energy

E_a and frequency factor log A could thus be obtained from the slope and the intercept respectively.

3.3.2.1.2. The Coats & Redfern method

Coats & Redfern method is an integral method [43, 44]; the kinetic parameters of decomposition process can be evaluated by using the relation as [41]

$$\log\left[\frac{-\log(1-\alpha)}{T^2}\right]=\left[\log\left\{\left(\frac{AR}{\beta E_a}\right)\left(1-\frac{2RT}{E_a}\right)\right\}-\left(\frac{E_a}{2.303RT}\right)\right] \quad (3.3)$$

To determine the value of activation energy, a plot of $\left[\frac{-\log(1-\alpha)}{T^2}\right]$ *versus 1/T* (Fig. 3. 3), a straight line graph is obtained. The value of activation energy can be calculated from the slope of a linear plot. The value of frequency factor also obtained from equation (3.3). The average calculated activation energy, frequency factor were depicted in Table 3.1. The other kinetic analysis parameters such as enthalpy of activation (ΔH^*), entropy of activation (ΔS^*) and free energy change of decomposition (ΔG^*) were evaluated [45] using equations

$$\Delta H^* \text{ (kJ mol}^{-1}) = E + \Delta nRT \quad (3.4)$$

Where Δn = Number of moles of product – number of moles of reactant in the reaction

$$\Delta S^*(JK^{-1}mol^{-1}) = 2.303R\left[\log\left(\frac{Ah}{kT}\right)\right] \quad (3.5)$$

$$\Delta G^* \text{ (kJ mol}^{-1}) = \Delta H^* - T\Delta S^* \qquad (3.6)$$

where A is (Arrhenius constant) determined from the intercept, k is Boltzmann constant and h is Plank's constant.

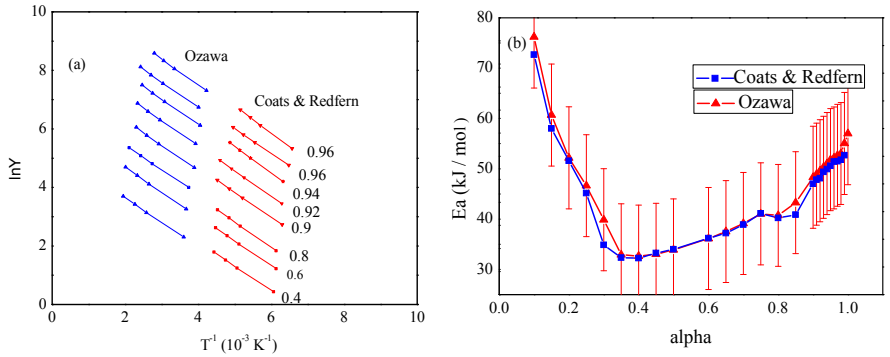

Fig. 3.5 Typical linear least - squares plot for Ozawa and Coats& Redfern method of the sample at different conversion values (a), the dependence of activation energy on conversion for two different methods (b)

Fig. 3.5a is the best linear least squares fit obtained using equations (3.2) and (3.3) for Ozawa and Coats & Redfern methods. The slopes of these straight lines have been used to calculate the activation energy (E_a) and their intercepts were used to calculate frequency factor (log A). The variation of the apparent E_a values as a function of α was almost similar for the above two methods (Fig. 3.5b).

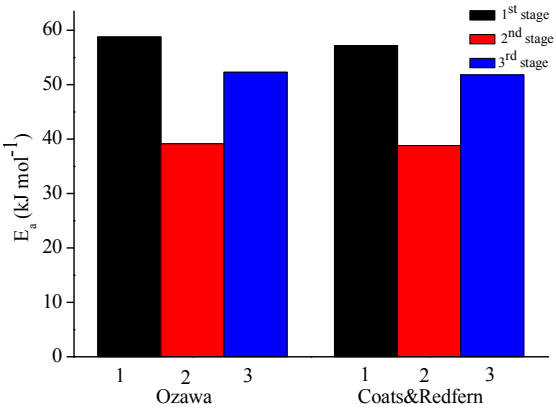

Fig. 3.6 Comparison of E_a values calculated by Ozawa and Coats & Redfern methods at different stages.

Fig. 3.6 shows comparison of activation energy needed for the each resolved stage of the thermal decomposition was calculated by Ozawa and Coats & Redfern methods in the temperature range 873-1173 K by column graph. From this graph it is shown that, during each step the estimation of E_a values by these methods are very close to each other.

The other thermodynamic parameters such as enthalpy of activation (ΔH^*), entropy of activation (ΔS^*), and free energy change of decomposition (ΔG^*) were calculated using equations (3.4)-(3.6). The calculated thermodynamic parameters were also depicted in Table 3.2.

Since the thermal decomposition is an independent kinetic process, the overall reaction consists of multistep thermal decomposition which is expressed by the following cumulative kinetic equation under linear non-isothermal conditions [46–49].

$$\frac{d\alpha}{dt} = \sum_{i=1}^{n} c_i A_i \exp\left(\frac{-E_{a,i}}{RT}\right) f_i\left(\alpha_i\right) \tag{3.7}$$

$$\text{with} \quad \sum_{i=1}^{n} c_i = 1 \quad \text{and} \quad \sum_{i=1}^{n} c_i \alpha_i = \alpha$$

where *n* and *c* are the number of component steps and the contribution ratio of each reaction step to the overall process, respectively, and the subscript *i* denotes each component reaction step. A_i and E_{ai} are the Arrhenius pre-exponential factor and the apparent activation energy respectively, of the process *i*. The kinetics of each component process of the overall reaction can be characterized by optimizing all the kinetic parameters in equation (3.6) using nonlinear least-squares analysis. Empirical kinetic model functions such as *RO (n)* [50] were employed for $f_i(\alpha_i)$ in equation (3.7) in order to accommodate any possible mechanistic feature of each reaction process.

$$f(\alpha) = (1-\alpha)^n \tag{3.8}$$

Where *n* is the character for a particular decomposition process, which corresponds to empirically obtain kinetic exponents. The number of component steps for all the samples are obtained through kinetic deconvolution of DSC peaks. The initial values of the kinetic parameters were determined through a formal kinetic analysis of the kinetic data, first subjected to mathematical deconvolution using a statistical function known as Fraser-Suzuki function. From the ratio of the peak areas for the separated first, second and third peaks, the

contribution c_i of each peak to the overall reaction was determined as (c_1, c_2 and c_3) = (0.45 ± 0.03, 0.40 ± 0.03, 0.15 ± 0.03). The mathematically separated peaks at different β were used as the kinetic rate data. For all peaks, the kinetic rate data indicates systematic shifts to higher temperatures with increasing β (Fig. 3.7).

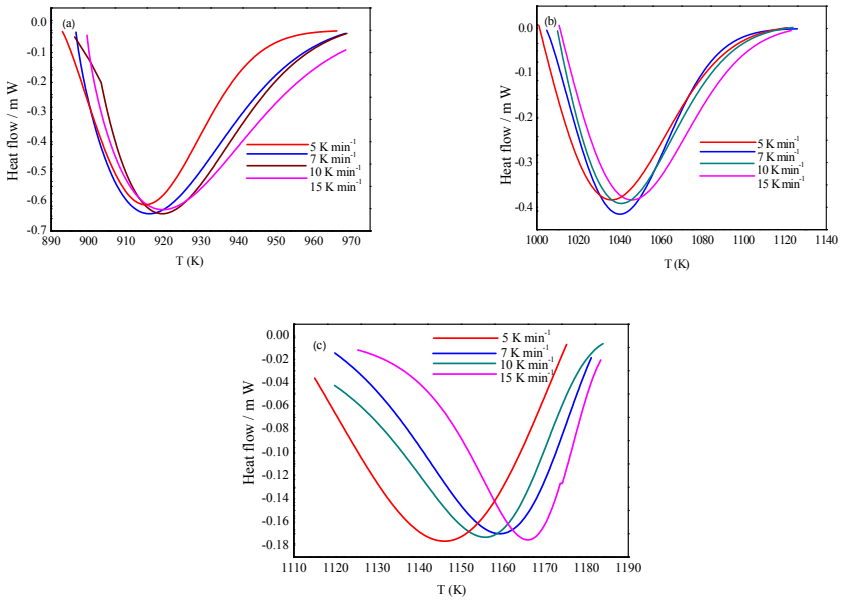

Fig. 3.7 Kinetic rate data at different β derived from the mathematically separated DSC peaks: first (i= 1) (a), second (i= 2) (b) and third peak (i= 3) (c)

The dependent in the apparent activation energies (E_a) determined by applying the Ozawa and the Coats & Redfern methods: were found for the kinetic rate data of the separated first, second and third DSC peaks (Fig. 3.5 b), for the first and second DSC peak, a systematic decrease in the E_a value during the course of the reaction was observed, and for the third DSC peak, increase in the E_a value was obtained. The systematic change in the E_a value with α observed for all

peaks indicate that the integration isoconversional relationship is one of the best method to point out the changes in the self-generated conditions as the reaction advanced and depending on β. In these methods Ozawa and the Coats & Redfern, the average values for E_a are 58.79 and 57.20 kJ/mol ($0.05 \leq \alpha \leq 0.4$) respectively was tentatively used for the first peak. The average value for E_a, for the second peak was 39.14 and 38.80 kJ/mol ($0.45 \leq \alpha \leq 0.85$) and also third peak was 52.29 and 51.80 kJ/mol ($0.9 \leq \alpha \leq 0.99$) respectively. During the first stage, the value of activation energy obtained by Ozawa method is close to that obtained by Coats & Redfern method, and in the second and third stages, the values of E_a obtained by these methods show small variation. The values of activation energy calculated using these methods studied show similar trend. These E_a values are nearly coincident with one another and also in agreement with that determined for the overall reaction under isothermal and controlled rate conditions. For the thermal decomposition reaction, the empirical kinetic deconvolution of the overlapping reaction steps, all the kinetic parameters in equation (3.7) should be determined by graphically comparing $(d\alpha/dt)_{exp}$ *versus* time $(d\alpha/dt)_{cal}$ *versus* time. The data from thermal analysis curves in the decomposition range $0.05 \leq \alpha \leq 0.4$ for first step, $0.45 \leq \alpha \leq 0.85$ for second step and $0.9 \leq \alpha \leq 0.99$ for third steps were used to determine value of kinetic model functions of this multistep process, by using the linear form of modified integral Coats and Redfern equation

$$\ln\left[\frac{g(\alpha)}{T^2}\right] = \ln\left(\frac{AR}{\beta E}\right) - \frac{E_a}{RT} \qquad (3.9)$$

The integral form of the conversion function *g(α)* which depends on the kinetic model of the occurring reaction, which describe specific solid state reaction mechanism. The plots of ln [*g (α)*/T^2] *vs 1/T* were drawn for each model by the linear regression method. The model giving the best fit *i.e.*, maximum correlation coefficient (*approximately to unity*) is taken as the best model describing the mechanism of the reaction. The straight line plot with suitable model and regression values are represented in the Fig. 3.8.

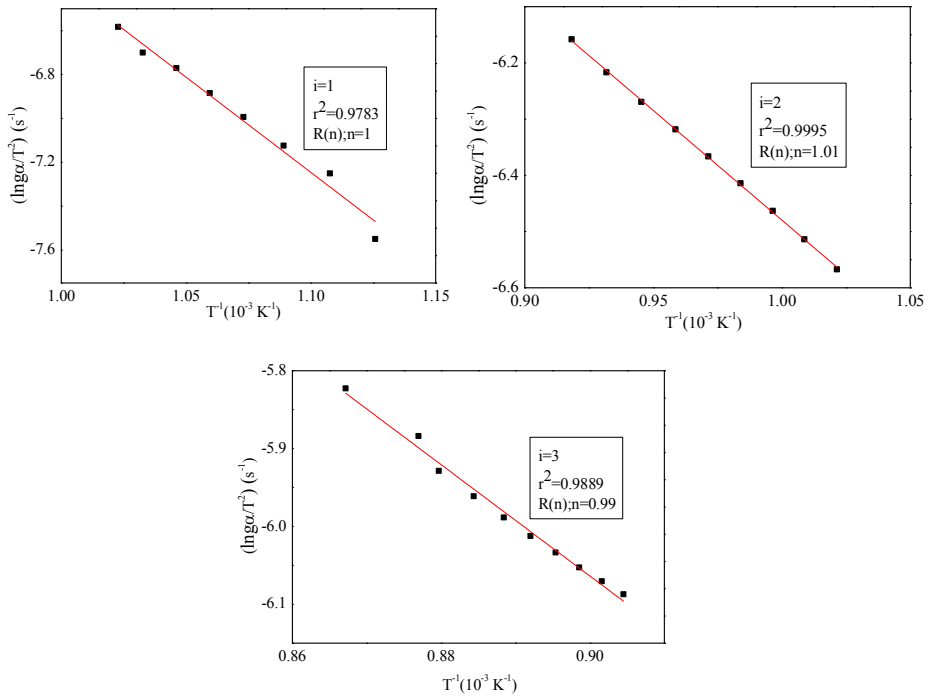

Fig. 3.8 Typical model fitting least-squares plot for *i*=1, *i*=2 and *i*=3

The initial values of kinetic parameters are provided in Table 3.1. According to this the activation energy (E_a), frequency factor (A) calculated from Ozawa and the Coats & Redfern methods and the values are found to be compatible with each other [45]. And the

thermodynamic parameters from Table 3.2, the positive value of ΔH^* show that the decomposition processes are endothermic in nature and ΔG^* values are positive, thus the processes are non-spontaneous [51]. The negative values of ΔS^* indicate that the activated complex has a high ordered structure than the reactants and further the high values of A indicate the fast nature of the reaction [45, 52].

Table 3.1 Initial values of kinetic parameters used for the kinetic deconvolution analysis of the thermal decomposition of sample under linear nonisothermal conditions.

Methods	i	C_i	E_{ai} (kJ/mol)	A_i (s^{-1})	$f(\alpha)$ $RO(n)$
Ozawa	1	0.45	58.79	0.47×10^8	n= 1
	2	0.40	39.14	0.88×10^4	n= 1.01
	3.	0.15	52.29	0.24×10^4	n=0.99
Coats &	1	0.45	57.20	0.75×10^8	n= 1
Redfern	2.	0.40	38.80	0.42×10^4	n= 1.01
	3.	0.15	51.80	0.12×10^4	n=0.99

Table 3.2 Thermodynamic parameters of thermal decomposition of sample under linear nonisothermal conditions.

Methods	i	ΔH (kJ/mol)	ΔS (J/mol)	ΔG (kJ/mol)
Ozawa	1	52.88	-106.96	147.03
	2	33.68	-190.13	222.71
	3	47.03	-192.61	259.21
Coats &	1	52.88	-114.11	142.93
Redfern	2	33.68	-166.56	200.32
	3	47.03	-177.63	245.45

After setting all of the initial values of kinetic parameters, a

parameter optimization was carried out to minimize the squares of the residues (F) when fitting the calculated curve $(d\alpha/dt)_{cal}$ *versus* time to the experimental curve $(d\alpha/dt)_{exp}$ *versus* time [53].

$$F = \sum_{j=1}^{n} \left[\left(\frac{d\alpha}{dt} \right)_{\exp,j} - \left(\frac{d\alpha}{dt} \right)_{cal,j} \right]^2 \tag{3.10}$$

Where n is the number of data points. To determine the initial values for all kinetic parameters, a statistical deconvolution method [54] was applied to the experimental kinetic rate data, and the separated kinetic rate data were analyzed using the formal kinetic analysis method on the basis of each single-step reaction under linear non-isothermal conditions using the mathematical peak deconvolution procedure. Fig. 3.9 shows the result of the kinetic deconvolution analysis for the thermal decomposition of sample using Ozawa and the Coats & Redfern methods on the basis of equation (3.10) after establishing the initial values for the kinetic parameters (Table 3.1), through mathematical deconvolution and the subsequent formal kinetic analysis of each resolved reaction step. Under the linear non isothermal conditions, for the sample was studied by Ozawa method (Fig. 3.9a) was resolved into three steps and similar way by Coats & Redfern method (Fig. 3.9 b), both go through more complex reaction pathways.

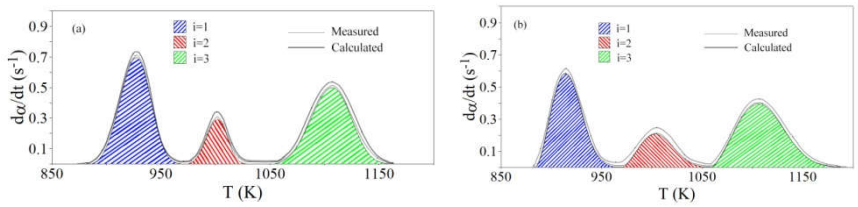

Fig. 3.9 Results of kinetic deconvolution analysis for the thermal decomposition of the sample using Ozawa (a), and Coats & Redfern method (b) under linear nonisothermal condition at β = 5 K min^{-1}

The average values of the kinetic parameters optimized for the each reaction stage at different β values are summarized in Table 3.3. For each resolved reaction steps, the value of E_a calculated for each reaction step are nearly in agreement with the respective corresponding values estimated by the Ozawa and the Coats & Redfern plots for the overall reaction under non isothermal conditions [55-56]. The physico-geometrical behavior of each sample was best described empirically by the *RO (n)* kinetic model functions are also shown in the Table 3.3.

Table 3.3 Average values of kinetics parameters optimized for each reaction step of the thermal decomposition of sample under linear nonisothermal conditions.

Methods	i	C_i	E_{ai} (kJ/mol)	A_i (s^{-1})	$f(\alpha)$ *RO (n)*
Ozawa	1	0.45±0.01	58.21±0.48	$(0.31\pm0.51)\times10^{8}$	1±0.1
	2	0.40±0.10	39.31±0.02	$(0.11\pm0.02)\times10^{4}$	1.01±0.1
	3.	0.15±0.81	52.51±0.20	$(0.22\pm0.20)\times10^{4}$	0.99±0.10
Coats & Redfern	1	0.45±0.04	57.16±0.42	$(0.86\pm0.50)\times10^{8}$	1±0.1
	2.	0.40±0.18	38.61±0.02	$(0.39\pm0.02)\times10^{4}$	1.1±0.48
	3.	0.15±0.08	51.42±0.21	$(0.12\pm0.20)\times10^{4}$	0.99±0.20

The required average value of E_a in Ozawa and the Coats & Redfern methods are 58.21± 0.48 kJ/mol, 57.16 ± 0.42 kJ/mol (for *i*=1) , 39.31 ± 0.02 kJ/mol, 38.61 ± 0.02 kJ/mol, (for *i*=2) and 52.51 ± 0.20 kJ/mol, 51.42 ± 0.21 kJ/mol, (for *i*=3) respectively. Using the respective E_a values, experimental master plots of (dα/dt) *versus* temperature for the separated first, second and third DSC peaks for each methods were drawn (Fig. 3.9) and satisfactorily fitted the *RO (n)* model were used as the empirical kinetic model function [57]. The values for the pre-exponential factor A for the first and second and third peaks determined through nonlinear regression analysis for the fitting using the *RO (n)* model for each methods, Ozawa and the Coats & Redfern were A_1= (0.31 ± 0.51) × 10^8, (0.86 ± 0.50) × 10^8 (for *i*=1), A_2=(0.11 ± 0.20) ×10^4 , (0.39 ± 0.02) × 10^4 (for *i*=2) and A_3=(0.22 ± 0.20) × 10^4, (0.12 ± 0.20) × 10^4 s^{-1} (for *i*=3) respectively.

3.3.2.1.2. SEM Analysis

Fig. 3.10 shows the SEM images of $BaTiO_3$ synthesized at different temperatures resulted in $BaTiO_3$ particles with a spherical shape however, some particles exhibit considerably pointed edges, and also most of the particles have smooth surfaces.

From the SEM images it is evident that the particles with different morphologies showed spherical grain agglomerations with smaller grain size with a porous surface containing particles with spherical shape.

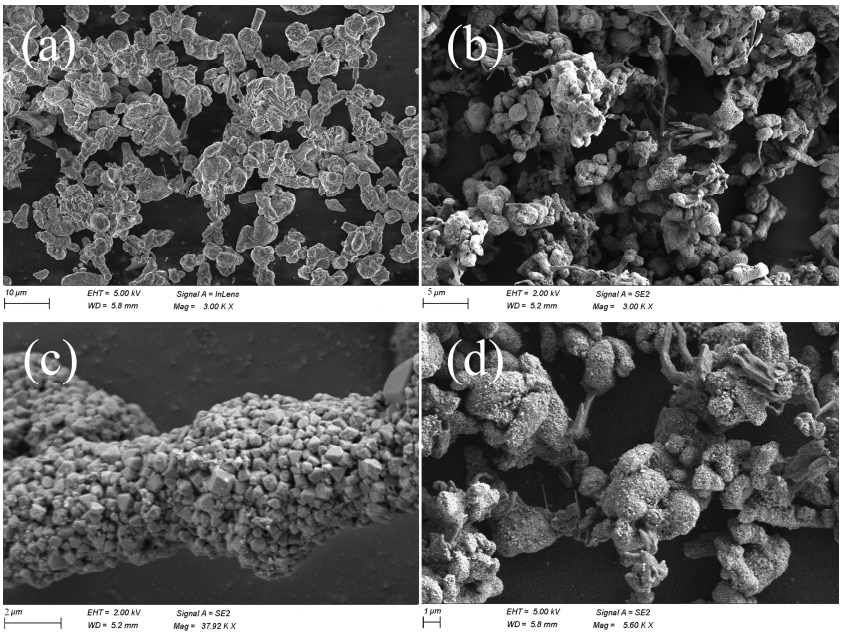

Fig. 3.10 SEM images showing the surface microstructure of the sample calcined at 1173 K for 1 h at 10 µm (a), 5 µm (b), 2 µm (c) and 1 µm (d)

3.3.2.1.4. TEM Analysis

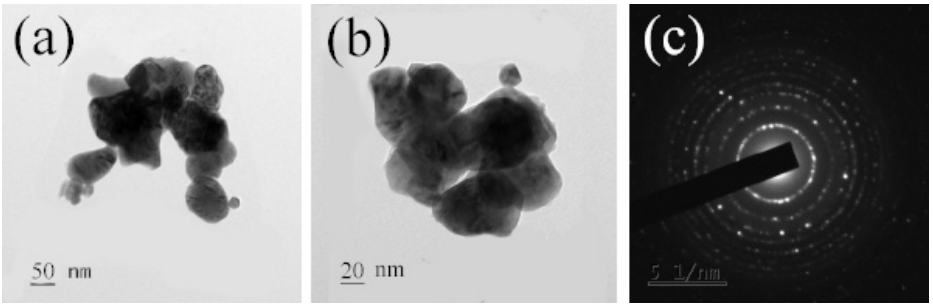

Fig. 3.11 The TEM images of the sample calcined at 1173 K for 1 h at 50 nm (a), 20 nm (b) and SEAD pattern (c).

TEM image (Fig. 3.11) of $BaTiO_3$ shows a small reduction in the size of nano spheres, which points out the complexity of formation of the BTNPs with 50-10 nm. Thus, the synthesized $BaTiO_3$ nanoparticles can be used for the wide range of applications in the electronic as well as opto-electronic field.

3.4 Conclusion

The kinetic, thermodynamic behavior of the formation of BTNPs from barium titanium oxalate *via* thermal decomposition under linear non isothermal condition has been studied using DSC. The decomposition shows multistage kinetics through complex reaction pathways. The comparison of the results obtained with different kinetic procedures, Ozawa and the Coats & Redfern methods depend on the empirical kinetic model function known as phase- boundary-controlled model *RO (n)* of the process. The kinetic deconvolution method is used to yield the dependency of E_a on the extent of conversion and it is established that, the final stage of decomposition of the sample show three stages and can be described by Reaction order *RO (n)* method. From the result of kinetic deconvolution of the sample the different phase changes of the reactant mixtures and the kinetic parameters of the respective thermal decomposition stages are evaluated accurately. The average calculated activation energy, pre-exponential factor and other thermodynamic parameters were calculated.

3.5 References

1. Unger KK, Kreysa G, Baselt JP. Characterization of porous solids. 1st ed. Amsterdam: Elsevier; 2000.

2. Smith MB, Page K, Siegrist T, Redmond PL, Walter EC, Seshadri R, Brus LE, Steigerwald ML, Barbara S. Crystal structure and the paraelectric-to-ferroelectric phase transition of nanoscale $BaTiO_3$. J. Am. Ceram. Soc. 2008;130:6955–63.

3. Genchi GG, Marino A, Rocca A, Mattoli V, Ciofani G, Barium titanate nanoparticles□: Promising multitasking vectors in nanomedicine. Nanotech. 2016;27:232001.

4. Ciofani G, Danti S, D'Alessandro D, Moscato S, Petrini M , Menciassi A. Barium titanate nanoparticles: highly cytocompatible dispersions in glycol-chitosan and doxorubicin complexes for cancer therapy. Nanoscale Res. Lett. 2010;5:1093–101.

5. Städler D. Harmonic nanocrystals for biolabeling: a survey of optical properties and biocompatibility. ACS Nano. 2012;6:2542–49.

6. Templeton LK, Pask JA. Formation of $BaTiO_3$ from $BaCO_3$ and TiO_2 in air and in CO_2. J. Am. Ceram. Soc.1959;42:212-16.

7. Mulder BJ. Surface and colloid chemistry in advanced ceramics processing. J. Am. Ceram. Soc. Bull. 1970;49:990-93.

8. Stockenhuber M, Mayer H, Lercher JA. Preparation of barium titanates from oxalates. J. Am. Ceram. Soc.1993;76:1185-90.

9. Kumazawa H, Annen S, Sada E. Hydrothermal synthesis of barium titanate fine particles from amorphous and crystalline titania. J. Mat. Sci.1995;30:4740-44.

10. Chen D, Jiao X. Solvothermal synthesis and characterization of barium titanate powders. J. Am. Ceram. Soc. 2000;83:2637-39.

11. Phule PP, Raghavan S, Risbud SH. Comparison of $Ba(OH)_2$, BaO, and Ba as starting materials for the synthesis of barium titanate by the alkoxide method. J. Am. Ceram. Soc. 1987;70:109-09.

12. Maison W, Kleeberg R, Heimann RB, Phanichphant S. Phase content, tetragonality, and crystallite size of nanoscaled barium

titanate synthesized by the catecholate process: effect of calcinations temperature. J. Eur. Ceram. Soc. 2003;23:127-32.

13. Shaikh AS, Vest GM. Dielectric properties of ultrafine grained $BaTiO_3$. J. Am. Ceram. Soc.1986;69:682-88.

14. Luo S, Tang Z, Yao W, Zhang Z. Low-temperature combustion synthesis and characterization of nanosized tetragonal barium titanate powder. J. Microelectron. Eng. 2003;66:147–52.

15. Anuradha TV, Ranganathan S, Mimani T, Patil KC. Combustion synthesis of nanostructured barium titanate. Scripta Mater. 2001;44: 2237–41.

16. Zhong Z, Gallagher PK. Combustion synthesis and characterization of $BaTiO_3$. J. Mater. Res. 1995;10:945–52.

17. Sanggin Lee, Tachwan Son, Jondoyun. Preparations of barium titanate nano particles by combustion spray pyrolysis. Mater. Lett. 2004;58:2932-36.

18. Shaohou, Hampolen Smith MJ. Wiley-VCH, Canada, 1988.

19. Simon-Seveyrat L, Eziane Y, Guiffrad B, Re-investigation of synthesis of $BaTiO_3$ by conventional solid- state reaction and oxalate coprecipitation route for piezoelectric applications. Ceram. Int.2005;33:35-40.

20. Wang L, Liu L, Xue D, Kang H, Liu C. Wet routes of high purity $BaTiO_3$ nanopowders. J. Alloys Comp. 2007;440:78-83.

21. Wada S, Suzuki T, Noma T. Preparation of barium titanate ceramics from amorphous fine particles of the Ba-Ti-O system and its dielectric properties. J. Mater. Res.1995;10:306-11.

22. Boulos M, Guillement Fritsch S, Mathieu F, Durand B, Lebey T, Bley V. Hydrothermal synthesis of nanosized $BaTiO_3$ powders and dielectric properties of corresponding ceramics. Solid State Ionics. 2005;176:1301-08.

23. Li B, Wang X, Li L. Synthesis and sintering behavior of $BaTiO_3$ prepared by different chemical methods. Mater. Chem. Phys. 2002; 78:292-98.

24. Prasadarao AV, Suresh M, Komarneni S. pH dependent coprecipitated oxalate precursors-a thermal study of barium titanate. Mater. Lett. 1999;39:359-63.

25. Bai H, Liu X. Low temperature solvothermal synthesis, optical and electric properties of tetragonal phase $BaTiO_3$ nanocrystals using $BaCO_3$ powder. Mater. Lett. 2013;100:1-3.

26. Gläsel HJ, Hartmann E, Hirsch D, Böttcher R, Klimm C, Michel D, Semmelhack HC, Hormes J, Rumpf H. Preparation of barium titanate ultrafine powders from a monomeric metallo-organic precursor by combined solidstate polymerisation and pyrolysis. J. Mater. Sci. 1999;34:2319–23.

27. Ashiri R, Moghtada A, Shahrouzianfar A, Ajami R. Low temperature synthesis of carbonate free barium titanate nanoscale crystals: toward a generalized strategy of titanate based perovskite nanocrystals synthesis. J. Am. Ceram. Soc. 2014;97:2027–31.

28. Mojić-Lanté B, Djenadic R, Srdić V, Hahn H. Direct preparation of ultrafine $BaTiO_3$ nanoparticles by chemical vapor synthesis. J. Nanopart. Res. 2014;16:2606-18.

29. Otta S, Bhattamisra SD. Kinetics and mechanism of the thermal decomposition of barium titanyl oxalate, J. Therm. Anal. 1994;41: 419-33.

30. Balek V, Kaisersberger E. Preparation of $BaTiO_3$ by thermal decomposition of BTO simultaneously investigated by emanation thermal analysis, TG-DTA and EGA. Thermochim. Acta.1985;85: 207–10.

31. Kim J, Jung W, Kim H, Yoon D. Properties of $BaTiO_3$ synthesized from barium titanyl oxalate. Ceram. Int. 2009;35:2337–42.

32. Swilam MN, Gadalla AMM. Decomposition of barium titanyl oxalate and assement of barium titanate produced at various temperatures. Trans. J. Brit. Ceram. Soc.1975;74:159-69.

33. Ragulya AV, Vasylkiv OO, Skorokhod VV. Synthesis and sintering of nanocrystalline barium titanate powder under nonisothermal conditions. I. Control of dispersity of barium titanate during its synthesis from barium titanyl oxalate. Powder Metall. Met. Ceram. 1997;36:170–75.

34. Gopalakrishna Murthy HS, Subba Rao M, Narayanan Kutty TR. Thermal decomposition of titanyl oxalates—I. Barium Titanyl Oxalate. J. Inorg. Nucl. Chem.1975;37:891–98.

35. Jung W, Min B, Park J, Yoon D. Formation mechanism of barium titanate by thermal decomposition of barium titanyl oxalate. Ceram. Int. 2011;37:669–72.

36. Patterson AL. The Scherrer formula for X-Ray particle size determination. Phys. Rev. 1939;56:978- 82.

37. Nakamoto K. Infrared spectra of inorganic and co-ordination compounds. 2nd Ed. NewYork,Wiley, 1969;245.

38. Bera J, Sarkar D. Formation of $BaTiO_3$ from barium oxalate and TiO_2. J. Electroceram. 2003;11:131-37.

39. Kotru PN, Raina KK, Koul ML. The Kinetics of Solid-State Decomposition of neodymium tartrate. Indian J. Pure Appl. Phys. 1987;25:220-22.

40. Ozawa T. A new method of analyzing thermogravimetric data. Bull. Chem. Soc. Jpn. 1965;38:1881-86.

41. Coats AW, Redfern JP. Kinetic parameters from thermogravimetric data. Nature. 1964;201:68-69.

42. Cooney JD, Wiles DM. Thermal degradation of poly(ethylene terephthalate): A kinetic analysis of thermoravimetric data. J. Appl. Polym. Sci. 1983;28:2887-902.

43. Laidler KJ. Chemical kinetics. 3rd Edition, Harper & Row, New York, 1987.

44. Dabhi RM, Joshi MJ. Thermal studies of gel grown zinc tartrate spherulites. Ind. J. Phys. 2002;76:211-13.

45. Dalal PV, Saraf KB, Shimpi NG, Shah NR. Pyro and kinetic studies of barium oxalate crystals grown in agar gel. J. Cryst. Process Technol. 2012;2;156–60.

46. Wada T, Koga N. Kinetics and mechanism of the thermal decomposition of sodium per carbonate: role of the surface product layer. J. Phys. Chem. A. 2013;117:1880–89.

47. Wada T, Nakano M, Koga N. Multistep kinetic behaviour of the thermal decompositionof granular sodium per carbonate: hindrance effect of the outer surface layer. J. Phys. Chem. A. 2015;119:9749–60.

48. Yoshikawa M, Yamada S, Koga N . Phenomenological interpretation of the multistep thermal decomposition of silver carbonate to form silver metal. J. Phys. Chem. C. 2014;118:8059–70.

49. Kitabayashi S, Koga N. Physico-geometrical mechanism and overall kinetics of thermally induced oxidative decomposition of tin (II) oxalate in air: formation process of micro structural tin(IV) oxide. J. Phys. Chem. C. 2014;118:17847–61.

50. Koga N, Tanaka H. Accommodation of the actual solid-state process in the kinetic model function. 1. Significance of the non-integral kinetic exponents. J. Therm. Anal. 1994;41:455–69.

51. Mallakpour S, Dinari M. Eco-friendly fast synthesis and thermal degradation of optically active poly-amides under microwave accelerating conditions. Chin. J. Polym. Sci. 2010;28:685-94.

52. Mallikarjun KG. Thermal decomposition kinetics of Ni (II) chelates of substituted chalcones. J. Chem. 2004;1:105-09.

53. Barmak K. A Commentary on: Reaction kinetics in processes of nucleation and growth. Met. Mater. Trans. A. 2010;41:2711− 75.

54. Ferriol M, Gentilhomme A, Cochez M, Oget N, Mieloszynski JL. Thermal degradation of poly (methyl methacrylate) (PMMA): modelling of DTG and TG curves. Polym. Degrad. Stab. 2003;79:271–81.

55. R. De Levie. Nonisothermal analysis of solution kinetics by spreadsheet simulation. J. Chem. Educ. 2012;89:79–86.

56. Sanchez-Jimenez PE, Perejon A, Criado JM, Dianez MJ, PerezMaqueda LA. Kinetic analysis of complex solid-state reactions. A new deconvolutionprocedure. J. Phys. Chem. B. 2011;115:1780−91.

57. Koga N. Ozawa's kinetic method for analyzing thermoanalytical curves. J. Therm. Anal. Calorim. 2013;113;1527−41.

CHAPTER 4

EFFECT OF DOPANT ON THE MULTISTAGE THERMAL DECOMPOSITION KINETICS OF BARIUM TITANYL OXALATE

4.1 Introduction

Solid-state kinetic data are of practical interest for the large and growing number of technologically important processes, a number of reports regarding the kinetics mechanism of these processes [1–4]. The chemical and catalytic reactivity of a solid depends on its method of preparation, so that structural and electronic imperfections may have important effects on the behaviour of a solid state reaction. Chemical processes involving the chemical transformation of solids play an important role in research technology, as sophisticated solids can be produced by thermal decomposition reaction of precursor materials. The decomposition atmosphere, crystal shape, size, presence of defects and various pre-treatments such as irradiation, mechanical grinding, doping, *etc*., play an important role in the decomposition, especially in determining the kinetics of oxalate decomposition [5].

Normally, defects mainly refer to point defects, including vacancies, interstitial, electrons, and holes, which can be created easily by doping. Doping is a highly complex subject, as there are quantities of paper to explore the doping properties and several mechanisms to achieve charge balance [6–7]. Taking the perovskite $BaTiO_3$, doping with higher valence cations, the charge may be compensated by ionic mechanism by the creation of vacancies on either of the cation sublattices or of oxygen interstitials [8]. Moreover, electronic compensation is possible in which the valence of Ti reduces from 4^+ to 3^+. Conversely, on doping $BaTiO_3$ with lower valence cations, the dopants may substitute onto either of the cation sites or in some cases onto a mixture of both sites depending on dopants size. The charge

compensation mechanism involves primarily the creation of oxygen vacancies as ionic compensation [9–10]. Also, sintering at high temperatures can create point defects due to the reduced atmosphere in which the samples would lose a small amount of oxygen and thus oxygen vacancies would be created. [11].

The thermal decomposition processes of metal titanyl oxalates are relatively complicated because of the reduction property of $C_2O_4^{2-}$; the thermal decomposition of metal oxalates involves the cleavage of the C-C bond, since the products are CO and CO_2 which contain only one carbon atom each. In many cases the C-C bond cleavage is the rate determining step [8]. The cleavage may be heterolytic to produce CO_2 and CO_2^{2-} or homolytic to produce two CO_2^{-} anions [9]. Decomposition of metal oxalate, a chemical change believed to involve a small number of relatively simple steps occurring in and between the components of the crystalline reactant and the product, both of known lattice structures. In metal oxalate, the transfer of an electron from the $C_2O_4^{2-}$ to the cation is the first stage of the decomposition which leads to the rupture of the C-C bond [12]. Pre-treatment such as irradiation, mechanical grinding, doping, *etc*., affect the rate and temperature of decomposition of oxalates [13-15]. The first two factors generally increase the rate and decrease the decomposition and dehydration temperatures. In some cases even the treatment itself brings about dehydration and decomposition [16]. Doping with metal ions or other pre-treatment of samples may have important effects on the reactivity of solids and might alter the kinetics of a reaction and help to clarify the reaction mechanism [17]. It has been reported that the effect of

doping depends on the nature of dopants [18]. Gallagher *et al*. reported that the thermal decomposition of substituted barium titanyl oxalates and its effect on the semiconducting properties of the doped materials [19].

The effects of several pre-treatments on the kinetics and mechanism of the thermal decomposition of $Na_2C_2O_4$ have been studied [20–21]. A comparative differential thermal analysis (DTA) study of some oxalates in N_2 and O_2 atmosphere has been reported [22]. The onset temperatures of dehydration and decomposition reactions are reported and the influence of atmosphere upon the temperatures and products of decomposition is discussed. The activation energies of solid state reactions could vary between relatively large limits depending on the nature and the method of preparing the starting materials [23-24]. Guha *et al.* studied barium titanate doped with Nb impurities, the chemically processed material with high dielectric constant have become an important for the electronic industry [25].

Kotlyarchuk *et al*. synthesized calcium doped nanocrystalline barium titanate powder by oxalate route. Addition of Ca on the surface of the samples of semi decomposed barium titanyl oxalate reduces lattice parameter for samples that related with replacement of barium by calcium which is confirmed by characterization of the semi decomposed barium titanyl oxalate and doped barium titanate carried out by specific surface area measurements, TEM and XRD [26]. Yangsheng Liu *et al*. synthesized chromium doped barium titanyl oxalate particles *via* a facile chemical co-precipitation method and

their morphologies, structures as well as dielectric and electro rheological properties were studied [27]. The synthesis, characterisation and dielectric properties of Ni-doped $BaTiO_3$ and the effect of magnetic field on the dielectric properties studied by Yogeswar Kumar *et al.* [28]. Upon doping A^+ or B^- sites in barium titanyl oxalate or their oxides, the catalytic activity, ionic and electronic conductivity and flexible physical and chemical properties can be altered, that lend a hand for utilization in various applications [29]. Different cations with different sizes and charges can be hosted in the A^+ and B^-sites of these metal oxalates or their oxides; thus many studies can be performed to utilize doped perovskites in various applications.

In the present study, the peculiarity of K^+ ions to intrude into the BTO lattice due to its small size made us to consider K^+ ions as a promising candidate to study the effect of doping on the thermal decomposition kinetics of BTO.

4.2 Experimental

4.2.1 Materials

AnalaR grade barium nitrate ($Ba(NO_3)_2$) (Merck, India; assay ≥ 99.9 %) and potassium titanyl oxalate ($K_2TiO(C_2O_4)_2$) (BHO Laboratory England; assay ≥ 99.9 %) were used in the present investigation.

4.2.2 Preparation of doped BTO

K^+ doped samples of BTO were prepared as per the following procedure; 10 g of BTO was dissolved in 230 mL of distilled water at boiling temperature in a 500 mL beaker. 10mL of a solution containing the desired quantity of K^+ was added to the hot solution so as to achieve a total volume of 240 mL. The solution containing the desired quantity of dopant was then cooled slowly to room temperature. The beaker containing the solution was covered using a clean uniformly perforated paper and kept in an air oven at a temperature of 323 K over a period of 6–7 days to allow the slow crystallization of doped sample by evaporation. The resulting crystals were removed; air dried and powdered in an agate mortar. The samples prepared were sieved through the mesh and fixed the particle size in the range 45-53 μm and kept in a vacuum dessiccator. The doped samples were prepared at different concentrations, *viz*., 10^0, 10^{-2} and 10^{-4} mol % and are named as BTO_1, BTO_2 and BTO_3 respectively and control (pure) compound as BTO.

4.2.3 Methods

The Fourier Transform Infrared **(**FT-IR) spectrum of the samples in KBr pellet was recorded using a JASCO FT-IR-4100 instrument. The sample was first compressed with KBr into pellet and analyzed as KBr disk from 400 to 4000 cm^{-1}. The instrument offers high sensitivity, maximum resolution (0.9 cm^{-1}) and high signal-to-noise ratio (22,000:1). The X-ray diffraction (XRD) measurements of the samples were taken on a RIGAKU MINI FLEX-600 X-ray

diffraction spectrophotometer using Cu K_α (1.5418 A^0) radiation. FT-Raman spectroscopy of the samples were taken on MultiRAM spectrometer, range 3600 to 50 cm^{-1}, laser excitation 1064 nm (standard) or 785 nm (optional). It is equipped with Rayleigh filters, primary filters, room temperature 'InGaAs' detector and 'Si' avalanche detector. The Scanning Electron Microscopic (SEM) analyses of all the samples studied were performed with SEM-EDS combination using JEOL Model JSM - 6390LV, JEOL Model JED - 2300. The instrument offers a resolution of 3 nm (Acc V 30 KV, WD 8 mm, SEI) , 8 nm(Acc V 3.0 KV, WD 6 mm, SEI) and magnification of 5 × to 300, 000 × (Both in high and low vacuum mode). For the present investigation, the imaging techniques employed was secondary electrons (SE), backscattered electrons (BSE) and energy-dispersive X-ray analysis (EDXA). The transmission electron microscopy (TEM) analysis of the particles was achieved by using a JEOL 2100 field emission transmission electron microscope operated at 200 kV with a 0.18 nm resolution. The thermo gravimetric (TG) analysis of the samples was made on a T.A. thermal analyzer, model: TGA Q50 v20.2 Build 27 at a heating rate 10 K min^{-1}. The operational characteristics of the TG system are as follows: atmosphere: flowing air, at a flow rate of 60 mL min^{-1}; sample mass: 5 mg; and sample pan: silica. Duplicate runs were made under similar conditions and found that the data overlap with each other, indicating satisfactory reproducibility. The differential scanning calorimetric (DSC) measurements of the samples were taken on a Mettler ToledoDSC822e. The operational characteristics of the DSC system are as follows: atmosphere: flowing N_2 at a flow rate of 50 mL min^{-1}; sample mass: 5 mg; and sample holder: aluminium.

4.3 Results and Discussion

4.3.1 Sample Characterization

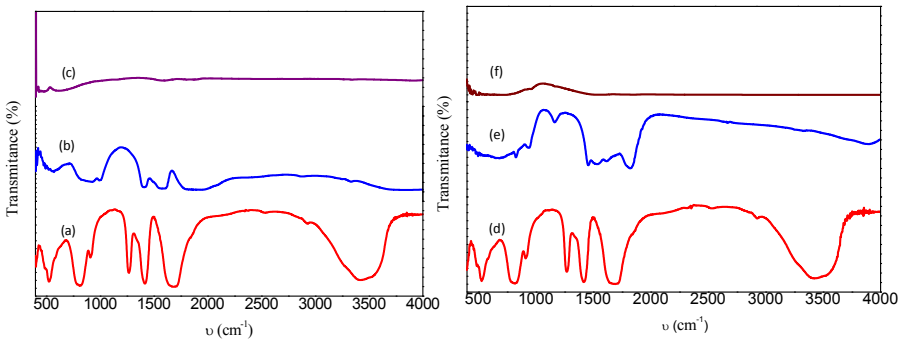

Fig. 4.1 The FT-IR spectra of sample BTO (a), BTO calcined at 628 K for 1 h (b), BTO calcined at 1023 K for 1 h (c), sample BTO_3 (d), BTO_3 calcined at 628 K for 1 h (e) and BTO_3 calcined at 1023 K for 1 h (f).

Fig. 4.1 represents the FT-IR spectra of pure BTO, BTO calcined at 628 and 1023 K for 1h, sample BTO_3 and BTO_3 calcined at 628 and 1023 K for 1 h. For the sample BTO (Fig. 4.1a), the principal band ($\square_{as}$, -C=O) occurs at 1686 cm^{-1}. The FTIR spectrum of the sample calcined at 628 K (Fig. 4.1b) in vacuum for 1h shows the appearance of an intense band at 2339 cm^{-1} which can be attributed to the asymmetric stretching frequency of free CO_2. The FTIR spectra of the sample calcined at 1023 K was presented in Fig. 4.1c, which represents the pure $BaTiO_3$. The FT-IR absorption spectrum of K^+ doped BTO crystalline particle (sample BTO_3) is shown in Fig. 4.1d. The broad band extending from 2800 to 3600 cm^{-1} is assigned to the symmetric and asymmetric stretching modes of the water molecules. The strong band appearing in the IR spectrum around 1615 cm^{-1} can be identified as the asymmetric stretching vibrations of CO groups of

the $C_2O_4^{2-}$ ions together with the bending mode of water. Fig. 4.1e displays the FTIR spectrum for the doped sample, BTO_3 calcined at 628K. The strong peak around 1316 cm^{-1} is also assigned to the asymmetric stretching of CO groups. The strong bands around 495 and 796 cm^{-1} are due to the combined effect of the in-plane deformation mode of OCO and MO bond and the weak one around 582 cm^{-1} observed in the spectrum represent the wagging mode [30-32]. The FTIR spectroscopic analysis of crystals of $Ba_{1-x}K_xTiO(C_2O_4)_2.4H_2O$ confirms the presence of functional groups associated with the oxalate ligands and the metal–oxygen bond. Fig. 4.1f represents the FT-IR spectrum of K^+ doped $BaTiO_3$. FTIR spectra displays two strong absorption peaks at 441 and 563 cm^{-1} for control (pure) BTO (Fig. 4.1c); and 430 and 557 cm^{-1} in doped sample (Fig. 4.1f). The former peaks (441 and 430 cm^{-1}) were assigned to Ti-O bending vibrations along the polar axis whereas the latter peaks (563 and 557 cm^{-1}) were assigned to Ti-O stretching vibrations. These peaks suggest that both doped and control sample had pure tetragonal phase [33, 34]. Further, the peaks at 868 cm^{-1} in control and doped sample were assigned to stretching vibrations of metal-oxygen. The peaks displayed at 1724 and 3429 cm^{-1}, in control and doped sample were attributed to moisture absorption by samples. All other doped samples have same FT-IR characteristics of BTO_3.

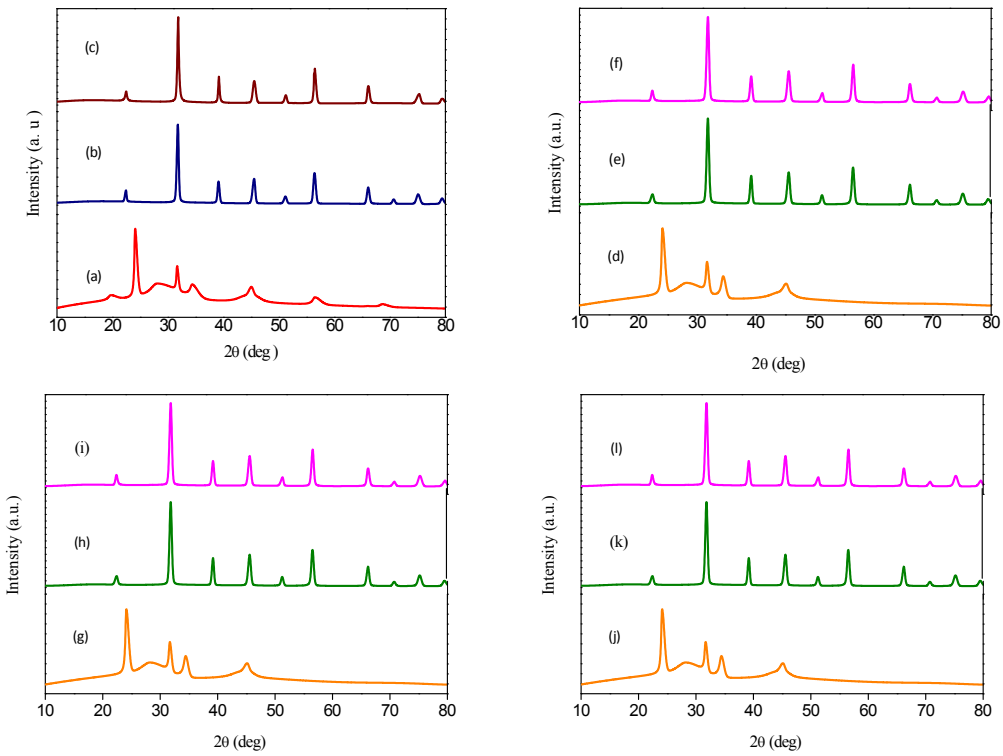

Fig. 4.2 The XRD pattern of sample BTO(a), BTO calcined at 773 K (b), BTO calcined at1023 K (c), sample BTO_1 (d), BTO_1 calcined at 773 K (e), BTO_1calcined at1023 K for 1 h (f), sample BTO_2 (g), BTO_2 calcined at 773 K (h), BTO_2 calcined at1023 K (i), sample BTO_3 (j), BTO_3 calcined at 773 K (k), BTO_3 calcined at1023 K for 1 h (l)

Powder XRD was used for the phase identification and the relative percentage of different phases of the prepared samples. The diffraction patterns were recorded over the angular range *2θ* from 20 to 80^0. Using the XRD data of the samples, particle size and lattice parameters were estimated. Fig. 4.2a exhibits the XRD pattern of sample BTO and sample BTO calcined at 773 and 1023 K (Figs. 4.2b & 4.2c respectively). Before the calcination of the sample BTO, slight amorphous phase was observed due to the presence of carbon atoms

and water in the mixture. After calcination at 773 K, the crystalline phase with cubic structure (a = 4.0073 A^0) was appeared (Fig. 4.2b). The calcinations of sample BTO at 1023 K for 1h tend to produce the crystalline phase with tetragonal phase ($a = b$ = 3.999 and c = 4.0053 A^0) (Fig. 4.2c).

Figs. 4.2 d, g, j displays the XRD pattern of K^+ doped BTO (sample BTO_1, BTO_2 & BTO_3) and its decomposed products at 773 and 1023 K (Figs. 4.2 e, f, h, i, k, & l respectively). It was observed that the formation of $BaTiO_3$ from BTO completes at about 773 K. The products of the samples BTO and doped samples calcined at 773 K consist of pure cubic $BaTiO_3$ (Figs. 4.2 b, e, h & k respectively). The products of the samples BTO and doped samples calcined at 1023 K (Figs. 4.2 c, f, i & l) indicate that the cubic form possibly transforms to tetragonal structure. This was revealed by the asymmetry introduced in the peaks at the 2θ values corresponding to 45.26, 50.90, 56.14, 74.89 and 79.5^0 respectively, which confirms the transformation of the cubic phase to the tetragonal phase [35].

Figs. 4.3 a & b shows the FT-Raman spectra of the sample BTO and BTO_3 at room temperature. Sample BTO exhibits the tetragonal structure belonging to the space group C_{4v} symmetry [36].

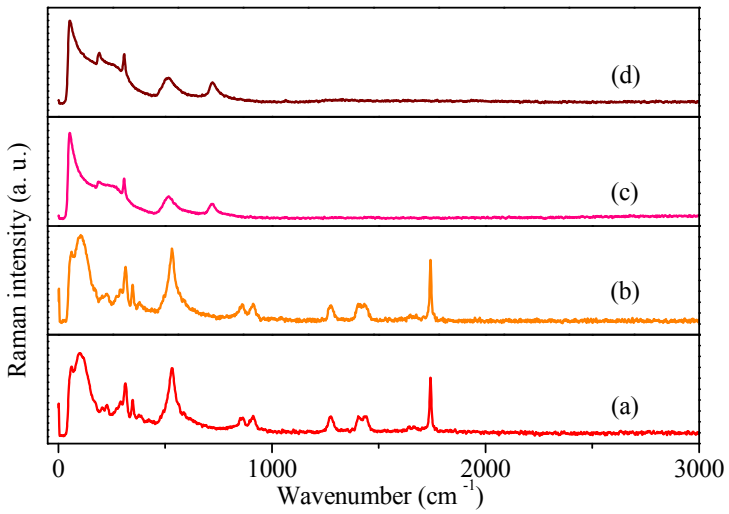

Fig. 4.3 The FT Raman spectra of sample BTO (a), BTO_3 (b) BTO calcined at 1023 K (c), BTO_3 calcinedat1023 K (d) for 1 h

The peak observed at 305 cm^{-1} corresponds to the E (TO_2) phonon mode of tetragonal BTO. The A_1 (TO_1), A_1 (TO_2), A_1 (TO_3) and A_1 (LO_3) modes were observed at about 180, 270, 516 and 720 cm^{-1} respectively [36]. The FT-Raman spectra obtained for the sample BTO_3 did not show any remarkable shift in wavelength. This can be attributed to the effective doping of K^+ ion into the lattice structure of BTO. It was also seen that all Raman modes are weaker and broader with change in the concentration. Figs. 4.3b & d show the FT-Raman spectra of decomposed product (calcined at 1023 K) of both the sample BTO and doped samples. For the sample BTO, the spectrum consists of peaks at 52, 174, 260, 306, 547 & 717 cm^{-1} and for the doped

samples BTO_1, BTO_2 and BTO_3 the spectrum made up of peaks at 185, 308, 515, 728 cm^{-1}. This confirms that all are characteristic bands of the tetragonal phase $BaTiO_3$. The strong peaks at 174 and 547 cm^{-1} were due to the TO_2 and TO_4 phonons respectively and the weak peak at 260 cm^{-1} to the silent TO_3 mode. The appearance of a peak at 305 cm^{-1} [A_1 (TO_2) mode] indicates the asymmetry within the TiO_6 octahedra of barium titanate phase with the particle size of 50 nm [37, 38]. According to Kaiser *et al*. [39] the weak shoulder below 300 cm^{-1} belongs to an A_1 (TO) phonon mode. The peak at ~307 cm^{-1} corresponds to the E (TO+LO) phonon mode of tetragonal $BaTiO_3$ [40] and the strong band at ~515 cm^{-1} can be attributed to the A_1 (TO) phonon mode of the tetragonal phase [41, 42]. The weak peak at ~718 cm^{-1} has been associated with the highest-frequency longitudinal optical mode (LO) of A_1 symmetry.

4.3.2 Thermal decomposition behaviour

Fig. 4.4 shows the result of thermo gravimetric analysis of the samples BTO, BTO_1, BTO_2 & BTO_3 which confirms the mass change in the various stages upon heating up to 1373 K (Table 4.1). TG curve shows the sequence of five steps with different mass losses involving dehydration and decarboxylation.

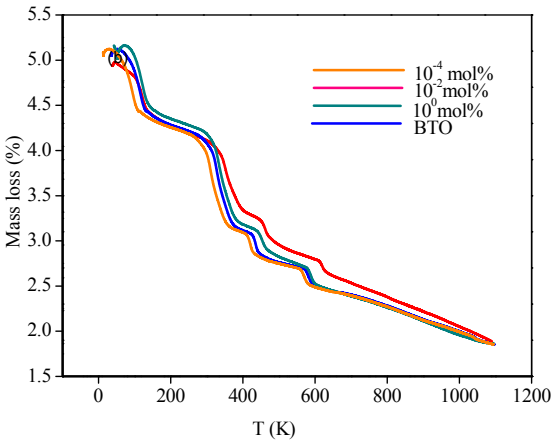

Fig. 4.4 The TG curves for the thermal decomposition of samples (m_0 = 5.3 mg) at 10 K min^{-1}; sample BTO, BTO_1 (10^0 mol %), BTO_2 (10^{-2} mol %) and sample BTO_3 (10^{-4} mol %)

Table 4.1 Mass loss data of samples

Decompo-sition steps	Temperature range (K)	Mass loss (%)			
		BTO	BTO_3	BTO_2	BTO_1
1	308-463	17.62	16.21	16.94	17.02
2	463-523	02.79	03.18	03.25	03.75
3	523-753	20.52	18.93	19.34	19.94
4	753-893	05.13	05.96	06.13	06.77
5	893-1053	06.99	07.68	07.06	07.92
	308-1053	53.05	52.46	52.72	55.40

For the sample BTO, the first major mass loss, of about 17.62 % is within the temperature range from room temperature to 463 K, which may be attributed to the dehydration of $BaTiO(C_2O_4)_2.4H_2O$ to $BaTiO(C_2O_4)$. The second stage of mass loss of about 2.79 % appearing in the temperature range 463-523 K, can be attributed to the initial low temperature decomposition of BTO. The third major mass loss of about 20.52 % observed in the temperature range 523-753 K is attributed to the complete decomposition of the oxalate groups, resulting in the formation of a carbonate with CO_2 and CO:

$$Ba_2Ti_2O_2\left(C_2O_4\right)_3.CO_3 \rightarrow Ba_2Ti_2O_5CO_3\left(CO_2\right) + 2CO_2 + 3CO \quad (4.1)$$

The fourth mass loss of about 5.13 %, observed in the temperature range 753-823 K, is due to the evolution of entrapped CO_2, the final decomposition of carbonate takes place between 893-1023 K with a mass loss of about 6.9 % , which is due to the formation of $BaTiO_3$ [43, 44]. From Table 4.1 it is clear that the mass loss percentage of each step is increased with increase in the concentration of the dopant.

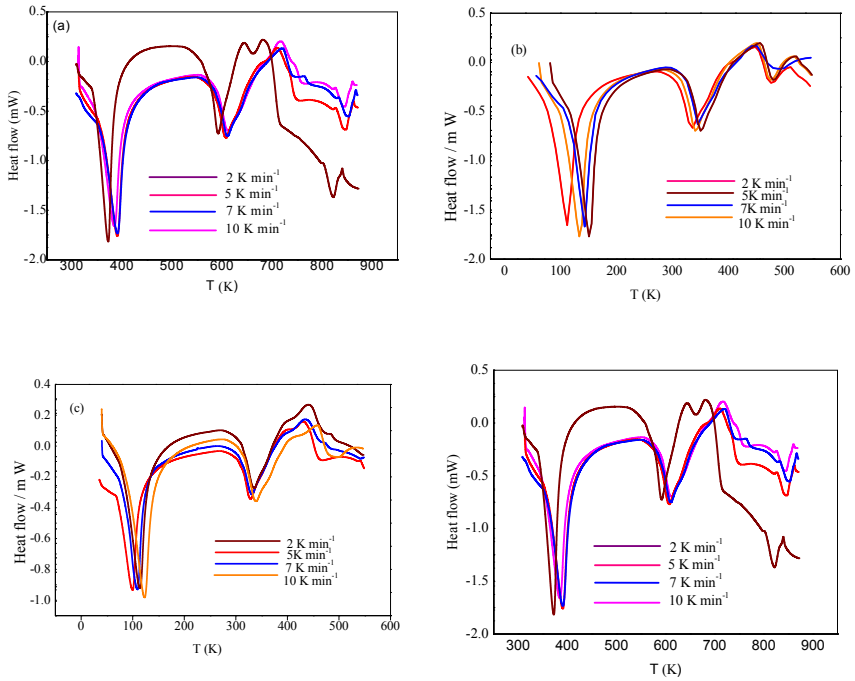

Fig. 4.5 The DSC curves for the thermal decomposition of sample BTO (m= 5.01 ± 0.01 mg) (a), sample BTO_1 (m_1= 5.01 ± 0.02 mg) (b), sample BTO_2 (m_2= 5.01 ± 0.01 mg) (c), sample BTO_3 (m_3= 5.01 ± 0.02 mg) (d) at different β in N_2 (50 mL min^{-1}).

DSC technique was used for the elucidation of kinetics of thermal decomposition of doped and undoped sample. Each sample of ~5 mg was weighed in an aluminium pan (6 mm in diameter and 2.5 mm in depth). A reference sample was made under the similar conditions. This method measures the difference in the amount of heat supplied to the examined sample and reference sample when both are subjected to the controlled changes of temperature. Figs. 4.5a, b, c & d respectively show the DSC curves for the thermal decomposition of BTO from RT–873 K and K^+ doped BTO samples (sample BTO_1,

BTO_2 & BTO_3) in an atmosphere of N_2 (with a flow rate of 50 mL min^{-1}) at a heating rates of 2, 5, 7, and 10 K min^{-1}. These calorimetric investigations indicate that many endothermic transformations takes place in both doped and undoped samples. The DSC curves of both the samples were separated into five reaction process. The reaction below 500 K corresponds to the dehydration of four moles of water associated with BTO. Low temperature decomposition of sample BTO and doped samples occur within the temperature region 550-650 K, third stage of decomposition, *i.e.*, complete decomposition of oxalate occurs within the temperature range of 523-753 K. The evolution of entrapped CO_2 occurs within the temperature range 753-873 K. Finally the formation of $BaTiO_3$ occurs in the temperature range 893-1023 K. It was noticed from the DSC curves that the curves are shifted towards right with increasing the value of β. At a β value of 2 K min^{-1} the DSC curves for both the sample depicts the intermediate stages. The α-T curve (Fig. 4.6) shows the multistep thermal decomposition reaction for both pure and doped barium titanyl oxalates. The α-T curve for BTO (Fig. 4.6a) shows five steps while the α-T curves for BTO_1, BTO_2 and BTO_3 show six steps goes through more complex reaction pathways during the decomposition reaction. The physico-geometrical kinetic behavior and the complex multistage reaction mechanism under linear and non-isothermal condition were illustrated through kinetic analysis using the kinetic deconvolution method.

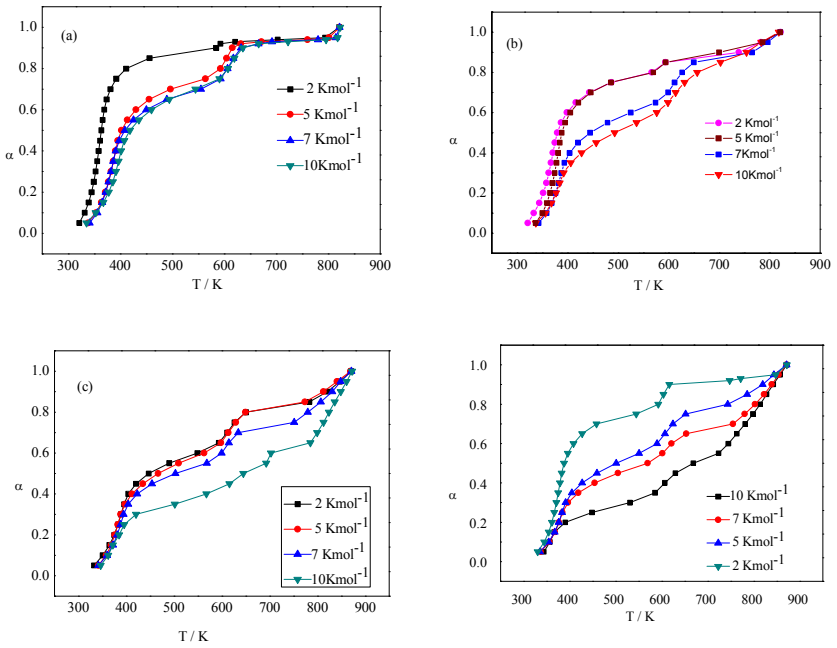

Fig. 4.6 *α–T* curve for the thermal decomposition of BTO (a), BTO_1 (b), BTO_2 (c) and BTO_3 (d) at different β in N_2 (50 mL min^{-1}).

4.3.3 Kinetic behavior

The kinetic analysis of solid state decomposition is described by two functions, one of the reaction temperature and another of the extent of conversions *i.e.* k(T) and $f(\alpha)$ respectively. The mathematical equations used to model kinetic reactions generally take the form of

$$\frac{d\alpha}{dt} = k(T) f(\alpha) \tag{4.2}$$

Where t is the time and T the temperature and α is the extent of conversion, which can be determined from the DSC as a fractional heat release. In general $k(T)$ is described by an Arrhenius equation:

$$k(T) = Ae^{-E_a/RT} \tag{4.3}$$

$$\frac{d\alpha}{dt} = Ae^{(-E_a/RT)} f(\alpha) \tag{4.4}$$

Where *α, A, E_a, and R* are the fractional reaction, Arrhenius pre exponential factor, apparent activation energy, and the gas constant respectively. The kinetic model function *f(α)* proposed is the physico-geometrical reaction mechanism of the reaction.

Kinetic analysis of thermal decomposition of BTO and doped BTO was executed with DSC data taken under linear non-isothermal heating program at different values of β: 2, 5, 7 and 10 K min^{-1}. Heat flow (dQ/dt) by the reaction and overall heat of reaction obtained from the experimentally resolved DSC curve after subtracting the baseline. The overall reaction rate can be expressed as

$$\frac{d\alpha}{dt} = \left(\frac{dQ}{dt}\right)\frac{1}{Q} \tag{4.5}$$

DSC curves for the thermal decomposition of BTO and doped BTO are resulted through five component processes such as dehydration, formation of carbonate, decomposition of oxalate ligand, evolution of entrapped CO_2 and formation of barium titanate. The direct application of the kinetic equation and the optimization of the composition of the reactant mixtures and the kinetic parameters of the respective reaction steps known as kinetic deconvolution, is a simple and rapid mathematical procedure of peak fitting for the deconvolution

of partially overlapped thermal decomposition processes of solids. The deconvolution of the kinetic rate data determined *via* DSC into the initial and established reaction stages should enable the discussion of the kinetics of the reaction stages from the physico-geometrical reaction mechanism, the different reaction stages were approximately treated as kinetically independent. Thus, the different partially overlapping reaction stages were separated through the mathematical deconvolution in order to elicit the kinetic behaviour of the respective reaction. The overall process of the thermal decomposition is composed of *n* independent kinetic processes, is expressed by the summation of the respective kinetic processes *i* by considering their contribution c_i, the following cumulative kinetic equation can be applied [45-52].

$$\frac{d\alpha}{dt} = \sum_{i=1}^{n} c_i A_i \exp\left(\frac{-E_{a,i}}{RT}\right) f_i\left(\alpha_i\right) \tag{4.6}$$

$$\text{with} \sum_{i=1}^{n} c_i = 1 \quad \text{and} \sum_{i=1}^{n} c_i \alpha_i = \alpha$$

where *n* and *c* are the number of component steps and the contribution ratio of each reaction step to the overall process, respectively and the subscript *i* denotes each component reaction step. The contribution c_{endo} and c_{exo} can be defined as

$$c_{endo} = \frac{Q_{endo}}{Q} < 0 \quad \text{and} \quad c_{exo} = \frac{Q_{exo}}{Q} > 0 \tag{4.7}$$

where Q_{endo} and Q_{exo} are the heats of endothermic and exothermic process respectively.

The kinetics of each component process of the overall reaction can be characterized by optimizing all the kinetic parameters in equation (4.6) using nonlinear least-squares analysis. In order to predict the physico-geometrical reaction mechanism, empirical kinetic model functions such as phase-boundary-controlled model, *RO (n)* [53] and the nucleation and growth-type model, *JMA(m)* were employed [54, 55].

$$RO\ (n): f(\alpha) = n(1-\alpha)^{1-1/n} \tag{4.8}$$

$$JMA\ (m): f(\alpha) = m(1-\alpha)\left[-ln(1-\alpha)\right]^{1-1/m} \tag{4.9}$$

where *n* and *m* are the kinetic exponents.

By allowing the non-integral values for the kinetic exponents in both equations (4.8) & (4.9), possible reaction mechanisms for each component process can be found. For both the samples, BTO and doped samples, *RO* (*n*) and *JMA (m)* functions with $n \approx 1$ can be utilized.

The Kissinger-Akahira-Sunose (KAS) [56] method (Eq. 4.10) is a possible method to determine the apparent activation energy for the overall reaction from the DSC curves recorded at different β:

$$\ln\left[\beta/T^2\right] = \ln\left[\frac{AR}{g(\alpha)Ea}\right] - \frac{Ea}{RT} \tag{4.10}$$

The plots of $ln[\beta/T^2]$ *versus* T^{-1}, E_a and A can be obtained from the slope and intercept respectively. The isoconversional plots indicate a linear relationship irrespective of α and this was observed for samples with different β values (Fig. 4.7).

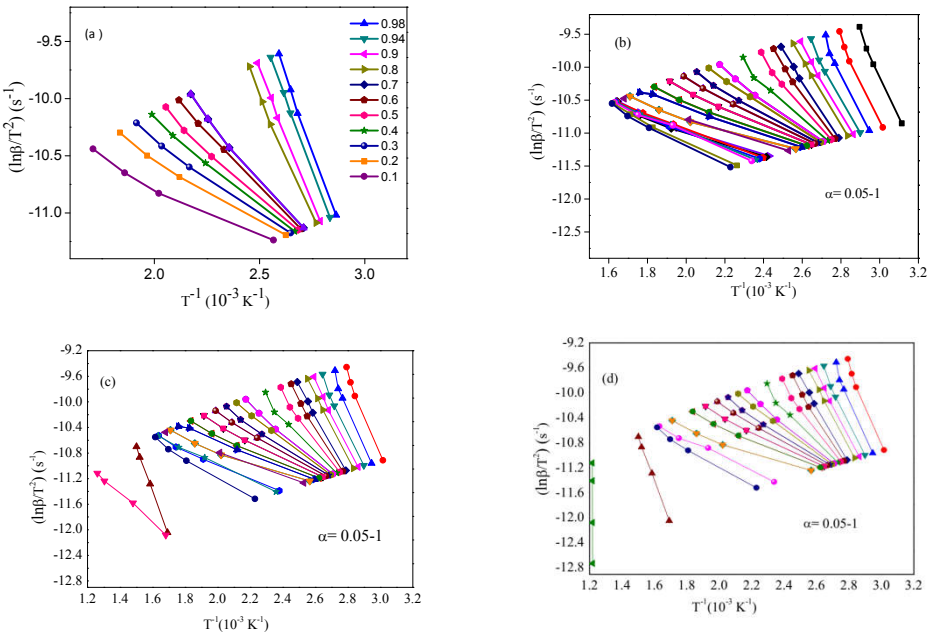

Fig. 4.7 Typical linear least-squares plot of KAS method for the samples, BTO (a), BTO_1 (b), BTO_2 (c) and BTO_3 (d).

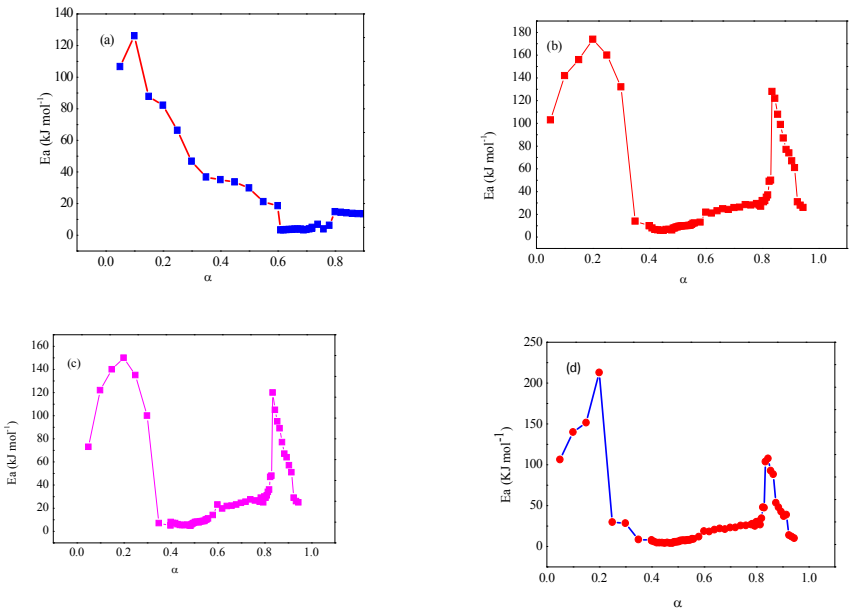

Fig. 4.8 The plot of E_a *vs* α for the samples BTO (a), BTO_1 (b), BTO_2 (c), BTO_3 (d)

The variation of the apparent E_a values as a function of α was not almost similar for the prepared samples (Fig. 4.8). For the sample BTO, although a small deviation of the slope of the KAS plot was observed during the initial stage, the E_a value was found to decrease from 055.83 to 039.80 kJ/mol ($0.05 \leq \alpha \leq 0.6$) approximately. In the decomposition part of the reaction, the average values of E_a was found approximately 119.58 ($0.61 \leq \alpha \leq 0.92$), 179.97($0.92 \leq \alpha \leq 0.944$) and 041.34 kJ/mol ($0.95 \leq \alpha \leq 0.99$) respectively. While the apparent E_a values for the sample BTO_1 was 111.37 kJ/mol ($0.05 \leq \alpha \leq 0.4$) which decreases to 062.21 kJ/mol ($0.485 \leq \alpha \leq 0.56$), 158.01 ($0.58 \leq \alpha \leq 0.78$), 266.12 ($0.785 \leq \alpha \leq 0.83$), 350.31 ($0.835 \leq \alpha \leq 0.945$) and 075.66 kJ/mol respectively. For the sample BTO_2 it was 094.00 kJ/mol

(0.05 ≤ α ≤ 0.4) which was found decreased to 054.80 kJ/mol (0.485 ≤ α ≤ 0.56, 131.30 (0.58 ≤ α ≤0.78), 253.00 (0.785 ≤ α ≤ 0.83), 335.00 (0.835 ≤ α ≤ 0.945) and 067.08 kJ/mol respectively. For the sample BTO_3 it was 085.63 kJ/mol (0.05 ≤ α ≤ 0.4) which was found decreased to 043.31 kJ/mol (0.485 ≤ α ≤ 0.56, 114.92 (0.58 ≤ α ≤0.78), 236.07(0.785 ≤ α ≤ 0.83), 325.68 (0.835 ≤ α ≤ 0.945) and 053.98 kJ/mol respectively. This indicates that the doped samples BTO_1, BTO_2 and BTO_3 which made large deviation to the slope of the KAS plot and the contribution of doping to the overall kinetics is a plausible explanation for this variation in E_a.

The initial values of the kinetic parameters were determined through a formal kinetic analysis of the kinetic data, first subjected to a statistical deconvolution [57, 58] using Weibull function. The number of component steps for both samples are obtained through kinetic deconvolution of DSC peaks. After setting all initial values of kinetic parameters (Table 4.2) for each reaction stage, a parameter optimization was performed to minimize F (Eq. 4.11), defined as the squared sum of the difference between the experimental kinetic data $(d\alpha/dt)_{exp}$ *versus* time and calculated kinetic data $(d\alpha/dt)_{cal}$ *versus* time [59-62].

$$F = \sum_{j=1}^{n} \left[\left(\frac{d\alpha}{dt} \right)_{\exp,j} - \left(\frac{d\alpha}{dt} \right)_{cal,j} \right]^2 \tag{4.11}$$

where n is the number of data points

Table 4.2 Initial kinetic parameters used for the thermal decomposition of samples under linear non-isothermal conditions.

Sample	i	C_i	E_{ai}(kJ/ mol)	A_i (s^{-1})	f_i (α)
BTO	1	0.560	055.83	6.34×10^{21}	R (n);n=1
	2	0.113	039.80	2.33×10^{6}	R (n);n=0.99
	3	0.250	119.58	1.78×10^{16}	R (n);n=1.1
	4	0.022	179.97	1.15×10^{25}	JMA (m);m=1
	5	0.055	041.34	5.71×10^{14}	JMA (m);m=1.2
BTO_1	1	0.350	111.37	1.05×10^{28}	R (n);n=1
	2	0.090	062.21	1.15×10^{3}	R (n);n=0.98
	3	0.060	158.01	1.50×10^{4}	R (n);n=1.01
	4	0.240	266.12	4.60×10^{15}	JMA (m);m=1
	5	0.050	350.31	1.01×10^{19}	JMA (m);m=1.02
	6	0.210	075.66	2.49×10^{15}	JMA (m);m=0.9
BTO_2	1	0.400	094.00	9.40×10^{24}	R (n);n=1.3
	2	0.080	054.80	6.60×10^{3}	R (n);n=0.99
	3	0.078	131.30	4.10×10^{3}	R (n);n=1
	4	0.230	253.00	6.09×10^{13}	JMA (m);m=1
	5	0.052	335.00	1.92×10^{18}	JMA (m);m=1.2
	6	0.160	067.08	7.40×10^{21}	JMA (m);m=0.9
BTO_3	**1**	**0.400**	**085.63**	**1.85×10^{28}**	**R (n);n=1**
	2	0.085	043.31	2.70×10^{5}	R (n);n=0.995
	3	0.075	114.92	1.70×10^{3}	R (n);n=1.2
	4	0.220	236.07	1.52×10^{15}	JMA (m);m=1
	5	0.060	325.68	9.64×10^{18}	JMA (m);m=1.3
	6	0.160	053.98	5.30×10^{20}	JMA (m);m=0.98

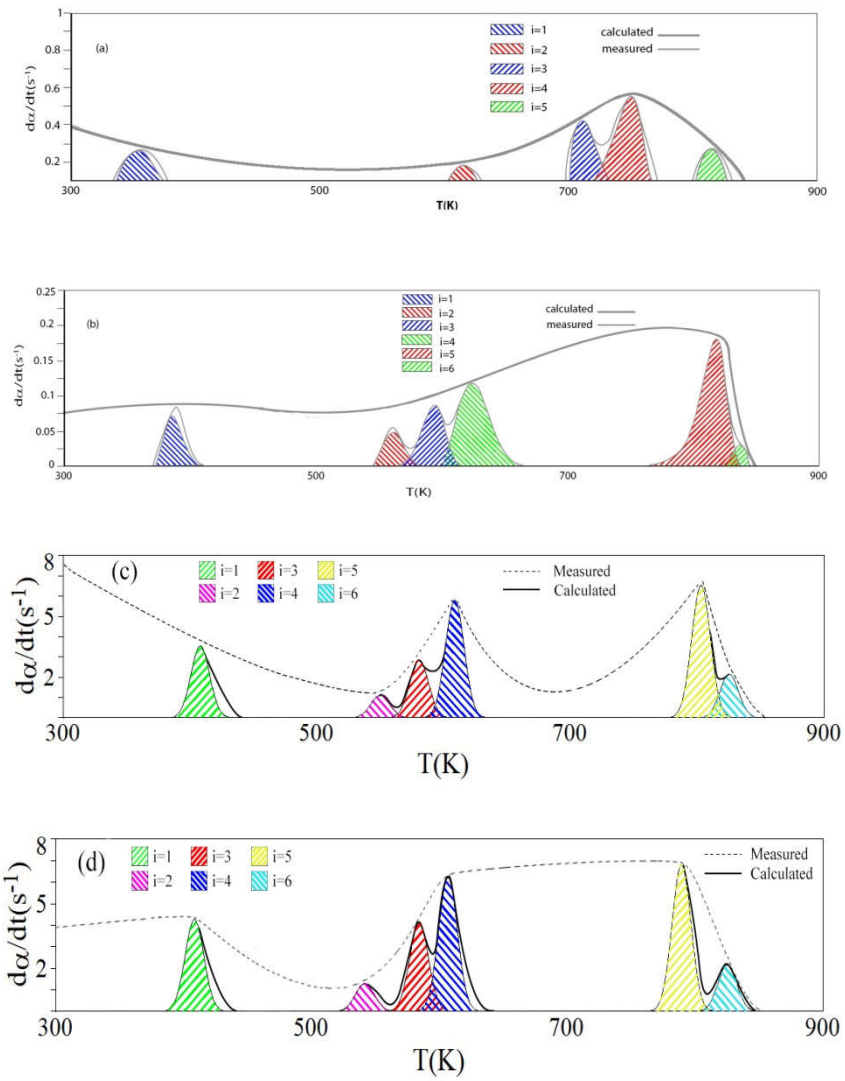

Fig. 4.9 Typical results of kinetic deconvolution of the thermal decomposition of the samples BTO (a), BTO_3 (b), BTO_2 (c) and BTO_1 (d) under linear non-isothermal condition at β= 5 K min^{-1}

Formation of barium titanate from barium titanyl oxalate *via* thermal decomposition reaction can be brought through the following scheme (Eq. 4.12-4.16):

$$BaTiO(C_2O_4)_2.4H_2O \xrightarrow{393-453K} BaTiO(C_2O_4)_2 + 4H_2O \quad (4.12)$$

$$BaTiO(C_2O_4)_2 \xrightarrow{453-523K} Ba_2Ti_2O_2(C_2O_4)_3.CO_3 + CO \quad (4.13)$$

$$Ba_2Ti_2O_2(C_2O_4)_3.CO_3 \xrightarrow{523-723K} Ba_2Ti_2O_5CO_3(CO_2) + 2CO_2 + 3CO \quad (4.14)$$

$$Ba_2Ti_2O_5CO_3(CO_2) \xrightarrow{723-873K} Ba_2Ti_2O_5CO_3 + CO_2 \quad (4.15)$$

$$Ba_2Ti_2O_5CO_3 \xrightarrow{873-1023K} 2BaTiO_3 + CO_2 \quad (4.16)$$

Barium titanate is formed from BTO through the evolution of H_2O, CO and CO_2. Initial low temperature reaction is known as the dehydration and low temperature decomposition occurs and forming the carbonate intermediate. Succeeding steps involves the decomposition of carbonate intermediate with the evolution of CO and CO_2.

Fig. 4.9 shows the result of the kinetic deconvolution analysis of the thermal decomposition of the samples BTO and doped samples BTO_1, BTO_2 and BTO_3 on the basis of equation (4.6) after establishing the initial values of the kinetic parameters through mathematical deconvolution and the subsequent formal kinetic analysis of each resolved reaction step [63]. Under linear non isothermal conditions, for the sample BTO the overall reaction was resolved into five steps (Fig.

4.9a) and that of doped samples into six overlapping reaction steps (Fig. 4.9b, c & d). The first low temperature reaction observed is considered as the dehydration reaction [64, 65]. Both undoped and doped samples take one independent step for the removal of water molecules, whereas in the high temperature reaction, both go through more complex pathways.

The average values of the kinetic parameters optimized for each reaction stage at different β values are summarized in Table 4.3. For each resolved reaction steps, the value of E_a calculated for each reaction step are nearly in agreement with the respective corresponding values estimated by the KAS plots for the overall reaction under non isothermal conditions [66]. The data from thermal analysis curves in the decomposition range $0.05<\alpha<1$ were used to determine the kinetic parameters of the process, the integral method of a linear form of modified Coats and Redfern equation

$$\ln\left[\frac{g(\alpha)}{T^2}\right] = \ln\left(\frac{AR}{\beta E}\right) - \frac{E_a}{RT} \tag{4.17}$$

The *g(α),* the integral form of the conversion function which depends on the kinetic model of the decomposition reaction. If the correct form of *g(α)* is used, the plot of $\ln(g(\alpha)/T^2$ against *1/T* should give a straight line. For the sample BTO, the straight line plot with suitable model and regression values are represented in Figs. 4.10. 4.11, 4.12 & 4.13 represents typical model fitting least-squares plots for the samples BTO_1, BTO_2 & BTO_3.

For BTO the required average values of E_a for each resolved steps are 56.30 ±0.01 (i=1), 40.1 ± 0.2 (i=2), 120.5 ± 0.1 (i =3), 180.21 ± 0.09 (i=4) and 40.92 ± 0.01 kJ/mol (i=5) respectively.

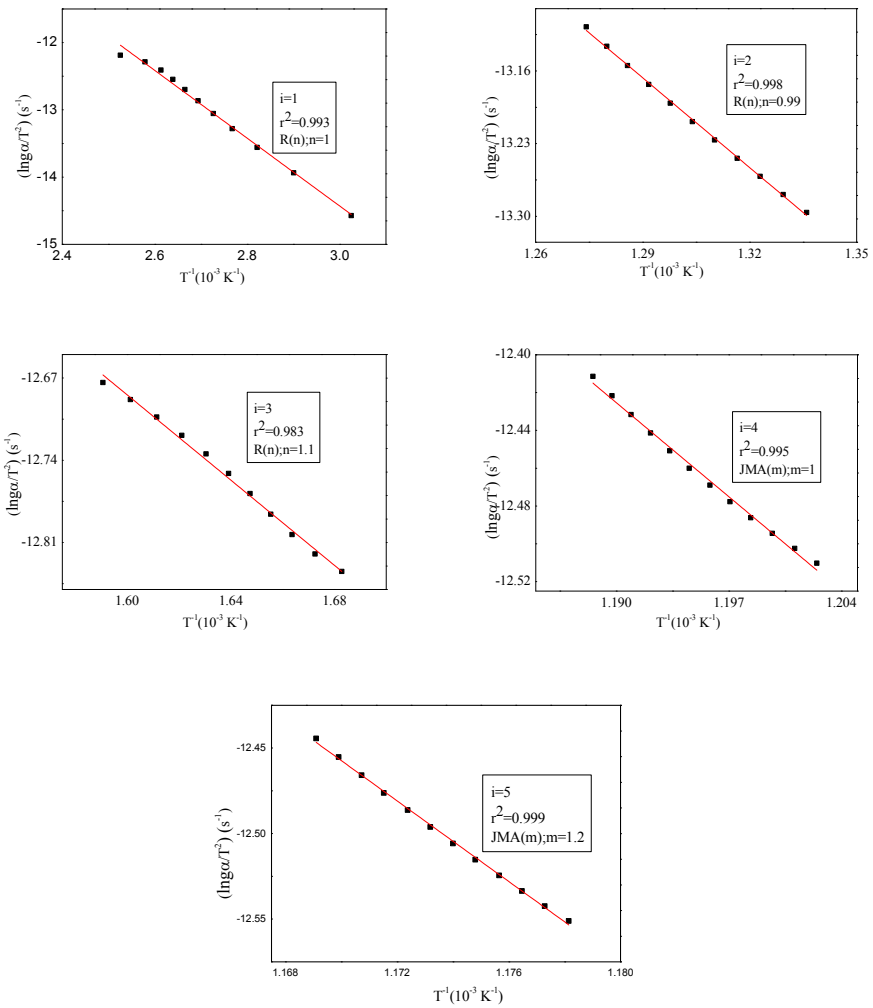

Fig. 4.10 Typical model fitting least-squares plot for the different steps of thermal decomposition of BTO

For the sample BTO_1, thermal decomposition occurs *via* more complex reaction strategies *i.e.*, through six overlapping stages. The average values of energy needed for the respective stages are 111.37 ± 0.11 (*i*=1), 62.21 ± 0.04 (*i*=2), 158.01 ± 0.21 (*i*=3), 266.12 ± 0.08 (*i*=4), 350.31 ± 0.03 (*i*=5) and 76.66 ± 0.31 kJ/mol (*i*=6) respectively.

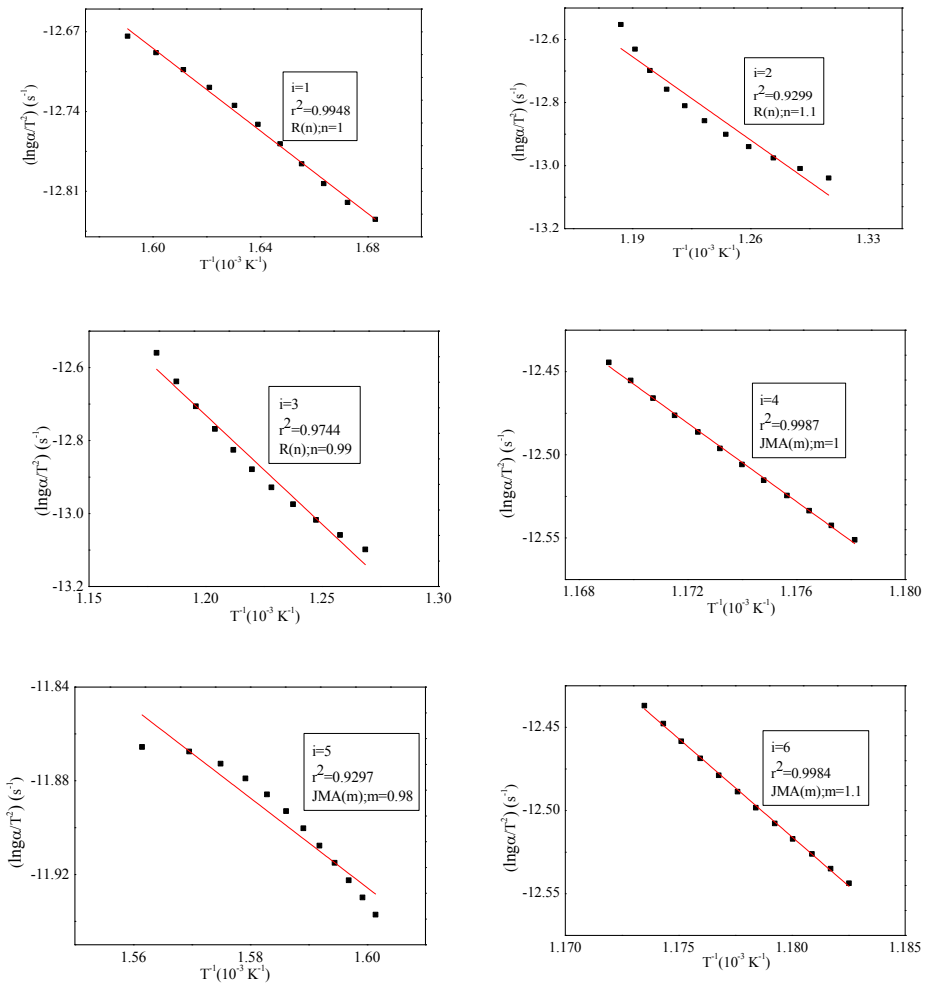

Fig. 4.11 Typical model fitting least-squares plot for the different steps of BTO_1

For BTO_2, the average values of energy needed for the respective steps are 94.01 ± 0.02 (*i*=1), 54.80 ± 0.01 (*i*=2), 131.30 ± 0.02 (*i*=3), 253.01 ± 0.03 (*i*=4), 335.02 ± 0.03 (*i*=5) and 67.08 ± 0.02 kJ/mol (*i*=6) respectively.

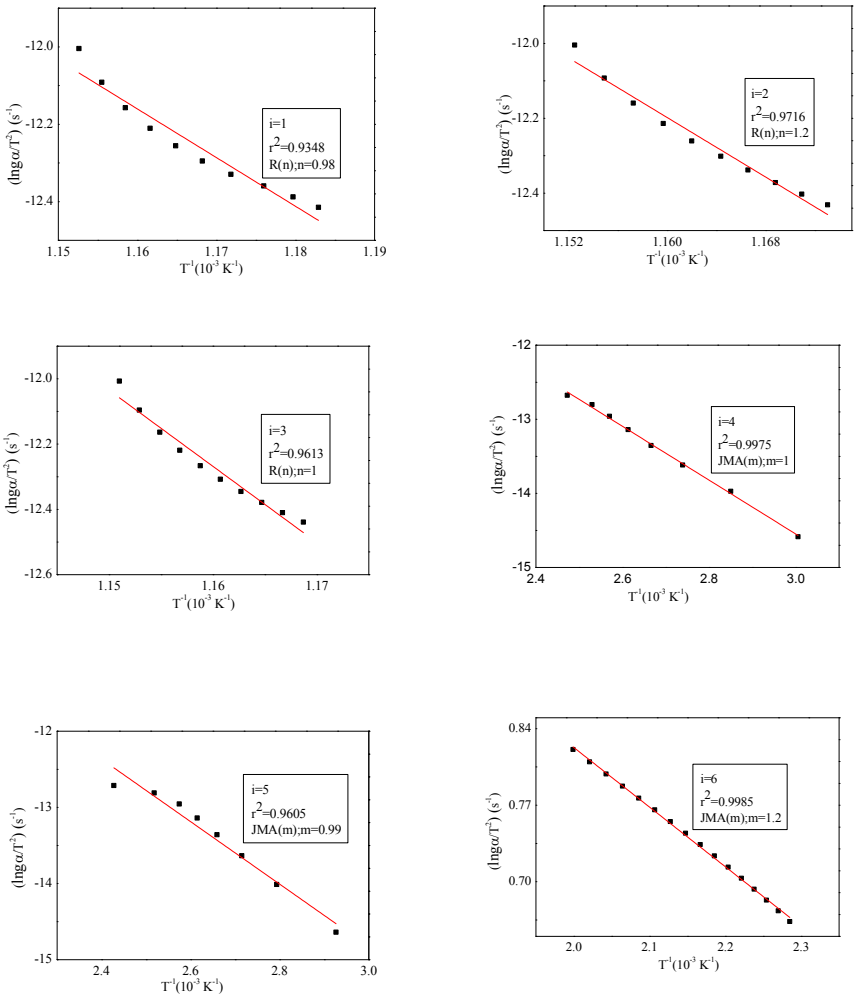

Fig. 4.12 Typical model fitting least-squares plot for the different steps of BTO_2

For BTO_3, the average values of energy needed for the respective steps are 85.71 ± 0.02 (*i*=1), 44.12 ± 0.05 (*i*=2), 115.23 ±

0.02 (*i*=3), 236.81 ± 0.04 (*i*=4), 326.43 ± 0.03 (*i*=5) and 55.14 ± 0.44 kJ/mol (*i*=6) respectively

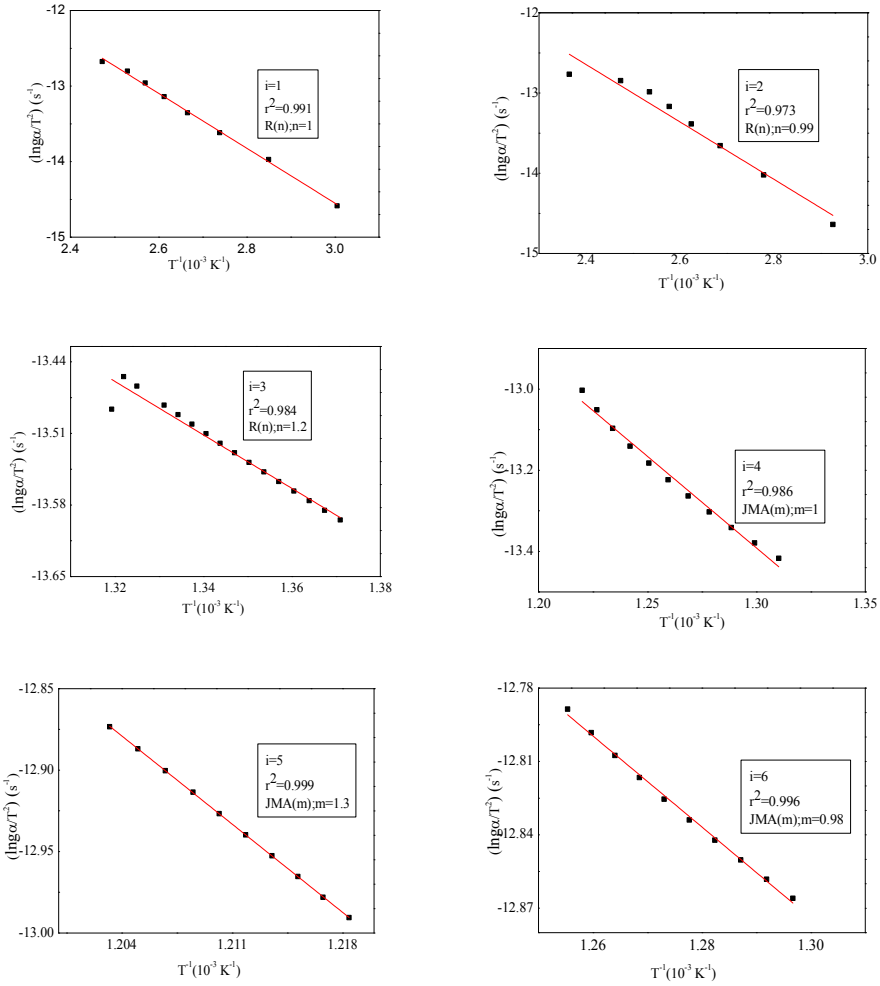

Fig. 4.13 Typical model fitting least-squares plot for the different steps of BTO_3

The physico-geometrical behaviour of each sample was best described empirically by the *RO (n)* and *JMA (m)* kinetic model functions as shown in the Table 4.3.

Table 4.3 Average kinetic parameters optimized for each reaction step of the thermal decomposition of samples under linear non-isothermal conditions.

Sample	i	C_i	E_{ai} (kJ mol^{-1})	A_i (s^{-1})	$f_i(\alpha)$;RO(n) JMA(m)
BTO	1	0.57±0.04	56.30 ± 0.01	6.34±0.09 x 10^{21}	n=1.0± 0.1
	2	0.13±0.02	40.10 ± 0.20	2.33±0.05 x 10^{6}	n=0.99±0.02
	3	0.22±0.23	120.50 ±0.10	1.78 ±0.04 x 10^{16}	n=1.1± 0.4
	4	0.02±0.12	180.21±0.09	1.15±0.08 x 10^{25}	m=1.00± 0.13
	5	0.06±0.01	40.92 ± 0.01	5.71 ±0.02 x 10^{14}	m=1.2± 0.1
BTO_1	1	0.35± 0.02	111.37± 0.11	1.05± 0.21 x 10^{28}	n=1
	2	0.09± 0.11	062.21± 0.04	1.15± 0.11 x 10^{3}	n=1.10± 0.11
	3	0.06± 0.07	158.01± 0.21	1.50± 0.09 x 10^{4}	n=0.99± 0.02
	4	0.24± 0.01	266.12± 0.08	4.60± 0.05 x 10^{15}	m=1
	5	0.05± 0.04	350.31± 0.05	1.01± 0.01 x 10^{19}	m=0.98± 0.01
	6	0.21± 0.41	075.66± 0.31	2.49± 0.02 x 10^{15}	m=1.1± 0.2
BTO_2	1	0.40± 0.21	094.01± 0.02	9.40± 0.31 x 10^{24}	n=0.98± 0.10
	2	0.08± 0.11	054.80± 0.01	6.60± 0.08 x 10^{3}	n=1.20± 0.01
	3	0.08± 0.05	131.30± 0.02	4.10 ± 0.41x 10^{3}	n=1
	4	0.23± 0.31	253.01± 0.03	6.09± 0.11 x 10^{13}	m=1.0± 0.1
	5	0.05± 0.09	335.02± 0.01	1.92 ± 0.08x 10^{18}	m=0.99± 0.20
	6	0.16± 0.01	075.66± 0.04	7.40 ± 0.02x 10^{21}	m=1.2± 0.3
BTO_3	1	0.36± 0.00	085.71± 0.02	1.85±0.05 x 10^{28}	n=1
	2	0.08±0.02	044.12± 0.05	2.71±0.01 x 10^{5}	n=0.99± 0.02
	3	0.07±0.05	115.23±0.02	1.73 ±0.02x 10^{3}	n=1.20± 0.03
	4	0.23±0.07	236.81± 0.04	1.52 ±0.03x 10^{15}	m=1.0± 0.1
	5	0.04±0.03	326.43± 0.03	9.64 ±0.07x 10^{18}	m=1.3± 0.2
	6	0.22±0.92	055.14± 0.44	5.31 ±0.04x 10^{20}	m=0.98±0.42

It should also be noted that difference in the values of A for the initial and final steps were larger for each of the samples indicating the larger lags of reaction time and temperature.

4.3.4 Morphological Analysis

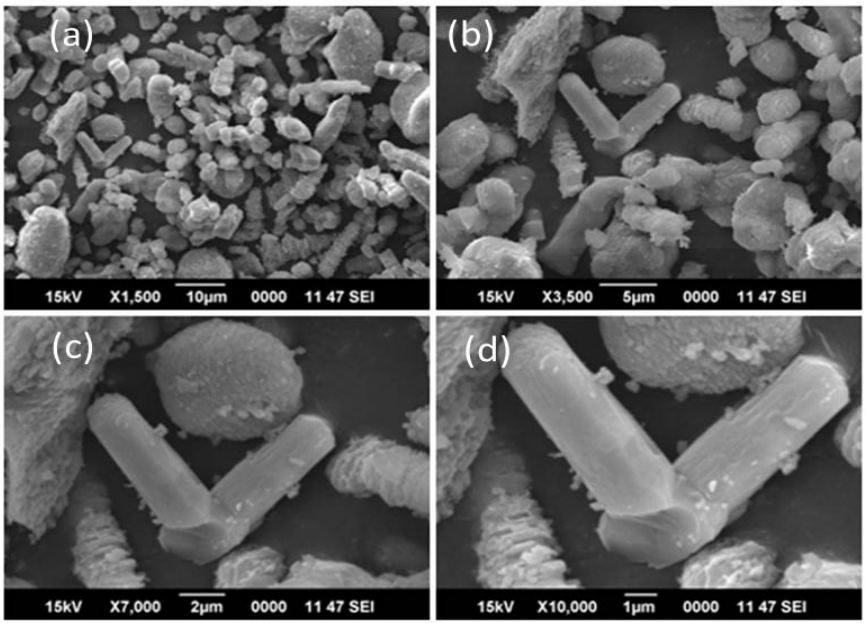

Fig. 4.14 The SEM micrographs showing the surface microstructure of the sample BTO at 10 µm (a), 5 µm (b), 2 µm (c) and 1 µm (d).

Figs. 4.14, 4.15, 4.16 and 4.17 show the SEM images of the BTO and doped BTO, which confirm the bone shaped morphology of BTO having smooth surfaces. Figs. 4.18 & 4.19 exhibit the SEM images of $BaTiO_3$ which was formed by the multistage thermal decomposition of BTO. Bone like morphology of BTO was retained in the decomposed product. Doping with K^+ ion brought slight variation in the bone like morphology of BTO and decomposed product. Doping found to destroy the smoothness of the surfaces. Presence of pores and holes, created by the increased internal gaseous pressure during the process of thermal decomposition of doped BTO depicts the complexity of the reaction upon doping. These holes and pores act as diffusion channels for the removal of CO_2 and water.

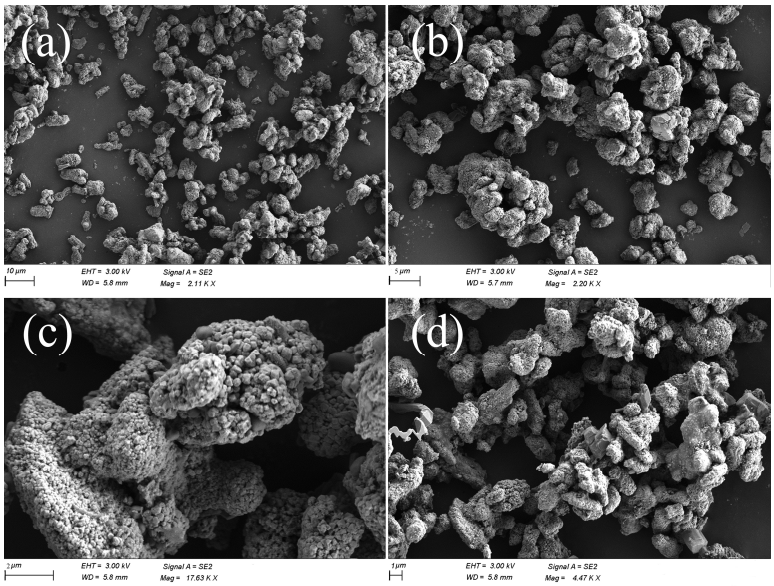

Fig. 4.15 The SEM micrographs showing the surface microstructure of the sample BTO_1 at 10 μm (a), 5 μm (b), 2 μm(c) and 1 μm (d).

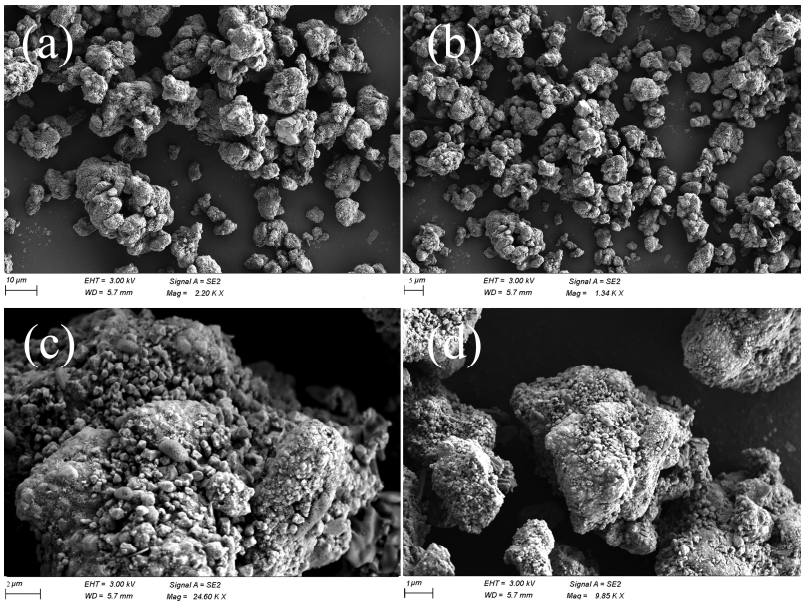

Fig. 4.16 The SEM micrographs showing the surface microstructure of the sample BTO_2 at 10 μm (a), 5 μm (b), 2 μm (c) and 1 μm (d).

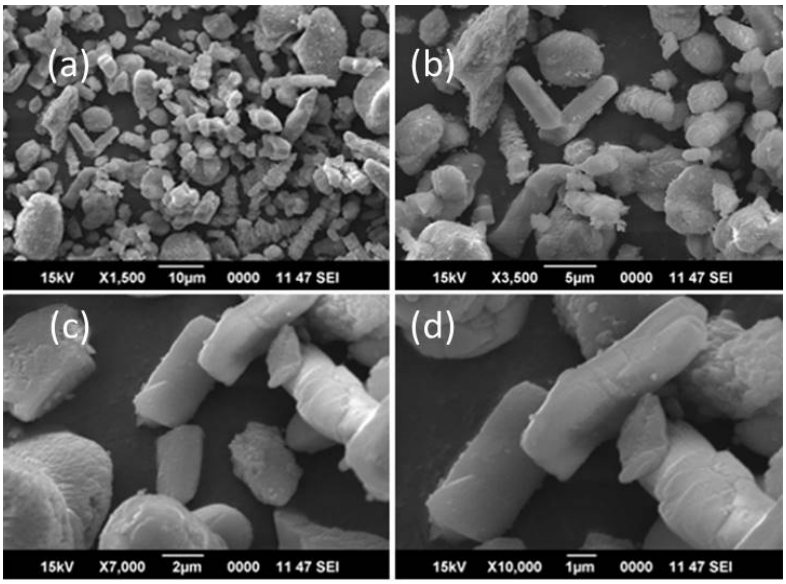

Fig. 4.17 The SEM micrographs showing the surface microstructure of the sample BTO_3 at 10 µm (a), 5 µm (b), 2 µm (c) and 1µm (d).

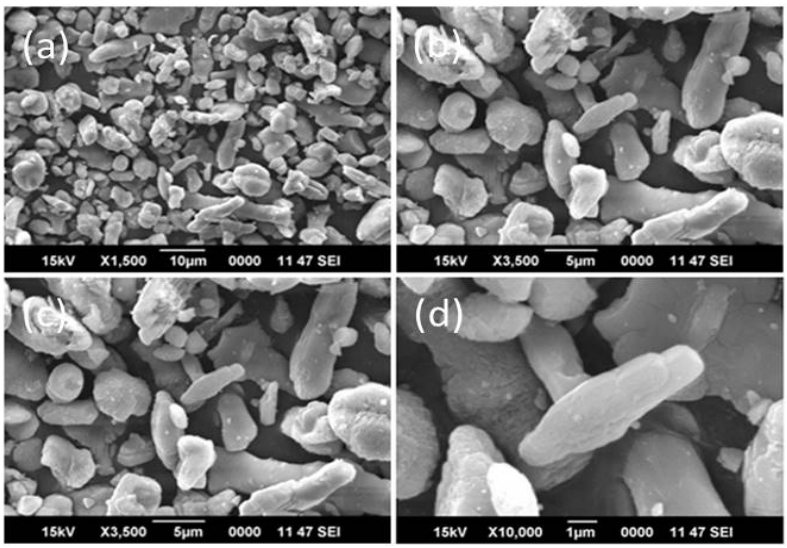

Fig. 4.18 The SEM micrographs showing the surface microstructure of the sample BTO calcined at 1023 K for 1 h at 10 µm (a), 5 µm (b), 2 µm (c) and 1 µm (d).

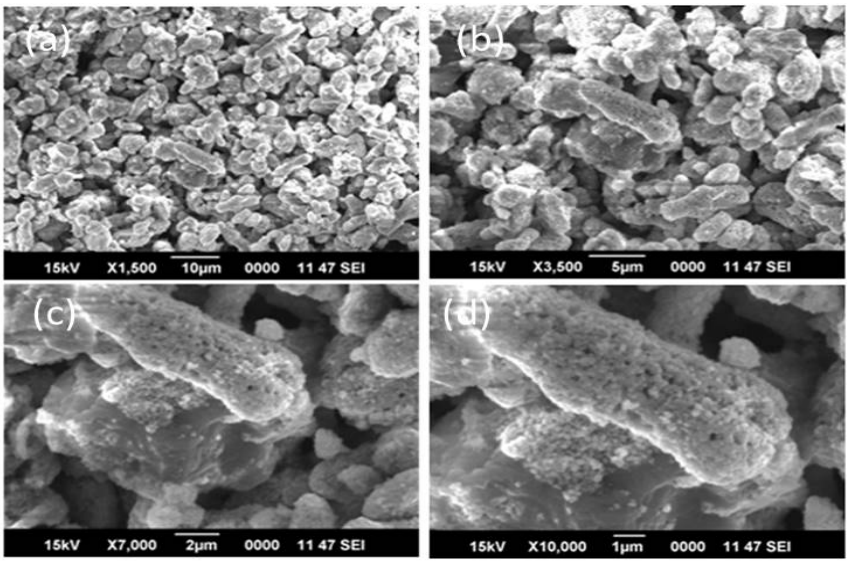

Fig. 4.19 The SEM micrographs showing the surface microstructure of the sample BTO_3 calcined at 1023 K for 1 h; 10 μm (a), 5 μm (b),2 μm (c) and 1 μm (d).

Figs. 4.20 & 4.21 show the TEM images of the $BaTiO_3$ and doped $BaTiO_3$ calcined at 1023 K for 1h. The estimated particle size of the both doped and undoped BT from the TEM image is in the range of 5-170 nm. The TEM image reveals that the particle exhibits as nano sphere having uniform grain size distribution and these nano spheres were underwent oriented growth to form the bone shaped morphology of barium titanate as shown in Figs. 4.18 and 4.19.

TEM image of K^+ doped $BaTiO_3$ shows a small depression in the nano spheres, which points out the complexity of formation of final product upon doping. Formation of cracks and holes in the surface of the product indicates the formation of surface product layer during the early stages of the reaction. As the temperature increases, there occurs change in the reaction condition at the reaction interface, leading to the

complexity of the process. The cracks and holes act as the channels for the diffusional removal of gaseous products such as H_2O, CO_2, CO, *etc*. Thus the synthesized $BaTiO_3$ nanoparticles can be used for the wide range of applications in the electronic as well as opto-electronic field.

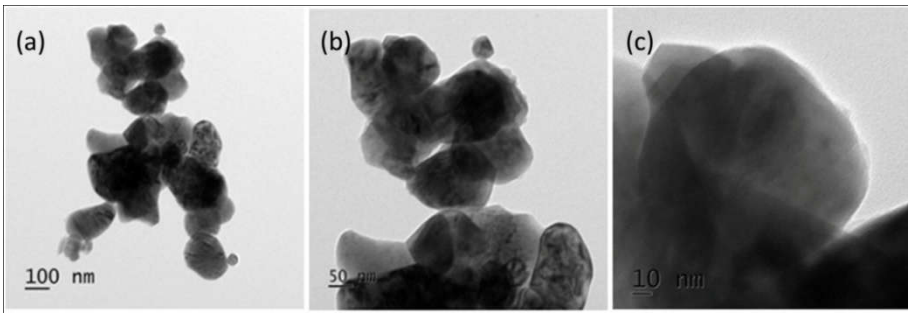

Fig. 4.20 The TEM images of the sample BTO calcined at 1023 K for 1 h at 100 nm (a), 50 nm (b) and 10 nm (c).

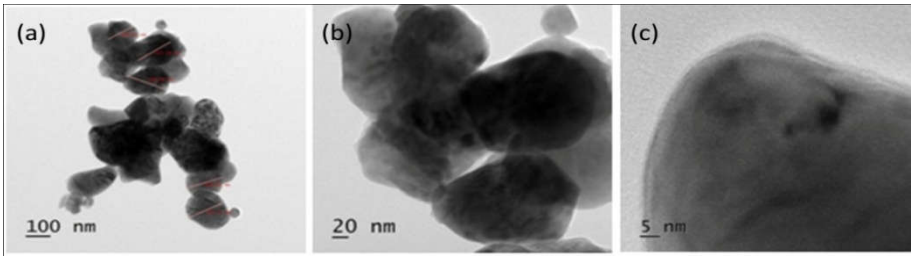

Fig. 4.21 The TEM images of the sample BTO_3 calcined at 1023 K for 1 h at 100 nm (a), 20 nm (b) and 5 nm (c)

Figs. 4.22a & b displays the SEAD pattern of BTO and BTO_3. These images confirm the nano semi crystalline nature of the synthesized barium titanate. Doping does not affect the semi crystalline properties of the synthesised $BaTiO_3$.

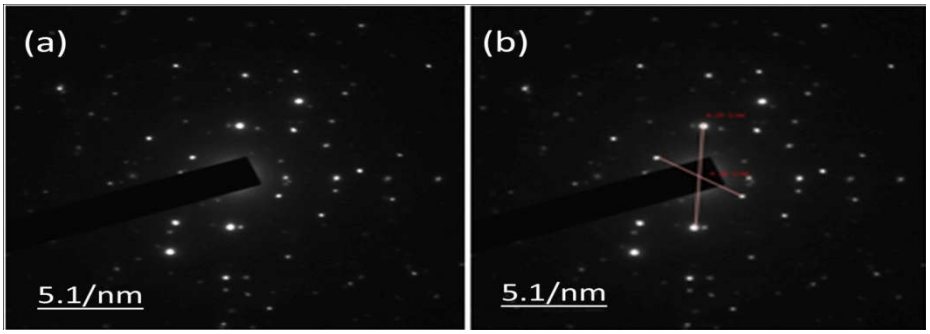

Fig. 4.22 SAED pattern of BTO (a) and BTO_3 (b)

4.4 Conclusion

The effect of K^+ ion doping on the thermal decomposition kinetics of the BTO was investigated using kinetic deconvolution method. The kinetic parameters and reaction model were revealed under linear non isothermal condition using the DSC technique in N_2 atmosphere. Both the samples went through multistage reaction pathways. BTO takes five steps for the formation of barium titanate, whereas K^+ doped BTO samples go through six steps. Doping of K^+ increases the complexity as well as activation energy of the decomposition reaction and hence enhances the thermal stability of BTO. The physico-geometrical reaction behaviours of both the samples were best described empirically by *RO (n)* and *JMA (m)* models. Morphological analysis disclosed that the synthesized nano spheres undergo oriented crystal growth forming the micro dimensional bone shaped $BaTiO_3$. The estimated size of the spheres is in the range 5-170 nm. The SAED pattern of both samples of doped and undoped BTO exposed the nano semi crystalline nature. The XRD pattern reveals the transformation of cubic phase of barium titanate in to tetragonal structure with increase in temperature.

4.5 References

1 Vyazovkin S, Wight CA. Isothermal and nonisothermal reaction kinetics in solids: in search of ways toward consensus. J. Phys. Chem. 1997;101:8279–84.

2. Brown ME, Dollimore D, Galwey AK. Reactions in the solid state, comprehensive chemical kinetics. Elsevier, Amsterdam. 1980;22: 340.

3. Vyazovkin S, Wight CA. Isothermal and nonisothermal kinetics of thermally stimulated reactions of solids. Int. Rev. Phys. Chem. 1998;17:407–33.

4. Galwey AK. Is the science of thermal analysis kinetics based on solid foundations? : a literature appraisal. Thermochim. Acta. 2004;413:139–83.

5 Brown ME, Dollimore D, Galwey AK. Comprehensive chemical kinetics, reactions in the solid state, Chapter 4: Decomposition reactions of solids. Ed. C.H. Bamford and C.F.H. Tipper, Elsevier, Amsterdam. 1980;22:218-23.

6 Masó N, Beltrán H, Cordoncillo E, Sinclair DC, West AR. Polymorphism and dielectric properties of Nb-doped. $BaTiO_3$. J. Am. Ceram. Soc. 2008;91:144-50

7 Hagemann HJ, Ihrig H. Valence change and phase stability of 3d-doped $BaTiO_3$ annealed in oxygen and hydrogen. Phys. Rev. B. 1979;20:3871-78.

8 L'vov BV. Kinetics and mechanism of thermal decomposition of nickel, manganese, silver, mercury and lead oxalates. Thermochim. Acta. 2000;364:99−109.

9 Kullyakool S, Danvirutai C, Siriwong K, Noisong P. Determination of kinetic triplet of the synthesized $Ni_3(PO_4)_2{\cdot}8H_2O$ by non-isothermal and isothermal kinetic methods. J. Therm. Anal. Calorim. 2014;115:1497–507.

10 Duval C. Inorganic thermogravimetric analysis. 2nd Ed. Elsevier. Amsterdam. 1963.

11 Li Z, Fan HQ. Polaron relaxation associated with the localized oxygen vacancies in $Ba_{0.85}Sr_{0.15}TiO_3$ ceramics at high temperatures. J. Appl. Phys. 2009;106:054102.

12 Dollimore D, Griffiths DL, Nicholson D. The thermal decomposition of oxalates. Part II. Thermogravimetric analysis of various oxalates in air and in nitrogen. J. Chem. Soc. 1963;2:2617-23.

13. Rossberg M, Khairetdinov EF, Linke E, Boldyrev VV. Effect of mechanical pretreatment on thermal decomposition of silver oxalate under nonisothermal conditions. J. Solid State Chem. 1982;41:266-71.

14. Dollimore D. The thermal decomposition of oxalates. A review. Thermochim. Acta. 1987;117:331-63.

15. Feldheim DL, Keating CD. Self-assembly of single electron transistors and related devices. J. Chem. Soc. Rev. 1998;27:1-12.

16. Greenberg E, Settle JL, Hubbard WN. Fluorine bomb calorimetry. iv. The heats of formation of titanium and hafnium tetrafluorides. J. Phys. Chem. 1962;66:1345–08.

17 Khawam A, Flanagan DR. Role of isoconversional methods in varying activation energies of solid-state kinetics: I. isothermal kinetic studies. Thermochim. Acta. 2005;429:93-101.

18 Freeberg FE, Hartman KO, Hisatsune IC, Schempf JM. The kinetics of calcium oxalate pyrolysis. J. Phys. Chem. 1967;71:397-402.

19. Gallagher PK, Frank Schrey. Thermal decomposition of some substituted barium titanyl oxalates and its effect on the semiconducting properties of the doped materials. J. Am. Ceram. Soc. 1963;46:567-73.

20 Muraleedharan K, Jose John M, Kannan MP, Abdul Mujeeb VM. Effect of chloride dopant on the kinetics of the thermal decomposition of sodium oxalate. Thermochim. Acta. 2012;537:25–30.

21. Muraleedharan K, Mallikassery JJ, Kannan MP. The effect of pre-heating on the kinetics of the thermal decomposition of pure and chloride and phosphate doped sodium oxalate. Thermochim. Acta. 2013;552:10-14.

22. Dollimore D, Griffiths DL. Differential thermal analysis study of various oxalates in oxygen and nitrogen. J. Therm. Anal. Calorim.1970;2:229-50.

23. Ornran ZA, Mousa MA, Abdel-Fattah AA. Kinetic analysis of thermal decomposition reactions Part IV: Kinetics of formation of

barium titanate in crystalline mixtures of barium carbonate and titanium dioxide. Thermochim. Acta. 1989;145:271-77.

24. Masset PJ. Thermogravimetric study of the dehydration reaction of LiCl H_2O. J. Therm. Anal. Calorim. 2009;96:439–41.

25 Guha BK, Samaddar BN. Niobium doped barium titanate-A chemically processed material with high dielectric constant. Trans. Ind. Cerm. Soc. 1994;53:33-48.

26 Kotlyarchuk A, Klymenko V, Dubovitskaya N, Lobunets T, Shatskikh S, Ragulya A. Doped barium titanate at intermediate stages of synthesis of BTO. Proceedings of the international conference nanomaterials: applications and properties. 2012;1:3.

27 Liu Y, Guan J, Xiao Z, Sun Z, Ma H. Chromium doped barium titanyl oxalate nano-sandwich particles: a facile synthesis and structure enhanced electrorheological properties. J. Mater. Chem. Phys. 2010;122:73-78.

28 Kumar Y, Mohiddon MA, Srivastava A, Yadav KL. Effect of Ni doping on structural and dielectric properties of $BaTiO_3$. J. Eng. Mater. Sci. 2009;16:390-94.

29 Dho J, Hur NH. Magnetic and transport properties of lanthanum perovskites with B site half doping. Solid State Commun. 2006;138:152–56.

30 Vyazovkin S, Wight CA. Kinetics in solids. Annu. Rev. Phys. Chem. 1997;48:125-49.

31 Khawam A, Flanagan DR. Role of isoconversional methods in varying activation energies of solid-state kinetics. Thermochim. Acta. 2005;429:93-101.

32 Otta S, Bhattamisra SD. Kinetics and mechanism of the thermal decomposition of barium titanyl oxalate. J. Therm. Anal. 1994;41:419-33.

33 Deb N. Some heterobimetallic oxalate coordination precursors of lanthanum(III) of the type $M_3[La(C_2O_4)_3(H_2O)m]_2.nH_2O$ (M=Mn(II), Co(II), Ni(II) and Cu(II)) an investigation on the solidstatepyrolytic decomposition. J. Therm. Anal. Calorim. 2012;107:561–71.

34 Nakamoto K. Infrared spectra of inorganic and co-ordination compounds. 2nd Ed. NewYork, Wiley.1969;245.

35 Hammer M, Monty C, Endriss A, Hoffmann MJ. Correlation between surface texture and chemical composition in undoped, hard

and soft piezoelectric PZT ceramics. J. Am. Ceram. Soc. 1998;81: 721-24.

36 Dobal PS, Katiyar RS. Studies on ferroelectric perovskites and bi-layered compounds using microraman spectroscopy. J. Raman Spectrosc. 2002;33:405–23.

37 Wang B, Zhang L. Size effects on structure and Raman spectra of $BaTiO_3$ thin films. Phys. Stat. Sol. 1998;169:57-62.

38 Lee JH, Pontes FM, Leite ER, Longo E, Magnani R, Pisan PS, Varela JA. Effects of post annealing on the dielectric properties of Au/BaTiO /Pt thin film capacitors. J. Mater. Lett. 2004;58:1715-21.

39 Kaiser L, Vaudin MD, Gillen G, Hwang CS, Robins LH, Rotter LD. Growth and characterization of barium titanate thin films prepared by metalorganic chemical vapor deposition. J. Cryst. Growth. 1994;136:1-2.

40 Cho R, Kwun SH, Noh TW, Jang MS. Electrical properties of sol-gel deposited $BaTiO_3$ thin flms on Si (100) substrates. Jpn. J. Appl. Phys. 1997;36:2196-99.

41 Kuo WK, Ling YC. Effects of mono-substituting chelating agents on $BaTiO_3$ prepared by the sol-gel process. J. Mater. Sci. 1994;29:5625-30.

42 Xiao CJ, Jin CQ, Wang XH. Crystal structure of dense nanocrystalline $BaTiO_3$ ceramics. J. Mater. Chem. Phys. 2008;111: 2-3.

43 Bera J, Rout SK. On the formation mechanism of $BaTiO_3$–$BaZrO_3$ solid solution through solid-oxide reaction. J. Mater. Lett. 2005;59:135–38.

44 Bera J, Sarkar D. Formationof $BaTiO_3$ from barium oxalate and TiO_2. J. Electroceram. 2003;11:131-37.

45 Wada T, Koga N. Kinetics and mechanism of the thermal decomposition of sodium per carbonate: role of the surface product layer. J. Phys. Chem. A. 2013;117:1880–89.

46 Wada T, Nakano M, Koga N. Multistep kinetic behaviour of the thermal decomposition of granular sodium per carbonate: hindrance effect of the outer surface layer. J. Phys. Chem. A. 2015;119:9749–60.

47 Koga N, Kasahara D, Kimura T. Aragonite crystal growth and solid-state aragonite-calcite transformation: a physico-geometrical

relationship via thermal dehydration of included water. J. Cryst. Growth. Des. 2013;13:2238–46.

48 Koga N, Yamada S, Kimura T. Thermal decomposition of silver carbonate: phenomenology and physico-geometrical kinetics. J. Phys. Chem. C. 2013;117:326–36.

49 Sanchez-Jimenez PE, Perejon A, Criado JM, Dianez MJ, Perez-Maqueda LA. Kinetic model for thermal dehydrochlorination of poly(vinyl chloride). Polym. 2010;51:3998–4007.

50 Koga N, Suzuki Y, Tatsuoka T. Thermal dehydration of magnesium acetate tetra hydrate: formation and in situ crystallization of anhydrous glass. J. Phys. Chem. B. 2012;116:14477-86.

51 Noda Y, Koga N. Phenomenological kinetics of the carbonation reaction of lithium hydroxide monohydrate: role of surface product layer and possible existence of a liquid phase. J. Phys. Chem. C. 2014;118:5424–36.

52 Koga N. Multistep kinetic behavior in the thermal degradation of poly (l-lactic acid): a physico-geometrical kinetic interpretation. J. Phys. Chem. B. 2014;118:11397–405.

53 Koga N, Tanaka H. Accommodation of the actual solid-state process in the kinetic model function. 1. Significance of the non-integral kinetic exponents. J. Therm. Anal. 1994;41:455–69

54 Avrami M. Kinetics of Phase Change. I. General Theory. J. Chem. Phys. 1939;7:1103−12.

55 Avrami M. Kinetics of phase change. II. Transformation−time relations for random distribution of nuclei. J. Chem. Phys. 1940;8:212−23.

56 Kissinger HF. Reaction kinetics in differential thermal analysis. J. Anal. Chem. 1957;29:1702–06.

57 Font R, Conesa JA, Molto J, Munoz M. Kinetics of pyrolysis and combustion of pine needles and cones. J. Anal. Appl. Pyrol. 2009;85: 276–86.

58 Lopez G, Aguado R, Olazar M, Arabiourrutia M, Bilbao J. Kinetics of scrap tyre pyrolysis under vacuum conditions. Waste Manag. 2009; 29:2649–55.

59 Avrami M. Kinetics of phase change. III. Granulation, phase change, and microstructure. J. Chem. Phys. 1941;9:177−84.

60 Barmak K. A Commentary on: Reaction kinetics in processes of nucleation and growth. J. Metall. Mater. Trans. A. 2010;41:2711−75.

61 Koga N, Goshi Y, Yamada S, Pérez-Maqueda LA. Kinetic approach to partially overlapped thermal decomposition processes. J. Therm. Anal. Calorim. 2013;111:1463−74.

62 Ferriol M, Gentilhomme A, Cochez M, Oget N, Mieloszynski JL. Thermal degradation of poly (methyl methacrylate) (PMMA): modelling of DTG and TG curves. Polym. Degrad. Stab. 2003;79: 271–81.

63 Cai J, Liu R, Weibull. Mixture model for modelling nonisothermal kinetics of thermally stimulated solid-state reactions: Application to simulated and real kinetic conversion data. J. Phys. Chem. B. 2007;111:10681−86.

64 Perejon A, Sanchez-Jimenez PE, Criado JM, Perez- Maqueda LA. Kinetic analysis of complex solid-state reactions. A new deconvolutionprocedure. J. Phys. Chem. B. 2011;115:1780−91.

65 Perez-Maqueda LA, Criado JM, Sanchez-Jimenez PE. Combined kinetic analysis of solid-state reactions: A powerful tool for the simultaneous determination of kinetic parameters and the kinetic model without previous assumptions on the reaction mechanism. J. Phys. Chem. A. 2006;110:12456−62.

66 Levie RD. Nonisothermal analysis of solution kinetics by spreadsheet simulation. J Chem. Educ. 2012;89:79–86.

CHAPTER 5

SYNTHESIS, CHARACTERIZATION AND APPLICATION STUDIES OF MIXED METAL TITANATES PREPARED *VIA* THERMAL DECOMPOSITION OF OXALATE PRECURSORS

5.1 Introduction

The perovskite family mainly various titanates (metal oxide) used in a wide range of applications in electronic, electro-optical, and electromechanical modelling of ceramics. Perovskite compounds become one of the hottest topics in *Materials science* due to their special properties and potential applications. Precursors for metal oxide have been continuously studied because they can often be tailored structurally; certain precursors are known to transform into the corresponding nano metal oxides with high degrees of shape retention or similarity. $BaTiO_3$ with a perovskite structure, show exceptional dielectric, piezoelectric, electrostrictive, and electrooptic properties with corresponding electronic applications [1–3]. Barium titanate with a high dielectric constant, widely utilized to manufacture electronic components as multilayer capacitors (MLCs), PTC thermistors, piezoelectric transducers, and a variety of electro-optic devices [4]. The ferroelectricity observed in barium titanate is utilized in memory applications, *i.e.*, in RAM. The pyroelectricity and piezoelectricity are also used in the passive infrared detectors and Sonars (Sound Navigation and Ranging). Besides PTCR properties, semiconductor barium titanate is used for sensor applications [5]. Pure barium titanate is an insulator whereas upon doping it transforms into a semiconductor [6].

Various studies have been performed to obtain $BaTiO_3$ of better electronic properties by doping different elements [7–10]. In order to obtain $BaTiO_3$ of low resistivity, Zhao *et al.* [11] prepared Ag^+ doped into $BaTiO_3$. Wu *et al*. [12] studied the influences on conductivity of

doping different rare-earth elements into $BaTiO_3$. Hao *et al*. prepared $BaTiO_3$ ceramics doped with Nb_2O_3 [13], Sm_2O_3 [14], Gd_2O_3 [15] and La^{3+} [16] by gaseous penetration method and resistivity was explained. There are lots of reports on the structural, dielectric and ferroelectric properties of modified $BaTiO_3$ ceramics *via* doping [17-20].

Recently many potential antibacterial agents, nanometer sized metal oxides have been identified [21]. Some of these agents were found to be cytotoxic against bacteria but not against human cells thus, possible for many medical applications. The use of inorganic nanoparticles has attracted lots of interest mostly because of their reliable antimicrobial activity found to be effective at low concentrations [22]. This is due to their high specific surface area which allows a broad range of reactions with the bacterial surface. Barium titanate nanoparticles exhibit bacteriocidal activity which is highly dependent on the particle size and concentration and to act against both Gram-positive and Gram-negative bacteria [23]. These nanoparticles are considered as a promising novel antibacterial agent, being harmless to human cells and the environment [24]. Gupta *et al*. [25] investigated the antimicrobial activity of TiO_2 and Ag-doped TiO_2 nanoparticles against Gram-positive (S. aureus) and Gram-negative (P. aeruginosa, E. coli) bacteria and were found to be effective [26]. Raja *et al*. [27] synthesized and discussed the remedial aspect of $BaTiO_3$ nanoparticles against bacteria. Therefore, in the present study the characterization of the hydrated and dehydrated products of the prepared barium-potassium mixed titanyl oxalates and also the

nanosized products were tested for conductance behaviour as well as anti bacterial efficiency.

5.2 Experimental

5.2.1 Materials

AnalaR grade barium nitrate ($Ba(NO_3)_2$) (Merck, India; assay ≥ 99.9 %), potassium titanyl oxalate ($K_2TiO(C_2O_4)_2$) (BHO Laboratory England; assay ≥ 99.9 %), Luria Bertani (LB) broth and agar plates, glass speader, Escherichia coli, Staphylococcus aureus , Pseudomonas aeroginosa and Staphylococcus pneumonia culture were used in the present investigation.

5.2.1.1 Sample preparation for conductance study

The K^+-doped $BaTiO_3$ powders were prepared by precipitation method well explained in Chapter 3. The samples were prepared at different concentrations, *viz.* 10^{-4}, 10^{-3}, 10^{-2}, 10^{-1} and 10^{0} mol % are named as a, b, c, d and e respectively and control compound as BT. The prepared sample powders were calcined at 773 K for 1 h. The samples were formed as pellets with 15 mm in diameter and 1 mm in thickness. Finally, the pellets were sintered at 723 K for 2 h.

5.2.1.2 Sample preparation for anti bacterial study

Barium titanyl oxalate is prepared from $Ba(NO_3)_2$ and $K_2TiO(C_2O_4)_2$. The precipitate obtained was filtered, washed with ethanol and water repeatedly and air-dried in an oven at 333 K for 24 h. Both barium titanyl oxalate (BTO) and potassium titanyl oxalate (KTO) were powdered in an agate mortar and sieved through the mesh

and fixed the particle size in the range 95-105 μm. The samples are prepared by physical mixting of potassium and barium titanyl oxalate

Different compositions: 100 m/m (%) barium titanyl oxalate (AS_1), 99 m/m (%) barium titanyl oxalate (AS_2), 98 m/m (%) barium titanyl oxalate (AS_3), 95 m/m (%) barium titanyl oxalate (AS_4), 93 m/m (%) barium titanyl oxalate (AS_5), 90 m/m (%) barium titanyl oxalate (AS_6), 80 m/m (%) barium titanyl oxalate (AS_7) and 100 m/m (%) potassium titanyl oxalate (AS_8), were prepared each by thorough mechanical mixing in an agate mortar. The samples were decomposed by keeping in a muffle furnace at about 1023 K for 1 h.

5.2.2 Methods

The resistivity of the prepared pallets was determined by using a standard four-probe method (Keithley's source meter, model 2400, America). In vitro antibacterial activity of mixed barium titanate nano particles was studied by agar disc diffusion assay method. The structures of the calcined materials were determined by measurement of XRD. The XRD analysis was carried out on a Rigaku-Dmax 2000 diffractometer with Cu Kα radiation (40kV, 30mA, λ = 1.5405Å). Fourier Transform Infrared spectroscopic measurements were performed by using an IR spectrophotometer (Nicolet AVATAR 320, America) ranging from 400 to 4000 cm^{-1}. Absorption spectra were scanned by using a UV-Vis spectrophotometer (Shimadzu, UV-2450) with a deuterium lamp. SEM analyses of the samples studied were performed with FE-SEM-EDS combination using Carl Zeiss Gemini SEM 300.

5.3 Results and Discussion

5.3.1 Conductance study

5.3.1.1 XRD Analysis

Fig. 5.1 shows the XRD patterns; K^+ doped $BaTiO_3$ possesses the same perovskite structure as that of the pure $BaTiO_3$ material. It can be concluded that no new substance was formed during the doping and calcination process other than $BaTiO_3$ which implies that the dopants have entirely entered the unit-cell maintaining the perovskite structure of the solid. During doping K^+ entered into crystal lattices of $BaTiO_3$ leading to the increase of the conductivity of the samples [28]. The particle size of samples was calculated using Scherrer formula. The particle size of the sample (a) is calculated and found to be 11.81 nm, while the particle sizes of sample (b), (c), (d), (e) and (f) are in the range 20.31-18.29 nm.

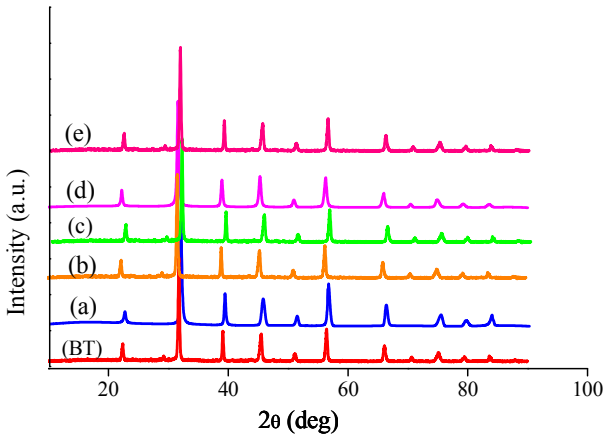

Fig. 5.1 XRD patterns of the $BaTiO_3$ powders (BT) doped with10^4 (a), 10^{-3} (b), 10^{-2} (c), 10^{-1} (d) and 1mol % K (e), after the calcination at 1023 K for 1 h.

5.3.1.2 FTIR Spectra Analysis

The FTIR spectra of samples are shown in Fig. 5.3. The characteristic absorption at 3410 cm^{-1} is assigned to–OH stretching vibration, due to the water brought by KBr or absorbed on the powder surface. The characteristic absorption at 1440 cm^{-1} is assigned to the stretching vibrations of carboxylate [29]. All the three samples exhibit strong absorptions around 550 and 450 cm^{-1}, which can be assigned to the stretching and bending vibrations of the Ti-O bond in $[TiO_6]^{2-}$ octahedron. But the strongest absorption observed around 550 cm^{-1} varied slightly for all the five samples: 559.1, 552.2, 545.7, 553.1, and 621.7 cm^{-1} respectively for samples a, b, c, d, & e. Since the wave number increases when infrared light of higher frequency and thus stronger energy is absorbed, it can be concluded that the Ti-O bond was strengthened after the doping and further strengthened after calcination [30].

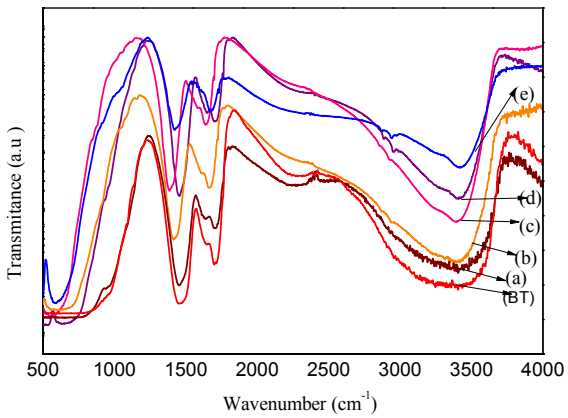

Fig. 5.2 FTIR spectrum of samples: undoped $BaTiO_3$ (BT),10^{-4} (a) 10^{-3} (b), 10^{-2} (c), 10^{-1} (d) and 1 mol % K (e), after the calcination at 373 K for 1 h.

5.3.1.3 Four probe method

The electrical characteristics of any material can be analyzed on electrical resistivity and based on this, materials are be classified as conductors, semiconductors and insulators. The resistivity of the conductors (metals) is very low because of the large number of free electrons. In the case of semiconductors usually the sheet or surface resistance of the thin layers are be considered. In any direct resistance measurement the metal terminals when come into contact with the layer, then there is a contact resistance similar to a rectifier due to metal semiconductor interface. There is another resistance also involved due to the spreading of charges into the semiconductor material apart from the surface called spreading resistance. The resistance observed in the direct measurement is the sum of actual surface resistance, contact resistance, spreading resistance and the resistance between the probes [31].

In order to eliminate the contact resistance as well as spreading resistance [32], while taking the resistance measurement, the four probe method is used to measure sheet resistivity. Here we are used four probe measuring set up using Keithley's source meter, model 2400. Along with four probe set up, each probe separated by a distance of 0.6 cm and constant current (1 μA) is applied. The samples are prepared as bare sample and five number of K^+ doped at various concentrations in $BaTiO_3$ and pelletized and then sintered at 723 K for 2 h. The measured sheet resistance and the conductance of different samples are given in the Table 5.1.

5.3.1.4 Electric Properties of samples.

During the calcination process $K_2TiO(C_2O_4)_2$ decomposes into K_2O, which entered $BaTiO_3$ lattice. Since K^+ possesses only one positive charge and Ba^{2+} possesses two, the substitution must be charge-compensated to maintain charge neutrality by using defect theory [33]. According to the defect theory the incorporation of K^+ as an acceptor dopant can be written as in equation (5.1):

$$K_2O \xrightarrow{BaTiO_3} 2K_{Ba} + V_O^{\cdot\cdot} + O_O \qquad (5.1)$$

The formation of oxygen vacancy is responsible for conducting properties of the samples. Here the strength of Ti-O bond in the $[TiO_6]^{2-}$ octahedron is stronger in the sample doped with K^+ than the undoped $BaTiO_3$ sample. Since the O^{2-} leaving the cell, the $[TiO_6]^{2-}$ octahedron was distorted and Ti^{4+} gaines a stronger attraction of the O^{2-} left, rendering the Ti-O bond stronger [33].

The oxygen vacancy formed was in equilibrium with the formation of hole:

$$V_O^{\cdot\cdot} \rightarrow V_O + 2h \qquad (5.2)$$

So that the ultimate result, when doping with $K_2TiO(C_2O_4)_2$, would render $BaTiO_3$ semi conductive. The electric resistivity of $BaTiO_3$ at different K^+ concentrations is measured. In Fig. 5a, while increasing the concentration of $K_2TiO(C_2O_4)_2$ the resistivity decreases since the conductivity is proportional to the concentration of oxygen vacancy.

However, we should also be aware that a high concentration of defect would distort the crystal structure thus undermining conductivity.

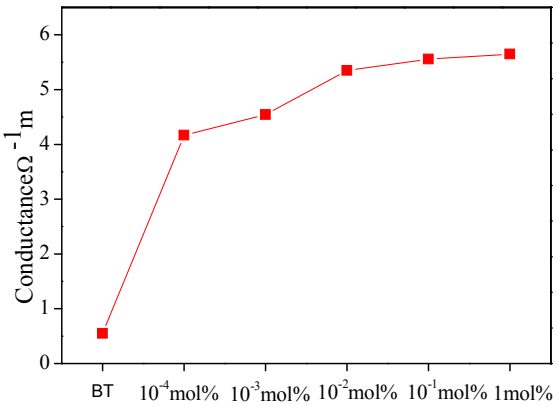

Fig. 5.3 The variations of the conductance of $BaTiO_3$ powders (BT) doped with 10^{-4}, 10^{-3}, 10^{-2}, 10^{-1} and 1 mol % K^+ after the sintered at 723 K for 2 h.

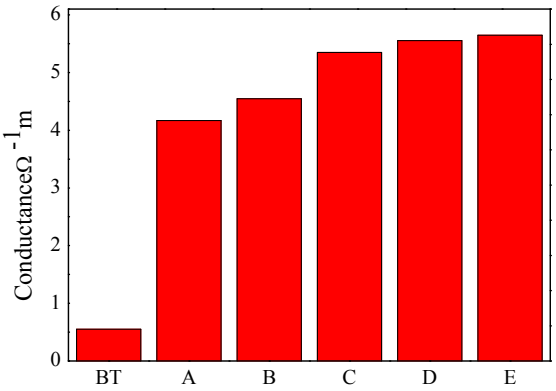

Fig. 5.4 The comparison of the conductance of $BaTiO_3$ powders (BT) doped with 10^{-4} (A),10^{-3} (B), 10^{-2} (C), 10^{-1} (D) and 1 mol % K (E), after the sintered at 723 K for 2 h.

Fig. 5.4 shows comparison of conductance calculated by four probe method by column graph. It shows that, during doping the conductance of the sample BT increases while the resistivity decreases which is proportional to the concentration of the dopant (Table 5.1).

5.3.1.5 UV- Visible spectroscopic studies

For UV/VIS absorption analysis was carried out on a Shimadzu, UV-2450 spectrometer capable of taking measurement in the range 200-1100 nm. Analysis of samples in different forms, *viz*., film, solution and powder are possible with this spectrometer. For the determination of optical properties, the band gap the UV–Vis diffuse reflectance spectrum of $BaTiO_3$ and K doped $BaTiO_3$ samples was measured (Fig. 5.5). It absorbs the UV light below 400 nm. Fig. 5.6a shows the UV–Vis diffuse reflectance spectrum of $BaTiO_3$ and K^+ doped $BaTiO_3$ samples and it show noticeable shift towards higher wavelength, *i.e*., red shift, due to the presence of K^+ ions.

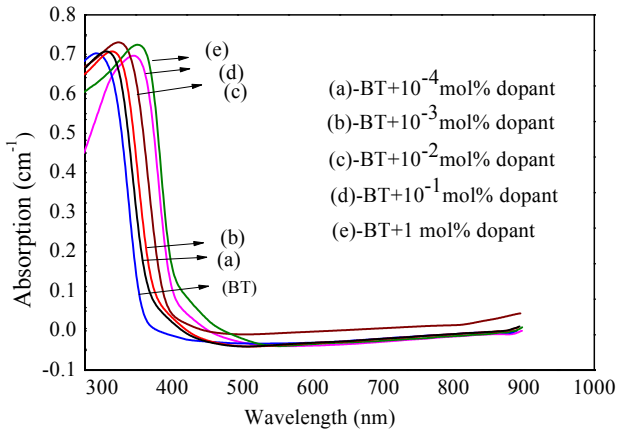

Fig. 5.5 UV-Vis absorption spectra of $BaTiO_3$ + x mol % K (x = 10^{-4}, 10^{-3}, 10^{-2}, 10^{-1} and 1).

The concentration increased in K^+ doped $BaTiO_3$ when UV-Vis absorption shifted to long wave region in K^+ doped samples. The red shift of UV-Vis absorption was observed, the red shift effect was enhances with increase of the concentration of K^+ shown in Fig. 5.6a. Absorption is expressed in terms of a coefficient $\alpha(hv)$, which is related to the energy gap E_g according to Tauc-equation

$$\alpha\, hv = A(hv - E_g)^n \tag{5.3}$$

Where A is a constant, h is Plank's constant; v the frequency of the incident beam and n is equal to ½ for a direct gap and 2 for an indirect gap [34]. Band gap measurements are mainly carried out by this technique on the basis of Tauc plot as the intercept value of the plot of $(\alpha hv)^2$ against light energy (hv). The optical band gap (E_g) is estimated by the extrapolation of the linear portion to $(\alpha hv)^2=0$ in the *hv versus* $(\alpha hv)^2$ curve (Tauc-plot) is shown in Fig. 5.6b, and band gap was found and tabulated (Table 5.1), which reveals that the band gap decreases from 2.97 to 2.78 eV supporting the red shift. The reported value of E_g corresponding to $BaTiO_3$ is 3.1 eV [35]. The decrease in the value of E_g of a material reflects the increase of conducting properties. It has been reported that electron donors accelerate thermal process and electron acceptors retard the thermal process [36]. Therefore, the presence of K^+ along with $BaTiO_3$ causes an increase in the conducting properties of $BaTiO_3$.

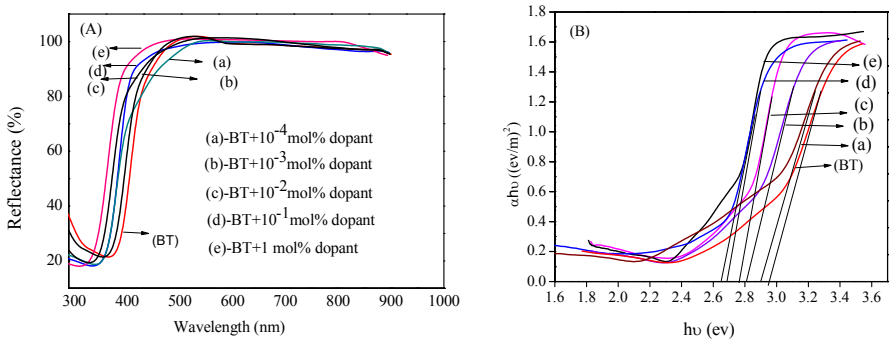

Fig. 5.6 UV-vis reflectance spectra (A) and Tauc-plot (B) of $BaTiO_3$ + x mol % K (x = 10^{-4}, 10^{-3}, 10^{-2}, 10^{-1} and 1) within the range of wavelength.

The conductance increases with increase of K^+ concentration in the system, it was seen that the dopant decreases the band-gap energy between the valence band and conduction band so that electrons could jump from the valence band to the conduction band easily. The understanding about the experimental results is helpful to reveal the mechanism of doping. Moreover, it provides a possible way to modify the optical property and the conductive property of the materials that are potential candidate in electronic industry.

Table 5.1 Parameters obtained from Four probe method and UV-Vis. spectroscopy.

Samples	Conductance ($\Omega^{-1}m^{-1}$)	Band gap (eV)
BT	0.549	2.97
BT+10^{-4} mol % K	4.167	2.91
BT+10^{-3} mol % K	4.545	2.81
BT+10^{-2} mol % K	5.347	2.79
BT+10^{-1} mol % K	5.405	2.73
BT+1 mol % K	5.649	2.68

5.3.2 Anti bacterial Study

5.3.2.1 XRD analysis

XRD analysis was employed to affirm the composition of as prepared oxide nanoparticles. Fig. 5.7 shows the structural characteristics of pure barium titanyl oxalate, potassium titanyl oxalate and their mixtures when heated to 973 K for 1h investigated by XRD. The XRD results of the hydrated samples AS_1 and AS_8 show significant amount of amorphous phase and the dehydrated mixed samples AS_2, AS_3, AS_4, AS_5, AS_6 and AS_7, the peak positions with 2θ values of 31.84, 39.17, 45.5, 51.21, 60.04 and 75.25^0 can be assigned to (002), (111), (202), (020), (202) and (311) planes which matches well with the values of tetragonal phase of $BaTiO_3$ reported with the JCPDS file no. 05-0626 [37]. The relative crystallite sizes determined from the XRD line broadening using the Scherrer equation: $d = 0.9\lambda/\beta\cos\theta$, where d is the crystallite size, λ is the wavelength used in XRD (1.5418 A^0), θ is the Bragg angle, β is the pure diffraction broadening of a peak at half height, *i.e.,* broadening due to crystallite dimensions. The crystallite size of the mixed oxides ranges from 28-35 nm and hydrated AS_1 and AS_8 obtained as 45 & 50 nm according to the Scherrer equation [38]

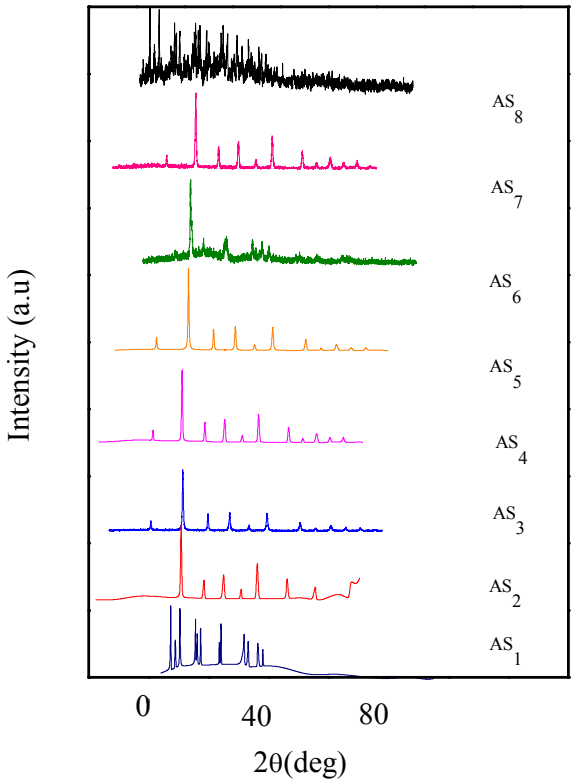

Fig. 5.7 XRD pattern of barium titanyl oxalate tetrahydrate (AS_1), potassium titanyl oxalate dehydrate (AS_8) and the different mixtures AS_2, AS_3. AS_4. AS_5, AS_6, AS_7 heated to 973 K for 1 h.

5.3.2.2 SEM Analysis

Fig. 5.8 shows the FE-SEM images of AS_1, AS_2, AS_3, AS_4 and AS_5 respectively. From the images it is evident that all the mixed BTNPs are highly porous, in addition to which, agglomeration of the particles is also clear. Similar trend was observed for all other mixed samples. SEM images reveals different morphology such as spherical and rod shape particles with temperature of calcination.

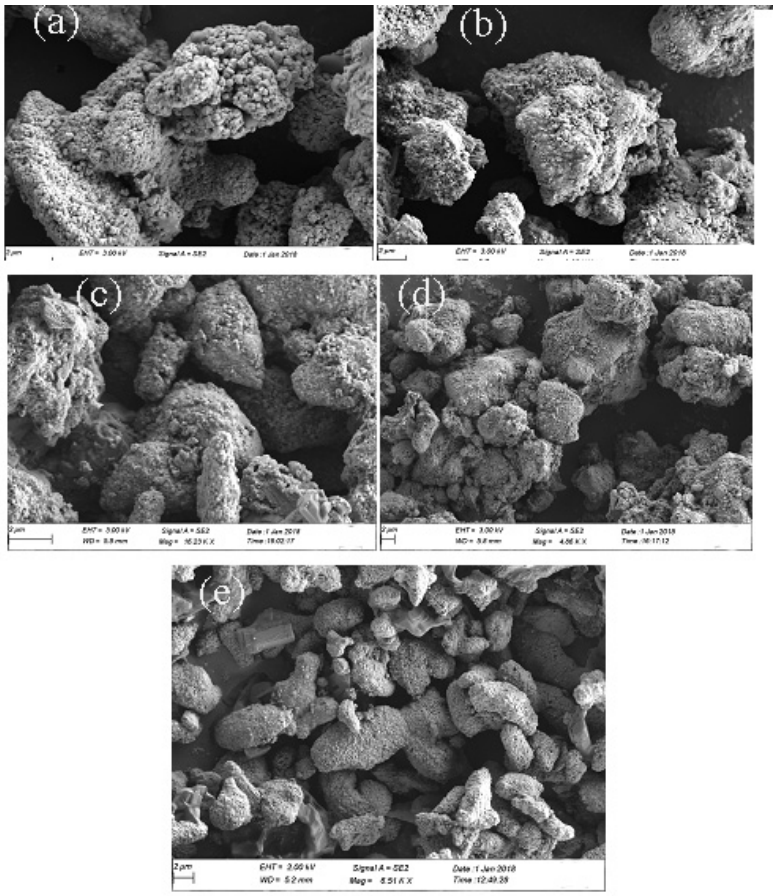

Fig. 5.8 FE-SEM image of AS_1 (a), mixed oxides AS_2 (b), AS_3 (c), AS_4 (d) and AS_5 (e)

EDS Analysis

Energy dispersive X-ray spectroscopic analysis (EDS) carried out to identify the purity of the mixed BTNPs synthesized by calcining at a temperature of 750 K. From the EDS analysis, it is found that mixed BTNPs did not contain any impurities (Fig. 5.9). The high intensity peaks observed in the EDS patterns of the nanoparticles, in Fig. 5.9, corresponds to Ba, K, O and Ti elements [39].

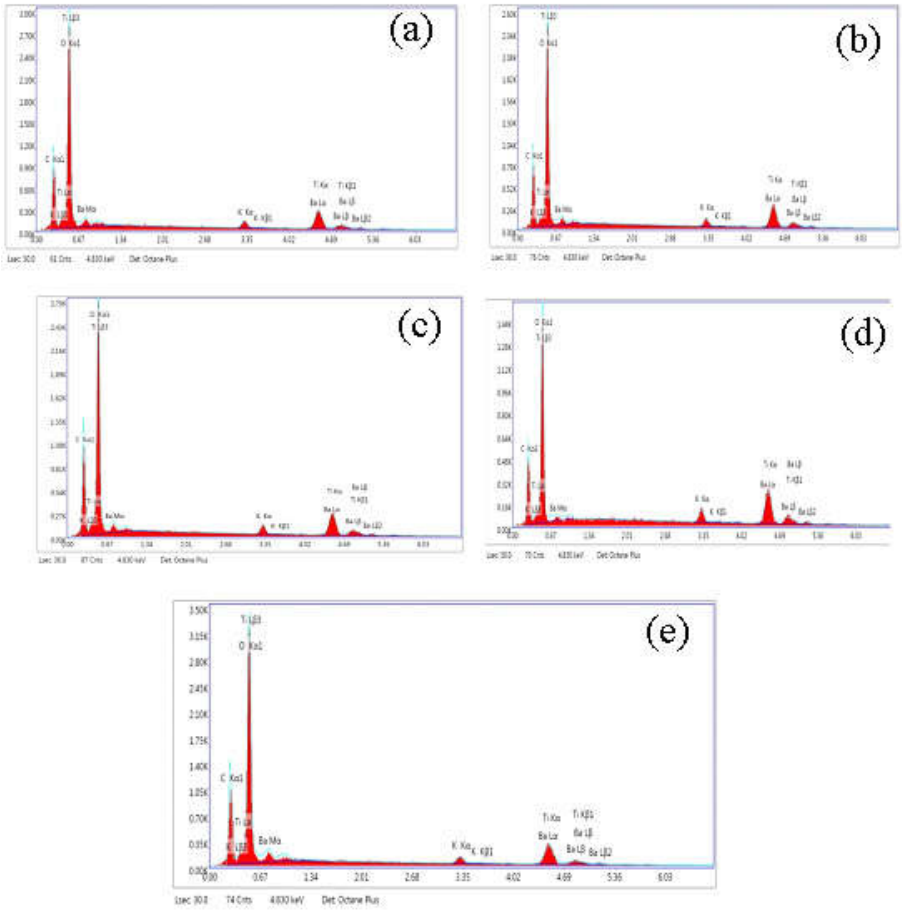

Fig. 5.9 EDX spectrum of mixed oxides AS_2 (a), AS_3 (b), AS_4 (c) AS_5 (d) and AS_6 (e)

5.3.2.3 Agar- well diffusion method

The microbial toxicity of mixed metal oxide nanoparticles was demonstrated using Gram-positive (G+) and Gram-negative (G−) bacteria. The antibacterial activity of mixed metal oxide nanostructures was evaluated by well diffusion method using four pathogenic bacteria

Escherichia coli (G−), Staphylococcus aureus (G+), Pseudomonas aeruginosa (G−) and Staphylococcus pneumonia (G+).

5.3.2.3.1 Antibacterial activity test

In order to investigate the antibacterial activity, mixed $BaTiO_3$ nanoparticles along with standard antibiotic [Gentamicin (G)] were tested against four bacterial strains: Escherichia coli (Gram-negative), Pseudomonas aeruginosa (Gram-negative), Staphylococcus pneumonia (Gram-positive) and Staphylococcus aureus (Gram-positive) by disc diffusion methods.

Luria Bertani (LB) medium was prepared in distilled water and sterilized. Sterile LB agar was poured into Petri dishes and allowed to set in a laminar air flow cabinet. The plates were then stored in a refrigerator for further use. A 24 h exponentially grown bacterial culture further inoculated into LB broth and shake well in 310 K incubator shaker till it reaches 0.5 Macfarlane's turbidity. The culture was then spread on LB agar plates already prepared, with sterile glass spreader. On drying of the spreader layer, small wells were dug in the plates according to the number of samples to be screened particles in 1 mg/ml concentration was pipette out into the respective wells and incubated for 16 h at 310 K. The obtained zone of inhibition of bacterial growth was then analyzed by measuring it and recorded in mm.

5.3.2.3.2 Observations

The antibacterial activity was assayed by measuring the diameter of the inhibition zone formed around the well. The mixed barium titanate nanoparticles exerted a fairly significant antibacterial properties against four pathogens investigated when compared to control (Fig. 5.10). The diameter of inhibition zones increased for the test mixed metal oxide nanoparticles. The negative controls (N) indicated the microbial growth profile in the absence of nanoparticles.

The inhibition data is tabulated in Table 5.2 and zone of inhibition is shown in Fig. 5.11. The well diffusion test was conducted as a qualitative test only and no inference of dosage details is mentioned. The mixed metal oxides show remarkable antibacterial activity against the four studied bacterial stains. The presence of different concentration ratios increases the antibacterial activity of barium titanate nanoparticles significantly. It can be hypothesised that these nanoparticles form stable complexes with vital enzymes inside the cells which hamper cellular functioning resulting in their death.

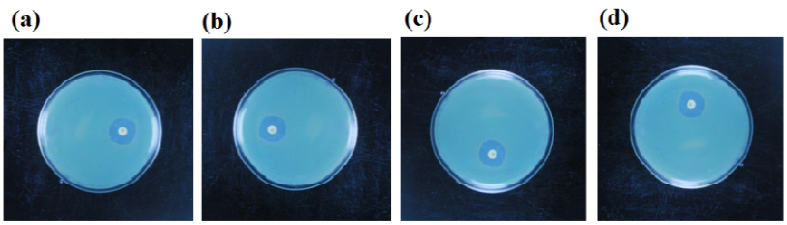

Fig. 5.10 The zones of inhibition against Escherichia coli (a), Staphylococcus aureus (b), Pseudomonas aeruginosa (c) and Staphylococcus pneumonia (d), when treated with Gentamicin.

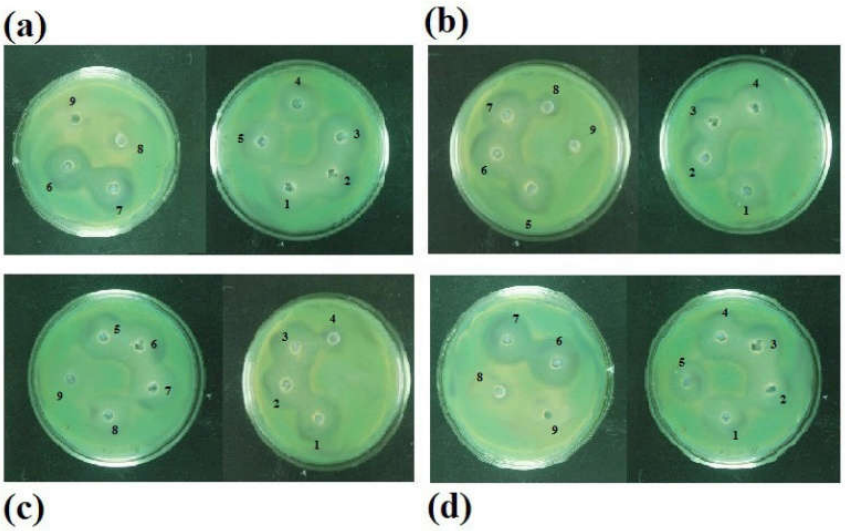

Fig. 5.11 The zones of inhibition against Escherichia coli (a), Staphylococcus aureus (b), Pseudomonas aeruginosa (c) and Staphylococcus pneumonia (d), when treated with the prepared mixed metal oxides.

Table 5.2 Comparision of activities of samples on Gram-negative and Gram-positive bacteria

Inhibition zone of samples										
Bacterias	AS_1	AS_2	AS_3	AS_4	AS_5	AS_6	AS_7	AS_8	N	G
Escherichia coli	24	23	32	26	30	28	22	10	-	21
Staphylococcus aureus	25	24	30	28	26	31	23	12	-	20
Pseudomonas aeruginosa	26	29	30	28	32	30	28	14	-	21
Staphylococcus pneumonia	28	32	30	31	27	29	19	13	-	20

5.4 Conclusion

- In conductance study, the addition of K^+ in $BaTiO_3$ system increases the conductance. UV-Vis spectra reveal that it was

attributed to the decrease of the energy gap. The red shift of absorption edge observed in the K^+ doped $BaTiO_3$, confirms that electrons possess a larger possibility for jumping from the valence band to the conductance band. The decrease of resistance was approving for the materials to assemble the demand of electronic circuit. The red shift of absorption edge made the materials available in a wider range of wavelength. The information is important for the material to be applied in a certain range of wavelength. The understanding about the correlation between the conductivity and UV-Vis spectra in this kind of functional material is helpful to improve performances of related devices in electronic industry. The prepared samples were characterized using XRD and FT-IR.

- The microbial toxicity of mixed metal oxides was demonstrated using Gram-positive (G+) and Gram-negative (G−) bacteria. The antibacterial activity of mixed metal oxides nanostructures was evaluated by well diffusion method using four pathogenic bacteria Escherichia coli (G−), Staphylococcus aureus (G+), Pseudomonas aeruginosa (G−), Staphylococcus pneumonia (G+). The mixed metal oxides showed remarkable antibacterial activity against the four studied bacterial strains. The synthesized BTO, KTO and the series of mixtures of barium-potassium titanyl oxalate were decomposed and characterized using XRD and FE-SEM.

5.5 References

1. Moulson AJ, Herbert JM. Electroceramics: Materials, properties and applications. Chapman and Hall, London, UK. 1990.

2. Yao K, Zhu W. $BaTiO_3$ glass-ceramic thin films for integrated high dielectric media. Thin Solid Films. 2002;408:11–14.

3. Wei J, Guan J, Shi J, Yuan R. The structure and electrorheological effect of PAn/$BaTiO_3$ nanocomposite. Chin. J. Chem. Phys. 2003;16:401–05.

4. Chatterjee S, Stojanovic BD, Maiti HS. Effect of additives and powder preparation techniques on PTCR properties of barium titanate. J. Mater. Chem. Phys. 2003;78:702–10.

5. Sonia Patel RK, Kumar P, Prakash C, Agrawal DK. Low temperature synthesis and dielectric, ferroelectric and piezoelectric study of microwave sintered $BaTiO_3$ ceramics. Ceram. Int. 2012;38:1585–89.

6. Smyth DM. The effects of dopants on the properties of metal oxides. Solid State Ionics. 2000;129:5-12.

7. Nemoto H, IOda I. Direct examinations of PTC action of single grain boundaries in semiconducting $BaTiO_3$ ceramics. J. Am. Ceram. Soc. 1980;63:398–401.

8. Tangjuank S, Tunkasiri T. Characterization and properties of Sb-doped $BaTiO_3$ powders. J. Appl. Phys. Lett. 2007;90 Article ID 072908.

9. Preis W, Sitte W. Electronic conductivity and chemical diffusion in n-conducting barium titanate ceramics at high temperatures. Solid State Ionics. 2006;177:3093–98.

10. Jana A, Kundu TK. Microstructure and dielectric characteristics of Ni ion doped $BaTiO_3$ nanoparticles. J. Mater. Lett. 2007;61:1544–48.

11. Zhao L, Chang Z, Wu S, Xiong W. Effect of Ag-doping on $BaTiO_3$ based PTCR ceramics by once-through method in sol-gel process. Electro. Comp. Mat. 2003;22:24–26.

12. Wu S, Chang Z, Li D, Xiong W. Influence of various rare-earth dopants on conductivities of $BaTiO_3$ ceramics. J. Funct. Mater. 1997;28:509–10.

13. Hao SE, Wei YD. Electric characteristics of Nd_2O_3 doped $BaTiO_3$ ceramics. J. Harbin Inst. Tech. (New Series), 2003;10:388–91.

14. Hao SE, Wei YD. Gas penetration of Sm into $BaTiO_3$ ceramics and their electric characteristics. J. Mater. Sci. Technol. 2004; 12:258–64.

15. Hao S, Wei Y, Kuang C. Effects of Gd_2O_3 doping on electric characteristics of $BaTiO_3$ ceramics. Fine Chemicals. 2002;19: 717–19.

16. Hao S, Sun L, Liu X, Wei Y. Effects of La on structure and electrical characteristics of $BaTiO_3$ ceramics. J. Funct. Mat. Dev. 2004;10:408–12.

17. Wei XK, Zhang QH, Li FY, Jin CQ, Yu RC. Structural evolution induced by acceptor doping into $BaTiO_3$ ceramics. J. Alloy Compd. 2010;508:486–93.

18. Kajtoch C. Dielectric properties of $Ba(Ti_{1-x}Sn_x)O_3$ ceramics in the paraelectric phase. Ceram. Int. 2011;37:387–91.

19. Ren PR, Fan HQ, Wang X. Impedance spectroscopy studies of bulk electrical conduction in A-site acceptor (K)-doped $BaTiO_3$. J. Mater. Sci. 2013;48:7028–35.

20. Sareein T, Unruan M, Ngamjarurojana A, Ananta S, Yimnirun R. Dielectric relaxation time behaviour of B-site hybrid-doped $BaTiO_3$ ceramics. Ferroelectrics. 2014;458:56–63.

21. Vidic J, Stankic S, Haque F, Ciric D, Le Goffic R, Vidy A, Jupille J, Delmas B. Selective antibacterial effects of mixed ZnMgO nanoparticles. J. Nanopart. Res. 2013;15:1595-604.

22. Anagnostakos K, Kelm J, Regitz T, Schmitt E, Jung W. In vitro evaluation of antibiotic elution from and bacteria growth inhibition by antibiotic-loaded acrylic bone cement spacers. J. Biomed. Mater. Res. B. Appl. Biomater. 2005;72:373-08.

23. Koper OB, Klabunde JS, Marchin GL, Klabunde KJ, Stoimenov PL. Nanoscale powders and formulations with biocidal activity toward spores and vegetative cells of bacillus species, viruses, and toxins. Curr. Microbiol. 2002;44:49-55.

24. Jin T, He Y. Antibacterial activities of magnesium oxide (MgO) nanoparticles against food borne pathogens. J. Nanopart. Res. 2011;13:6877-85.

25. Gupta K, Singh PR, Pandey A. Photocatalytic antibacterial performance of TiO_2 and Ag-doped TiO_2 against S. aureus, P. aeruginosa and E. coli. Beilstein J. Nanotechnol. 2013;4:345-51.

26. Haghi M, Hekmatafshar M, Mohammad B, Janipour, Gholizadeh SS, Faraz MK, Sayyadifar F, Ghaedi M. Antimicrobial effect of TiO_2 nanoparticles on pathogenic strain of E.coli. Int. J. Adv. Biotechnol. Res. 2012;3:621-24.

27. Raja S, Bheeman D, Rajamani R, Pattiyappan S, Sugamaran S, Bellan C. Synthesis, characterization and remedial aspect of $BaTiO_3$ nanoparticles against bacteria. J. Nanomed. Nanobio. 2015;2:16-20.

28. Park K, Kim JG, Lee KJ, Cho WS, Hwang WS. Electrical properties and microstructure of Y-doped $BaTiO_3$ ceramics prepared by high-energy ball-milling. Ceram. Int. 2008;34:1573–77.

29. Qi Y, Zhang L, Jin G , Wan Y ,Tang Y, Xu D, He Q. UV-visible spectra and conductive property of Mn-doped $BaTiO_3$ and $Ba_{0.93}Sr_{0.07}TiO_3$ ceramics. Ferroelectrics. 2014;458:64-69.

30. Miguel G, Juan H, Leticia B, Joaquin N, Mario ERG. Characterization of calcium carbonate, calcium oxide and calcium hydroxide as starting point to the improvement of lime

for their use in construction. J. Mater. Civ. Eng. 2009;21:625–708.

31. Valdes LB. Resistivity measurements on germanium for transistors. Proc. IRE. 1950;40:1429-34.

32. Smits FM. Measurement of sheet resistivities with the four-point probe. J. Bell Syst. Tech. 1958;37:711-18.

33. Panda B, Dhar A, Nigam GD, Bhattacharga D, Ray SK. Optical properties of RF sputtered strontium substituted barium titanate thin films. Thin Solid Films. 1998;332:46–49.

34. Kobayashi T, Naito H. Optical properties of condensed matter and applications. Ed. J. Sing, John Wiley & Sons. 2006.

35. Gao H. Theoretical investigation on the structure and electronic properties of barium titanate. J. Mol. Struc. 2011;1003:75-81.

36. Schroder DK. Semiconductor material and device characterization. Third Ed., John Wiley & Sons, New York, 2006.

37. Joint Committee on Powder Diffraction Standard (JCPDS), International Center for Diffraction Data, Swathmore, PA, JCPDS file No. 5-0626, 1980.

38. Patterson AL. The Scherrer formula for X-Ray particle size determination. Phys Rev.1939;56:978-82.

39. Fuentes S, Zarata RA, Chavez E, Munoz P, Ayala M, Gonzalez RE, Leyton P. Synthesis and characterization of $BaTiO_3$ nanoparticles in oxygen atmosphere. J. Alloys Comp. 2010;505:568-72.

CHAPTER 6

A COMPARATIVE ABINITIO DFT STUDY OF ELECTRONIC STRUCTURE OF $BaTiO_3$ AND K DOPED $BaTiO_3$

6.1 Introduction

Theoretical chemistry is becoming an increasingly powerful tool which allows researchers to understand the fundamental processes underpinning the chemical reactions which are imperative for material sciences, and it become most powerful when it is used to compliment an experimental investigation.

First-principles calculation is one of the most feasible methods to carry out the theoretical studies of the electronic properties of solids. The first principles studies based on density functional theory within local density approximation have been used to investigate the structural, electronic and optical properties of solids [1]. Sanna *et al*. conducted several first-principles calculations on $BaTiO_3$; they had focused more on the structural and electronic properties of the four different phases [2]. Razak *et al.* used the first principle study to explain the band structure of tetragonal barium titanate [3] while Cai *et al*., investigated the optical properties of perovskite barium titanate by using the first principles under scissor approximation [4]. Zhang *et al*. [5] have carried out a theoretical work based on the first principles study of bulk barium titanate, in the core-level spectra, under scissor approximation (FLAPW-SAT) and they manage to explain the optical properties. Salehi *et al*. [6] carried out a detailed study of the electronic structure of Ni-doped $BaTiO_3$ powder using FP-LAPW method. They had used the Large Unit Cell (LUC) approach [7, 8] with 40 atoms in their periodic model.

Vienna Ab-initio Simulation Package (VASP) [9], is a package performing ab-initio quantum mechanical molecular dynamics by using pseudo potential or Projected Augmented Wave (PAW) method and a plane wave basis set for atomic scale materials modeling like electronic structure calculations and quantum mechanical molecular dynamics. It approximates solution to the many body Schrodinger equation either within the density functional theory (DFT) [10] or within the HF approximation [11-12]. In VASP, for one electron orbital, the electronic charge density has been expressed in terms of plane wave basis sets. The interactions between electrons and ions are described by using norm-conserving or ultra pseudo potentials or PAW methods. To determine the electronic ground states, VASP makes use of the elective iterative matrix diagonalisation technique like, residual minimization method with direct inversion of iterative subspace (RMM-DIIS) or blocked Davison algorithm and are reported to be the fastest schemes currently available, which in turn enable efficient calculations [13].

VASP was gifted for the electronic structure of states (EOS) and structural optimization calculations, the structure and equation of state of a stable phase of $BaTiO_3$ and doped $BaTiO_3$. The static and dynamic properties of $BaTiO_3$ were characterized by quantum mechanical calculations, especially the structure, equation of state, phase stability, and phase transformations were studied in Generalized Gradient Approximation implemented DFT [14]. Wahl *et al*. [15] calculated the structural, electronic, and phonon properties of tetragonal and cubic $BaTiO_3$ by use of the projected augmented wave

method with several types of exchange correlation functional within DFT. Khenata *et al*. [16] studied the structural parameters of $BaTiO_3$ using the full-potential linear augmented plane wave (FP-LAPW); compared the computed results with the experimental data and theoretical calculations.

In this study the electronic structure of states (EOS), band energy, band structure, and density of states (DOS) in $BaTiO_3$ and K doped $BaTiO_3$ are studied by the first-principles calculation; Perdew and Wang generalized gradient approximation (PWGGA) method within the framework of density functional theory. The calculated electronic structures, band energy, band structure, density of states are in good agreement with the experimental results. Moreover, the experimental order of conductivity has been retained in the computed results also.

6.2 Methodology

Quantum mechanical calculations of EOS have been performed in the general framework of DFT [17- 19] by using projector augmented wave method [20]. In this DFT computation, the generalized gradient approximation (GGA) exchange and correlation energy functional as suggested by Perdew and Wang have been used. The crystal structure of $BaTiO_3$ (Fig. 6.1a) and K doped $BaTiO_3$ (Fig. 6.1b), are in cubic phase and belongs to the space group Pm3m. This cubic unit cell contains one molecule with the Ba sitting at the origin (0.0, 0.0, 0.0) a, the Ti at the body center (0.5, 0.5, 0.5) a and the three oxygen atoms at the three face centers

(0.5, 0.5, 0.0) a, (0.0, 0.5, 0.5) a, and (0.5, 0.0, 0.5) a; the lattice constant is 7.57 a.u (1 a.u = 0.529 A^0) [6, 9]. Fig. 1b shows the unit cell of K doped $BaTiO_3$ in which one Ba is replaced by K sitting at the origin (0.0, at the three face centers (0.5, 0.5, 0.0) a, (0.0, 0.5, 0.5) a, and (0.5, 0.0, 0.5) a) and the three oxygen atoms over the Brillouin zone were summed on a Monkhorst-Pack mesh [21] of 10×10×10. The kinetic energy cut off of the electronic wave functions was expanded in the plane waves up to 225 eV. The $5s^2$, $5p^6$, $6s^2$ levels of Ba, $3s^2$, $3p^6$, $3d^2$, $4s^2$ of Ti, $2s^2$, $2p^4$ of O were treated as valence states. The core of atoms was represented by the pseudo potentials of the respective atoms. VASP was used for the EOS and structural optimization calculations and to obtain response function calculations within the recent advances in density functional theory. Within ab-inito, GGA exchange-correlation formalism with a norm-conserving pseudo potential approach [22-23] was used with the same valence states defined above. The atomic crystal structures of cubic $BaTiO_3$ and K doped $BaTiO_3$ used in this work are illustrated in Figs. 6.1a and b respectively. The electronic wave functions, expanded in plane waves are same for both systems which is accurate enough to sample the Brillouin Zone. The band structure, total density of states and partial DOS has been systematically constructed to investigate the electronic configuration of this perovskite compound.

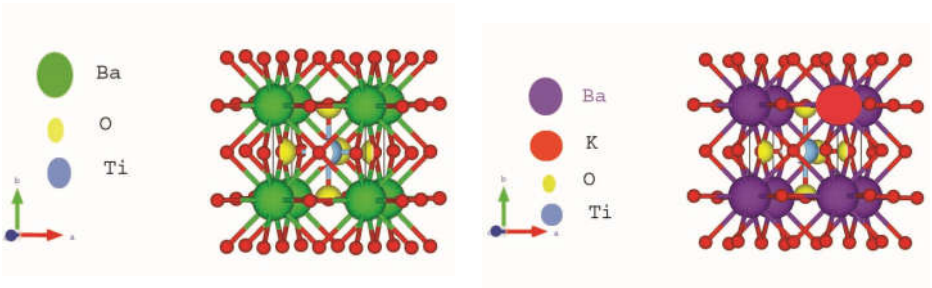

(a) (b)

Fig. 6.1 Crystal structure of $BaTiO_3$ (a) and K doped $BaTiO_3$ (b)

6.3. Result and discussion

6.3.1 Structural properties of $BaTiO_3$ and K doped $BaTiO_3$

In the atomic crystal structures of $BaTiO_3$ and K doped $BaTiO_3$; the values of unit cell lattice parameter, volume and bond length were computed from the geometry optimization calculation and are listed in Table 6.1. In this calculation, the lattice constant '*a*' of both systems is 4.010 A^0 and is in good agreement with the experimental value [24] of 4.012 A^0. It has been observed that for $BaTiO_3$ the results obtained from the VASP are in good agreement with those obtained from experiment [25-26]. The accuracy of the lattice calculation and its atomic position become a significant factor of the material stability and for further use in other calculations in perovskite oxide. The K doped $BaTiO_3$ also got almost same values of structural parameters which reveal the occurrence of an effective doping. The reported BTO lattice parameters from experimental data [27] are in good agreement with LDA obtained from the present work.

Table 6.1 Structural parameters of $BaTiO_3$ and K doped $BaTiO_3$

$BaTiO_3$		K doped $BaTiO_3$	
a (A^0)	4.01	a (A^0)	4.01
V(A^0)	64.483	V (A^0)	64.483
O_a-Ti	2.005	O_a-Ti	2.005
O_b-Ti	2.005	O_b-Ti	2.005
O_c-Ti	2.005	O_c-Ti	2.005
O_a-O_b	2.8355	O_a-O_b	2.8356
O_a-O_c	2.8355	O_a-O_c	2.8354
O_b-O_c	2.8355	O_b-O_c	2.8353
O_a-Ba	2.8355	O_a-K	2.8354
O_b-Ba	2.8355	O_b-K	2.8356
O_c-Ba	2.8355	O_c-K	2.8354

6.3.2 Band structures and density of states of $BaTiO_3$ and K doped $BaTiO_3$

The calculated electronic band structures of $BaTiO_3$ and K doped $BaTiO_3$ along the direction of high-symmetry points are shown in Figs. 6.2a and b respectively.

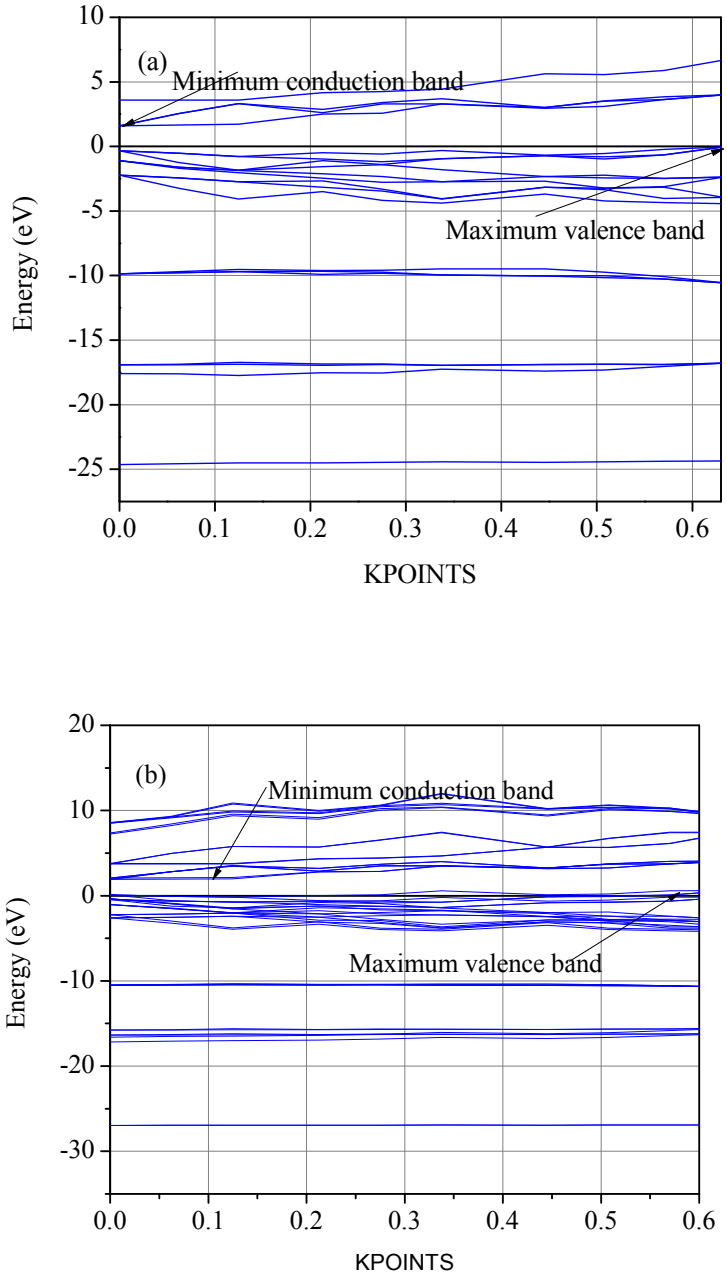

Fig. 6.2 The calculated energy-band structure for $BaTiO_3$ (a) and K doped $BaTiO_3$ (b)

In both systems the band structure was separated by four portions in the valence band [28]. In Fig. 6.2a the narrow band positioned at -17.01 eV was derived from O 2s states and O 2p states, and the one positioned at -9.94 eV was originated from the Ba 5p states. There is a multiple peak in the valence band near Fermi level and also the conduction bands near Fermi level have a strong Ti 3d characteristic. These results could be confirmed by the partial density of states, the calculated total density of states (TDOS) for $BaTiO_3$ in the valence-band region is shown in Fig. 6.3 and spin resolved density of states are also shown in Fig. 6.5. The band gap observed was 2.23 eV. In experimental study, the band gap of $BaTiO_3$ has been reported around 3.40 eV and can be categorized as an indirect band gap [29-30]. Saha *et al*. showed that the calculated fundamental gap of 1.2 eV is smaller than the experimentally reported value 3.4 eV, because of the discontinuity in the exchange correlation potential, which is not taken into account [31]. In order to find the composition which determined the band structure, the partial density of states has been employed with consideration of the spin polarization. The O 2s states positioned at -17 eV and Ba 5p states at -10 eV further confirms the band structure (Fig. 6.5).

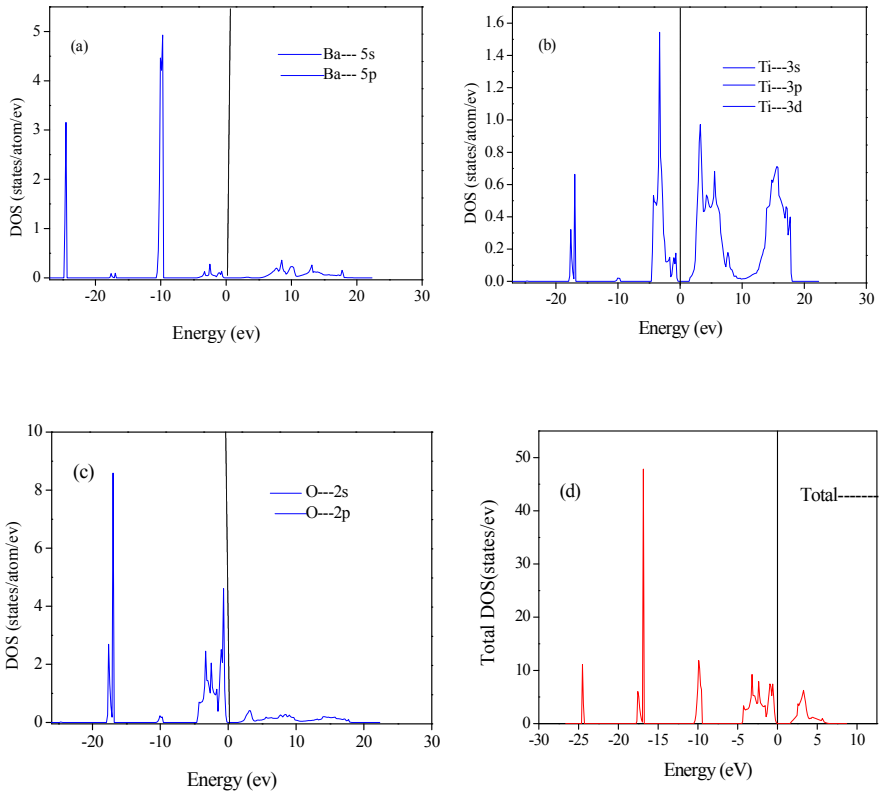

Fig. 6.3 Partial density of states for Ba (a), Ti (b), O (c) and Total DOS of atoms in $BaTiO_3$ (d)

In the case of K doped $BaTiO_3$ the results show a direct band gap of 1.92 eV at the point in the Brillouin zone. In Fig. 6.2b the narrow bands positioned at -17.01 eV was derived from O 2s states and O 2p states, and the one positioned at -9.94 eV was originated from the 3p and 4s states of K. There is a shoulder peak in the valence band near Fermi level and also the conduction band near Fermi level has a strong Ti 3d characteristic. These results also confirm the partial density of states, the total density of states in Fig. 6.4 and also spin resolved density of states in Fig. 6.6. The band gap on comparing with $BaTiO_3$

system it has observed a decrease by 0.31 eV unit, while on doping the conducting character is proven within this approach.

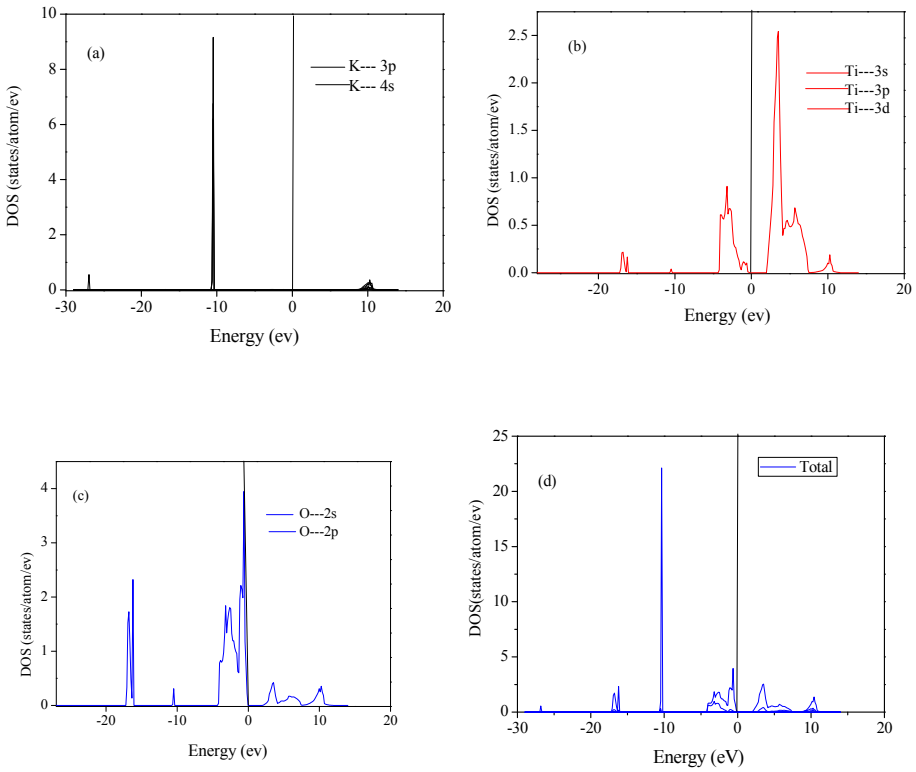

Fig. 6.4 Partial density of states for K (a), Ti (b), O (c), and Total DOS of atoms in K doped $BaTiO_3$ (d)

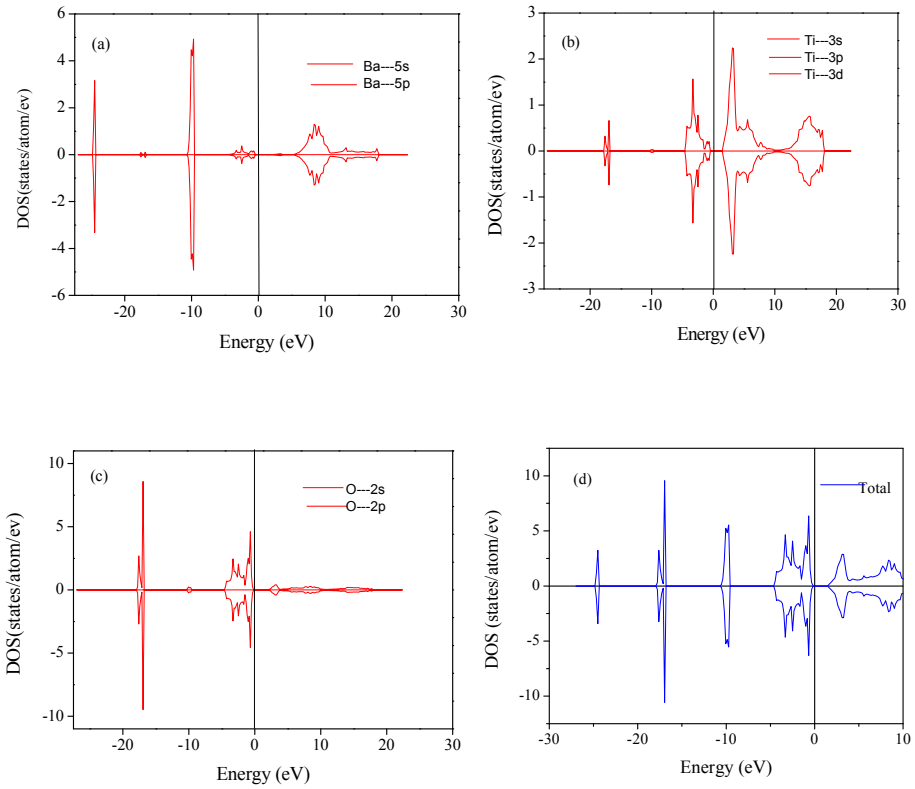

Fig. 6.5 Spin resolved DOS of Ba (a), Ti (b), O (c) and Total DOS of atoms in $BaTiO_3$ (d)

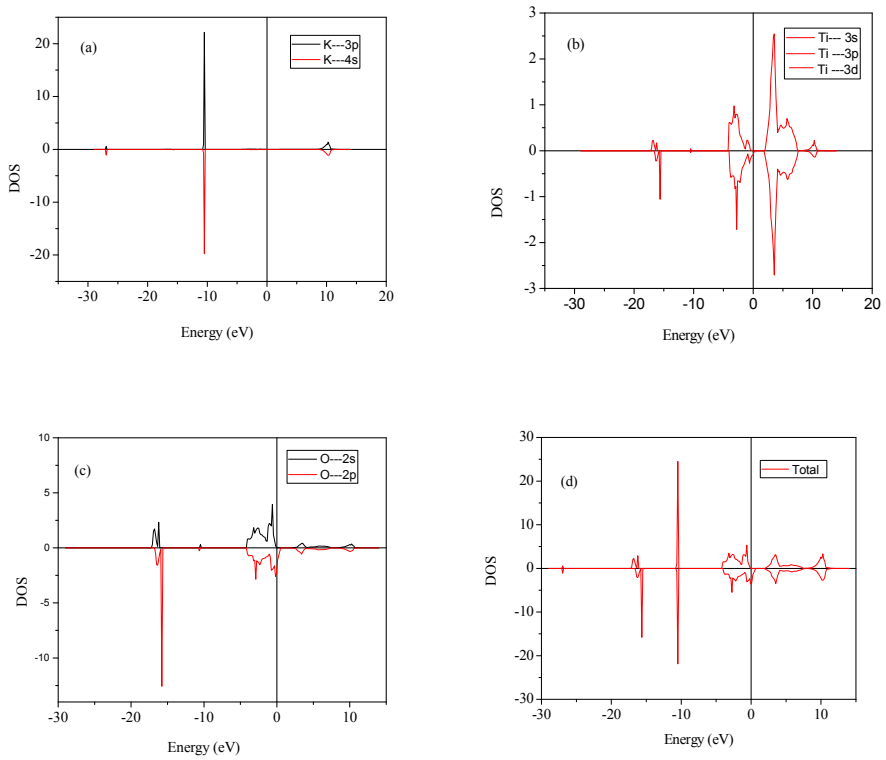

Fig. 6.6 Spin resolved DOS of K (a), Ti (b), O (c) and Total DOS of atoms in k doped $BaTiO_3$ (d)

In semiconducting material, the band gap is of two types, a direct band gap or an indirect band gap [32]. The minimal-energy state in the conduction band and the maximal-energy state in the valence band are each characterized by a certain crystal momentum (*k*-vector) in the Brillouin zone. If the *k*-vectors are the same, it is called a direct gap. If they are different, it is called an indirect gap. For $BaTiO_3$, the highest *y* value (0.0) in valence band is at $x = 0.63$ and lowest *y* value (1.6) in conduction band is at $x = 0$, so that $BaTiO_3$ is an indirect semi conductor. For K doped $BaTiO_3$ also, highest value of *y* in valence

band and lowest value of y in conduction band is not at the same x value, so it also an indirect semi conductor.

6.3.3 The Charge Density Distribution Plots

To describe the electronic structure in solids, the electron density distribution studies were relevant. This can be achieved through the analysis of electron density contour maps. Here the electron densities are plotted from maximum to minimum in different colour. The region of high electron densities had been plotted in red colour while low density region were shown in blue colour. The electron density distribution of a particular plane under investigation can be easily understood from these kinds of two dimensional contour plots [33]. Here the contour plots of both $BaTiO_3$ and K doped $BaTiO_3$ crystals along different crystalline planes *i.e.* (001), (100), (110) and (111) crystalline plane have been shown in Figs 6.7 and 6.8 respectively. The difference in electron density distribution between Ba, Ti and O shows that the bond between Ba and O was ionic while that between Ti and O are partially covalent [31]. This covalent nature of Ti-O bond has been attributed to the hybridization of 3d orbitals of Ti with 2p orbitals of oxygen [34]. Even the charge distribution projected on the (110) and (111) crystalline plane can find the bonding between Ti and O, and this point further confirm the fact that the Ti 3d orbitals interacted strongly with the octahedral oxygen to split into bonding and antibonding states [28].

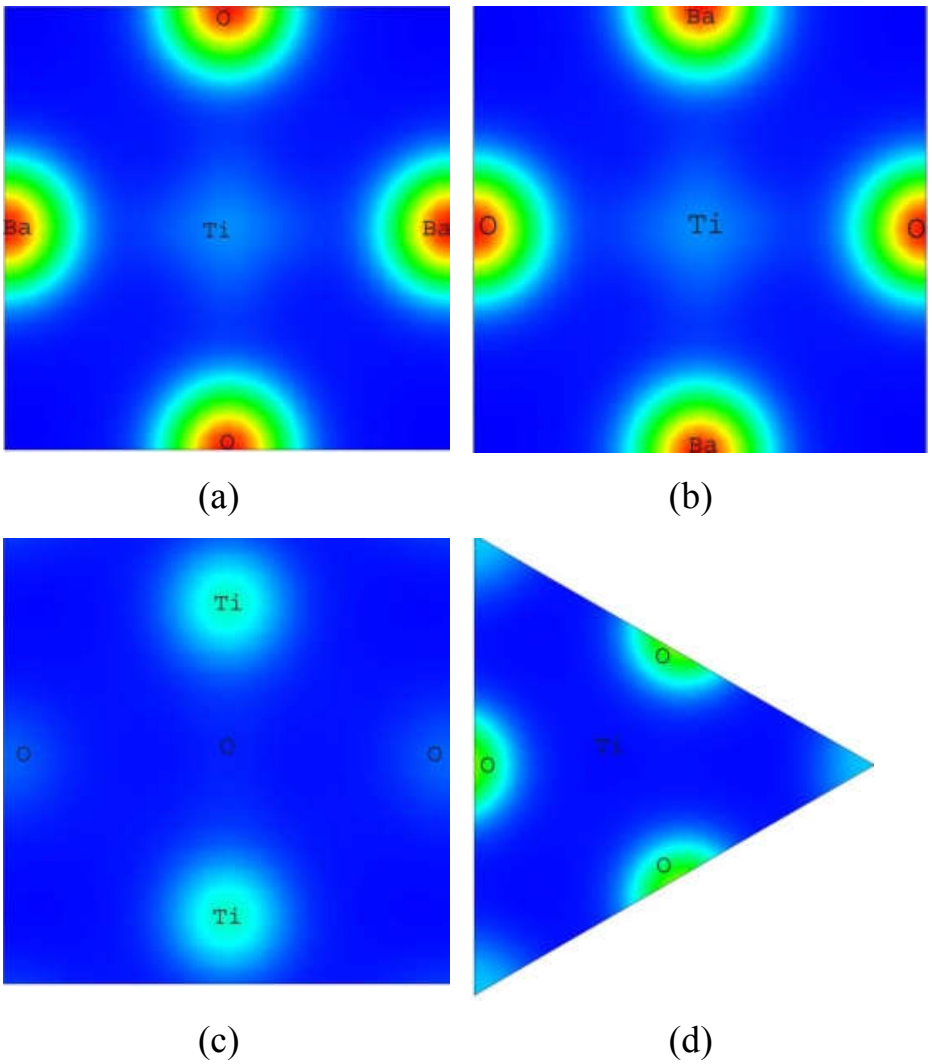

Fig. 6.7 The charge density distribution along 001 (a), 100 (b), 110 (c) and 111 planes (d) of $BaTiO_3$ crystal

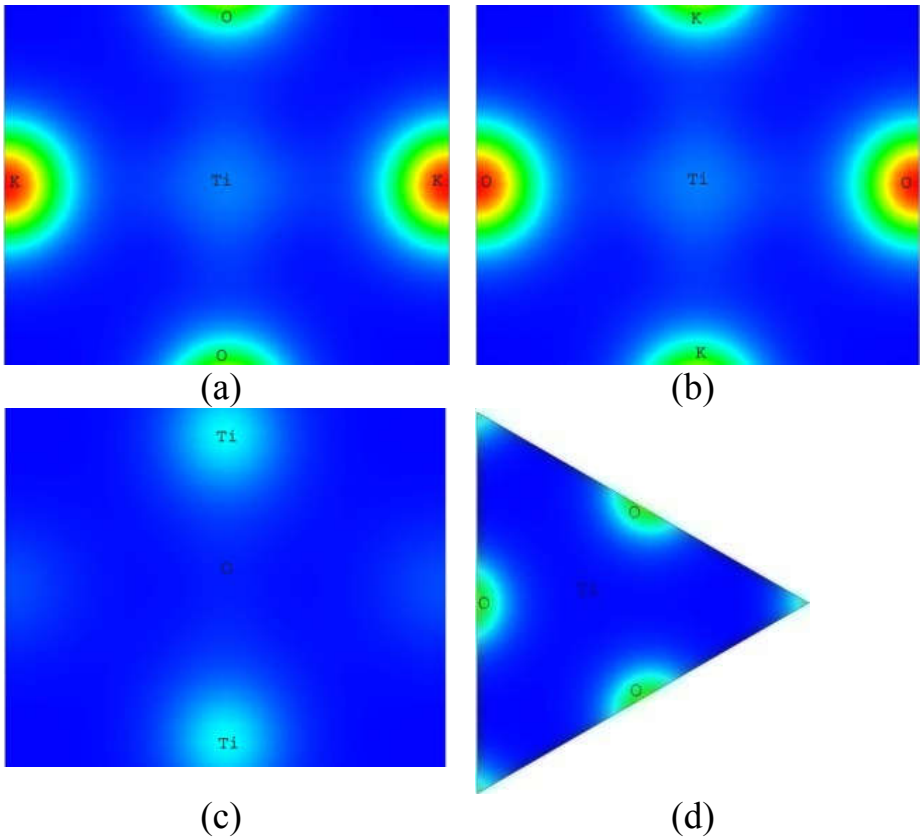

Fig. 6.8 The charge density distribution along 001 (a), 100 (b), 110 (c) and 111 planes (d) of K doped $BaTiO_3$ crystal

6.4. Conclusion

In this study, structure and equation of state of cubic phase of $BaTiO_3$ and K doped $BaTiO_3$ were investigated by means of DFT. Computed results were compared with the available experimental data and theoretical calculations. Generalized gradient approximation exchange and correlation functional as suggested by Perdew and Wang within DFT has been used to study the ground states electronic properties of barium titanate. From the band structure, the band gap

obtained for $BaTiO_3$ and K doped $BaTiO_3$ were 2.24 and 1.93 eV respectively. These optical data compared with UV–vis diffuse reflectance analyses which are in good agreement. The total DOS and partial DOS have been described using the data calculated from the computation, the O 2s states positioned at -17 and Ba 5p states at -10 eV have confirmed the band within the band structure. The strong interaction between O 2p and Ti 3d orbital can be confirmed from the orbital-resolved DOS of Ti and O. In addition the Ti 3d (e_g) states has interplayed with the oxygen octahedral orbitals to split into bonding and antibonding orbital. The topmost band structure was mostly attributed to the Ba 6s states which can be obtained in the partial DOS of Ba. Electronic maps along (001) and (100) planes proved the covalent bonds between Ti and O, and the Ba-O bonds was found to be metallic type.

6.5 References

1. Taib MFM, Hussin NH, Samat MH, Hassan OH, Yahya MZA. Structural, electronic and optical properties of $BaTiO_3$ and $BaFeO_3$ from first principles LDA+U study. Int. J. Electroact. Mater. 2016;4: 14 – 17.

2. Sanna S. Barium titanate ground and excited-state properties from first-principles calculations. Phys. Rev. 2011;83:54112-18.

3. Razak NAA, Zabidi NA, Rosli AN. A first principle study of band structure of tetragonal barium titanate. AIP Conf. Proc. 2017;1875:020017.

4. Cai MQ, Yin Z, Zhang MS. First-principles study of optical properties of barium titanate, J. Appl. Phys. Lett. 2003;83:2805-07.

5. Lixia C, Yuanhao T, Zhang H. First-principles investigation of transition metal atom M (M = Cu, Ag, Au) adsorption on CeO_2 (110). Phys. Chem. Chem. Phys. 2012;14:1923-33.

6. Salehi H, Hosseini SM, Shahtahmasebi N. Band structure of tetragonal $BaTiO_3$. Eur. Phys. J. B. 2003;32:177-80.

7. Patino E, Stashans A. Structural and electronic effects in $BaTiO_3$ due to the Nb doping. Ferroelectrics. 2001;256:189-200.

8. Duque C, Stashans A. Oxygen-vacancy defects on $BaTiO_3$ (001) surface: a quantum chemical study. Physica. B. Condens. Matter. 2003;336:227-35.

9. Kresse G, Furthmuller J. Efficient iterative schemes for ab initio total-energy calculations using a plane-wave basis set. Phys. Rev. B. 1996;54:11169-86.

10. Sholl DS, Steckel JA. Density Functional Theory: A Practical Introduction. Wiley, New York, 2009.

11. Kohn W, Sham LJ. Self-consistent equations including exchange and correlation effects. Phys. Rev. 1965;140:1133-38.

12. Kumar L, Monkhorst HJ, Harris FE. Electronic structure studies of solids. III. Hartree-Fock hand functions and energies for cubic lithium crystals. Phys. Rev. B**.** 1972:4084:3-99

13. Kresse G, Hafner J. Norm-conserving and ultrasoft pseudopotentials for first-row and transition elements. J. Phys. Condens. Matter. 1994; 6:8245-57.

14. Uludogan M, Agın TC. First principles approach to $BaTiO_3$. Turk. J. 2006;30:277-285.

15. Wahl R, Vogtenhuber D, Kresse G. $SrTiO_3$ and $BaTiO_3$ revisited using the projector augmented wave method: Performance of hybrid and semilocal functional. J. Phys. Rev. 2008;78:104116.

16. Khenata R, Sahnoun M, Baltache H, Rerat M, Rashek AH, Illes N, Bouhafs B. First-principle calculations of structural, electronic and optical properties of $BaTiO_3$ and $BaZrO_3$ under hydrostatic pressure. Solid State Commun. 2005;136:120–25.

17. Hohenberg P, Kohn W. Inhomogeneous Electron Gas. Phys. Rev. 1964;136:864-71.

18. Monkhorst HJ. Hartree Fock density of states for extended systems. Phys. Rev. **B.** 1979;2**0:**1504-20.

19. Payne MC, Teter MP, Allan DC, Arias TA, Joannopoulos JD. Iterative minimization techniques for ab initio total-energy calculations: molecular dynamics and conjugate gradients. Rev. Mod. Phys. 1992;64:1045-97.

20. Kresse G, Joubert J. From ultrasoft pseudopotentials to the projector augmented-wave method. Phys. Rev. B. 1999;59:1758-75.

21. Monkhorst HJ, Pack JD. Special points for Brillouin-zone integrations. Phys. Rev. B. 1976;13:5188-92.

22. Grinberg I, Ramer NJ, Rappe AM. Transferable relativistic Dirac-Slater pseudopotentials. Phys. Rev. B. 2000;62:2311-14.

23. Rappe AM, Rabe KM, Kaxiras E, Joannopoulos JD. Optimized pseudopotentials. Phys. Rev. B. 1990;41:1227-30.

24. Kay HF, Vousden P. Symmetry changes in barium titanate at low temperatures and their relation to its ferroelectric properties. Philos. Mag. 1949;40:1019–40.

25. Kwei GH, Lawson AC, Billinge SJL. Structures of the ferroelectric phases of barium titanate. J. Phys. Chem. 1993;97:2368–77.

26. Bagayoko D, Zhao GL, Fan JD, Wang JT. Ab initio calculations of the electronic structure and optical properties of ferroelectric tetragonal $BaTiO_3$. J. Phys. Condens. Mat. 1998;10:5645–55.

27. Li Z, Iitaka T, Tohyama T. Pressure-induced ferromagnetism in cubic perovskite $SrFeO_3$ and $BaFeO_3$. Phys. Rev. B. 2012;86:94422.

28. Feng H, Liu FM, Electronic structure of barium titanate: an abinitio DFT study, Department of physics, school of sciences, Beijing University of Aeronautics &. Astronautics, Beijing. 2007; 100083.

29. Gao H, Cao J. Liu L, Yang Y. Theoretical investigation on the structure and electronic properties of barium titanate. J. Mol. Struct. 2011;1003:75-81.

30. Uchino K, Sadanaga E, Hirose T. Dependence of the crystal structure on particle size in barium titanate. J. Am. Ceram. Soc. 1989; 72:1555–58.

31. Saha S, Sinha TP, Mookerjee A. Electronic structure, chemical bonding, and optical properties of paraelectric $BaTiO_3$. Phys. Rev. B. 2000;62:8828-34.

32. Fan HY. Temperature dependence of the energy gap in semiconductors. Phys. Rev.1951;82:900–05.

33. Siraji AA, Alam MS. Improved calculation of the electronic and optical properties of tetragonal barium titanate. J. Electron. Mater. 2014;43:1443–49.

34. Furuta T, Miura K. First-principles study of ferroelectric and piezoelectric properties of tetragonal $SrTiO_3$ and $BaTiO_3$ with in plane compressive structures. Solid State Commun. 2010;150:2350-53.

.

CHAPTER 7

CONCLUSION AND FUTURE PERSPECTIVES

The thesis deals with the solid-state thermal decomposition studies on barium titanyl oxalate mixtures, in view of the application of its decomposition products; mixed metal titanates. Among the different synthetic routes to prepare metal titanates, the thermal decomposition of metal titanyl oxalates is important mainly due to the easiness in the synthesis, phase purity, composition, *etc.*, of the decomposition products. The thermal decomposition of metal titanyl oxalate to metal titanates with no interfering solid byproducts might be a highly desirable outcome. An important conclusion that can be drawn from this work is that the mixed metal titanates synthesized from respective metal titanyl oxalates are highly desirable for applications than the simple metal oxides.

As of the first, barium titanyl oxalate was prepared, characterized and thermally decomposed. The first step, thermal dehydration data were used to elucidate the kinetics of that reaction. The differential scanning calorimetric data were analyzed by modern kinetic investigation procedures: isoconversional/ model free methods such as Bosewell, Tang, Starink$^{1.95}$and Starink$^{1.92}$ method, using multi heating rates to find out the kinetic parameters of the thermal dehydration and the values are found to be compatible with each other. The activation energy (E_a) values of the decomposition reactions obtained by Bosewell method is close to that obtained by Tang method and also Starink$^{1.92}$ method. The kinetic analysis of prepared barium titanyl oxalate shows a considerable variation in average activation energy with increase in the conversion value. The E_a value is found to increase with extent of conversion which indicates the complexity of the reaction. The morphology of the prepared sample explained on the experimental result obtained from SEM, TEM, FT-IR, XRD analyses.

The study presents an in depth analysis of the characterization and the effect of doping of potassium titanyl oxalate with barium titanyl oxalate (BTO) and the multistage thermal decomposition kinetics and mechanism. Kinetic deconvolution procedure was utilized to study the overall kinetics. The study indicates the transformation of cubic $BaTiO_3$ into tetragonal phase and the introduction of K^+ ion into the lattice of BTO enhanced the thermal stability. Subsequently, the thermal decomposition of barium titanyl oxalate yields barium titanate nano particles at the temperature range of 973-1173 K and that particular stage was deconvoluted into three steps has been studied by differential scanning calorimetric analysis under non-isothermal heating conditions. Coats & Redfern and Ozawa methods were used to determine the apparent activation energies of these multi step thermal processes. The study details the characterization of synthesized BTNPs and their oxalate precursors and to predict the physico-geometrical reaction mechanism, empirical kinetic model functions such as phase nucleation and growth-type *JMA (m)* model.

The study also presents the characterization and application studies of the decomposition products of the as prepared mixed metal titanyl oxalates of barium and potassium. The nano mixed metal oxides of barium and potassium were tested for anti bacterial efficiency as well as conductance behavior. The presence of different ratios of mixed metal oxide nanoparticles increases the antibacterial activity significantly. The conductivity studies using four probe methods helped to reveal the influence of dopant which enhances the semiconducting property of the perovskite material, and cost effective semiconductor for electronic applications. The production method adopted device fabrication is simple, cost-effective, and eco-friendly.

Study of conducting property of doped samples and their stoichiometry and conducting phenomena by experimental and theoretical methods using VASP code is discussed. The aim of this work is to develop an understanding of fundamental interactions which underpin the use of metal oxide nano particles as multifunctional applications. We obtained the lattice constant '*a*', volume, band gap which agree well with the experimental data for cubic phase, especially for the band structure parameters. The role of band structure calculation as regards the optical properties of $BaTiO_3$ is also discussed.

The humidity control is essential for various fields of industry as well as human life. $BaTiO_3$ is hygroscopic in nature, absorbs water molecules, and it has humidity sensitive characteristics. Thus with its high ease of process ability and also hygroscopic BTNPs has the potential to form good humidity sensing element. As part of this work we have a plan to fabricate humidity sensor and to study the electrical characteristics of the samples.

The result of investigations presented here indicates that the major objective of the work has been accomplished. This study also reveals the scope for lot of future investigation possibilities in the electronic applications of doped perovskite structure. Further the conductivity measurements are to be evaluated to understand the materials potential in electronic devices. These studies provide a starting point for the exploitation of the particular oxalates for the growing industrial world.

PUBLICATIONS

Peer-reviewed Research Publication

Sl. No	Journal Name, Volume,Number, Year	Title of the article	Publisher	Impact factor
1	Journal of Materials Research Bulletin 94 (2017) 231-240	Kinetic modelling of formation of K^+ doped $BaTiO_3$ bones from barium titanyl oxalate *via* multi stage thermal decomposition	Elsevier ISSN 0025-5408	2.527
2	Journal of Thermal Analysis and Calorimetry doi.org/10.1007S10973-018-7777-7	Kinetic study for the multistep thermal behavior of barium titanyl oxalate prepared *via* chemical precipitation method	Springer ISSN 1388-6150	2.21
3	Thermochimica Acta (Under revision)	Synthesize of $BaTiO_3$ nanoparticles: A multi dimensional approach.	Elsevier ISSN 0040-6031	2.2
4	Journal of solid-state Chemistry (Submitted)	A comparative experimental and theoretical study of the electronic structure of $BaTiO_3$ and K doped $BaTiO_3$	Elsevier ISSN 0022-4596	2.3

5	Journal of Thermal Analysis And Calorimetry (Submitted)	Kinetics and thermodynamics of the formation of $BaTiO_3$ nanoparticles *via* multi stage thermal decomposition of oxalate precursors	Springer ISSN 1388-6150	2.21

CONFERENCE PAPERS

I International Conferences

1 Sindhu N. V., K. Muraleedharan, A comparative study of the multistep kinetic behavior of the thermal dehydration of barium titanyl oxalate, MESMAC International conference, MES Mampad College, Palakkad, Kerela, 9-11 January 2018.

2 Sindhu N. V., K. Muraleedharan, Thermal decomposition kinetics of $BaTiO_3$ and doped $BaTiO_3$ synthesized by thermal decomposition, MESMAC International conference, MES Mampad College, Palakkad, Kerela, 9-11 January 2018.

3 Sindhu N. V., K. Muraleedharan, Kinetics in solid-state synthesis of K+doped barium titanyl oxalate,International seminar, AMBIENTE 2017, St. Joseph's college for Women, Alappuzha, Kerala, 18-19 December 2017.

4 Sindhu N. V., K. Muraleedharan, Synthesis and characterization of K^+doped $BaTiO_3$ via oxalate decomposition method, International Conference on Emerging frontiers in chemical sciences -2017, Farook College, Calicut, Kerala, 23-25 September 2017.

5 Sindhu N. V., K. Muraleedharan, Thermodynamic and kinetic study on the formation of $BaTiO_3$ nanoparticles prepared *via* thermal decomposition, International conference on advanced

materials science and technology-2017, Bennari Amman institute of technology. Tamil Nadu, 17-19August 2017.

6 Sindhu N. V., K. Muraleedharan, Thermal decomposition kinetics and the effect of doping on the formation of barium titanate, International conference on advanced materials science and Technology-2017, Bennari Amman institute of technology. Tamil Nadu, 17-19August 2017.

7 Sindhu N. V., K. Muraleedharan, Study of multistep kinetic behavior of the thermal dehydration of barium titanyl oxalate, Proceedings of BRNS& CSIR sponsored international conference on energy, environment and advanced materials for a sustainable future -2017, Kongu Engineering College, Perundurai, Erode.Tamil Nadu, 23-24 May 2017.

8 Sindhu N. V., K. Muraleedharan, Thermal decomposition kinetics of formation of bone shaped $BaTiO_3$ from barium titanyl oxalate and the effect of doping of potassium titanyl oxalate, Proceedings of BRNS& CSIR sponsored international conference on energy, environment and advanced materials for a sustainable future -2017, Kongu Engineering college, Perundurai, Erode.Tamil Nadu, 23-24 May 2017.

II National Conferences

1 Sindhu N. V., K. Muraleedharan, Kinetic behavior of the thermal decomposition of barium titanyl oxalate, National seminar, Theoretical and Experimental approaches for exploring Advanced Materials, Govt. Arts & Science College, Calicut, 13-14 December 2017.

2 Sindhu N. V., K. Muraleedharan, Thermal, kinetic and antimicrobial studies of $BaTiO_3$ nanoparticles synthesized via oxalate decomposition, 5 th National conference on condensed matter physics and applications 2017, Manipal university, 22 September 2017.

3 Sindhu N. V., K. Muraleedharan, Dehydration and decomposition kinetics of barium titanyl oxalate. National seminar on frontiers in chemistry 2017, Dept. of chemistry, University of Calicut, 28-30 March 2017.

4 Sindhu N. V., Sarada .K, K. Muraleedharan, Catalytic effect of metal mixed oxides of lanthanum and copper on the thermal decomposition of ammonium perchlorate, Proceedings of the National Seminar on Advances in biomedical science and engineering, NIT Calicut, 17-18 October 2016.

5 Sindhu N. V., K. Muraleedharan, Synthesize of $BaTiO_3$ nanoparticles, UGC sponsored national seminar on new materials in chemistry 2015, NMC 2015, Dept. of chemistry, University of Calicut, 30-31 January 2015.

Remarkable recognition

Best Oral Presentation Award- International conference on advanced materials science and technology-2017, Bennari Amman institute of technology, Tamil Nadu

Materials Research Bulletin 94 (2017) 231–240

Contents lists available at ScienceDirect

Materials Research Bulletin

journal homepage: www.elsevier.com/locate/matresbu

Kinetic modelling of formation of K^+ doped $BaTiO_3$ bones from barium titanyl oxalate *via* multi stage thermal decomposition

Sindhu N.V., K. Muraleedharan*

Department of Chemistry, University of Calicut, Calicut, 673635, India

ARTICLE INFO

Article history:
Received 14 March 2017
Received in revised form 23 May 2017
Accepted 27 May 2017
Available online 10 June 2017

Keywords:
Decomposition kinetics
Differential scanning calorimetry
Kinetic deconvolution
KAS method

ABSTRACT

The thermal decomposition kinetics of formation of bone shaped $BaTiO_3$ from barium titanyl oxalate (BTO) and the effect of doping of potassium titanyl oxalate (1×10^{-4} mol%) with BTO upon the reaction pathway and the mechanism were studied at four different heating rates: 2, 5, 7 and 10 K min^{-1} under linear non-isothermal heating program using DSC technique in an inert atmosphere (N_2). Kinetic deconvolution procedure was applied to perform the overall kinetics of the formation of doped and undoped $BaTiO_3$. The prepared samples and their decomposed products were identified and characterized by means of FT-IR, FT-Raman, XRD, SEM, TEM and SAED pattern. Activation energy needed for each resolved stage of the thermal decomposition was calculated by the KAS method in the temperature range 303–873 K. XRD pattern at different stages of thermal decomposition indicates that cubic $BaTiO_3$ is transformed into tetragonal phase. The introduction of K^+ −ion into the lattice of BTO enhances the thermal stability of BTO and shows a high energy reaction pathway revealing the complex mechanism.

1. Introduction

Nano-materials which form the most challenging areas of the scientific and technological research are still being explored because of their tremendous possibilities in generating novel shapes, structures and unusual phenomena. Currently, researchers in chemistry, physics, biochemistry, and engineering are exploring a new class of nano sized materials for the applications in electronics, optics, catalysis and for solar light conversion, etc [1]. The chemical and catalytic reactivity of a solid state material depends on its method of preparation and the structural and electronic imperfections. Chemical processes involving the chemical transformation of solids play an important role in research technology, as sophisticated solids can be produced by thermal decomposition reaction of precursory solids. The processes of forming titanates, in crystalline mixtures have become very important in the ceramic industry and other technologies. The "*first ferroelectric ceramic*", barium titanate (BT) is a good candidate for various applications due to its excellent dielectric, ferroelectric and piezoelectric properties [2]. It is the one member of perovskite family having the general formula ABO_3. The crystalline size of BT determines the final crystal structure of $BaTiO_3$. It has rhombohedral, orthorhombic, cubic and tetragonal phases. The cubic structures are paraelectric while rhombohedral, orthorhombic and tetragonal phases are ferroelectric in nature [2]. Paraelectric cubic phase can be transformed into ferroelectric tetragonal phase at its Curie temperature (around 393 K). The ferroelectric and dielectric properties of BT are correlated with its size. Nano-sized BT possessed higher activity, potential for device miniaturization and enhanced dielectric properties. It is an important raw material for electronic devices such as multi layered ceramic capacitors and nonlinear resistors [3]. It finds vast applications in transducers, actuators, capacitors and memories [2]. Takin et al. [4] explored the applications of barium titanate core–gold shell nanoparticles for hyperthermia treatment against cancer cells. They proposed that this nano shells have suitable cytocompatibility at concentrations up to 50ηg/L. Recently, it has been extensively studied particularly for its application as a capacitor material in down- sized portable machines and dynamic random access memory (DRAM) devices. $BaTiO_3$-based ceramics have found their application in the design of microwave tunable devices [5,6].

Many methods such as so-gel [7], hydrothermal [8], combustion [9,10], crystal growth [11], thermal decomposition [12] and other different chemical routes [13] were used for the BT synthesis. Among these, thermal decomposition using oxalate precursor has been widely used due to its simplicity and the precise

* Corresponding author.
E-mail address: kmuralika@gmail.com (K. Muraleedharan).

http://dx.doi.org/10.1016/j.materresbull.2017.05.056
0025-5408/

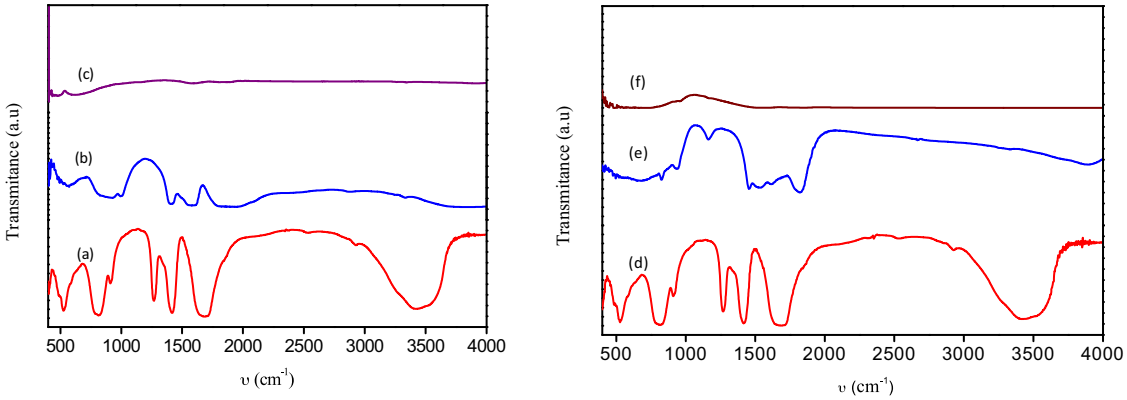

Fig. 1. The FT-IR spectra of sample A_1 (a), A_1 calcined at 628 K for 1 h (b), A_1 calcined at 1023 K for 1 h (c), sample A_2 (d), A_2 calcined at 628 K for 1 h (e) and A_2 calcined at 1023 K for 1 h (f).

stoichiometry of the produced BT phase. Thermal decomposition of alkaline earth metal titanyl oxalate yield nano titanate particles. The decomposition proceeded through five steps and was not affected much by surrounding gaseous atmosphere. The first step is the dehydration of the tetra hydrate which was followed by low temperature decomposition of the oxalate groups. In the temperature range of 393–453 K, carbon monoxide is evolved with the formation of a transient intermediate substance containing both carbonate and oxalate groups. The oxalate groups were completely destroyed in the range of 453–523 K, resulting in the formation of a carbonate which retains free CO_2 in the matrix. The trapped CO_2 was released in the temperature range of 523–723 K. The final decomposition of carbonate takes place between 873 and 1023 K and yield barium titanate. Gopalakrishnamurthy et al. [14] investigated the evolution of water and CO_2 vapours during the thermal decomposition of BTO and the effect of doping and mixing conditions of the reactant molecules on the reactivity of the system. Doping with the metal ions and other pre-treatments of samples has important effects on the structural, chemical and physical properties of the solids, which might alter the kinetics of the reaction mechanism. Upon doping A^+ or B^- sites in barium titanyl oxalate or their oxides, the catalytic activity, ionic and electronic conductivity and flexible physical and chemical properties can be altered, that lend a hand for utilization in various applications [15–17]. Ni^{2+} and Fe^{2+} doped $BaTiO_3$ showed enhanced dielectric permittivity than undoped $BaTiO_3$ [18]. This can be ascribed due to the change in the lattice parameters of the specimen.

There are several studies concerning the determination of kinetic parameters and possible physicochemical or physico-geometrical reaction models through the formal kinetic analysis of thermal decomposition process [19–21]. The kinetics of thermal decomposition of solids are restrained by interactions between concurrent and consecutive processes related with different physicochemical events, including surface nucleation, destruction of reactant crystals, crystal growth of the product solid and diffusional removal of gaseous product[19]. The knowledge of understanding the possible physicochemical events occurring during thermal decomposition of BTO is essential for the tuning of $BaTiO_3$ nanoparticle.

This study focus on the elucidation of the kinetics and mechanism of thermal decomposition of barium titanyl oxalates, and K^+ – doped barium titanyl oxalates by the DSC technique flowing N_2 atmosphere. The kinetic deconvolution procedure was used to yield the dependency of the E_a on the extent of conversion and the most probable kinetic model.

2. Experimental

2.1. Materials

AnalaR grade barium nitrate ($Ba(NO_3)_2$) (Merck, India; assay $\geq$ 99.9%) and potassium titanyl oxalate ($K_2TiO(C_2O_4)_2$) (BHO Laboratory England; assay $\geq$ 99.9%) were used in the present investigation.

2.2. Preparation of doped and undoped BTO

Sample A_1, barium titanyl oxalate (BTO) was synthesized by the precipitation reaction of equi molar aqueous solution of barium

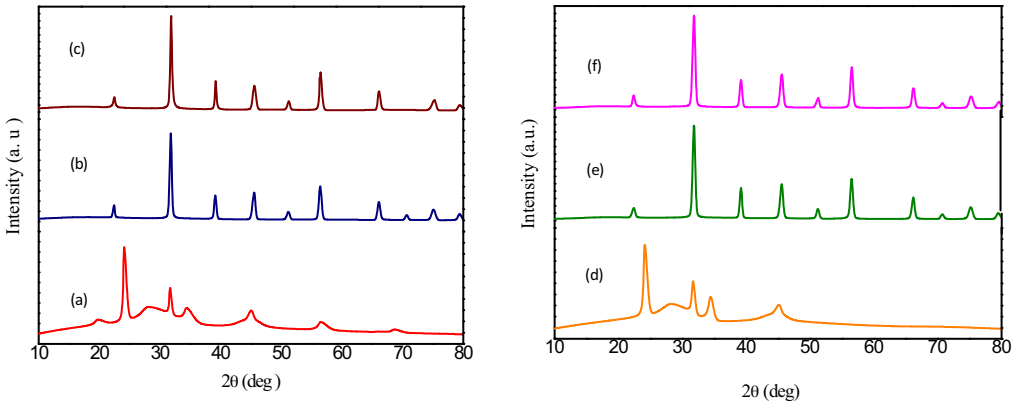

Fig. 2. The XRD pattern of sample A_1 (a), A_1 calcined at 773 K (b), A_1 calcined at 1023 K for 1 h (c), sample A_2 (d), A_2 calcined at 773 K (e) and A_2 calcined at 1023 K for 1 h (f).

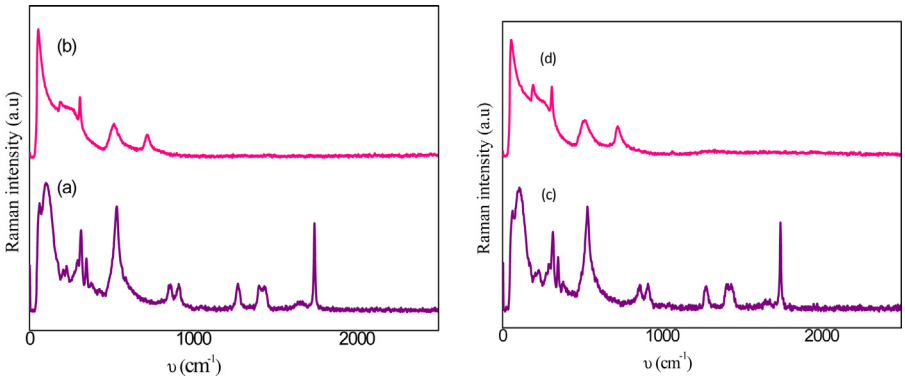

Fig. 3. The FT Raman spectra of sample A_1 (a), A_1 calcined at 1023 K for 1 h (b), sample A_2 (c) and A_2 calcined at 1023 K for 1 h (d).

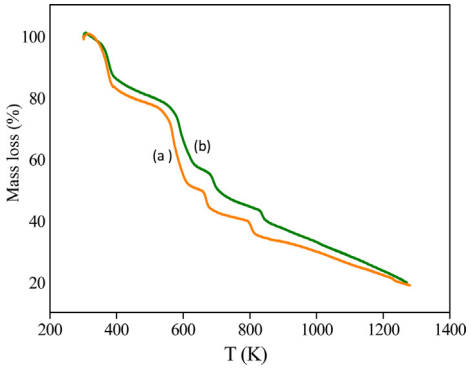

Fig. 4. The TG curves for the thermal decomposition of samples (m_0 = 5.3 mg) at 10 K min^{-1}; sample A_1 (a) and sample A_2 (b).

nitrate and potassium titanyl oxalate. The white precipitate of BTO was obtained, filtered and washed with deionised water and kept in an air oven at 50 °C for 24 h. K^+- doped sample of BTO (sample A_2) was prepared as per the following procedure; 10 g of BTO was dissolved in 230 mL of distilled water at boiling temperature in a 500 mL beaker. 10 mL of a solution containing the desired quantity of K^+ (10^{-4} mol%) was added to the hot solution so as to achieve a total volume of 240 mL. The solution was then cooled slowly to room temperature. The beaker containing the solution was covered using a clean uniformly perforated paper and kept in an air oven at a temperature of 50 °C over a period of 6–7 days to allow the slow crystallization of doped sample by the evaporation. The resulting crystals were air dried and powdered in an agate mortar. The samples prepared (doped and control) were sieved through the mesh and fixed the particle size in the range of 45–53 μm.

2.3. Methods

The Fourier Transform Infrared (FT- IR) spectrum of the samples in KBr pellet was recorded using a JASCO FT-IR-4100 instrument. The sample was first compressed with KBr into pellet and analyzed as KBr disk from 400 to 4000 cm^{-1}. The instrument offers high sensitivity; maximum resolution (0.9 cm^{-1}) and high signal-to-noise ratio (22,000:1).The X-ray diffraction (XRD) measurements of the samples were taken on a RIGAKU MINI FLEX-600 X-ray diffraction spectrophotometer using Cu Ka (1.5418A°) radiation. FT-Raman spectroscopy of the samples were taken on BRUKER MultiRAM FT Raman spectrometer, range 3600 to 50 cm^{-1}, laser excitation 1064 nm (standard) or 785 nm (optional). It is equipped with Rayleigh filters, primary filters, room temperature 'InGaAs' detector and 'Si' avalanche detector. The Scanning Electron Microscopic (SEM) analyses of all the samples studied were performed with SEM-EDS combination using JEOL Model JSM – 6390LV, JEOL Model JED – 2300. The instrument offers a resolution of 3 nm (Acc V 30 KV, WD 8 mm, SEI), 8 nm(Acc V 3.0 KV, WD 6 mm, SEI) and magnification of 5 to 300,000 × (Both in high and low vacuum mode). For the present investigation, the imaging techniques employed was secondary electrons (SE), backscattered electrons (BSE) and energy-dispersive X-ray analysis (EDXA). The Transmission electron microscopic (TEM) analysis of the particles was achieved by using a JEOL Model JEM 2100 field emission transmission electron microscope operated at 200 kV with a 0.18 nm resolution. The thermo gravimetric (TG) analysis of the samples was made on a T.A. thermal analyzer, model: TGA Q50 v20.2 Build 27 in the temperature range 303–1373 K at a heating rate 10 min^{-1}. The operational characteristics of the TG system are as follows: atmosphere: flowing air, at a flow rate of 60 mL min^{-1}; sample mass: 5.6 mg; and sample pan: silica. Duplicate runs were made under similar conditions and found that the data overlap with each other, indicating satisfactory reproducibility. The differential scanning calorimetric (DSC) measurements of the

Table 1
Mass loss data of sample A_1 and sample A_2.

Decomposition steps	Temperature range (K)	Sample A_1 (Mass loss%)	Sample A_2 (Mass loss%)
1	308–463	17.62	16.94
2	463–523	2.79	3.75
3	523–753	20.52	19.94
4	753–893	5.13	6.77
5	893–1053	6.99	7.92
Total	308–1053	53.05	55.32

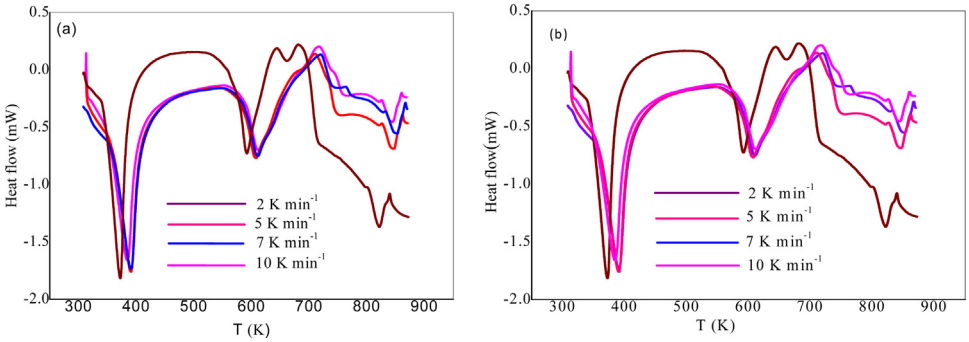

Fig. 5. The DSC curves for the thermal decomposition of sample A_1 ($m_1 = 5.01 \pm 0.01$ mg) (a) and sample A_2 ($m_2 = 5.01 \pm 0.02$ mg) (b) at different β in N_2 (50 mL min^{-1}).

samples were done in the temperature range 303–870 K on a Mettler Toledo DSC822e. The operational characteristics of the DSC system are as follows: atmosphere: flowing N_2 at a flow rate of 50 mL min^{-1}; sample mass: 5.1 mg; and sample holder: aluminium.

3. Results and discussion

3.1. Sample characterization

Fig. 1 represents the FT-IR spectra of undoped BTO (A1), BTO calcined at 628 and 1023 K for 1 h, sample A_2 and A_2 calcined at 628 and 1023 K for 1 h. For the sample A_1 (Fig. 1a), the principal band (ν_{as}, —C=O) occurs at 1686 cm^{-1}. The FTIR spectrum of sample A_1 calcined at 628 K (Fig. 1b) in vacuum for 1 h shows the appearance of an intense band at 2339 cm^{-1} which can be attributed to the asymmetric stretching frequency of free CO_2. The FT-IR spectra of the sample calcined at 1023 K was presented in Fig. 1c, which represents the undoped $BaTiO_3$. The FT-IR absorption spectrum of K^+- doped BTO crystalline particle (sample A_2) is shown in Fig. 1d. The broad band extending from 2800 to 3600 cm^{-1} is assigned to the symmetric and asymmetric stretching modes of the water molecules. The strong band appearing in the IR spectrum around 1615 cm^{-1} can be identified as the asymmetric stretching vibrations of CO groups of the $C_2O_4^{2-}$ ions together with the bending mode of water. Fig. 1e displays the FT-IR spectrum for doped sample A_2 calcined at 628 K. The strong peak around 1316 cm^{-1} is also assigned to the asymmetric stretching of CO groups (Fig. 1e). The strong bands around 495 and 796 cm^{-1} are due to the combined effect of the in-plane deformation mode of OCO and MO bond and the weak one around 582 cm^{-1} observed in the spectrum represent the wagging mode [22–24]. The FT-IR spectroscopic analysis of crystals of $Ba_{1-x}K_xTiO(C_2O_4)_2{\cdot}4H_2O$ confirmed the presence of functional groups associated with the oxalate ligands and the metal–oxygen bond. Fig. 1f represents the FT-IR spectrum of K^+-doped $BaTiO_3$. FT-IR spectra displays two strong absorption peaks at 441 and 563 cm^{-1} in control (Fig. 1c); and 430 and 557 cm^{-1} in doped samples (Fig. 1f). The former peaks (441 and 430 cm^{-1}) were assigned to Ti-O bending vibrations along the polar axis whereas the latter peaks (563 and 557 cm^{-1}) were assigned to Ti-O stretching vibrations. These peaks suggest that both doped and control sample had pure tetragonal phase [25,26]. Further, the peaks at 868 cm^{-1} in control and doped sample were assigned to stretching vibrations of metal-oxygen. The peaks displayed at 1724 and 3429 cm^{-1}, in control and doped sample were attributed to moisture absorption by samples.

Powder X-ray diffractometer (XRD) was used for the phase identification and the relative percentage of different phases of the prepared samples. The diffraction patterns were recorded over the angular range 2θ from 20 to 80°. Using the XRD data of the samples, particle size and lattice parameters were estimated. Fig. 2a exhibits the XRD pattern of sample A_1 and sample A_1 calcined at 773 and 1023 K (Figs. 2b & c respectively). Before the calcination of samples A_1 & A_2 (Figs. 2a & d), amorphous phase was observed due to the presence of carbon atoms and water in the mixture. After calcination at 773 K, the crystalline phase with cubic structure (a = 4.0073Å) was appeared (Fig. 2b). The calcination of sample A_1 at 1023 K for 1 h tend to produce the crystalline phase with tetragonal phase (a = b = 3.999 and c = 4.0053 Å) (Fig. 2c).

Fig. 2d displays the XRD pattern of K^+ doped BTO (sample A_2) and its decomposed products at 773 and 1023 K (Figs. 2e & f respectively). It was observed that the formation of $BaTiO_3$ from BTO completes at about 773 K. The products of the samples A_1 and A_2 calcined at 773 K consist of pure cubic $BaTiO_3$ (Figs. 2b & e respectively). The products of the samples A_1 and A_2 calcined at 1023 K (Figs. 2c & f) indicate that the cubic form possibly transforms to tetragonal structure. This was revealed by the asymmetry introduced in the peaks at the 2θ values corresponding to 45.26, 50.90, 56.14, 74.89 and 79.5^0 respectively, which confirms the transformation of the cubic phase to the tetragonal phase [27]. Figs. 3a & c show the FT-Raman spectra of the sample A_1 and A_2 at room temperature. Sample A_1 exhibits the tetragonal structure belonging to the space group C_{4v} symmetry. The peak observed at 305 cm^{-1} corresponds to the E (TO_2) phonon mode of tetragonal

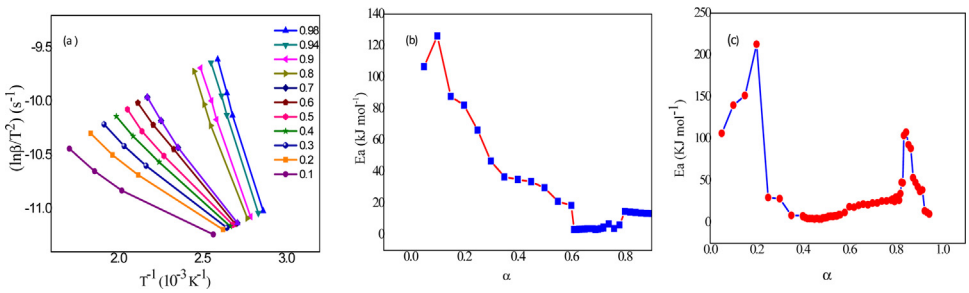

Fig. 6. Typical linear least – squares plot of KAS method for the sample A_1 (a) and the plot of *Ea vs α* for the samples A_1 (b) and A_2 (c).

Table 2
Initial kinetic parameters used for the kinetic deconvolution analysis of the thermal decomposition of samples A_1 and A_2 under linear non-isothermal conditions.

Sample	i	C_i	Ea_i (kJ mol $^{-1}$)	A_i (sec^{-1})	f_i (α)
	1	0.560	55.83	6.34×10^{21}	R (n);n = 1
A_1	2	0.113	39.80	2.33×10^{6}	R (n);n = 0.99
	3	0.250	119.58	1.78×10^{16}	R (n);n = 1.1
	4	0.022	179.97	1.15×10^{25}	JMA (m);m = 1
	5	0.055	41.34	5.71×10^{14}	JMA (m);m = 1.2
A_2	1	0.400	85.63	1.85×10^{28}	R (n);n = 1
	2	0.085	43.31	2.70×10^{5}	R (n);n = 0.995
	3	0.075	114.92	1.70×10^{3}	R (n);n = 1.2
	4	0.220	236.07	1.52×10^{15}	JMA (m);m = 1
	5	0.060	325.68	9.64×10^{18}	JMA (m);m = 1.3
	6	0.160	53.98	5.30×10^{20}	JMA (m);m = 0.98

BTO. The A_1 (TO_1), A_1 (TO_2), A_1 (TO_3) and A_1 (LO_3) modes were observed at about 180, 270, 516 and 720 cm^{-1} respectively [28]. The FT-Raman spectra obtained for the sample A_2 did not show any remarkable shift in wavelength. This can be attributed to the effective doping of K^+- ion into the lattice structure of BTO. It was also seen that all Raman modes are weaker and broader with change in the concentration. Figs. 3b & d show the FT-Raman spectra of decomposed product (calcined at 1023 K) of both the samples A_1 and A_2. For the sample A_1, the spectrum consists of peaks at 52, 174, 260, 306, 547 & 717 cm^{-1} and for the sample A_2, the spectrum made up of peaks at 185, 308, 515, 728 cm^{-1}. This confirms that all are characteristic bands of the tetragonal phase $BaTiO_3$. The strong peaks at 174 and 547 cm^{-1} were due to the TO_2 and TO_4 phonons respectively and the weak peak at 260 cm^{-1} to the silent TO_3 mode. The appearance of a peak at 305 cm^{-1} [A_1 (TO_2) mode] indicates the asymmetry within the TiO_6 octahedra of barium titanate phase with the particle size of 50 nm [29,30]. According to Kaiser et al.[31] the weak shoulder below 300 cm^{-1} belongs to an A_1 (TO) phonon mode. The peak at ~307 cm^{-1} corresponds to the E(TO + LO) phonon mode of tetragonal $BaTiO_3$ [32] and the strong band at ~515 cm^{-1} can be attributed to the A_1(TO) phonon mode of the tetragonal phase [33,34]. The weak peak at ~718 cm^{-1} has been associated with the highest-frequency longitudinal optical mode (LO) of A_1 symmetry.

3.2. Thermal decomposition behavior

Fig. 4 shows the result of thermo gravimetric analysis of both the samples A_1 and A_2, which confirms the mass change in the various stages upon the heating up to 1373 K (Table 1). TG curve shows the sequence of 5 steps with different mass loss steps involving dehydration and decarboxylation. For sample A_1, the first major mass loss, of about 17.62% is within the temperature range from room temperature to 463 K, which may be attributed to the dehydration of $BaTiO(C_2O_4)_2{\cdot}4H_2O$ to $BaTiO(C_2O_4)$. The second mass loss of about 2.79% appearing in the temperature range 463–523 K, can be attributed to the initial low temperature decomposition of BTO. The third major mass loss of about 20.52% is found in the temperature range 523–753 K attributed to the complete decomposition of the oxalate groups, resulting in the formation of a carbonate with CO_2 and CO:

$$Ba_2Ti_2O_2(C_2O_4)_3.CO_3 \rightarrow Ba_2Ti_2O_5CO_3(CO_2) + 2CO_2 + 3CO \quad (1)$$

The fourth mass loss of about 5.13%, observed at 753–823 K, is due to the evolution of entrapped CO_2, the final decomposition of carbonate takes place between 893 and 1023 K with a mass loss of about 6.9%, which is due to the formation of $BaTiO_3$ [35,36].

DSC technique was used for the elucidation of kinetics of thermal decomposition of doped and undoped sample. Each sample of 5.01 mg was weighed in an aluminium pan (6 mm in diameter and 2.5 mm in depth). A reference sample was made under similar conditions. This method measures the difference in the amount of heat supplied to the examined sample and reference sample when both are subjected to the controlled changes of temperature. Fig. 5a & b respectively show the DSC curves for the thermal decomposition of BTO from 303 to 873 K (sample A_1) and K^+ doped BTO (sample A_2) in the atmosphere of N_2 (50 mL min^{-1}) at a heating rate of 2, 5, 7 and 10 K min^{-1}. These calorimetric investigations indicate that many endothermic transformations takes place in both doped and undoped samples. The DSC curves of both the samples were separated into 5 reaction process. The reaction below 500 K corresponds to the dehydration of 4 mol of water associated with BTO. Low temperature decomposition of sample A_1 and A_2 occur within the temperature region of 550–650 K, third stage of decomposition, i.e., complete decomposition of oxalate occurs within the temperature range of 523–753 K. The evolution of entrapped CO_2 occurs within the temperature range

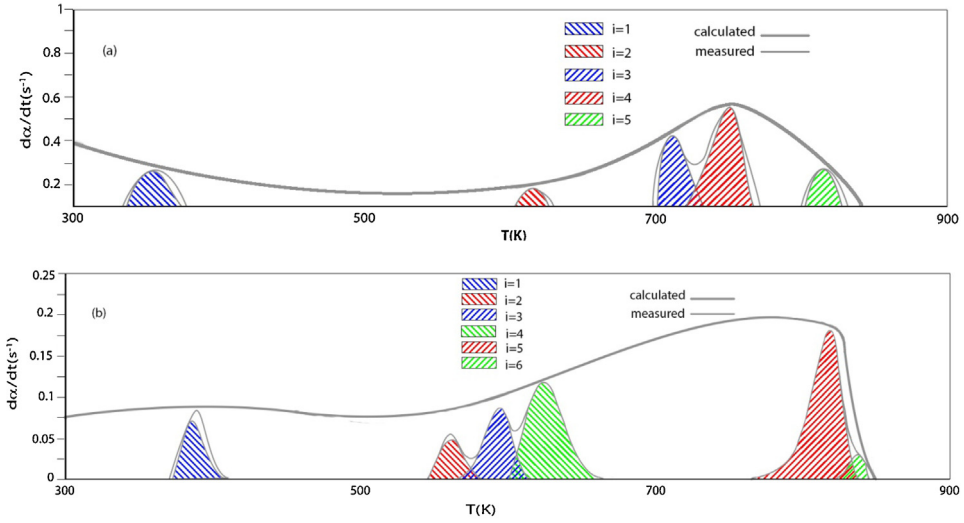

Fig. 7. Typical results of kinetic deconvolution of the thermal decomposition of the samples A_1 (a) and A_2 (b) under linear non-isothermal condition at $\beta = 5$ K min^{-1}.

Table 3
Average kinetic parameters optimized by kinetic deconvolution analysis of the thermal decomposition of samples A_1 and A_2 under linear non-isothermal conditions.

Sample	*i*	C_i	Ea_i (kJ mol^{-1})	A_i (sec^{-1})	$f_i(\alpha)$	R^2
	1	0.57 ± 0.04	56.3 ± 0.1	$(6.34 \pm 0.09) \times 10^{21}$	R(n); n = 1.1 ± 0.1	0.9931
A_1	2	0.13 ± 0. 02	40.1 ± 0.2	$(2.33 \pm 0.05) \times 10^{6}$	R(n); n = 0.99 ± 0.02	0.9921
	3	0.22 ± 0.23	120.5 ± 0.1	$(1.78 \pm 0.04) \times 10^{16}$	R(n); n = 1.2 ± 0.4	0.9813
	4	0.02 ± 0.12	180.21 ±0.09	$(1.15 \pm 0.08) \times 10^{25}$	JMA(m); m = 0.99 ± 0.13	0.9966
	5	0.06	40.92 ± 0.01	$(5.71 \pm 0.02) \times 10^{14}$	JMA(m); m = 1	0.9999
A_2	1	0.36	85.71 ± 0.02	$(1.85 \pm 0.05) \times 10^{28}$	R(n); n = 1	0.9999
	2	0.08 ± 0.02	44.12 ± 0.05	$(2.71 \pm 0.01) \times 10^{5}$	R(n); n = 0.995 ± 0.021	0.9951
	3	0.07 ± 0.05	115.23 ± 0.02	$(1.73 \pm 0.02) \times 10^{3}$	R(n); n = 1.21 ± 0.03	0.9958
	4	0.23 ± 0.07	236.81 ± 0.04	$(1.52 \pm 0.03) \times 10^{15}$	JMA(m); m = 1.1± 0.1	0.9901
	5	0.04 ± 0.03	326.43 ± 0.03	$(9.64 \pm 0.07) \times 10^{18}$	JMA(m); m = 1.3± 0.2	0.9997
	6	0.22 ± 0.92	55.14± 0.4	$(5.31 \pm 0.04) \times 10^{20}$	JMA(m); m = 0.98 ± 0.42	0.9831

753–873 K. Finally the formation of $BaTiO_3$ occurs at the temperature range 893–1023 K. It was noticed from the DSC curves that the curves are shifted towards right with increasing the value of β. At a β value of 2 K min^{-1} the DSC curves for both the sample depicts the intermediate stages. The physico-geometrical kinetic behavior and the reaction mechanism under linear non-isothermal condition were illustrated through kinetic analysis using the kinetic deconvolution method.

4. Kinetic behavior

The kinetic analysis of solid state decomposition is described by two functions, one of the reaction temperature and another of the extent of conversions *i. e*. *K*(T) and $f(\alpha)$ respectively. The mathematical equations used to model kinetic reactions generally take the form of

$$\frac{d\alpha}{dt} = K(T)f(\alpha) \tag{2}$$

where *t* is the time and *T* the temperature and α is the extent of conversion, which can be determined from the DSC as a fractional heat release. In general K(T) is described by an Arrhenius equation:

$$K(T) = Ae^{-Ea/RT} \tag{3}$$

$$\frac{d\alpha}{dt} = Ae^{(-Ea/RT)}f(\alpha) \tag{4}$$

Where α, *A*, *Ea*, and *R* are the fractional reaction, Arrhenius pre exponential factor, apparent activation energy, and the gas constant respectively. The kinetic model function f(α), proposed the physico-geometrical reaction mechanism of the reaction.

Kinetic analysis of thermal decomposition of BTO and doped BTO was executed with DSC data taken under linear non-isothermal heating program at different values of β: 2, 5, 7 and 10 K min^{-1}. Heat flow (dQ/dt) by the reaction and overall heat of reaction obtained from the experimentally resolved DSC curve after subtracting the baseline. The overall reaction rate can be expressed as

$$\frac{d\alpha}{dt} = \left(\frac{dQ}{dt}\right)\frac{1}{Q} \tag{5}$$

DSC curves for the thermal decomposition of BTO and doped BTO are resulted through five component processes such as dehydration, formation of carbonate, decomposition of oxalate ligand, evolution of entrapped CO_2 and formation of barium titanate. The direct application of the kinetic equation and the optimization of the composition of the reactant mixtures and the

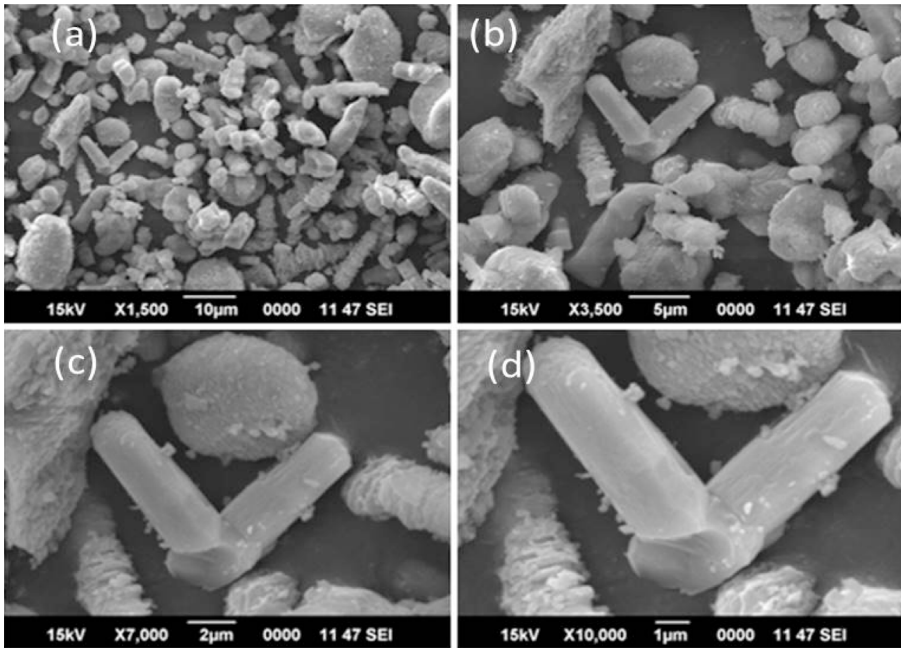

Fig. 8. The SEM images showing the surface microstructure of the sample A_1 at 10 μm (a), 5 μm (b), 2 μm (c) and 1 μm (d).

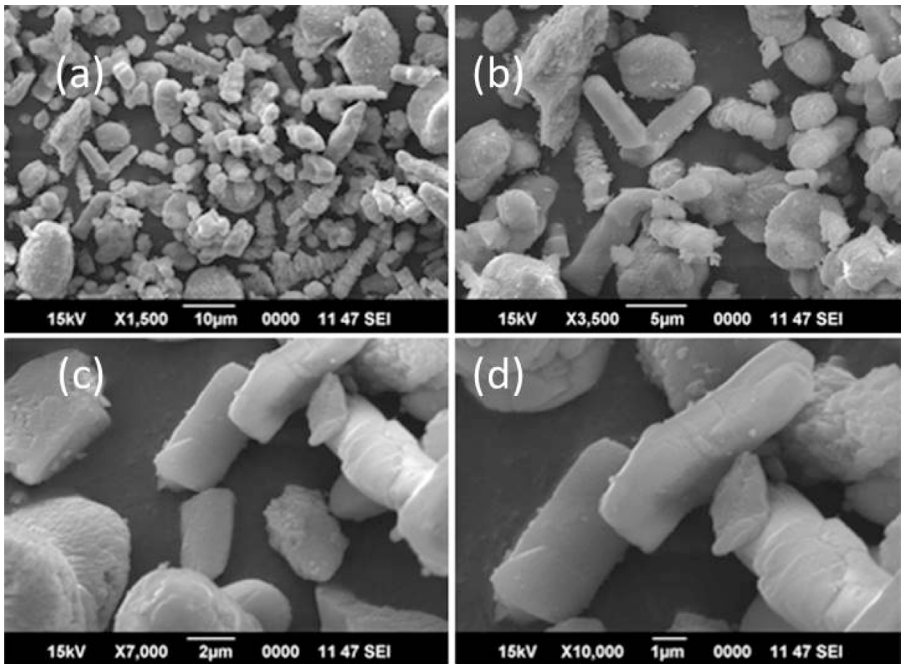

Fig. 9. The SEM images showing the surface microstructure of the sample A_2 at 10 μm (a), 5 μm (b), 2 μm (c) and 1 μm (d).

kinetic parameters of the respective reaction steps known as kinetic deconvolution, is a simple and rapid mathematical procedure of peak fitting for the deconvolution of partially overlapped thermal decomposition processes of solids. The deconvolution of the kinetic rate data determined via DSC into the initial and established reaction stages should enable the discussion of the kinetics of the reaction stages from the physico-geometrical reaction mechanism, the different reaction stages were approximately treated as kinetically independent. Thus, the different partially overlapping reaction stages were separated through the mathematical deconvolution in order to elicit the kinetic behavior of the respective reaction. The overall process of the thermal decomposition is composed of n independent kinetic processes, is expressed by the summation of the respective kinetic processes i by considering their contribution c_i, the following cumulative kinetic equation can be applied. [37–44].

$$\frac{d\alpha}{dt} = \sum_{i=1}^{n} c_i A_i \exp\left(\frac{-E_{a,i}}{RT}\right) f_i(\alpha_i) \tag{6}$$

with $\sum_{i=1}^{n} c_i = 1$ and $\sum_{i=1}^{n} c_i \alpha_i = \alpha$ where n and c are the number of component steps and the contribution ratio of each reaction step to the overall process, respectively and the subscript i denotes each

Fig. 10. The SEM images showing the surface microstructure of the sample A_1 calcined at 1023 K for 1 h at 10 μm (a), 5 μm (b), 2 μm (c) and 1 μm (d).

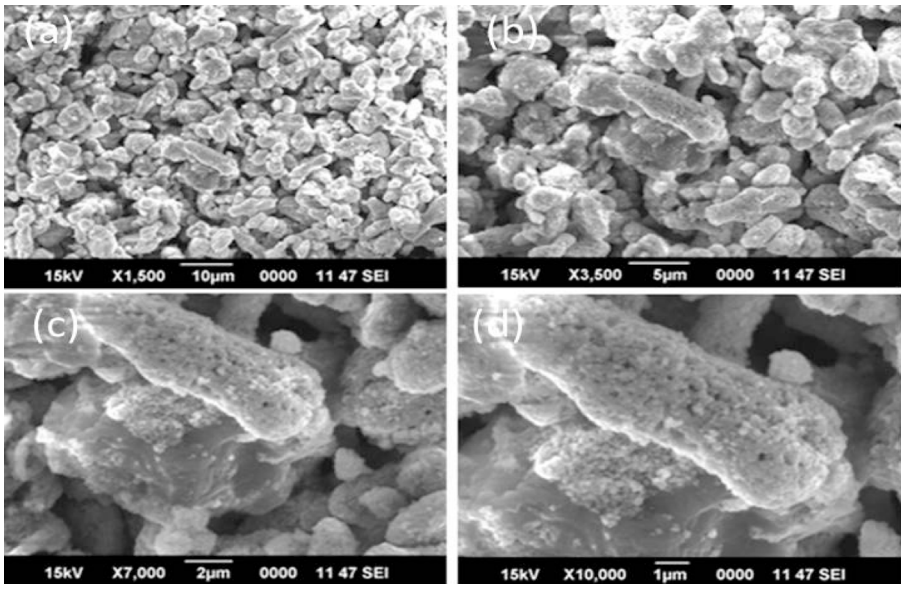

Fig. 11. The SEM images showing the surface microstructure of the sample A_2 calcined at 1023 K for 1 h 10 μm (a), 5 μm (b), 2 μm (c) and 1 μm (d).

component reaction step. The contribution c_{endo} and c_{exo} can be defined as

$$c_{endo} = \frac{Q_{endo}}{Q} < 0 \quad \text{and} \quad c_{exo} = \frac{Q_{exo}}{Q} > 0 \tag{7}$$

where Q_{endo} and Q_{exo} are the heats of endothermic and exothermic process respectively.

The kinetics of each component process of the overall reaction can be characterized by optimizing all the kinetic parameters in Eq. (6) using nonlinear least- squares analysis. In order to predict the physico-geometrical reaction mechanism, empirical kinetic model functions such as phase- boundary- controlled model, RO (n) [45] and the nucleation and growth- type model, JMA (m) were employed [46,47].

$$RO(n) : f(\alpha) = n(1-\alpha)^{1-1/n} \tag{8}$$

$$JMA(m) : f(\alpha) = m(1-\alpha)[-ln(1-\alpha)]^{1-1/m} \tag{9}$$

where n and m are the kinetic exponents.

By allowing the non-integral values for the kinetic exponents in both Eqs. (8) & (9), possible reaction mechanisms for each component process can be found. For both the samples A_1 and A_2, RO (n) and JMA (m) functions with $n \approx 1$ can be utilized. The Kissinger-Akahira-Sunose (KAS) [48] method (Eq. (10)) is a possible method to determine the apparent activation energy for the overall reaction from the DSC curves recorded at different β:

$$\ln\left[\beta/T^2\right] = \ln\left[\frac{AR}{g(\alpha)Ea}\right] - \frac{Ea}{RT} \tag{10}$$

The plots of $ln\,[\beta/T^2]$ versus T^{-1}, Ea and A can be obtained from the slope and intercept respectively. The isoconversional plots indicate a linear relationship irrespective of α and this was observed for samples with different β values (Fig. 6a).

The variation of the apparent Ea values as a function of α was not almost similar for the two prepared samples A_1 and A_2 (Figs. 6b & c). For the sample A_1, though a small deviation of the slope of the KAS plot was observed during the initial stage, the E_a value was found to decrease from 55.83 to 39.80 kJ mol^{-1} ($0.05 \le \alpha \le 0.60$) approximately. In the decomposition part of the reaction, the average values of Ea was found approximately 119.58 ($0.61 \le \alpha \le 0.92$), 179.97 ($0.920 \le \alpha \le 0.944$) and 41.34 kJ mol^{-1} ($0.95 \le \alpha \le 0.99$) respectively. While the apparent E_a values for the sample A_2 was 85.63 kJ mol^{-1} ($0.05 \le \alpha \le 0.40$) which was found to be decreased to 43.31 kJ mol^{-1} ($0.485 \le \alpha \le 0.560$), 114.92 ($0.58 \le \alpha \le 0.78$), 236.07 ($0.785 \le \alpha \le 0.830$), 325.68 ($0.835 \le \alpha \le 0.945$) and 53.98 kJ mol^{-1} respectively. This indicates that the sample A_2 made

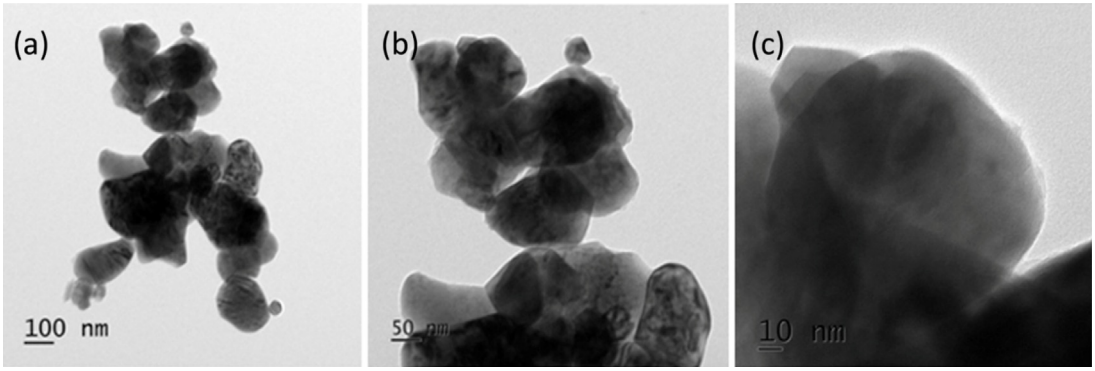

Fig. 12. The TEM images of the sample A_1 calcined at 1023 K for 1 h at 100 nm (a), 50 nm (b) and 10 nm (c).

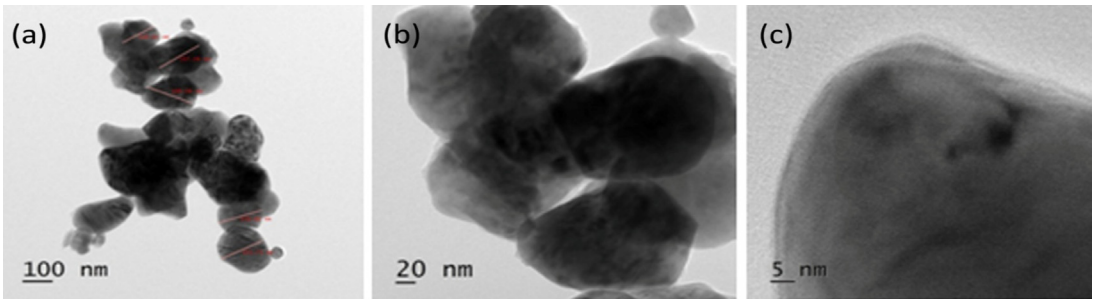

Fig. 13. The TEM images of the sample A_2 calcined at 1023 K for 1 h at 100 nm (a), 20 nm (b) and 5 nm (c).

large deviation to the slope of the KAS plot and the contribution of doping to the overall kinetics is a plausible explanation for this variation in *Ea*.

In the proposed work, the initial values of the kinetic parameters were determined through a formal kinetic analysis of the kinetic data, first subjected to a statistical deconvolution [49,50] using a function (Weibull). The number of component steps for both samples are obtained through kinetic deconvolution of DSC peaks. After setting the all initial values of kinetic parameters (Table 2) for each reaction stage, a parameter optimization was performed to minimize F (Eq. (11)), defined as the squared sum of the difference between the experimental kinetic data $(d\alpha/dt)_{exp}$ versus time and calculated kinetic data $(d\alpha/dt)_{cal}$ versus time [51–54]

$$F = \sum_{j=1}^{n}\left[\left(\frac{d\alpha}{dt}\right)_{\exp,j} - \left(\frac{d\alpha}{dt}\right)_{cal,j}\right]^2 \quad (11)$$

where n is the number of data points

Formation of barium titanate from barium titanyl oxalate *via* thermal decomposition reaction can be brought through the following scheme (Eqs. (12)–(16)):

$$BaTiO(C_2O_4)_2.4H_2O \overset{393-453K}{\rightarrow} BaTiO(C_2O_4)_2 + 4H_2O \quad (12)$$

$$BaTiO(C_2O_4)_2 \overset{453-523K}{\rightarrow} Ba_2Ti_2O_2(C_2O_4)_3.CO_3 + CO \quad (13)$$

$$Ba_2Ti_2O_2(C_2O_4)_3.CO_3 \overset{523-723K}{\rightarrow} Ba_2Ti_2O_5CO_3(CO_2) + 2CO_2 + 3CO \quad (14)$$

$$Ba_2Ti_2O_5CO_3(CO_2) \overset{723-873K}{\rightarrow} Ba_2Ti_2O_5CO_3 + CO_2 \quad (15)$$

$$Ba_2Ti_2O_5CO_3 \overset{873-1023K}{\rightarrow} 2BaTiO_3 + CO_2 \quad (16)$$

Barium titanate formation from BTO comes about through the evolution of H_2O, CO and CO_2. Initial low temperature reaction is known as the dehydration (<500 K) and low temperature decomposition occurs >500 K forming the carbonate intermediate. Succeeding steps involves the decomposition of carbonate intermediate with the evolution of CO and CO_2.

Fig. 7 shows the result of the kinetic deconvolution analysis of the thermal decomposition of the samples A_1 and A_2 on the basis of Eq. (6) after establishing the initial values of the kinetic parameters through mathematical deconvolution and the subsequent formal kinetic analysis of each resolved reaction step [55]. Under the linear non isothermal conditions, for the sample A_1 the overall reaction was resolved into five steps (Fig. 7a) and that of sample A_2 into six overlapping reaction steps (Fig. 7b). The first low temperature reaction observed is considered as the dehydration reaction [56,57]. Both the samples A_1 and A_2 take one independent step for the removal of water molecules, whereas for the higher temperature reaction, both the samples go through more complex reaction pathways.

The average values of the kinetic parameters optimized for the each reaction stage at different β values are summarized in Table 3. For each resolved reaction steps, the value of *Ea* calculated for each reaction step are nearly in agreement with the respective corresponding values estimated by the KAS plots for the overall reaction under non isothermal conditions [58,59]. The physico-geometrical behavior of each sample was best described empirically by the RO (n) and JMA (m) kinetic model functions as shown in Table 3. The required average values of *Ea* for each resolved steps are 56.3 ± 0.1 ($i=1$), 40.1 ± 0.2 ($i=2$), 120.5 ± 0.1 ($i=3$), 180.21 ± 0.09 ($i=4$) and 40.92 ± 0.01 kJmol^{-1} ($i=5$) respectively. For the sample A_2, thermal decomposition occurs via more complex reaction strategies i.e, through six overlapping stage. The average values of energy needed for the respective steps are

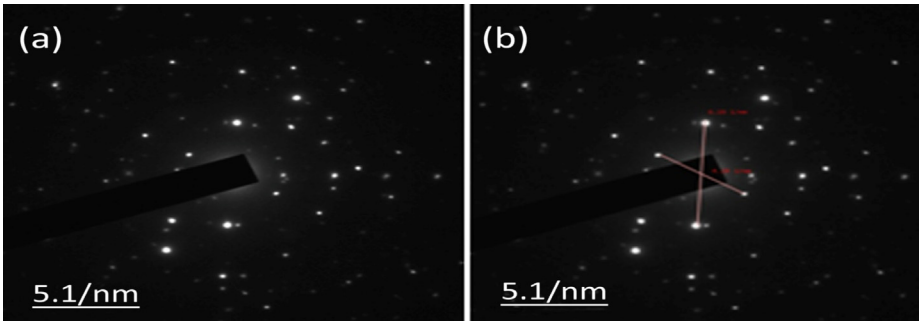

Fig. 14. SAED pattern of barium titanate (a) and K^+- doped barium titanate (b).

85.71 ± 0.02 ($i = 1$), 44.12 ± 0.05 ($i = 2$), 115.23 ± 0.02 ($i = 3$), 236.81 ± 0.04 ($i = 4$), 326.43 ± 0.03 ($i = 5$) and 55.14 ± 0.44 kJ mol^{-1} ($i = 6$) respectively. It should also be noted that difference in the values of A for the initial and final steps were larger for both the samples A_1 and A_2, indicating the larger lags of reaction time and temperature.

5. Morphological analysis

Figs. 8 and 9 show the SEM images of the BTO and doped BTO, which confirm the bone shaped morphology of BTO. It was noticed that most of the bones have smooth surfaces. Figs. 10 and 11 exhibit the SEM images of $BaTiO_3$ which was formed by the multistage thermal decomposition of BTO. Bone like morphology of BTO was retained in the $BaTiO_3$. Doping with K^+ ion brought slight variation in the bone like morphology of BTO and BT. Doped BTO and BT destroy the smoothness of the surfaces. Presence of pores and holes, created by the increased internal gaseous pressure during the process of thermal decomposition of doped BTO depicts the complexity of the reaction upon doping. These holes and pores act as diffusion channels for the removal of CO_2 and water.

Figs. 12 and 13 show the TEM images of the BaTiO3 and doped BaTiO3 calcined at 1023 K for 1 h. The estimated particle size of the both doped and undoped BT from the TEM image is in the range of 5–170 nm. From the TEM image, it was revealed that the particle exhibits as nano sphere having uniform grain size distribution and these nano spheres were underwent oriented growth to form the bone shaped morphology of barium titanate as shown in Figs. 10 and 11.

As the temperature increases, the morphology of the $BaTiO_3$ does not varied. TEM image of K^+-doped $BaTiO_3$ shows a small depression in the nano spheres, which points out the complexity of formation of final product upon doping. Formation of cracks and holes in the surface of the product indicates the formation of surface product layer during the early stages of the reaction. As the temperature increases, there occurs change in the reaction condition at the reaction interface, leading to the complexity of the process. The cracks and holes act as the channels for the diffusional removal of gaseous products such as H_2O, CO_2, CO, etc. Thus, the synthesized $BaTiO_3$ nanoparticles can be used for the wide range of applications in the electronic as well as opto-electronic field.

Fig. 14a & b display the SEAD pattern of BT and doped BT. These images confirm the nano semi crystalline nature of the synthesized barium titanate. Doping does not varied the semi crystalline properties of the synthesized $BaTiO_3$.

6. Conclusion

The kinetics and mechanism of formation of $BaTiO_3$ *via* thermal decomposition strategy was illustrated through the kinetic deconvolution procedure. The effect of doping of K^+-ion (10^{-4} mol%) on the kinetics and mechanism was studied under linear non isothermal condition using the DSC technique in N_2 atmosphere. Both the samples went through multistage reaction pathways. BTO takes five steps for the formation of barium titanate, whereas $K^{\pm}$ doped BT go through six steps for the discharge of barium titanate. Doping of K^+ ion caused to increase the complexity of the reaction process and hence enhances the thermal stability of BTO. The physico-geometrical reaction behaviours of both the samples were best described empirically by RO (n) and JMA (m) models. Morphological analysis disclosed that the synthesized nanospheres undergo oriented crystal growth forming the micro dimensional bone shaped $BaTiO_3$. The estimated size of the spheres covers the range 5–170 nm. The SAED pattern of both samples of doped and undoped BT exposed the nano semi crystalline nature. The XRD pattern revealed the transformation of cubic phase of barium titanate in to tetragonal structure on increasing the temperature.

References

[1] M.A. Mousa, W.A.A. Bayoumy, M. Khairy, Mater. Res. Bull. 48 (2013) 4576–4582.
[2] S. Paul, D. Kumar, Manokamna Gagandeep, J. Biosphere. 2 (2013) 55–58.
[3] C. Min, S. Kim, C. Lee, Bull. Korean Chem. Soc. 18 (1997) 600–603.
[4] A. Feteira, D.C. Sinclair, I.M. Reaney, Y. Somiya, M.T. Lanagan, J. Am. Ceram. Soc. 1087 (2004) 1082–1087.
[5] Y. Suyama, J. Am. Ceram. Soc. 43 (1999) 939–943.
[6] E.F. Takin, G. Ciofani, G.L. Puleo, G. de Vito, C. Filippesch, B. Mazzolai, V. Piazza, V. Mattoli, Int. J. Nanomed. 8 (2013) 2319–2331.
[7] I.K. Battisha, A.B. Abou Hamad, R.M. Mahani, Phys. B 404 (2009) 2274–2279.
[8] D. Hennings, S. Schreinmacher, J. Eur. Ceram. Soc. 9 (1992) 41–46.
[9] T.V. Anuradha, S. Ranganathan, T. Mimani, K.C. Patil, Scripta. Mater. 44 (2001) 2237–2241.
[10] Z. Zhong, P.K. Gallagher, J. Mater. Res. 10 (1995) 942–952.
[11] J.M. Saldan, B. Mullierb, G.A. Schneidera, J. Eur. Ceram. Soc. 22 (2002) 681–688.
[12] S.W. Lu, B.I. Lee, Z.L. Wang, W.D. Samuels, J. Cryst. Growth. 219 (2000) 269–276.
[13] M. Zeng, Appl. Surf. Sci. 257 (2011) 6636–6643.
[14] H.S. Gopalakrishnamurthy, M.S. Rao, T.R.N. Kutty, J. Inorg. Nucl. Chem. 37 (1975) 891–898.
[15] Q. Shu, J. Zhang, B. Yan, J. Liu, Mater. Res. Bull. 44 (2009) 649–653.
[16] M. Oishi, K. Yashiro, K. Sato, J. Mizusaki, T. Kawad, J. Solid State Chem. 181 (2008) 3177–3184.
[17] J. Dho, N.H. Hur, Solid State Commun. 138 (2006) 152–156.
[18] T.K. Kundu, A. Jana, P. Barik, Bull. Mater. Sci. 31 (2008) 501–505.
[19] M. Yoshikawa, S. Yamada, N. Koga, J. Phys. Chem. C 118 (2014) 8059–8070.
[20] S. Kitabayashi, N. Koga, J. Phys. Chem. C 118 (2014) 17847–17861.
[21] N. Koga, Y. Goshi, S. Yamada, L.A. Perez-Maqueda, J. Therm. Anal. Calorim. 111 (2013) 1463–1474.
[22] S. Vyazovkin, C.A. Wight, Annu. Rev. Phys. Chem. 48 (1997) 125.
[23] A. Khawam, D.R. Flanagan, Thermochim. Acta 429 (2005) 93.
[24] S. Otta, S.D. Bhattamisra, J. Therm. Anal. 41 (1994) 419–433.
[25] N. Deb, J. Therm. Anal. Calorim. 107 (2012) 561–571.
[26] K. Nakamoto, 2nd ed., Wiley, New York, 1969, pp. 245.
[27] M. Hammer, C. Monty, A. Endriss, M.J. Hoffmann, J. Am. Ceram. Soc. 81 (1998) 721–724.
[28] P.S. Dobal, R.S. Katiyar, J. Raman Spectrosc. 33 (2002) 405–423.
[29] B. Wang, L. Zhang, Phys. Stat. Sol. 169 (1998) 57–62.
[30] J.H. Lee, F.M. Pontes, E.R. Leite, E. Longo, R. Magnani, P.S. Pisan, J.A. Varela, Mater. Lett. 58 (2004) 1715–1721.
[31] L. Kaiser, M.D. Vaudin, G. Gillen, C.S. Hwang, L.H. Robins, L.D. Rotter, J. Crystal Growth. 136 (1994) 1–2.
[32] R. Cho, S.H. Kwun, T.W. Noh, M.S. Jang, Jpn. J. Appl. Phys. 36 (1997) 2196.
[33] W.K. Kuo, Y.C. Ling, J. Mater. Sci. 29 (1994) 5625.
[34] C.J. Xiao, C.Q. Jin, X.H. Wang, Mater. Chem. Phys. 111 (2008) 2–3.
[35] J. Bera, S.K. Rout, Mater. Lett. 59 (2005) 135–138.
[36] J. Bera, D. Sarkar, J. Electroceram. 11 (2003) 131–137.
[37] T. Wada, N. Koga, J. Phys. Chem. A 117 (2013) 1880–1889.
[38] T. Wada, M. Nakano, N. Koga, J. Phys. Chem. A 119 (2015) 9749–9760.
[39] N. Koga, D. Kasahara, T. Kimura, Cryst. Growth Des. 13 (2013) 2238–2246.
[40] N. Koga, S. Yamada, T. Kimura, J. Phys. Chem. C 117 (2013) 326–336.
[41] P.E. Sanchez-Jimenez, A. Perejon, J.M. Criado, M.J. Dianez, L.A. Perez-Maqueda, Polymer 51 (2010) 3998–4007.
[42] N. Koga, Y. Suzuki, T. Tatsuoka, J. Phys. Chem. B 116 (2012) 14477–14486.
[43] Y. Noda, N. Koga, J. Phys. Chem. C 118 (2014) 5424–5436.
[44] N. Koga, J. Phys. Chem. B 118 (2014) 11397–11405.
[45] N. Koga, H. Tanaka, J. Therm. Anal. 41 (1994) 455–469.
[46] M. Avrami, J. Chem. Phys. 7 (1939) 1103–1112.
[47] M. Avrami, J. Chem. Phys. 8 (1940) 212–223.
[48] H.F. Kissinger, Anal. Chem. 29 (1957) 1702–1706.
[49] R. Font, J.A. Conesa, J. Molto, M. Munoz, J. Anal. Appl. Pyrol. 85 (2009) 276–286.
[50] G. Lopez, R. Aguado, M. Olazar, M. Arabiourrutia, J. Bilbao, Waste Manag. 29 (2009) 2649–2655.
[51] M. Avrami, J. Chem. Phys. 9 (1941) 177–184.
[52] K. Barmak, Metall. Mater. Trans. A 41 (2010) 2711–2775.
[53] N. Koga, Y. Goshi, S. Yamada, L.A. Pe'rez-Maqueda, J. Therm. Anal. Calorim. 111 (2013) 1463–1474.
[54] M. Ferriol, A. Gentilhomme, M. Cochez, N. Oget, J.L. Mieloszynski, Polym. Degrad. Stab. 79 (2003) 271–281.
[55] J. Cai, R. Liu, Weibull . J. Phys. Chem. B 111 (2007) 10681–10686.
[56] A. Perejon, P.E. Sanchez-Jimenez, J.M. Criado, L.A. Perez- Maqueda, J. Phys. Chem. B 115 (2011) 1780–1791.
[57] L.A. Perez-Maqueda, J.M. Criado, P.E. Sanchez-Jimenez, J. Phys. Chem. A 110 (2006) 12456–12462.
[58] R. De Levie, J Chem. Educ. 89 (2012) 79–86.
[59] K. Nusrath, K. Muraleedharan, J. Anal. Appl. Pyrol. 120 (2016) 379–388.

Kinetic study of the multistep thermal behaviour of barium titanyl oxalate prepared via chemical precipitation method

N. V. Sindhu & K. Muraleedharan

Journal of Thermal Analysis and Calorimetry
An International Forum for Thermal Studies

ISSN 1388-6150

J Therm Anal Calorim
DOI 10.1007/s10973-018-7777-7

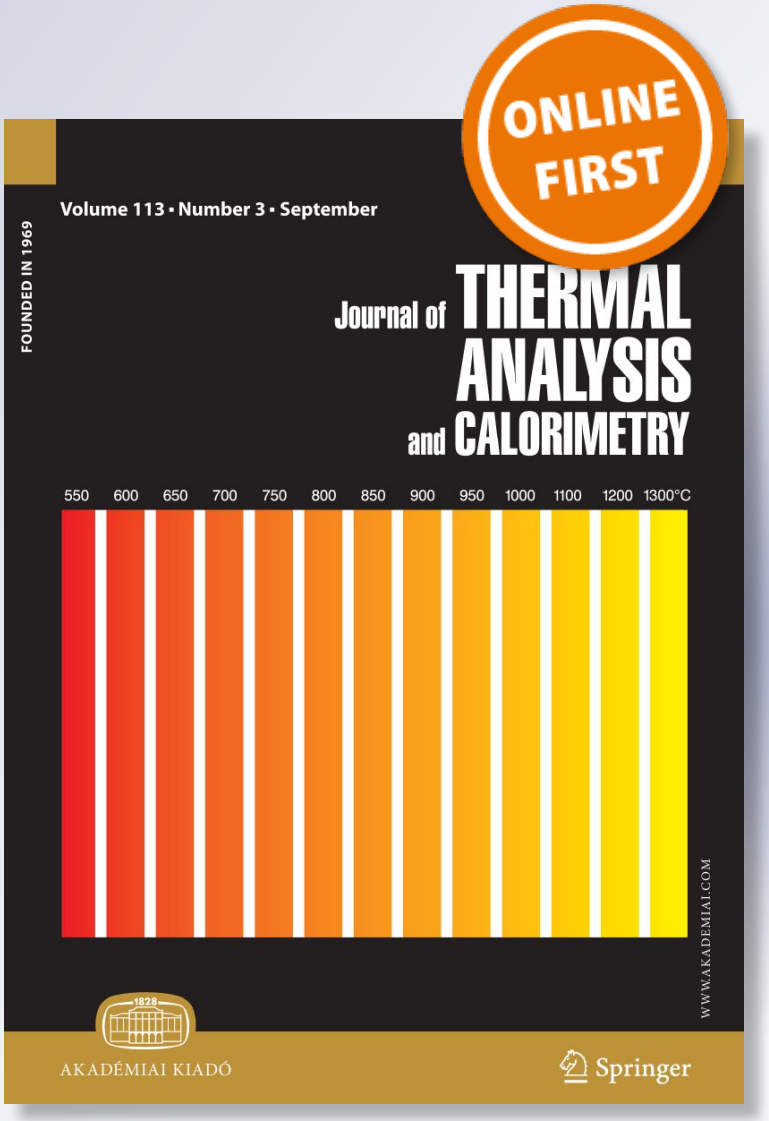

Springer

Journal of Thermal Analysis and Calorimetry
https://doi.org/10.1007/s10973-018-7777-7

Kinetic study of the multistep thermal behaviour of barium titanyl oxalate prepared via chemical precipitation method

N. V. Sindhu[1] · K. Muraleedharan[1]

Received: 24 October 2017 / Accepted: 2 October 2018

Abstract
This study describes the physico-geometrical mechanism and overall kinetics for the multistep thermal dehydration of barium titanyl oxalate tetrahydrate (BTO). The thermal dehydration kinetics of BTO was studied at four different linear heating rates under non-isothermal conditions. The reaction kinetics was performed using differential scanning calorimetry (DSC) and the curves obtained were analysed using different isoconversional model-free equations and the values are found to be compatible with each other. The kinetic deconvolution principle is used for identifying the partially overlapped kinetic processes of the thermal dehydration of BTO, and it occurs in two stages. The overall reaction kinetics parameters calculated via kinetic deconvolution of the sample indicate the multistep nature of the process and the kinetic analysis of the non-isothermal data of this reaction model shows that the reaction is best described by Sestak–Berggren (m, n) empirical kinetic model. The prepared sample was identified and characterized by means of FT-IR, XRD, SEM, and TEM.

Keywords Dehydration kinetics · Kinetic deconvolution · Boswell · Tang · Starink$^{1.95}$ · Starink$^{1.92}$

Introduction

'New materials' refers to all those novel materials capable of bringing about revolutions in the current material world and can provide new colours to material chemistry. They are with specific features and are considered as the backbone of modern devices. The discovery and design of 'new materials', i.e., new alloys, composite materials, optical fibres, polymers and plastics, nano-materials, biomaterials, newer semiconducting materials, ceramic materials, dielectric materials, smart materials are utilized for technological development. Many scientists and researchers still focus on these materials which form the most challenging area of scientific and technologic research because of their fabulous potentials associated with them. These materials often possess unique electric, magnetic, optical, catalytic, sensing, superconducting, and plasmonic properties that provide for biomedical purpose also.

Thermal decomposition of barium titanyl oxalate yields barium titanate nanoparticles, which have superior properties than the bulk substances: mechanical strength, thermal stability, catalytic activity, electrical conductivity, magnetic properties, optical properties, etc. It has a wide range of applications: quantum electronics, nonlinear optics, photonics, sensing, solar cells, information storage and processing, as adsorbents, in catalysis, solar cells, super-plastic ceramics, etc. [1]. Barium titanate (BT) is considered as a promising ceramic material for a variety of problems of techno-environmental factors due to its excellent properties. It is a well-known and widely investigated dielectric material and is mainly used as a capacitor due to its high dielectric constant. It is the first ferroelectric perovskite-type ceramics and a good candidate for making piezoelectric devices and semiconductors. Due to some advantages such as high activity, potential for device miniaturization, and improved dielectric properties, production of BT in nano-size is of great significance. Many methods such as sol–gel method [2], the hydrothermal method [3], the Pechini processing using a citric or oxalate complex as the precursor [4], the ball-milling method [5], the polymeric precursor method [6], the soft chemical process [7], the glycothermal method [8], the co-

✉ K. Muraleedharan
kmuralika@gmail.com

[1] Department of Chemistry, University of Calicut, Malappuram 673635, India

Published online: 10 October 2018

precipitation method [9], and the thermal decomposition method [10] were used for the synthesis of BT. Among these methods, the one with oxalate as a precursor has been widely used due to its simplicity and the precise stoichiometry of the produced BT phase. And also having the advantage of being easy and low cost for material and investment for facilities, the oxalate synthesis process was first commercialized. However, the oxalate synthesis process is disadvantageous in that it is difficult to control the powder composition (Ba/Ti) and particle distribution. Also, the particles have a strong tendency to aggregate upon thermolysis, resulting in an incomplete pulverization, after which there may remain aggregates as large as ones to tens of μm in size. Further, the particles are not well dispersed upon subsequent mixing processes. In addition, the presence of aggregates may result in the formation of abnormal crystal grains at sintering and shows poor crystallinity. Recently, a new preparation method with crystal growth under vacuum to prepare defect-free, impurity-free $BaTiO_3$ nanoparticles (17–500 nm) was proposed by Wada et al. [11]. Moreover, they developed a new measurement method for dielectric constants of $BaTiO_3$ particles. A combination between the powder dielectric measurement method and the defect-free, impurity-free $BaTiO_3$ nanoparticles resulted in the unique particle-size dependence with maximum dielectric constant of 15,000 at 68 nm. Recently it has been widely studied due to its important applications in nonlinear optics, multilayer ceramic capacitors (MLCC), microelectromechanical systems (MEMs), ferroelectric random access memories (FRAM), and high-density optical data storage, etc. Over the past few years, the unique ferroelectric, piezoelectric, and thermoelectric properties of barium titanate nanoparticles have become increasingly important in the electronic ceramics industry. The $BaTiO_3$ nanoparticles have been extensively applied in various fields such as integral capacitors in printed circuit boards (PCB), dynamic random access memories (DRAM), resistors with positive temperature coefficient of resistivity (PTCR), temperature–humidity–gas sensors, electro-optic modulators, piezoelectric transducers, pyroelectric detectors, actuators, thermistors, ultrasonic devices, medical imaging detectors, high-K dielectronics, and microwave dielectric ceramic. It has the highest reflectivity of the materials used for self-pumped phase conjugation (SPPC) applications [12].

The preparation of BTO has been reported by many workers [13–18]. Clabaugh et al. [13] reported that a high-purity barium titanate could be prepared by precipitating barium titanyl oxalate and subsequently converting to barium titanate by calcination. Kudaka et al. [14] also reported the optimum conditions for the formation of BTO in more detail. Yamamura et al. [15] employed a revised Clabaugh method to prepare BTO in which the ethanol solution of the oxalic acid was added to the mixed starting solution of $Ba(NO)_3$ and $TiO(NO_3)_2$. The decomposition kinetics of barium titanyl oxalate tetrahydrate has been extensively studied by many researchers [19–27]. Otta et al. [19] studied the kinetics and mechanism of the thermal decomposition of barium titanyl oxalate and suggested that $BaTiO_3$ was formed in the temperature range of 500–800 °C. Gallagher and Thomson [24] suggested that in the first step of the thermal decomposition four molecules of water are lost in the range of 20–250 °C. After losing the water of crystallization, oxygen is adsorbed to form active $BaCO_3$ and TiO_2 which react to form $BaTiO_3$ at a temperatures range of 500–700 °C and CO_2 is released. The thermal behaviour of $BaTiO_3$ prepared at a temperature of 600–900 °C was studied by Swillam and Gadalla [25]. They have shown that at lower temperatures $BaTiO_3$ compacts during calcination, with the formation of extremely fine pores, whereas at higher temperatures it agglomerates to shrink too much smaller particles, eliminating these pores. Gopalakrishnamurthy et al. [27] investigated the evolution of water and CO_2 vapours during the thermal decomposition of BTO, the decomposition proceeded through five steps and was not affected much by surrounding gaseous atmosphere. The first step is the dehydration of the tetrahydrate which was followed by low-temperature decomposition of the oxalate groups. In the temperature range of 393–453 K, carbon monoxide is evolved with the formation of a transient intermediate substance containing both carbonate and oxalate groups. The oxalate groups were completely destroyed in the temperature range of 453–523 K, resulting in the formation of a carbonate which retains free CO_2 in the matrix. The trapped CO_2 was released in the temperature range of 523–723 K. The final decomposition of carbonate takes place between 873 and 1023 K and yields barium titanate.

In kinetic studies, dehydration rate and activation energy are important parameters to determine the reaction mechanism in solid state phase. The use of thermo-analytical data to evaluate the kinetic parameters of solid-state reactions has been investigated by many workers [28–32]. Successful and deliberate attempts to evaluate kinetic and thermodynamic parameters are made by Kotru et al. [33] and Schaube et al. [34]. The kinetics of dehydration of gypsum [35], lithium sulphate monohydrate crystal [36], and the kinetic and thermodynamic parameters of the decomposition of chromium chromate in different gas atmospheres have been evaluated [37]. Kinetic parameters can be calculated from the kinetic data by applying integral and differential equations [38–40], which are proposed by different authors on the basis of different assumptions to the kinetics of the reaction and the Arrhenius law.

In the present investigation, the kinetic parameters of the thermal dehydration of incorporated water from barium

titanyl oxalate tetrahydrate were studied by using different isoconversional model free equations; the methods of Bosewell, Tang, Starink[1.95], and Starink[1.92] have been used to elucidate the thermal stability, the nature, and extent of the dehydration of barium titanyl oxalate tetrahydrate in nitrogen atmosphere. The values of kinetic parameters were calculated for the kinetic deconvolution of the sample, and this method is used to yield the dependency of E_a on the extent of conversion and the most probable kinetic model of the sample.

Experimental

Sample preparation

AnalaR grade barium nitrate ($Ba(NO_3)_2$) (Merck, India; assay $\geq$ 99.9%) and potassium titanyl oxalate ($K_2TiO(C_2O_4)_2$) (BHO Laboratory England; assay $\geq$ 99.9%) were used in the present investigation.

Barium titanyl oxalate tetrahydrate was synthesized by the precipitation reaction of mixing of barium nitrate and potassium titanyl oxalate with constant stirring. The white BTO precipitate obtained was filtered, washed with deionized water and dried in an air oven kept at a constant temperature of 50 °C for 48 h, powdered in an agate mortar, and the particle size was fixed in the range of 45–53 μm.

Methods

The FT- IR spectrum of the samples in KBr pellet was recorded using a JASCO FT-IR-4100 instrument. The sample was first compressed with KBr into pellet and analysed as KBr disc from 400 to 4000 cm^{-1}. The instrument offers high sensitivity, maximum resolution (0.9 cm^{-1}), and high signal-to-noise ratio (22,000:1). The X-ray diffraction (XRD) measurements of the samples were taken on a RIGAKU MINI FLEX-400 X-ray diffraction spectrophotometer using Cu Kα (1.5418 Å) radiation. The scanning electron microscope (SEM) analyses of all the samples studied were performed with SEM–EDS combination using JEOL Model JSM - 6390LV, JEOL Model JED - 2300. The instrument offers a resolution of 3 nm (Acc V 30 kV, WD 8 mm, SEI), 8 nm (Acc V 3.0 kV, WD 6 mm, SEI) and magnification of 5–300,000 × (both in high and low vacuum mode). For the present investigation, the imaging techniques employed was secondary electrons (SE), backscattered electrons (BSE), and energy-dispersive X-ray analysis (EDXA). The transmission electron microscopy (TEM) analysis of the particles was achieved by using a JEOL 2100 field emission transmission electron microscope operated at 200 kV with a 0.18 nm resolution. The differential scanning calorimetric (DSC) measurements of the samples were taken on a Mettler Toledo DSC822e. The operational characteristics of the DSC system are as follows: atmosphere: flowing N_2 at a flow rate of 50 mL min^{-1}; sample mass: 5.1 mg; and sample holder: aluminium.

Results and discussion

Sample characterization

Figure 1 represents the FT-IR spectrum of the hydrated and dehydrated sample. Figure 1a represents FT-IR spectrum of barium titanyl oxalate tetrahydrate. The broadband extending from 2800 to 3600 cm^{-1} is assigned to the symmetric and asymmetric stretching modes of the water molecules. The strong band appearing in the IR spectrum around 1615 cm^{-1} can be identified as the asymmetric stretching vibrations of CO groups of the $C_2O_4^{2-}$ ions together with the bending mode of water [41]. The IR spectrum of BTO heated to 510 K in vacuum for 1 h presented in Fig. 1b shows the appearance of an intense band at 2339 cm^{-1} which can be attributed to the asymmetric stretching frequency of free CO_2. The strong peak around 1316 cm^{-1} is also assigned to the asymmetric stretching of CO groups.

X-ray diffractometer (XRD) was used for the calculation of particle size, lattice parameters a, b, c, etc. Figure 2 shows the XRD pattern of the hydrated and dehydrated samples at 2θ values ranging from 10° to 80°. The crystallite sizes (d) of prepared samples were estimated from the peaks of XRD patterns, using Debye–Scherrer's equation, $d = K\lambda/ß\cos\theta$ where K is the shape coefficient

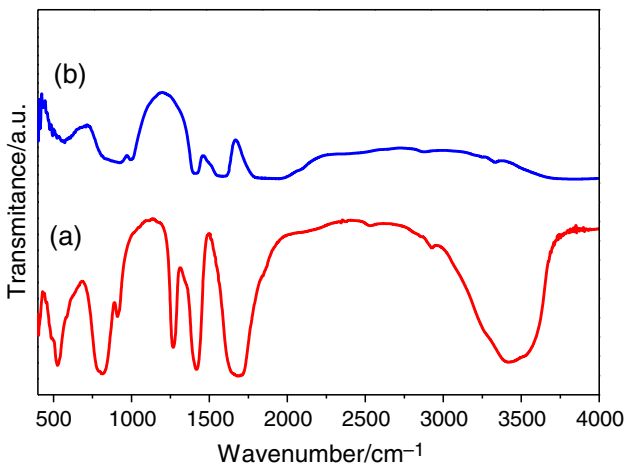

Fig. 1 The FT-IR spectra of sample (a), sample calcined at 510 K for 1 h (b)

(value between 0.9 and 1.0), λ is the wave length (1.5418 Å), β is the full width at half maximum, and θ is the diffraction angle which shows the structural characteristics of the sample. Figure 2a shows the XRD pattern of barium titanyl oxalate tetrahydrate at 2θ values 19.71°, 24.16°, 31.78°, 34.52°, 45.11°, 56.96°, and 69.22°. The reflections from the sample indicate that barium titanyl oxalate shows amorphous phase due to the presence of the carbon atoms and the water in the mixture. Figure 2b represents the XRD pattern of the dehydrated sample (510 K) at 2θ values 22.47°, 31.78°, 39.17°, 45.74°, 51.46°, 56.52°, 66.27°, 70.92°, 75.37°, and 79.39°. After calcinations, at 510 K, the crystalline phase with cubic structure (a = 4.0073 Å) was appeared [42]. From the XRD results, it was clear that the peak intensity and crystalline nature enhance with the calcinations of the sample. From the calculation, the average crystallite size of the hydrated and dehydrated barium titanyl oxalate has been obtained in nanometre region.

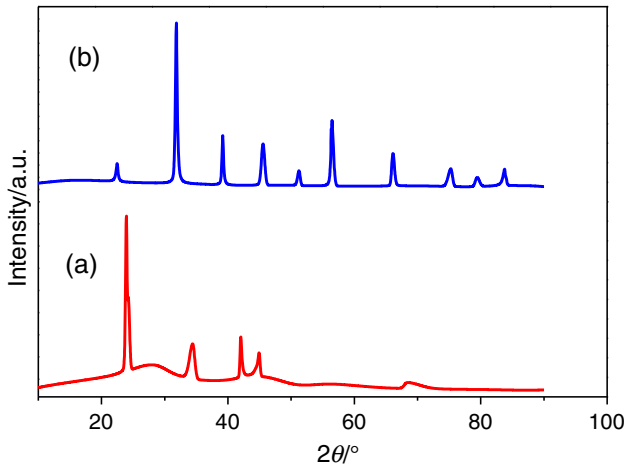

Fig. 2 The XRD pattern of sample (a), sample calcined at 510 K for 1 h (b)

The surface morphological analysis of the synthesized samples was conducted using a scanning electron microscope and a high-resolution transmission electron microscope. Figures 3 and 4 show the SEM images of the synthesized sample calcined at 450 and 510 K for 1 h, which indicates the porous microstructure of the sample; the pore size varies from 1 to 10 μm. However, some particles exhibit slightly sharp edges, and also most of the particles have smooth surfaces and slight depressions presenting different morphologies shows agglomerations of spherical grains with smaller grain size with a porous surface containing particles with cylindrical shape. The TEM could also yield information such as particle size, size distribution, and morphology of the sample when it is heated to 510 K for 1 h (Fig. 5). From the TEM image, it seems that the samples exhibit uniform grain size distribution. DSC is an effective tool in the investigation of phase transformations and enables very accurate determination of the temperature range and reaction heat in all transformations. It is used for recording the kinetic rate data of the thermal decomposition. This method measures the difference in the amount of heat supplied to the sample and reference sample when both are subjected to control heating. Figure 6 shows the DSC curves for the thermal dehydration of BTO from 337 to 510 K in the atmosphere

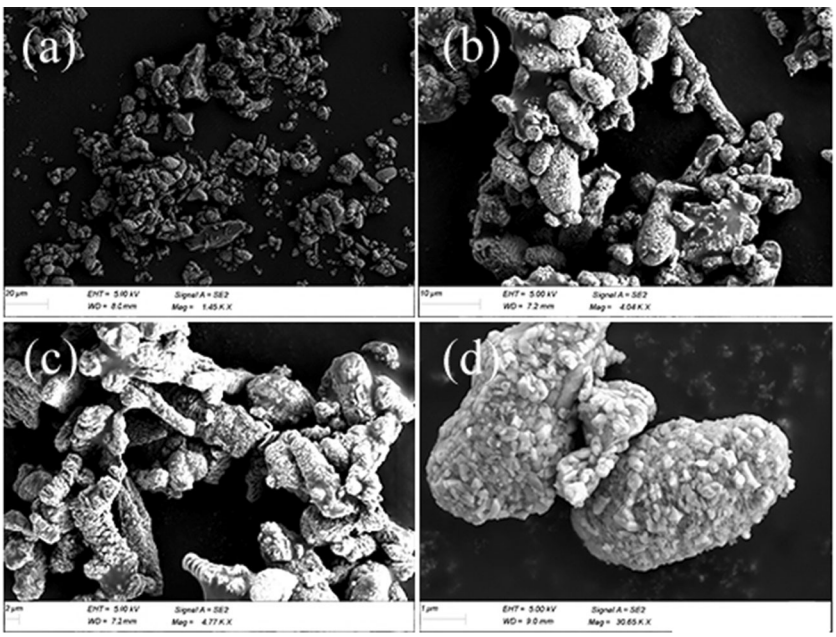

Fig. 3 The SEM images of the sample calcined at 450 K showing the surface microstructure of the sample at 20 μm (**a**), 10 μm (**b**), 2 μm (**c**), and 1 μm (**d**)

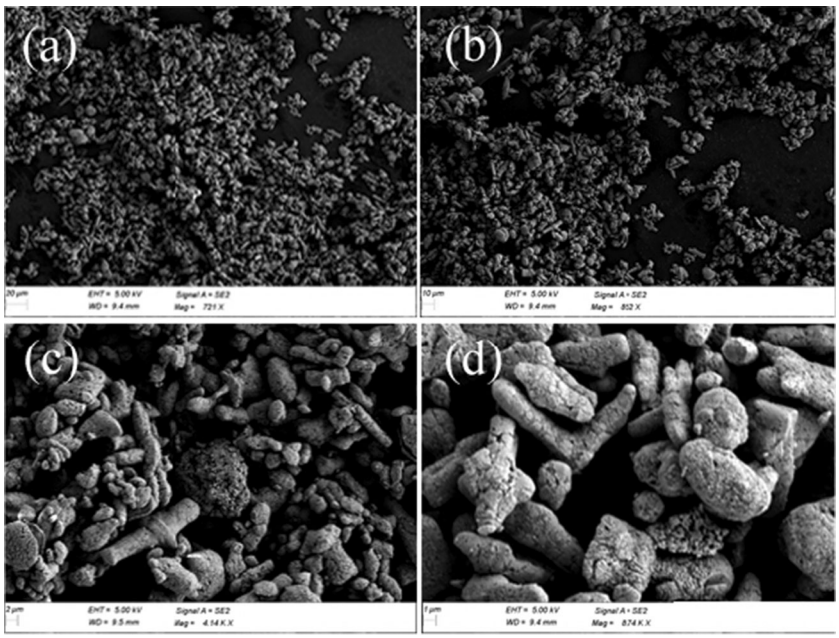

Fig. 4 The SEM images of the sample calcined at 510 K showing the surface microstructure of the sample at 20 μm (**a**), 10 μm (**b**), 2 μm (**c**), and 1 μm (**d**)

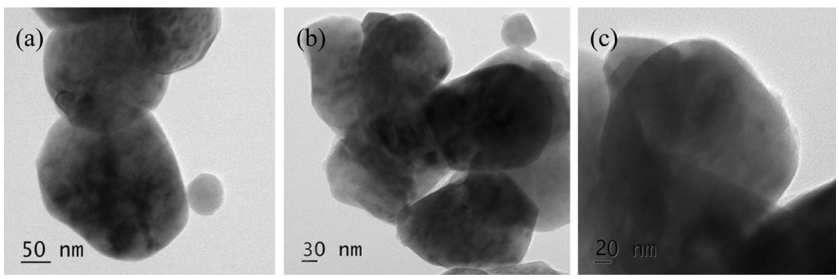

Fig. 5 The TEM images of the sample calcined at 510 K for 1 h 50 nm (**a**), 30 nm (**b**), 20 nm (**c**)

of N_2 (50 mL min^{-1}) at a heating rate of 2, 5, 7, and 10 K min^{-1}.

Figure 7 gives the TG curves recorded during the decomposition of $BaTiO(C_2O_4)_2.4H_2O$ at different heating rates under nitrogen gas and the results of thermogravimetric analysis of the sample, which confirm the mass change in the various stages upon the heating up to 1400 K. TG curve shows the sequence of 5 steps with different mass loss involving dehydration and decarboxylation. The major mass loss of the sample, of about 17.42%, may be attributed to the dehydration of $BaTiO(C_2O_4)_2{\cdot}4H_2O$ to $BaTiO(C_2O_4)$. The calculated mass loss of BTO is 16.03%, which is in agreement with the theoretical value [19, 27].

Kinetic analysis

The direct application of the kinetic equation and the kinetic parameters of the respective reaction steps are kinetically analysed using kinetic deconvolution procedure of peak fitting of the deconvolution of partially overlapped thermal stages of the reaction. The deconvolution of the kinetic rate data determined via DSC into the respective reaction stages should enable the discussion of the kinetics of the reaction stages from the physico-geometrical reaction mechanism, the different reaction stages were approximately treated as kinetically independent. The thermal dehydration kinetics of a sample at different β was

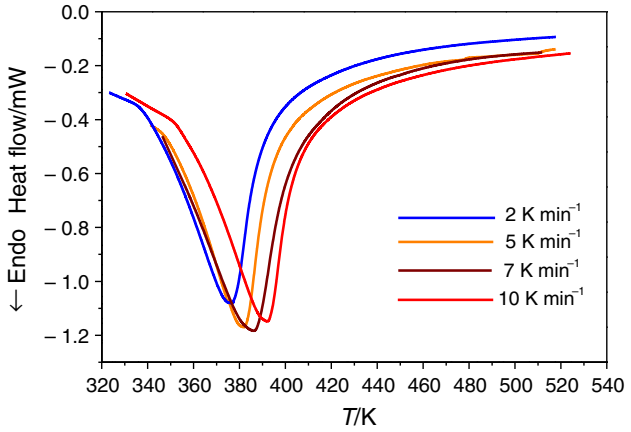

Fig. 6 The DSC curves for the thermal dehydration of sample (m_1 = 5.01 ± 0.01 mg) at different β in N_2 gas (50 mL min^{-1})

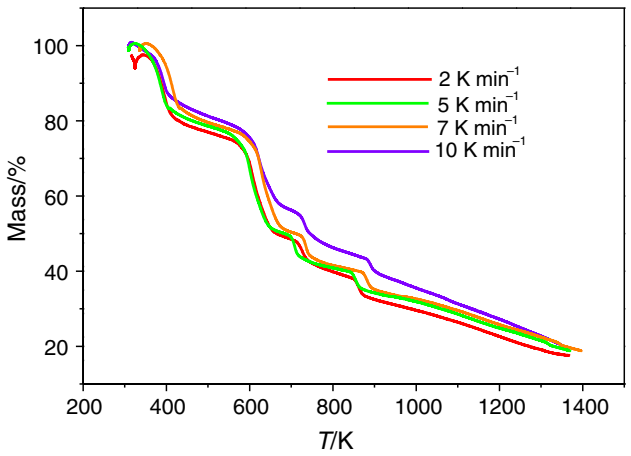

Fig. 7 The TG curves for the thermal decomposition of sample (m_1 = 5.01 ± 0.01 mg) at different β in flowing N_2 gas (20 mL min^{-1})

subjected to the formal kinetic analysis by assuming the fundamental kinetic equation [43, 44]

$$\frac{d\alpha}{dt} = Ae^{(-E_a/RT)}f(\alpha) \quad (1)$$

where α, A, E_a, and R are the fractional reaction, the Arrhenius pre-exponential factor, the apparent activation energy, and the gas constant, respectively. The kinetic model function $f(\alpha)$, proposed the physico-geometrical reaction mechanism of the reaction. Using the kinetic data for different β, apparent E_a as a function of the reacted fraction can be determined from isoconversional methods. All isoconversional methods take their origin in the isoconversional principle that states that the reaction rate at constant extent of conversion is only a function of temperature. The analysis of reaction kinetic parameters was performed using the DSC curves, obtained between 337 and 510 K using the non-isothermal isoconversional

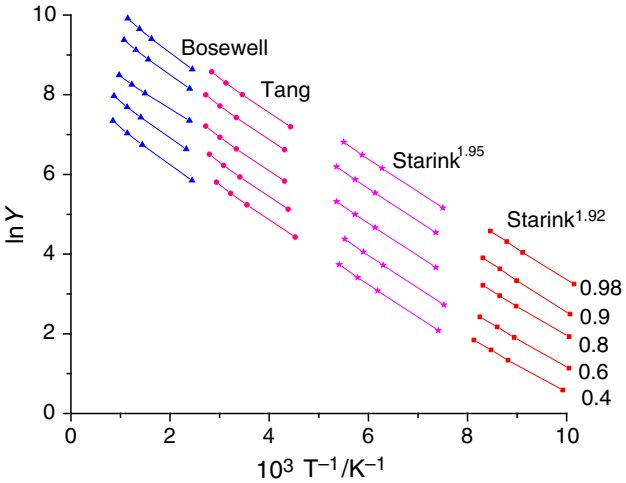

Fig. 8 Typical linear least squares plot for Bosewell, Tang, Starink$^{1.95}$, and Starink$^{1.92}$ methods of the sample at different conversion values

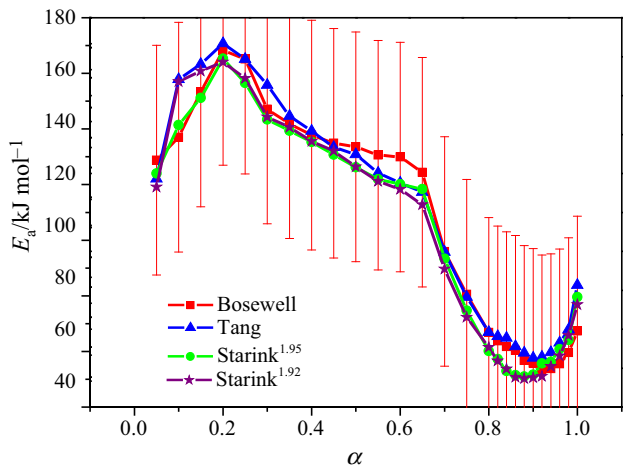

Fig. 9 The dependence of activation energy on conversion of barium titanyl oxalate tetrahydrate for different methods

methods such as Bosewell, Tang, Starink$^{1.95}$, and Starink$^{1.92}$. The value of enthalpy change of dehydration, measured by DSC, is found to be 151.94 kJ mol^{-1}.

Calculation of the values of E_a by isoconversional methods

Bosewell method

Bosewell method is an integral isoconversional method, according to which [45]:

$$\ln\frac{\beta}{T} = \ln\frac{AR}{E_a g(\propto)} - \frac{E_a}{RT} \quad (2)$$

The values of slope obtained from the linear least squares plots of $\ln\frac{\beta}{T}$ versus $1/T$ enable the calculation of E_a.

Table 1 Initial kinetic parameters used for the kinetic deconvolution analysis of the thermal dehydration of sample under linear non-isothermal conditions

Methods	i	C_i	E_{ai}/kJ mol^{-1}	A_i/s^{-1}	$f(\alpha) = \alpha^m(1-\alpha)^n$ SB (m, n)
Bosewell	1	0.78	105.76	8.21×10^{14}	$m = 0.99$, $n = 0.9$
	2	0.22	56.55	6.01×10^{6}	$m = 0.05$, $n = 1.3$
Tang	1	0.78	101.35	7.23×10^{12}	$m = 0.11$, $n = 1.1$
	2	0.22	55.76	5.42×10^{5}	$m = 0.04$, $n = 0$
Starink$^{1.95}$	1	0.78	98.13	6.84×10^{11}	$m = 0.3$, $n = 1.12$
	2	0.22	52.39	3.86×10^{4}	$m = 0.22$, $n = 0.19$
Starink$^{1.92}$	1	0.78	102.06	7.67×10^{13}	$m = 0.41$, $n = 0.99$
	2	0.22	52.51	4.91×10^{4}	$m = 0.25$, $n = 1$

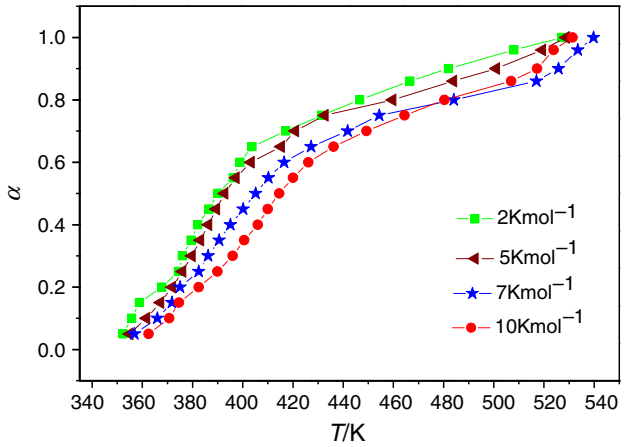

Fig. 10 α–T curve for the thermal dehydration of barium titanyl oxalate tetrahydrate at different β in N_2 (50 mL min^{-1})

Tang method

The Tang method, proposed by Tang et al., according to which [46]:

$$\ln\left(\frac{\beta}{T^{1.894661}}\right) = \left[\ln\frac{AE_a}{g(\propto)R} + 3.63504095 - 1.894661\ln\ln E_a\right] - 1.00145033\left(\frac{E_a}{RT}\right) \quad (3)$$

The values of slope obtained from the linear least squares plots of $\ln\left(\frac{\beta}{T^{1.894661}}\right)$ against $1/T$ enable the calculation of E_α.

Starink$^{1.95}$ method

The Starink method is based on the Starink approximation [47]:

$$\ln\frac{\beta}{T^{1.95}} = \ln\left[\frac{A}{g(\alpha)}\left(\frac{E_a}{R}\right)^{-0.95}\right] - 0.235 - \frac{E_a}{RT} \quad (4)$$

The slope obtained from the linear least squares plot of $\ln\frac{\beta}{T^{1.95}}$ against $1/T$ enables the calculation of E_a.

Starink$^{1.92}$ method

$$\ln\frac{\beta}{T^{1.92}} = \ln\left[\frac{A}{g(\alpha)}\left(\frac{E_a}{R}\right)^{-0.92}\right] - 0.312 - 1.0008\frac{E_a}{RT} \quad (5)$$

The values of slope obtained from the linear least squares plots of $\ln\frac{\beta}{T^{1.92}}$ against $1/T$ enable the calculation of E_a.

Figure 8 is the best linear fit obtained using Eqs. (2), (3), (4), and (5) for Bosewell, Tang, Starink$^{1.95}$, and Starink$^{1.92}$ methods. The slopes of these straight lines have been used to calculate Ea, and their intercepts were used to calculate frequency factor (log A). The variation of the apparent E_a values as a function of α was almost similar for the above four methods (Fig. 9). The average values of calculated activation energy and frequency factor are depicted in Table 1. The α–T curve (Fig. 10) shows the multistep dehydration reaction for barium titanyl oxalate, which shows two steps. For kinetic analysis, thermal dehydration of incorporated water is an independent kinetic processes; the following cumulative kinetic equation can be applied to the overall reaction under linear non-isothermal conditions [48–57]

$$\frac{d\alpha}{dt} = \sum_{i=1}^{n} c_i A_i \exp\left(\frac{-E_{a,i}}{RT}\right) f_i(\alpha_i) \quad \text{with} \quad \sum_{i=1}^{n} c_i = 1 \quad \text{and} \quad \sum_{i=1}^{n} c_i\alpha_i = \alpha \quad (6)$$

where n and c are the number of component steps and the contribution ratio of each reaction step to the overall process, respectively, and the subscript i denotes each component reaction step. A_i and E_{ai} are the Arrhenius pre-exponential factor and the apparent activation energy, respectively, of the process i. The kinetics of each

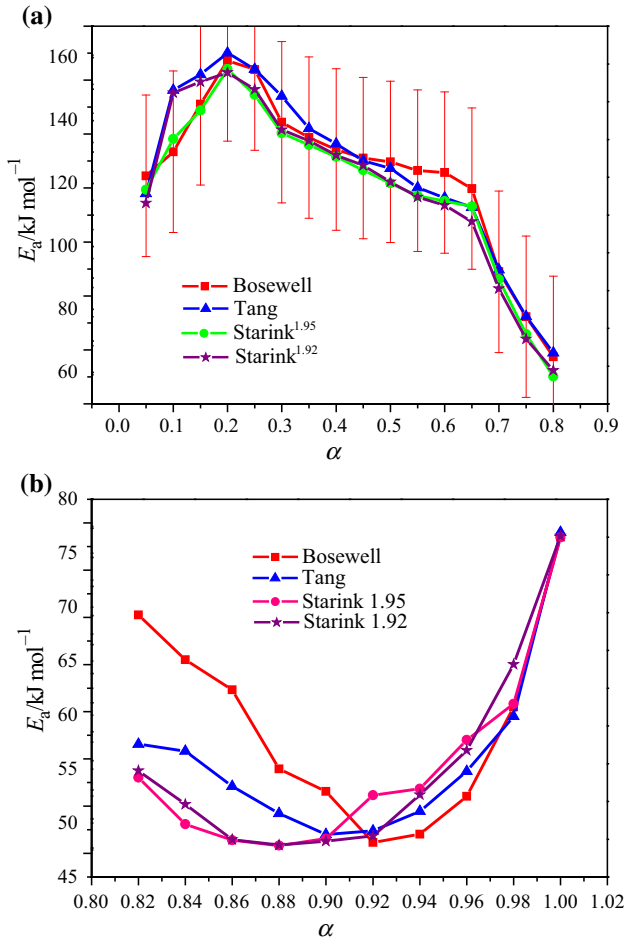

Fig. 11 E_a versus α curves of thermal dehydration stage for barium titanyl oxalate tetrahydrate: first peak (i = 1) (**a**) and second peak (i = 2) (**b**)

component process of the overall reaction can be characterized by optimizing all the kinetic parameters given in Eq. 6 using nonlinear least squares analysis. Empirical kinetic model functions such as Sestak–Berggren [58] SB (m, n) were employed for $f_i(\alpha_i)$ given in Eq. 7 in order to accommodate any possible mechanistic feature of each reaction process.

$$f(\alpha) = \alpha^{m}(1-\alpha)^{n} \tag{7}$$

where m and n are characters for a particular dehydration process, which correspond to empirically obtained kinetic exponents. For kinetic analysis, the DSC data were first subjected to statistical deconvolution procedure. During this, the DSC curve for the thermal dehydration of BTO recorded under linear non-isothermal conditions was separated into two partially overlapping peaks with satisfactory fit using Weibull functions (Eq. 8) [59, 60]:

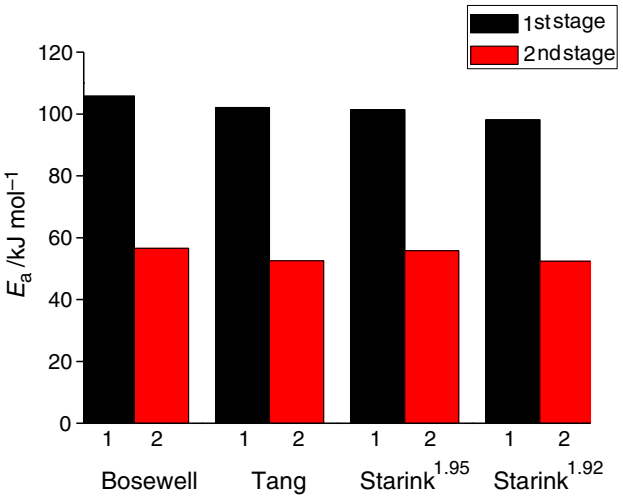

Fig. 12 Comparison of E_a values calculated by using Bosewell, Tang, Starink$^{1.95}$, and Starink$^{1.92}$ methods for the thermal dehydration of barium titanyl oxalate tetrahydrate

$$y = \left[a_0 \left(\frac{a_3-1}{a_3}\right)^{\frac{1-a_3}{a_3}} \left\{ \frac{x-a_1}{a_2} + \left(\frac{a_3-1}{a_3}\right)^{a_3-1} \right\} \right] \left[\exp\left[-\left\{ \frac{x-a_1}{a_2} + \left(\frac{a_3-1}{a_3}\right)^{\frac{1}{a_3}} \right\}^{a_3} + \frac{a_3-1}{a_3} \right] \right] \tag{8}$$

From the ratio of the peak areas for the separated first and second peaks, the contribution c_i of each peak to the overall reaction was determined as (c_1, c_2) = (0.78 ± 0.02, 0.22 ± 0.02). The mathematically separated peaks at different β were used as the kinetic rate data. For both the first and second peaks, the kinetic rate data indicated systematic shifts to higher temperatures with increasing β. The α-dependent changes in E_a determined by applying the Bosewell, Tang, Starink$^{1.95}$, Starink$^{1.92}$ methods were found for the kinetic rate data of the separated first and second DSC peaks. For the first DSC peak, a systematic decrease in the E_a value is observed during the course of the reaction and the second DSC peak also shows the same variation. The systematic change in the E_a value with α observed for the first peak and the second peak indicates that the isoconversional relationship is one of the best methods to point out the changes in the self-generated conditions depending on β as the reaction advances. In these methods, Bosewell, Tang, Starink$^{1.95}$, Starink$^{1.92}$, an average value obtained for E_a is 105.76, 101.35, 98.13 and 102.06 kJ mol^{-1} ($0.05 \leq \alpha \leq 0.8$), respectively, and was tentatively used for the first peak. The average value for Ea, obtained for the second peak was 56.55, 55.76, 52.39, and 52.51 kJ mol^{-1} ($0.82 \leq \alpha \leq 1$), respectively. During the first dehydration step, the value of activation energy obtained by Tang method is close to that obtained by Starink$^{1.92}$ method, and also the values of E_a obtained by Starink$^{1.95}$ and Starink$^{1.92}$

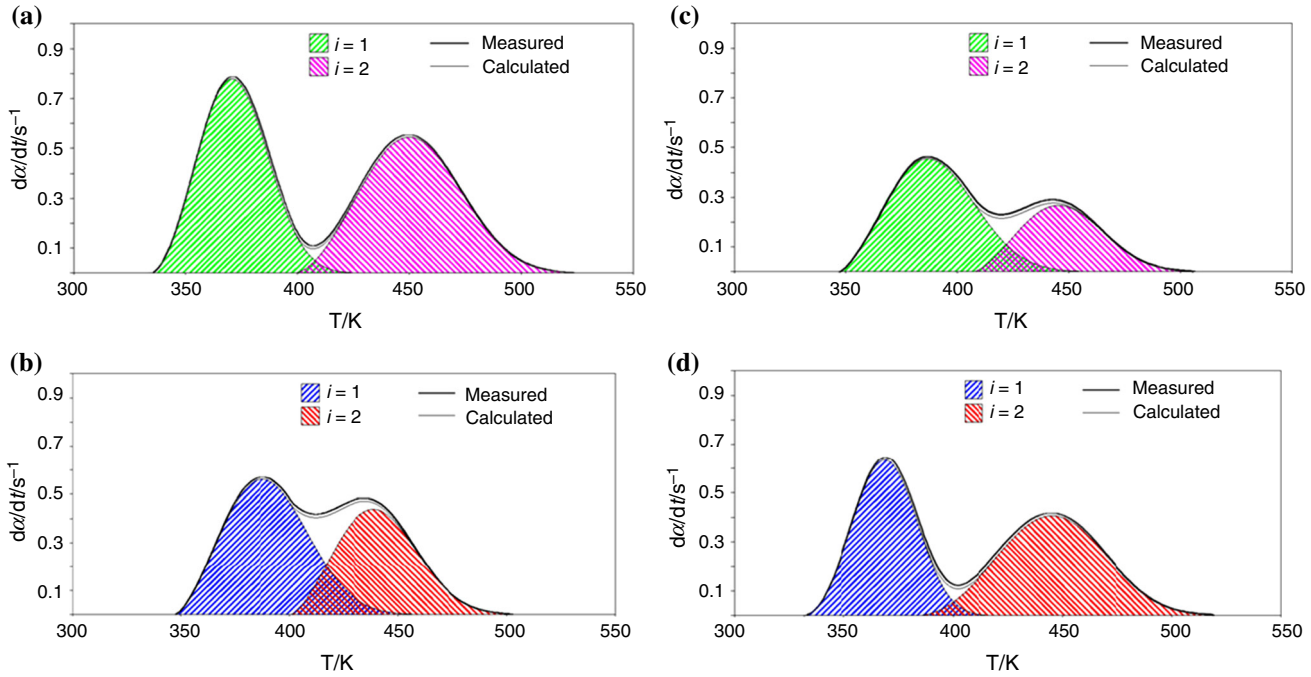

Fig. 13 Results of kinetic deconvolution analysis for the thermal dehydration of the sample using Bosewell (**a**), Tang (**b**), Starink[1.95] (**c**), and Starink[1.92] methods (**d**) under linear non-isothermal condition at β = 5 K min^{-1}

Table 2 Average values of kinetic parameters optimized for each reaction step of the thermal dehydration of sample under linear non-isothermal conditions

Methods	i	C_i	E_{ai}/kJ mol^{-1}	A_i/s^{-1}	$f(\alpha) = \alpha^m (1-\alpha)^n$ SB (m, n)	R^2
Bosewell	1	0.79 ± 0.01	105.81 ± 0.80	8.2 ± 0.9 × 10^{14}	m = 0.99 ± 0.01, n = 0.9 ± 0.2	0.9980
	2	0.21 ± 0.03	56.65 ± 0.30	6.01 ± 0.62 × 10^{6}	m = 0.05 ± 0.03, n = 1.3 ± 0.1	0.9971
Tang	1	0.79 ± 0.01	101.41 ± 0.42	7.2 ± 0.8 × 10^{12}	m = 0.11 ± 0.12, n = 1.1 ± 0.3	0.9981
	2	0.21 ± 0.05	55.81 ± 0.22	5.4 ± 0.2 × 10^{5}	m = 0.04 ± 0.01, n = 0.1 ± 0.4	0.9972
Starink[1.95]	1	0.79 ± 0.31	98.21 ± 0.48	6.8 ± 0.9 × 10^{11}	m = 0.3 ± 0.3, n = 1.12 ± 0.04	0.9986
	2	0.21 ± 0.42	52.42 ± 0.08	3.8 ± 0.5 × 10^{4}	m = 0.22 ± 0.05, n = 0.19 ± 0.08	0.9960
Starink[1.92]	1	0.79 ± 0.07	102.15 ± 0.07	7.6 ± 0.2 × 10^{13}	m = 0.41 ± 0.51, n = 0.99 ± 0.06	0.9987
	2	0.21 ± 0.11	52.55 ± 0.09	4.9 ± 0.3 × 10^{4}	m = 0.25 ± 0.02, n = 1 ± 0.2	0.9931

are very close to each other in the second step. The values of activation energy calculated using all the methods studied show similar trend. These E_a values are nearly coincident with one another and also in agreement with that determined for the overall reaction under isothermal and controlled rate conditions (Fig. 11). For the thermal dehydration, the empirical kinetic deconvolution of the overlapping reaction steps, all the kinetic parameters in Eq. 6 should be determined by graphically comparing the plot of $(d\alpha/dt)_{cal}$ versus t. After setting those initial values of kinetic parameters for each reaction stage (Table 1), an optimization operations (kinetic deconvolution) were performed to minimize F, defined as the squares of the sum of the difference between the experimental kinetic data $(d\alpha/dt)_{exp}$ versus t and $(d\alpha/dt)_{cal}$ versus t calculated for the linear non-isothermal kinetic data using Eq. (9) [61–63]

$$F = \sum_{j=1}^{n} \left[\left(\frac{d\alpha}{dt} \right)_{exp,j} - \left(\frac{d\alpha}{dt} \right)_{cal,j} \right]^2 \quad (9)$$

where M is the number of data points.

The thermal dehydration of barium titanyl oxalate and the removal of four molecules of water from BTO via thermal decomposition reaction can be brought through the following equation.

$$BaTiO(C_2O_4)_2{\cdot}4H_2O \overset{337-510\,K}{\longrightarrow} BaTiO(C_2O_4)_2 + 4H_2O \quad (10)$$

Figure 12 shows a comparison of activation energy needed for each resolved stage of the thermal dehydration as calculated by Bosewell, Tang, Starink[1.95], and Starink[1.92] methods in the temperature range of 337–510 K by column graph. From this graph, it is shown that during the first dehydration step the estimation of Ea values by Bosewell method is comparatively higher than that of all other methods and also activation energy obtained by Tang is very close to that obtained by Starink[1.92] method. In the second step, the values of Ea obtained by Starink[1.95] and Starink[1.92] are very close to each other.

To determine the initial values for all kinetic parameters, a statistical deconvolution method [64] was applied to the experimental kinetic rate data, and the separated kinetic rate data were analysed using the formal kinetic analysis method on the basis of each single-step reaction under linear non-isothermal conditions using the mathematical peak deconvolution procedure. Figure 13 shows the result of the kinetic deconvolution analysis for the thermal dehydration of sample using Bosewell, Tang, Starink[1.95], and Starink[1.92] methods on the basis of Eq. (9) after establishing the initial values for the kinetic parameters (Table 1), through mathematical deconvolution and the subsequent formal kinetic analysis of each resolved reaction step. Under linear non-isothermal conditions, for the sample at low temperature, the dehydration reaction was resolved into two steps [65]. During these overlapping processes for the removal of water molecules, all of the kinetic parameters were simultaneously optimized, and SB (m, n) model was used as the empirical kinetic model function. The average kinetic parameters optimized for the reaction at different β values are summarized in Table 2. For each resolved reaction steps, the value of E_a calculated for each reaction step is in agreement with the respective corresponding values estimated by the Bosewell, Tang, Starink[1.95], and Starink[1.92] plots for the overall reaction under non-isothermal conditions.

For the sample, each overlapping steps of the dehydration process have been empirically described by SB (m, n) kinetic model function as given in Table 2, the required average value of E_a in Bosewell, Tang, Starink[1.95], and Starink[1.92] methods is 105.81 ± 0.80, 101.41 ± 0.42, 98.21 ± 0.48, and 102.15 ± 0.07 kJ mol^{-1} (for $i = 1$) and 56.65 ± 0.30, 55.81 ± 0.22, 52.42 ± 0.08, and 52.55 ± 0.09 kJ mol^{-1} (for $i = 2$), respectively. Using the respective E_a values, experimental master plots of ($d\alpha/dt$) versus temperature for the separated first and second DSC peaks for each methods were drawn (Fig. 10) and satisfactorily fitted using the Sestak–Berggren SB (m, n) model m and $n \approx 0$–1, respectively. The values for the pre-exponential factor for the first and second peaks determined through nonlinear regression analysis for the fit using the SB (m, n) model for each method, Bosewell, Tang, Starink[1.95], and Starink[1.92], were $A_1 = (8.2 \pm 0.9) \times 10^{14}$, $(7.2 \pm 0.8) \times 10^{12}$, $(6.8 \pm 0.9) \times 10^{11}$, $(7.6 \pm 0.2) \times 10^{13}$ (for $i = 1$) and $A_2 = (6.01 \pm 0.6) \times 10^{6}$, $(5.4 \pm 0.2) \times 10^{5}$, $(3.8 \pm 0.5) \times 10^{4}$, and $(4.9 \pm 0.3) \times 10^{4}$ s^{-1} (for $i = 2$), respectively.

Conclusions

The kinetic behaviour, dehydration kinetics, and mechanism of BTO under linear non-isothermal condition have been studied using DSC, which show multistage kinetics through complex reaction pathways. The comparison of the results obtained with different calculation procedures, Bosewell, Tang, Starink[1.95], and Starink[1.92] shows that they strongly depend on the choice of model function of the process and also used to elucidate the thermal stability. The kinetic deconvolution method is used to yield the dependency of the E_a on the extent of conversion, and it is established that the dehydration of the sample shows a two-stage mechanism and can be described by Sestak–Berggren (SB) method. The results show that the two-parameter SB (m, n) is the most suitable for quantitative description of the dehydration process for the studied sample. The kinetic exponent m and n in SB (m, n) model for each reaction steps were set to $\approx$ 0–1 with expecting variation to a suitable value through the subsequent optimization occurs. From the result of kinetic deconvolution of the sample, the different phase changes of the reactant mixtures and the kinetic parameters of the respective thermal dehydration stages are evaluated accurately. The reaction mechanism was also proposed which depends on the morphology of the prepared sample and on the experimental result obtained from SEM, TEM, FT-IR, and XRD analyses.

References

1. Min C, Kim S, Lee C. Morphology of barium titanate particles produced by homogeneous precipitation. Bull Korean Chem Soc. 1997;18:600–3.
2. Pfaff G. Sol-gel synthesis of barium titanate powders of various compositions. J Mater Chem. 1992;2:591–4.
3. Hoffmann T, Doll T, Fuenzalida VM. Fabrication of $BaTiO_3$ microstructures by hydrothermal growth. J Electrochem Soc. 1997;144:292–3.
4. Pechini MP. Barium titanium citrate, barium titanium and processes for producing same. Patent US 3231328. 1996.

5. Kim JG, Ha JG, Lim TW, Park K. Preparation of porous $BaTiO_3$-based ceramics by high-energy ball-milling process. Mater Lett. 2006;60:1505–8.
6. Vinothini V, Singh P, Balasubramanian M. Synthesis of barium titanate nanopowder using polymeric precursor method. Ceram Int. 2006;32:99–103.
7. Ghosh S, Dasgupta S, Sen A, Maiti HS. Synthesis of barium titanate nanopowder by a soft chemical process. Mater Lett. 2007;61:538–41.
8. Jung YJ, Lim DY, Nho JS, Cho SB, Riman RE, Lee BW. Glycothermal synthesis and characterization of tetragonal barium titanate. J Cryst Growth. 2005;274:638–52.
9. Ragulya AV, Vasylkiv OO, Skorokhod VV. Synthesis and sintering of nanocrystalline barium titanate powder under non-isothermal conditions. I. Control of dispersity of barium titanate during its synthesis from barium titanyl oxalate. Powder Metall Met Ceram. 1997;36:170–5.
10. Bera J, Sarkar D. Formation of $BaTiO_3$ from barium oxalate and TiO_2. J Electroceram. 2003;11:131–7.
11. Wada S, Narahara M, Hoshina T, Kakemoto H, Tsurumi T. Preparation of nm-sized $BaTiO_3$ particles using a new 2-step thermal decomposition of barium titanyl oxalate. J Mater Sci. 2003;38:2655–60.
12. Huang C, Chen K, Chiu P, Sze P, Wang Y. The novel formation of barium titanate nanodendrites. J Nanomed. 2014;2014:1–7.
13. Clabaugh WS, Swiggard EM, Gilchrist R. Preparation of barium titanyl oxalate tetrahydrate for conversion to barium titanate of high purity. J Res Nat Bur Stand (U.S.). 1956;56:289–91.
14. Kudaka K, Ilzumi K, Sasaki K. Preparation of stoichiometric barium titanyl oxalate tetrahydrate. J Am Ceram Soc Bull. 1982;61:1236.
15. Fang TT, Lin HB. Factors affecting the preparation of barium titanyl oxalate tetrahydrate. J Am Ceram Soc. 1989;72:1899–906.
16. Fang TT, Lin HB, Hwang JB. Thermal analysis of precursors of barium titanate prepared by co-precipitation. J Am Ceram Soc. 1990;73:3363–7.
17. Yamamura H, Watanabe A, Shirasaki S, Moriyoshi Y, Tanada M. Preparation of barium titanate by oxalate method in ethanol solution. Ceram Int. 1985;11:17–22.
18. Amala Sekar M, Dhanaraj G, Bhat HL, Patil KC. Synthesis of fine-particle titanates by the pyrolysis of oxalate precursors. J Mater Sci. 1992;3:237–9.
19. Otta S, Bhattamisra SD. Kinetics and mechanism of the thermal decomposition of barium titanyl oxalate. J Therm Anal. 1994;41:419–33.
20. Gallagher PK, Schrey F. Preparation of semiconducting titanates by chemical methods. J Am Ceram Soc. 1963;46:567.
21. Balek V, Kaisersberger E. Preparation of $BaTiO_3$ by thermal decomposition of BTO simultaneously investigated by emanation thermal analysis, TG-DTA and EGA. Thermochim Acta. 1985;85:207–10.
22. Kiss K, Magder J, Vukasovigh MS, Lockhart RJ. Ferroelectrics of ultrafine particles size: 1. Synthesis of titanate powders of ultrafine particle size. J Am Ceram Soc. 1966;49:291.
23. Saburi O. Semiconducting bodies in the family of barium titanates. J Am Ceram Soc. 1961;44:54–63.
24. Gallagher PK, Thomson J. Thermal analysis of some barium and strontium titanyl oxalates. J Am Ceram Soc. 1965;48:644–7.
25. Swilam MN, Gadalla AM. Decomposition of barium titanyl oxalate and assesment of barium titanate produced at various temperatures. Trans J Brit Ceram Soc. 1975;74:159.
26. Yen FS, Chang CT, Chang YH. Characterization of BTO tetrahydrate. J Am Ceram Soc. 1990;73:3422.
27. Gopalakrishnamurthy HS, Rao MS, Kutty TRN. Thermal decomposition of titanyl oxalates–1. Barium titanyl oxalate. J Inorg Nucl Chem. 1975;37:891–8.
28. Sarada K, Muraleedharan K. Effect of addition of silver on the thermal decomposition kinetics of copper oxalate. J Therm Anal Calorim. 2016;123:643–51.
29. Fu XL, Fan XZ, Wang BZ, Huo H, Li JZ, Hu RZ. Thermal behavior, decomposition mechanism and thermal safety of 5, 7-diamino-4,6-dinitrobenzenfuroxan (CL-14). J Therm Anal Calorim. 2016;124:993–1001.
30. Atakol M, Atakol A, Yiğiter AÖ, Svoboda I, Atakol O. Investigation of energetic materials prepared by reactions of diamines with picryl chloride: synthesis, structure and thermal behaviour. J Therm Anal Calorim. 2017;127:1931–40.
31. Dollimore D, Griffiths DL, Nichoison D. The thermal decomposition of oxalates. Part II. Thermogravimetric analysis of various oxalates in air and in nitrogen. J Chem Soc. 1963;3:2617–23.
32. Koga N, Suzuki Y, Tatsuoka T. Thermal dehydration of magnesium acetate tetra hydrate: formation and in situ crystallization of anhydrous glass. J Phys Chem B. 2012;116:14477–86.
33. Kotru PN, Raina KK, Koul ML. The kinetics of solid-state decomposition of neodymium tartrate. Indian J Pure Appl Phys. 1987;25:220.
34. Schaube F, Koch L, Worner A, Steinha HM. A thermodynamic and kinetic study of the de- and rehydration of $Ca(OH)_2$ at high H_2O partial pressures for thermo-chemical heat storage. Thermochim Acta. 2012;538:9–20.
35. Fatu D. Kinetics of gypsum dehydration. J Therm Anal Calorim. 2001;65:213–20.
36. Modestov N, Poplankhin PV, Lyakhov NZ. Dehydration kinetics of lithium sulfate monohydrate single crystals. J Therm Anal Calorim. 2001;65:121–30.
37. Halawy SA, Fouad NE, Mohamed MA, Zaki MI. Kinetic and thermodynamic parameters of the decomposition of chromium chromate in different gas atmospheres. J Therm Anal Calorim. 2001;65:167–76.
38. Dalal PV, Saraf KB, Shimpi NG, Shah NR. Pyro and kinetic studies of barium oxalate crystals grown in agar gel. J Cryst Process Technol. 2012;2:156–60.
39. Horowitz HH, Metzger G. New analysis of thermogravimetric traces, analytical chemistry. Anal Chem. 1963;35:1464–8.
40. Freeman ES, Carroll B. The application of thermoanalytical decomposition of calcium oxalate mono-hydrate. J Phys Chem. 1958;62:394–7.
41. Nakamoto K. Infrared spectra of inorganic and co-ordination compounds. 2nd ed. NewYork: Wiley; 1969. p. 245.
42. Xiao CJ, Jin CQ, Wang XH. Crystal structure of dense nanocrystalline $BaTiO_3$ ceramics. Mater Chem Phys. 2008;111:2–3.
43. Koga N, Sesták J, Simon P. Some fundamental and historical aspects of phenomenological kinetics in the solid state studied by thermal analysis. In: Sesták J, Simon P, editors. Thermal analysis of micro, nano- and non-crystalline materials. Berlin: Springer; 2013. p. 1–28.
44. Koga N, Sesták J, Simon P. Ozawa's kinetic method for analyzing thermoanalytical curves. J Therm Anal Calorim. 2013;113:1527–41.
45. Bosewell PG. On the calculation of activation energies using a modified Kissinger method. J Therm Anal. 1980;18:353–8.
46. Tang W, Liu Y, Zhang H, Wang C. New approximate formula for Arrhenius temperature integral. Thermochim Acta. 2003;408:39–43.
47. Starink MJ. Activation energy determination for linear heating experiments: deviations due to neglecting the low temperature end of the temperature integral. J Mater Sci. 2007;42:483–9.
48. Wada T, Koga N. Kinetics and mechanism of the thermal decomposition of sodium per carbonate: role of the surface product layer. J Phys Chem A. 2013;117:1880–9.

49. Wada T, Nakano M, Koga N. Multistep kinetic behaviour of the thermal decomposition of granular sodium per carbonate: hindrance effect of the outer surface layer. J Phys Chem A. 2015;119:9749–60.
50. Yoshikawa M, Yamada S, Koga N. Phenomenological interpretation of the multistep thermal decomposition of silver carbonate to form silver metal. J Phys Chem C. 2014;118:8059–70.
51. Kitabayashi S, Koga N. Physico-geometrical mechanism and overall kinetics of thermally induced oxidative decomposition of tin(II) oxalate in air: formation process of micro structural tin(IV) oxide. J Phys Chem C. 2014;118:17847–61.
52. Koga N, Goshi Y, Yamada S, Perez-Maqueda LA. Kinetic approach to partially overlapped thermal decomposition processes; co-precipitated zinc carbonates. J Therm Anal Calorim. 2013;111:1463–74.
53. Koga N, Kasahara D, Kimura T. Aragonite crystal growth and solid-state aragonite-calcite transformation: a physico-geometrical relationship via thermal dehydration of included water. Cryst Growth Des. 2013;13:2238–46.
54. Koga N, Yamada S, Kimura T. Thermal decomposition of silver carbonate: phenomenology and physico-geometrical kinetics. J Phys Chem C. 2013;117:326–36.
55. Sanchez-Jimenez PE, Perejon A, Criado JM, Dianez MJ, Perez-Maqueda LA. Kinetic model for thermal dehydrochlorination of poly(vinyl chloride). Polymer. 2010;51:3998–4007.
56. Noda Y, Koga N. Phenomenological kinetics of the carbonation reaction of lithium hydroxide monohydrate: role of surface product layer and possible existence of a liquid phase. J Phys Chem C. 2014;118:5424–36.
57. Nusrath K, Muraleedharan K. Effect of nano-transition metal oxides of Fe, Co and Ni and ferrites of Co and Ni on the multistage thermal decomposition of oxalates of Ce(III). J Therm Anal Calorim. 2018. https://doi.org/10.1007/s10973-018-7648-2.
58. Sestak J, Berggren G. Study of the kinetics of the mechanism of solid-state reactions at increasing temperatures. Thermochim Acta. 1971;3:1–12.
59. Cai J, Liu R. Weibull mixture model for modelling nonisothermal kinetics of thermally stimulated solid-state reactions: application to simulated and real kinetic conversion data. J Phys Chem B. 2007;111:10681–6.
60. Avrami M. Kinetics of phase change. III. Granulation, phase change, and microstructure. J Chem Phys. 1941;9:177–84.
61. Barmak K. A commentary on: Reaction kinetics in processes of nucleation and growth. Met Mater Trans A. 2010;41:2711–75.
62. Ferriol M, Gentilhomme A, Cochez M, Oget N, Mieloszynski JL. Thermal degradation of poly(methyl methacrylate) (PMMA): modelling of DTG and TG curves. Polym Degrad Stab. 2003;79:271–81.
63. Font R, Conesa JA, Molto J, Munoz M. Kinetics of pyrolysis and combustion of pine needles and cones. J Anal Appl Pyrol. 2009;85:276–86.
64. Lopez G, Aguado R, Olazar M, Arabiourrutia M, Bilbao J. Kinetics of scrap tyre pyrolysis under vacuum conditions. Waste Manag. 2009;29:2649–55.
65. Sanchez-Jimenez PE, Perejon A, Criado JM, Dianez MJ, Perez-Maqueda LA. Kinetic analysis of complex solid-state reactions. A new deconvolution procedure. J Phys Chem B. 2011;115:1780–91.